A Family Album: the Growth and Evolution of Milky Way Analogues from $z = 5$ to the Local Universe

Vivian Yun Yan Tan

A Dissertation submitted to the Faculty of Graduate Studies in Partial Fulfillment of the Requirements for the Degree of Doctor of Philosophy

Graduate Program in Physics and Astronomy
York University
Toronto, Ontario

September 2025

Abstract

We present a breakdown of the evolutionary history of Milky Way-like galaxies up to redshift $z = 5$, using multi-wavelength optical and NIR photometry from the Hubble Space Telescope and the James Webb Space Telescope. We use abundance matching to find progenitors of Milky Way Analogs (MWAs) by evolving the cumulative number density of the current Milky Way backwards through time, and matching the stellar mass to the expected number density with stellar mass functions obtained from large-scale galaxy surveys. We determine resolved physical properties of MWA progenitors such as stellar mass density, star-formation rate (SFR), age, and metallicity, via SED-fitting to spatially resolved pixel bins of their photometry.

In the first part of this thesis, we use photometric data from the Hubble Frontier Fields DeepSpace catalog, a survey of six lensing clusters and their flanking fields in order to chart the mass assembly of MWA progenitors up to $z = 2$.

In the second part of this thesis, we extend the study of the mass assembly of MWA progenitors to $z = 5$ with the data from the Canadian NIRISS Unbiased Cluster Survey (CANUCS), using JWST NIRCam and NIRISS imaging. In the early universe, MWA progenitors show clear inside-out mass assembly with specific star-formation rates more enhanced on the outskirts than the inner regions, and more stellar mass added to the outskirts. They are also increasing in size but morphologically remain disk-dominated. Merger fractions increase with increasing redshift, pointing to hierarchical assembly at early times.

In the third part of this thesis, we examine the resolved age and stellar metallicities of the MWA progenitors in CANUCS to uncover details of their star-formation history. The slopes of the radial gradients of non-merging galaxies are in line with inside-out growth. The slopes of the radial gradients for ongoing and late stage mergers show enhanced star-formation across the entire galaxy. Metallicity evolves slowly with redshift for MWA progenitors, and mergers contribute to overall mass growth both through their added mass and their enhancement of star-formation, but do not meaningfully alter the chemical evolution history of the galaxy until $z \sim 1.5$.

Dedication

"One always finds one's burden again. But Sisyphus teaches the higher fidelity that negates the gods and raises rocks. He too concludes that all is well. This universe henceforth without a master seems to him neither sterile nor futile. Each atom of that stone, each mineral flake of that night filled mountain, in itself forms a world. The struggle itself toward the heights is enough to fill a man's heart. One must imagine Sisyphus happy."

— **Albert Camus**

To Past Me, you did it, you absolute freak!

Acknowledgements

First and foremost, I would like to extend my endless gratitude towards my tireless advisor, Dr. Adam Muzzin. Adam's brilliance as a researcher is only matched by his warmth and his kindness. He has an uncanny ability to bring out the best in his students and colleagues alike through his steadfast encouragement and his unending enthusiasm for astronomy. His keen eye for when research topics intersect is the core strength to our research group, and this allows us as his graduate students to help each other by applying our own expertise, and to know which postdocs or professors to turn to for specific science questions. I am truly grateful that Adam has introduced me to Dr. Lamiya Mowla and Dr. Kartheik Iyer, for which my collaboration with them resulted in a Nature publication. Although Adam keeps bemoaning that he dislikes teaching, Adam is truly one of the best teachers I've had, whether that is as my advisor or as a professor of some of my graduate astronomy courses. Adam's joviality and sense of humour also keeps up the spirits in our research group, which aided many of us, me included, through tumultuous periods such as lockdowns during the COVID-19 pandemic, and the long CUPE 3903 strike last year. Adam's passion is second to none. Without Adam's guidance, I would not be half the scientist I am today.

I am deeply grateful for my PhD committee members both present and past: Dr. Marshall McCall, Dr. Rahul Kannan, and Dr. Nassim Borzognia, for their attentive and rigorous guidance throughout my studies, and extend this gratitude to Dr. McCall, Dr. Rahul, Dr. Isaac Smith and Dr. Rachel Bezanson, whose careful reading of this thesis improved it in equal measure. During my Master's and the first half of my PhD, Dr. Cemile Marsan, who was first a postdoc, and then an adjunct professor at York University, gave me invaluable insight into the technical details behind SED-fitting, and offered me keen advice for my papers in the scope of analyses, and discussions of results. I thought of her as another mentor figure alongside Adam.

Next, I would like to thank everybody that I had the opportunity to work with in any capacity in this research group both graduate students and postdocs: Visal, Ghassan, Sunna, West, Naadiyah, Nelson, Katherine, Adit, Dr. Leo Alcorn, and Dr. Jacqueline Antwi-Danso. Visal started his Master's with Adam at around the same time I did, and we have worked closely to tackle the intricate details of resolved SED-fitting for the purposes of our individual projects. His ingenious solutions to tricky problems, such as his clump finding algorithm, inspired me to look for creative approaches to my own research questions. Ghassan, who is the powerhouse behind the CANUCS photometric catalogs and the first data release, has taken far too much of his busy time answering my questions about aperture photometry and flux error calibrations. Leo and Jacqueline, as the postdocs in our group, have given me invaluable feedback on my research process and drafts of my science papers. Cemile, Leo, and Jacqueline have also been instrumental in planning events for this cohort that helped us grow closer as a team, along with West and Naadiyah. I feel tremendously lucky that everyone in our research group is someone I would consider a friend.

Academia can be stereotyped as cold, distant, cut-throat and stuck-up, but that couldn't be further from the truth. Everyone that I've had the honour to work with so far has shattered these stereotypes. There has never been a community that is more welcoming, collaborative, and eager to support each other and bring out the best in one another as the astronomers I know.

Of course, I am ever grateful to my Mom and Dad for their unwavering support throughout the years. My parents were the first in their respective families to attend university, and so they understood the importance of a good education. As a child, my parents always nourished my interest in science. We borrowed many science books and educational shows from our local library, which was how I discovered my love for astronomy in the first place. I will never forget the birthday when they got me a simple refracting telescope, and my Dad and I attempted to observe Mars and Saturn with it on a clear night. My Mom frequently took me to the Ontario Science Centre during summer breaks, and we even got an annual pass for several years. If they were more typical Asian parents, they may have insisted I became something practical, like an engineer or an accountant. So I am extremely thankful they allowed me to pursue my passion, even if my Mom sometimes referred to my research as my "school project."

I am deeply thankful for my friends outside of astronomy, some of whom I've known since middle or high school, for keeping me "grounded" when my mind is in space. Without their companionship over the years, life would have been far more stressful, and I would be more narrow-minded without the richness of experience and the perspectives that they bring to my life. I would especially like to thank Jerry for graciously sharing his new living space with me during the last year of my PhD when my partner David relocated to Germany for his postdoc.

Last but certainly not least, I would like to thank my wonderful partner David, who stood beside me through my best and my worst days. We moved in together during graduate school, right as the COVID-19 lockdowns began. We survived cockroach infestations and awful landlords together. David is the light at the end of the tunnel that helped me get through the roughest of my mental health crises during the pandemic, and without him by my side, I could easily have given in to despair. David believed in me the most, even when I had lost faith in myself. I could not have asked for a better partner than him to go through this enormous stage of our lives together.

Contents

List of Tables

List of Figures

Table 1: List of galactic and extragalactic astronomy terms and acronyms used in this dissertation.

Acronym or symbol	**Meaning**	**Explanation**
MW	Milky Way	
MWA	Milky Way Analogue	
ΛCDM	Λ Cold Dark Matter	A cosmology that contains both cold dark matter (i.e. weakly interacting dark matter particles) and dark energy (represented by Λ). The curvature of this universe is assumed to be flat.
z	Cosmological redshift	The shift of an object's light to the redder end of the electromagnetic spectrum caused by the expansion of the universe. The age of the universe, as well as the lookback time at a specific redshift are determined by what cosmology is assumed.
Z	Metallicity	Abundance of all elements heavier than helium, usually expressed as a ratio to the amount of hydrogen within that object.
SED	Spectral Energy Distribution	The electromagnetic spectrum of an object, measured in energy density versus wavelength.
IFU	Integral Field Unit	An instrument that can obtain a spectrum/SED for each pixel in an image.
S/N or SNR	Signal to noise ratio	
SFR	Star Formation Rate	
SFH	Star Formation History	A function of SFR versus time, either in lookback time or age of the universe.
IMF	Initial Mass Function	A set of parameters representing the initial population of stars in a galaxy.
SPS	Stellar Population Synthesis	The method by which the observed flux of a galaxy and a set of initial parameters is given to determine the parameters of the *current* population of stars that exist in a galaxy.
UVJ Diagram		A way to determine if a galaxy is star-forming or quiescent by comparing its total flux in the rest frame UV, optical, and IR bands (u, v, and j bands respectively).
Sérsic profile		A method of quantifying how bulge-dominated or disk-dominated a galaxy is through measuring its flux distribution, introduced by Sérsic (1963).
R_e or R_{eff}	Effective radius	A radius which defines a circle that contains either half the total luminosity or half the total mass of a galaxy. Sometimes called the half-light radius or half-mass radius.
B/T ratio	Bulge to Total ratio	The luminosity or mass ratio between the bulge component of a galaxy and the entire galaxy.
NMI	Normalized Mutual Information	A method of determining how similar two images are by the quantifying the mutual information contained in the images.

Cont'd on following page

Table 1, cont'd

Acronym or symbol	Meaning	Explanation
HFF	Hubble Frontier Fields	High redshift galaxy survey using mainly Hubble Space Telescope photometry.
CANUCS	Canadian NIRISS Unbiased Cluster Survey	High redshift galaxy survey using James Webb NIRCam and NIRISS photometry as well as Hubble IR filters where available.
EAzY	Easy and Accurate (photo-)z's from Yale	SED-fitting code specializing in determining photometric redshifts from Brammer et al. (2008).
FAST	Fitting and Assessment of Synthetic Templates	Parametric SED-fitting code from Kriek et al. (2009)
DB	Dense Basis	Non-parametric SED-fitting code from Iyer & Gawiser (2017).
FIRE	Feedback In Realistic Environments	A series of hydrodynamical galaxy simulation projects with a focus on understanding feedback mechanisms (such as gas inflows/outflows).
TNG50	Illustris 'The Next Generation' 50 Mpc	A high resolution hydrodynamical simulation of a 50 Mpc^3 region of the universe.
MaNGA	Mapping Nearby Galaxies at APO (Apache Point Observartory)	A large survey of local galaxies ($z \sim 0$) which have resolved IFU spectroscopy.
CALIFA	Calar Alto Legacy Integral Field spectroscopy Area survey	A resolved IFU spectroscopic survey of nearby galaxies from the Calar Alto Observatory.

Chapter 1

Introduction

1.1 Our Place in the Universe

Humanity's idea of its place in the universe is ever-evolving. The Copernican Revolution is well-known for dismantling the idea of the Earth as the centre of the universe, but it was only in the last century that we upturned the belief that the entire universe was the Milky Way. The myriad of other galaxies that were observable with instruments at the time used to be known as "spiral nebulae." The German philosopher Immanuel Kant even dubbed them "island universes." It was a hundred years ago, in December 1925, that Edwin Hubble published his measurements of the Cepheid variables in NGC 6822 that proved definitively, that NGC 6822 was situated beyond the extent of our galaxy (Hubble, 1925). Edwin Hubble's findings settled a long-standing debate about the nature of the universe, but it also laid the groundwork for an entire field: extragalactic astronomy.

In extragalactic astronomy, the local or nearby universe is also synonymous with "The Present." Since the speed of light is fixed, the further a galaxy is, the further back in time the light was emitted. There is another effect on this light, which is that the more distant a galaxy is, the more its spectrum is shifted towards the red. This is called *cosmological redshift*, because it comes from the expansion of space. This was another discovery from our good friend Edwin Hubble (Hubble, 1929), and thus the Hubble constant, the rate of the expansion of space, was named after him. From this universal expansion came the development of our current understanding of cosmology, known as ΛCDM cosmology. Galaxy evolution under ΛCDM posits that early density perturbations in the universe gave rise to dark matter haloes, within which gas condensed into early galaxies, and the merging of those haloes and the primordial galaxies within them formed the larger galaxies that we see in the universe today. In order to test if these models are true, we must confirm them through observations.

After the separation of the galactic from the extragalactic, there were two generalized observational paths for the study of galaxy evolution. One method is to uncover the past history of the Milky Way by way of galactic archaeology, pioneered by Roman (1950). The other is by observing other galaxies and establishing a global view of universal galaxy assembly (i.e. Madau & Dickinson 2014). Both pathways have their limitations. Galactic archaeology has access to spectral, chemical, and kinematic data of unprecedented depth, but it is nevertheless limited to one galaxy. Observations of other galaxies, on the other hand, grant diversity in numbers, but resolution is limited and the amount to which they are limited depends highly on redshift. Panchromatic surveys of the nearby universe such as the Sloan Digital Sky Survey (SDSS, York et al. 2000), especially those equipped with IFU spectroscopy like CALIFA (Walcher et al., 2014), SAMI (Allen et al., 2015), and MaNGA (Bundy et al., 2015; Wake et al., 2017) can measure and map out spatially various physical properties of local universe galaxies. They allow direct comparison with the Milky Way on a structural level, such that we now have broad definitions for what constitutes a 'Milky Way Analogue' (MWA) at $z \sim 0$.

With pre-JWST deep space surveys such as the Hubble Deep Fields, VISTA(Emerson et al., 2004; McCracken et al., 2012), COSMOS (Scoville et al., 2007), CANDELS (Grogin et al., 2011; Koekemoer et al., 2011), and DESI (DESI Collaboration et al., 2016) among many others targeted towards higher redshift, we also have been able to determine global, integrated properties of all galaxies throughout time. The universal evolution of stellar mass growth, star formation rate, and even metallicity has been measured. However, spatially resolved studies of galaxies, similar to what has been done in the local universe, were limited in scope to the brightest galaxies at higher redshift, which tend to be progenitors of massive galaxies at $z = 0$. Now in the the era of JWST, with improvements to resolution and wavelength coverage in the IR, it is possible to resolve progenitors of Milky Way Analogues with greater precision.

This thesis takes the extragalactic approach, but specifically focuses on the evolution of the Milky Way and Milky Way Analogues. In a sense, the main goal of the thesis is to bridge the gap between the galactic and the extragalactic approach to galaxy evolution. Since we are in an era of a wealth of data both from within the Milky Way and from the distant universe, there has never been a better time to apply the tools used for extragalactic astronomy towards uncovering our own galaxy's history and growth since cosmic dawn.

1.2 The Milky Way's Past and Present

1.2.1 Galactic Archaeology

If our goal is a complete picture of the Milky Way's formation history, the place to begin is by observing the galaxy itself. Even though galactic archaeology was pioneered by Roman (1950), it was not dubbed 'archaeology' until Spite & Spite (1979). Other examples of early works in this field

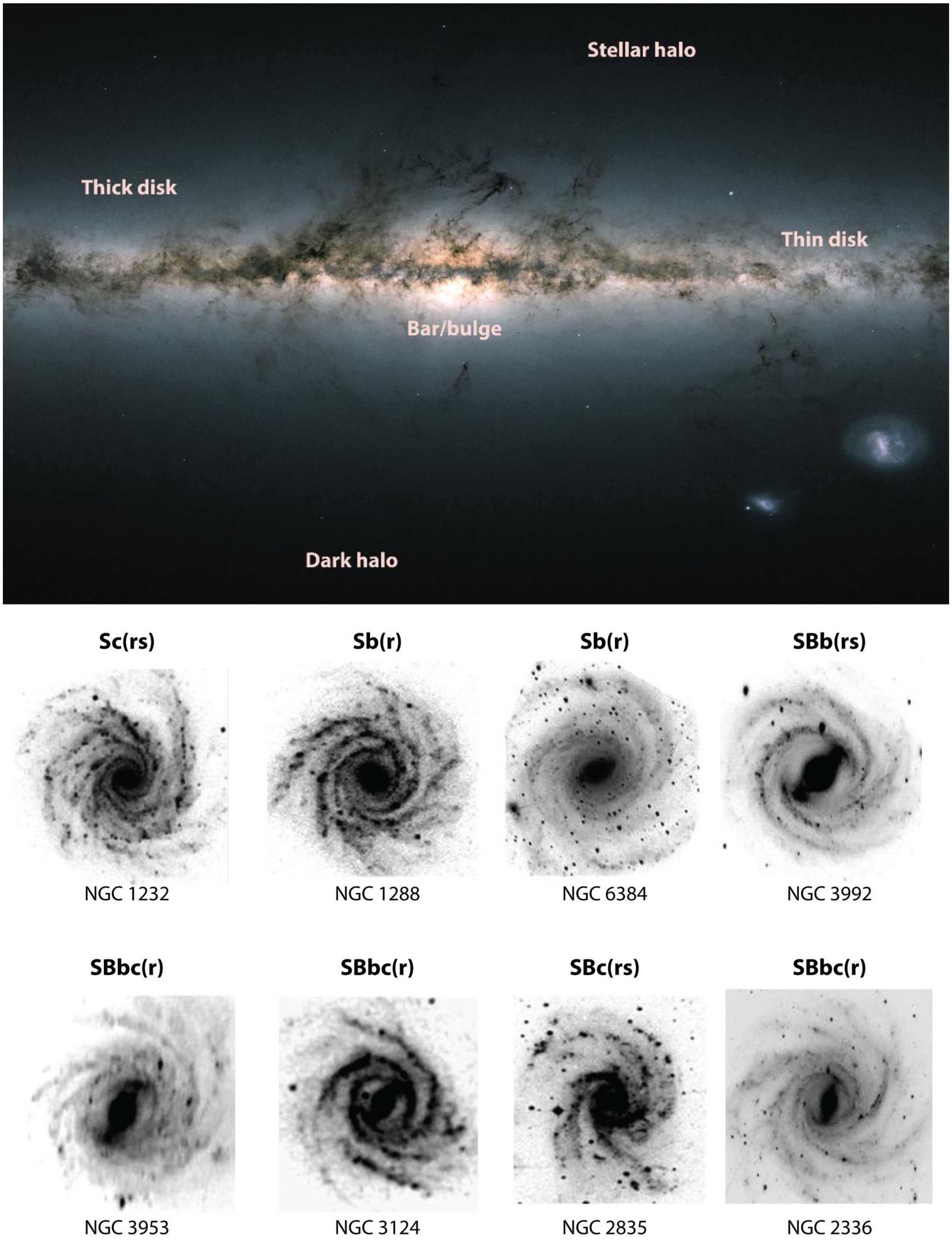

Figure 1.1: *Top panel:* Mosaic colour image reconstruction of the Milky Way from Gaia Collaboration et al. (2018), with labeled major parts, as shown in Helmi (2020). *Bottom panel:* A sample of spiral galaxies that morphologically resemble the Milky Way from Efremov (2011), replotted in Bland-Hawthorn & Gerhard (2016). Labels are their Hubble morphological type.

include Eggen et al. (1962); Searle & Zinn (1978), and Tinsley (1980) who also expanded stellar populations to other nearby galaxies (a more detailed description of this process is in §1.3). These papers established the process of uncovering the Milky Way's formation history via cataloging and modelling the evolution of the different stellar populations that exist in the different regions of our galaxy. By finding connections between certain chemical abundance patterns and their kinematics, we can extrapolate which stars formed "in-situ" in the disk, and which stars are merger remnants of past satellite galaxies (see the reviews from Freeman & Bland-Hawthorn 2002; Belokurov 2013; Frebel & Norris 2015; Bland-Hawthorn & Gerhard 2016, and Helmi 2020). Due to the connections between the early universe and the past formation history of the Milky Way, the term 'near-field cosmology' was coined by Bland-Hawthorn (1999) to describe the expanded purpose of galactic archaeology. It is linking the physical components of the Milky Way to the process of galaxy formation under the framework of ΛCDM cosmology.

1.2.2 The Milky Way's Components

The general components of the Milky Way are: (1) The thin disk of younger stars within which the Solar System resides. (2) The thick disk, which is dynamically hotter and thus has a longer vertical scale height. (3) The galactic bulge, which is not a classical bulge but a boxy/peanut-shaped 'pseudo-bulge'. (4) The galactic bar, which is a dynamical structure in the disk that is related to the oddity of the bulge. (5) The galactic halo, where there are older, metal poor populations such as globular clusters, as well as streams which may be remnants of past mergers (see review from Helmi 2020). The Milky Way's components as imaged by the Gaia Survey are shown and labeled in the top panel of Figure 1.1. The bottom panel displays face-on images of local universe morphological analogs of the Milky Way, both with and without bars. For the purposes of this thesis, we mostly discuss the formation of the two disks and the bulge, as it is near impossible to spatially resolve the stellar halos of other galaxies.

The thin disk has perhaps the least disputed mode of formation. Its oldest stars are aged 8-9 Gyrs (Tononi et al., 2019), which means it is younger than the thick disk (Kilic et al., 2017; Carollo et al., 2019). It formed inside-out as evidenced by the radially declining metallicity profile of the thin disk, and its shape is maintained through rotational support (Licquia & Newman, 2015). The most notable feature of the thick disk, apart from its thickness, is that it is more metal poor than the thin disk, and has a separate chemical sequence from the thin disk when plotted in [α/Fe] versus [Fe/H] space (Bensby et al., 2003; Fuhrmann, 2011). This means many of the stars in the thick disk have a different stellar evolution history than the stars in the thin disk. The formation of the thick disk has been a subject of debate since its discovery by Gilmore & Reid (1983), and even its existence was called into question (e.g. Bahcall & Soneira 1984; Fuhrmann 2011; Bovy et al. 2012). Before new data from the Gaia Collaboration clarified the history of the formation of the galactic thick disk, proposed formation pathways include: a minor merger onto a pre-existing disk (Quinn et al., 1993), accretion of satellites at a preferential direction (Abadi et al., 2003a), gas-rich early disks preventing the thick disk from dynamically settling (Brook et al., 2004; Bird et al., 2013), and stellar migration from the thin disk (Schönrich & Binney, 2009). After new data from Gaia, it is now understood that a large portion of the stars within the Milky Way's thick disk are linked to the major merger event, Gaia-Enceladus (or Gaia-Sausage-Enceladus, or the GSE merger), which occurred $\sim$ 10 Gyr ago. The estimate of the time frame of the merger is due to distribution of stellar ages in the thick disk peaking at $\sim$ 10 Gyr. This also means that the merger event triggered a starburst in the gas-rich early disk that became the thick disk today (Gallart et al., 2019).

The Milky Way does not have a classical bulge (i.e. a spheroidal, dispersion-supported bulge with a de Vaucouleurs profile), it instead has a boxy/peanut shaped bulge or 'pseudobulge' (McWilliam & Zoccali, 2010; Nataf et al., 2010; Wegg & Gerhard, 2013), which is dynamically tied to the bar, and the spheroidal component of the bulge is estimated to be $< 8\%$ of the mass of the disk (Shen et al., 2010). According to the review by Barbuy et al. (2018), there are two main bulge formation pathways: early bulge formation, where the bulge formed first through hierarchical assembly of proto-galaxies (e.g. Steinmetz & Muller 1995; Springel & Hernquist 2005), and late bulge formation, where a bar forms in a disk, and the bulge forms through bar instabilities (e.g. Combes et al. 1990; Raha et al. 1991; Norman et al. 1996). The processes that lead to early bulge formation were expected to only form classical bulges. However, Athanassoula et al. (2017) show hierarchical assembly through mergers can form a pseudobulge in a barred disk. As it is difficult to separate a 'pure' sample of old bulge stars with current data, a clear formation scenario for our galaxy's bulge remains inconclusive.

1.3 Spatially Resolved Galaxy Properties

One of the ways in which galactic and extragalactic astronomy is intricately linked is in studying the spectral energy distribution of other galaxies. All galaxies are comprised of stars, gas, and dark matter. The baryonic matter (mostly stars and gas) emit, absorb, scatter or otherwise interact with light across the electromagnetic spectrum. Measuring the full integrated light coming from a single galaxy in its spectral energy distribution (SED), allows us to understand the composition, current star formation, and formation history of that galaxy. Constraining stellar populations based on stellar evolution was pioneered by Tinsley (1968), and the groundwork was laid in the 1970s to fit combinations of stellar spectra to galaxies (Spinrad & Taylor, 1971; Searle et al., 1973; Faber, 1973; Tinsley & Gunn, 1976; Bruzual, 1983) Work in the following two decades greatly improved our understanding of stellar evolutionary theory, and 'stellar population synthesis' became the standard for modeling the SEDs of galaxies.

1.3.1 SED-fitting

SED fitting has become the most important tool of extragalactic astronomy because the SED encodes all of the past formation history of that galaxy. The review from Iyer et al. (2025) compiled 51 different SED-fitting codes as of its writing. It is important to recognize that SED-fitting is an inherently complex tool due to the large parameter space that must be explored for a "best fit" spectrum, but that spectrum is still only a fit, and may not be truly representative of the galaxy's real SED. Different codes may also give different results for the same set of data (see Pacifici et al. 2023 for testing various contemporary SED-fitting codes on the same dataset, and Iyer et al. 2025 for the most up-to-date explanations of the inner workings of SED-fitting). Although fitting to spectroscopic data is more accurate due to the higher density of data points, SED fitting to photometry is reliable when there is high signal-to-noise, and the range of filters can adequately sample the continuum from the UV to the IR with multiple bands, which aptly describes the photometry we use from HST and JWST.

The main part of a galaxy's SED is the stellar continuum. To generate the stellar continuum, SED-fitting use a process called stellar population synthesis (SPS). First, a simple stellar population (SSP) is generated, which contains a set of related SEDs from template libraries of stellar spectra that represent a single population of stars in one epoch. An SSP can be generated through an input of an age t and a metallicity Z, but the inner mechanisms for the SSP is built from the choice of initial mass function (IMF), the stellar isochrones, and the libraries of template SEDs. Some examples of SSPs are shown in panels (A) and (B) of Figure 1.2, where (A) are a set of SSPs with fixed metallicity and varying age, and (B) is fixed age with varying metallicities.

The initial mass function (IMF) describes the birth mass of stars for a particular galaxy. The IMF is considered to be a fundamental quantity to galaxy evolution. However, since it is not a quantity that we can observe directly, and must be inferred from observations, there are disagreements on the correct shape of the IMF (see the reviews Kroupa et al. 2013; Hopkins et al. 2018, and Hennebelle & Grudić 2024). Choice of IMF as the input can greatly affect the stellar continuum, and thus measurements like the total stellar mass and SFR. The most common choices of IMF used are Salpeter (1955), Kroupa (2001), and Chabrier (2003). All three are plotted in panel (C) of Figure 1.2.

Isochrones are the evolutionary tracks of different stars on the Hertzprung-Russell diagram, which is luminosity as a function of effective temperature. Isochrone tables exist for stars with $0.1M_{\odot} < m < 100M_{\odot}$. The outputs of isochrones can only be converted to template SEDs from spectral libraries (Conroy, 2013). Both spectral libraries and isochrones can be empirical or theoretical, where theoretical isochrones and spectra are based on complex models of stellar evolution of various types of stars. Some examples of common SPS codes include Bruzual & Charlot (2003), FSPS (Conroy & Gunn, 2010), MILES (Vazdekis et al., 2010; Falcón-Barroso et al., 2011) PARSEC (Bressan et al., 2012), and MIST (Choi et al., 2016). SPS codes that account for binary fractions in stars include BPASS (Eldridge et al., 2017) and POSYDON (Fragos et al., 2023). Isochrones and stellar spectral libraries are shown in panel (D) and (E) respectively of Figure 1.2. Once simple stellar populations are generated, the star formation history (SFH) and chemical enrichment history $Z(t)$, combined with a treatment for dust attenuation and re-emission, finalizes the composite stellar population (CSP), which represents the output SED to the initial flux data. This is panel (F) in Figure 1.2.

1.3.2 Resolving Milky Way Analogues

Without SED-fitting, the only comparisons we could make between the Milky Way and other galaxies are through morphology and colour. Older extragalactic studies have done so, and to their credit, these studies are still extremely valuable, and much of the peculiarities of the Milky Way that we know of today were discovered through colour-magnitude comparisons. For example, Gadotti (2009) performed bulge-disk decompositions of 1000 galaxies of similar stellar mass to the Milky Way using *gri* band imaging. Mutch et al. (2011) discovered the Milky Way lies in the "green valley" region, in between the star-forming blue cloud and the quiescent red sequence. Licquia et al. (2015) expanded this comparison with Milky Way Analogues (MWAs) in the SDSS, and showed how the MW and MWAs lie in both colour-magnitude but also the star-forming main sequence (SFR versus stellar mass). We must make a note that the latter requires calculating the total stellar mass and SFR of the Milky Way via an implementation of SPS, as explained in Licquia & Newman (2015), and the SDSS sample of MWAs also used SED-fitting to determine total stellar mass and SFR (Aihara et al., 2011) As data improves, we naturally move towards SED-fitting for obtaining more accurate physical quantities such as stellar mass and SFR.

With IFU surveys such as SAMI, CALIFA, and MaNGA that can measure spectra of different parts of a single galaxy, we do not have to limit ourselves to studying only the integrated properties. IFU surveys allowed astronomers to resolve physical properties of different parts of a single galaxy. Thus we can start to ask questions about how these parts interacted and evolve together; the same questions that we investigate within the Milky Way can be applied to others. For example, are there signatures of past feedback in disk galaxies of the local universe? What are the chemical abundances variations or age variations within other galaxies?

Sánchez et al. (2014) measured radial metallicity gradients in CALIFA for disk galaxies, with a focus on barred versus unbarred galaxies. They found that there were no differences in the gradients between barred and unbarred galaxies, which meant bars do not radially mix stellar populations. González Delgado et al. (2015) measured gradients of dust, metallicity, and age across the Hubble sequence, and concluded that gradients are most correlated to stellar mass surface density, or the depth of the potential well, and not to morphology. This has implications for feedback mechanisms at higher redshift. Goddard et al. (2017) investigated age and metallicity gradients in MaNGA

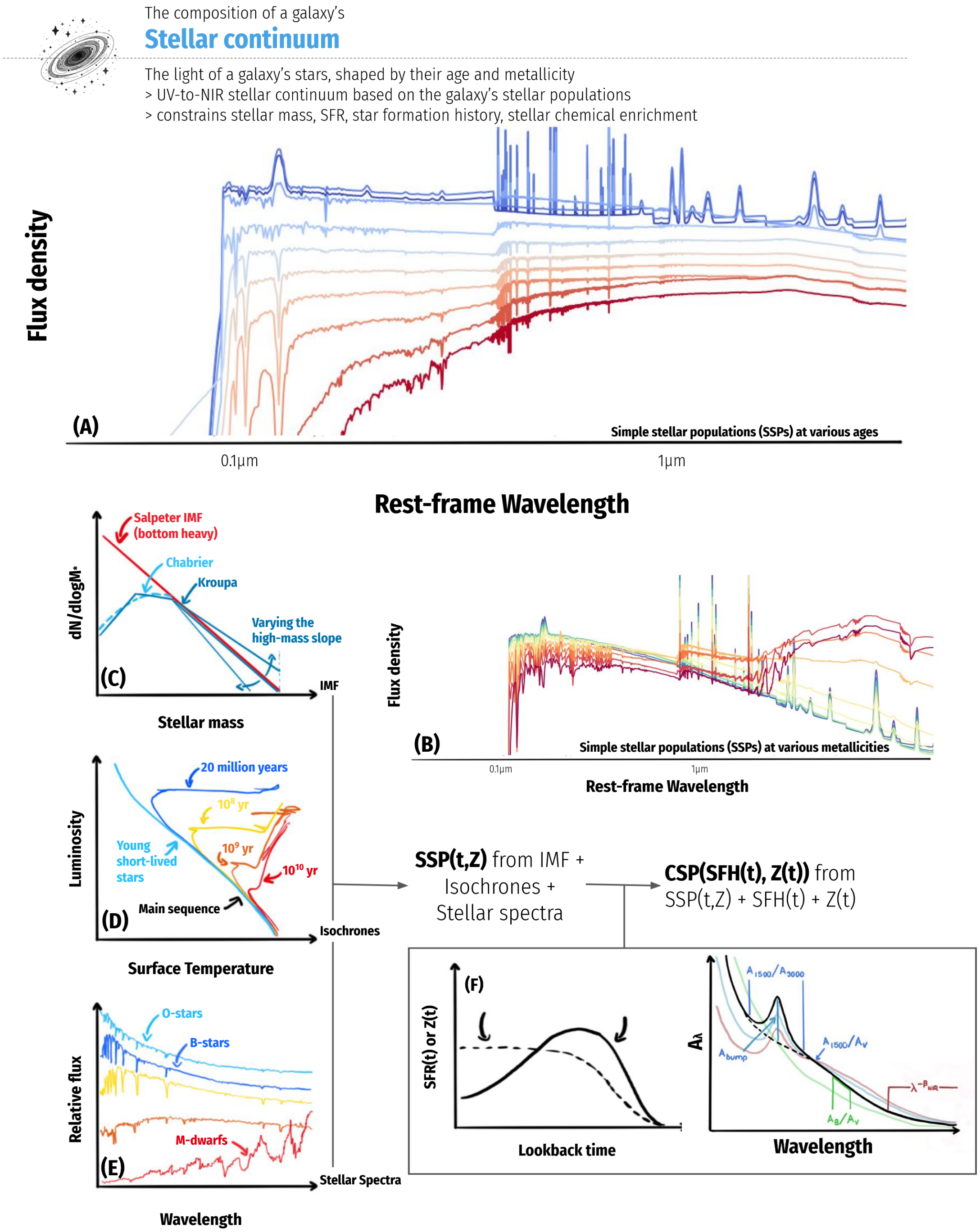

Figure 1.2: A demonstration of stellar population synthesis, an integral part of SED-fitting. This figure is adapted from Figures 3 and 5 of Iyer et al. (2025). Panels (A) and (B) show a set of SSPs at the same metallicity but various ages, or the same age and different metallicities respectively. Panels (C), (D), and (E) show varios IMFs, isochrones, and surface temperatures: choices of which can better constrain the parameter space for the best-fitting SEDs from the SSPs presented. Finally, (F) displays the SFH and dust attenuation, which once applied to the SSPs create a composite stellar population (CSP) that becomes the SED to best represent the stellar continuum of the target galaxy.

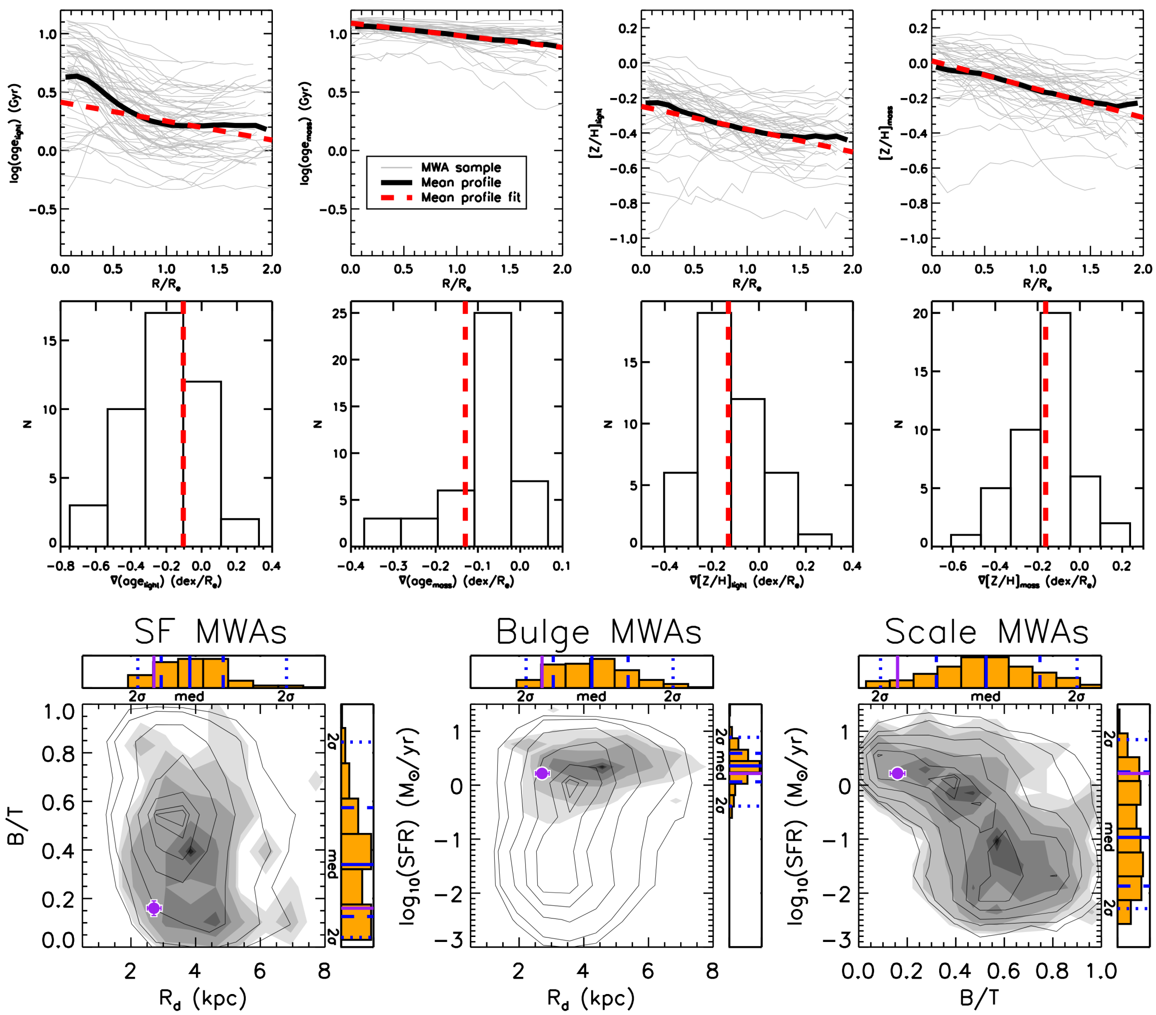

Figure 1.3: *Top panel:* Radial age and stellar metallicity [Z/H] gradients of MWAs in the MaNGA survey, bar plots represent the distributions of their slopes, from Boardman et al. (2020a). *Bottom panel:* 2D histograms of distributions of the properties of MWA population samples chosen by similarities to the MW in star formation, bulge-to-total (B/T) ratio, or radial scale length from Boardman et al. (2020b). The MW is shown in purple.

galaxies to show that elliptical galaxies have outside-in formation histories while disk galaxies have inside-out formation histories. Zheng et al. (2017) investigated the dependency of gradients on mass and environment, and found that both metallicity and age gradients as well as the integrated metallicity and age of the whole galaxy are more related to mass than to environment, although low mass galaxies are younger and have less metals in low density environments. Belfiore et al. (2017) also measured gas phase metallicity, specifically to determine the N/O ratio, and found the central regions of massive galaxies have reached a 'metallicity equilibrium' in the gas phase, but their outskirts continue to evolve for N/O. Boardman et al. (2020a,b) compares the spatially resolved properties of MWAs in MaNGA to the MW itself. Their main results are that depending on how a sample of MWAs in the local universe is defined, there will always be variability and scatter in their properties, even if their average properties are similar to within 1σ of the MW's properties. Key figures from the two papers are shown in Figure 1.3.

1.4 Galaxy Evolution and the High Redshift Universe

The current formalism for the study of galaxy evolution at high redshift actually began with theoretical models of how galaxies are born and grow in a universe with ΛCDM cosmology, in a process now known as hierarchical assembly (e.g. White & Rees 1978; Peebles 1982; Blumenthal et al. 1984; Davis et al. 1985; Kauffmann et al. 1993). To confirm these models, there have been many surveys of the high redshift universe that aim to create a complete picture of galaxy assembly from the earliest times to present day. The history of extragalactic astronomy, like most of recent scientific history, is one of the growth of large datasets.

Work began at the end of the last century with surveys targeting different parts of the electromagnetic spectrum in the aims of measuring the luminosity function of galaxies and their evolution with redshift. Measuring the star formation rate density (SFRD) of the universe requires UV, FIR, and emission lines, while the stellar mass density (SMD) relied primarily on NIR and optical. UV is emitted by bright, young type O and B stars, and so the UV continuum tracks star formation on timescales of roughly 10 Myr. Emission lines, particularly Hα, trace ionized hydrogen in nebulae, another signature of star formation. FIR traces star formation because dust grains absorb UV photons and re-emit them in the FIR. Meanwhile, the mass-to-light ratio peaks in the NIR because cooler stars are more numerous and live longer than UV-bright stars, so NIR is a tracer of stellar mass. SED-fitting on the entire continuum is also used widely to derive stellar masses.

Most of the studies that measure the cosmic star formation history use UV based observations because *rest frame* UV is more detectable for a larger range of redshifts. The first studies to perform SFRD measurements across different redshifts were Lilly et al. (1996) and Madau et al. (1996). Lilly et al. made a measurement of the SFRD up to $z = 1$ with UV and optical surveys, and Madau et al. extended this to $z \sim 3$ with Lyman break galaxies (UV-bright highly star-forming galaxies at high-z with a 'break' in their spectrum at 912Å caused by absorption of UV photons by neutral hydrogen). This technique is now one of the standards of detecting star-forming galaxies as well as measuring high-z star formation. The most recent constraints on the UV luminosity at high redshift ($8 < z < 13.2$) with JWST observations from Harikane et al. (2025) show much higher star formation efficiencies than at lower redshifts.

Studies comparing the stellar mass evolution of galaxies between low and high redshift began around the same time as the earliest SFRD measurements with Cowie et al. (1996) and Gavazzi et al. (1996). The total stellar mass of the local universe, and the local co-moving SMD could be measured at greater accuracy with the availability of spectroscopic data from large scale surveys such as 2dFGRS, 2MASS, and SDSS (e.g. Cole et al. 2001; Bell et al. 2003). A Schechter function best describes the cumulative density of both (a power law at the faint/low mass end and an exponential cutoff at the bright/high mass end). If low mass galaxies are not detected because they are below the magnitude limit at a certain redshift, the low end of the SMF can be estimated by fitting the existing data to a Schechter function. However, even detected low-mass galaxies may have uncertain stellar masses, since they tend to be the brightest low mass sources, so they are detected in the UV but may not be in the IR. This results in their stellar continuum having a greater outshining bias, leading to underestimated stellar mass.

Madau & Dickinson (2014) have compiled data from 17 studies for comsic SMD and 13 studies for cosmic SFRD of the universe up to $z \sim 8$. This can mitigate some of the issues with limited area for high redshifts, and test for agreement between different studies. The cosmic SMD and SFRD as a function of redshift are shown in the top left and top right panels of Figure 1.4. They found that all the surveys indicated a peak for cosmic star formation at around $z \sim 2-3$, an era now known as 'cosmic noon'. The review from Madau & Dickinson (2014) also note that while their overall fit to the combined results of all the studies agreed between the SFRD and SMD, typically the the total SFR over-predicts the stellar mass formed when converted. This can be seen in the bottom panels of Figure 1.4 when their best-fit model is converted into a SFH, and the derived global sSFR (SFR/$M_\star$) and metallicity does not match the sSFR and metallicity evolution from other observations in the literature.

1.4.1 Connecting Local to High Redshift

While the total cosmic stellar mass density or star formation rate density is important for the big picture quantities in galaxy evolution, it certainly does not capture the nuances of how the stars form inside galaxies, and what specific physics occur during episodes of star formation. Therefore, it can be useful to search the high redshift universe for progenitors of a specific population of local universe galaxies. Utilizing the evolution of the SMF with redshift, one can link progenitors and descendants

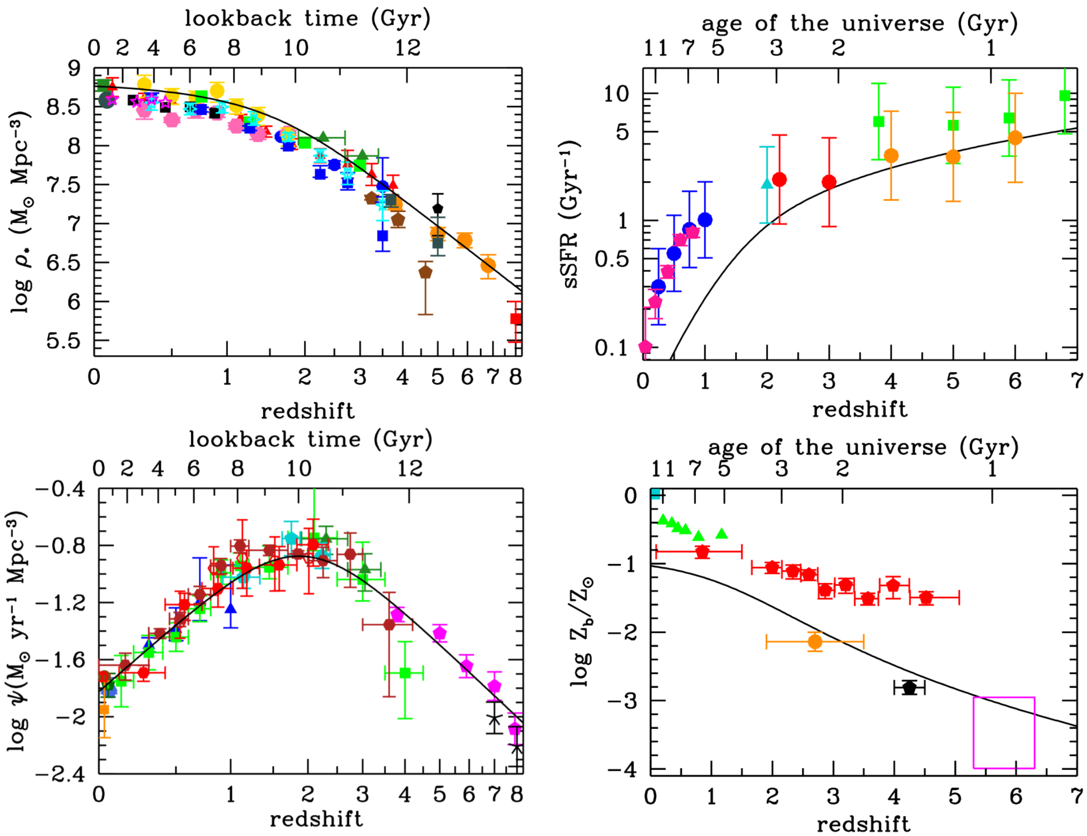

Figure 1.4: Clockwise from top left: The estimated global stellar mass density, specific star formation rate, mean metallicity, and star formation rate density as a function of redshift, from Madau & Dickinson (2014). The black line in the SFRD plot is the best fit to the data, while the black lines in the other panels were derived from the best fit SFRD as a comparison to other observations.

through number density. The earliest studies to link progenitors and descendants focused on massive galaxies and used a fixed cumulative number density (e.g.van Dokkum et al. 2010; Bezanson et al. 2011; Brammer et al. 2011; Ownsworth et al. 2014). There were also studies aimed at the progenitors of Milky Way-like galaxies for fixed number densities (e.g. van Dokkum et al. 2013; Patel et al. 2013; Morishita et al. 2015). However, due to aforementioned hierarchical assembly of galaxies at early times, an evolving number density is more accurate because mergers can change the rank order of galaxies, biasing the progenitor selection. A selection using halo abundance matching, starting with the number density of the galaxy in the *local universe* and finding its progenitors at high redshift is an effective way to determine a less biased sample (Behroozi et al., 2013a; Leja et al., 2013; Torrey et al., 2017). Papovich et al. (2015) has done a study of Milky Way and M31 progenitors to $z \sim 3.5$, and Hill et al. (2017b) has likewise done a similar abundance matching study for progenitors of massive galaxies up to $z \sim 5$. We note that all of the studies listed are spatially resolved, however, they still rely on sizes measured from profile-fitting to photometry, and obtain mass densities from assuming mass-to-light ratios for the radial profiles.

We also should not expect that galaxies at high redshift to simply be smaller versions of local galaxies once they are spatially resolved. One example of this is clumpy galaxies. A common feature among star-forming galaxies at cosmic noon is that the vast majority of them have bright UV clumps, regions of intense star formation (e.g. Förster Schreiber et al. 2009; Wuyts et al. 2012; Sok et al. 2022). However, the number of clumpy galaxies decline at low redshift, and there are no similar clumpy SFGs in the local universe. Lensed images of young galaxies in the early universe show that clumps were also common in the epoch of reionization (Vanzella et al., 2023; Adamo et al., 2024; Mowla et al., 2024). There is evidence that the presence of large star-forming clumps are correlated to gas rich disks and may form from disk instabilities (e.g. Krumholz & Dekel 2010; Mayer et al. 2016). However, Sok et al. (2025) finds from spectroscopic data of $z \sim 0.7$ galaxies that clumps form from the inflow of metal poor gas and has no relation to instabilities, leading to the possibility that clumpiness increases with higher redshift because of greater gas accretion. Additionally, the number of galaxy mergers is also expected to increase with redshift (e.g. Duncan et al. 2019; Duan et al. 2024), which could complicate the detection of clumps at $z > 4$, since it may be hard to distinguish between merging systems and star-forming clumps. Nevertheless, both mergers and star-forming clumps are vital to the assembly history of galaxies.

1.5 This Thesis

While there have been previous studies on the assembly of MWAs by linking the high and low redshift universe, those studies rely primarily on deriving physical measurements from rest-frame photometry without SED-fitting. This results in uncertainties from the outshining bias and mass-to-light ratios, which will change with increasing redshift.

Chapter 2's aim is to combine spatially resolved SED-fitting that has been performed in the local universe to higher redshift, in combination with finding a robust evolutionary sample for MWAs up to $z \sim 2$ using abundance matching. We make use of multiband photometry from the Hubble Frontier Fields DeepSpace catalog to ensure enough signal-to-noise for the spatial bins in each galaxy. The physical measurements of stellar mass density and SFR density are more constrained when obtained from SED-fitting. Additionally, we use the technique of obtaining morphological information directly from the stellar mass maps for more accurate morphological characteristics of MWAs. Chapter 3 utilizes a much larger sample of MWA progenitors from the Canadian NIRISS Unbiased Cluster Survey (CANUCS) up to $z \sim 5$, and further refines measurements of the mass density and SFR density both with the addition of JWST broad and medium band photometry, as well as an SED-fitting code that uses non-parametric SFHs. Expanding the sample of progenitors from $z \sim 2$ to $z \sim 5$ can reveal the early growth of disk galaxies in a turbulent universe with higher merger rates and more intense episodes of star formation. Chapter 4 takes advantage of the ability of Dense Basis to fit non-parametric SFHs in order to measure the resolved mass-weighted age and stellar metallicities of the MWA progenitors from CANUCS. Starbursts and stellar feedback can alter the chemical gradients of galaxies, but a major merger event can also leave chemical signatures in the stellar populations of the galaxy, as seen with our own galaxy. Measuring the resolved metallicity and age gradients in both mergers and non-mergers could uncover how events like the GSE merger affected the chemical evolution of galaxies like the Milky Way.

Chapter 2

The Assembly of Milky Way Analogues at Redshifts $0.5 < z < 2$

A version of this chapter is published as: **"A Measurement of the Assembly of Milky Way Analogues at Redshifts** $0.5 < z < 2$ **with Resolved Stellar Mass and Star-Formation Rate Profiles"** Tan et al. (2024a), ApJ vol. 964, p. 177.

Full Author List: Vivian Yun Yan Tan (main analysis, discussions, conclusions), Adam Muzzin (supervisor), Danilo Marchesini (comments), Visal Sok (comments), Ghassan T. E. Sarrouh (comments), and Cemile Marsan (comments).

Abstract

The resolved mass assembly of Milky-Way-mass galaxies has been previously studied in simulations, the local universe, and at higher redshifts using infrared (IR) light profiles. To better characterize the mass assembly of Milky Way Analogues (MWAs), as well as their changes in star-formation rate and color gradients, we construct resolved stellar mass and star-formation rate maps of MWA progenitors selected with abundance matching techniques up to z $\sim$ 2 using deep, multi-wavelength imaging data from the Hubble Frontier Fields. Our results using stellar mass profiles agree well with previous studies that utilize IR light profiles, showing that the inner 2 kpc of the galaxies and the regions beyond 2 kpc exhibit similar rates of stellar mass growth. This indicates the progenitors of MWAs from $z \sim 2$ to the present do not preferentially grow their bulges or their disks. The evolution of the star-formation rate (SFR) profiles indicate greater decrease in SFR density in the inner regions versus the outer regions. Sérsic parameters indicate modest growth in the central regions at lower redshifts, perhaps indicating slight bulge growth. However, the Sérsic index does not rise above $n \sim 2$ until $z < 0.5$, meaning these galaxies are still disk dominated systems. We find

that the half-mass radii of the MWA progenitors increase between $1.5 < z < 2$, but remain constant at later epochs ($z < 1.5$). This implies mild bulge growth since $z \sim 2$ in MWA progenitors, in line with previous MWA mass assembly studies.

2.1 Introduction

Observations of stars and gas within the Milky Way have long been the primary method of deciphering its formation and evolutionary history (Freeman & Bland-Hawthorn 2002; Freeman et al. 2013; Bovy et al. 2012; Bovy & Rix 2013; Rix & Bovy 2013, see Bland-Hawthorn & Gerhard 2016; Helmi 2020 for reviews). However, the Milky Way is certainly not unique, and is a rather typical galaxy in the universe. It is a spiral galaxy with a mass of $5 - 6 \times 10^{10} M_{\odot}$ (Mutch et al., 2011; Licquia et al., 2015; Bland-Hawthorn & Gerhard, 2016) which exists in a low density environment, and it currently resides in the green valley, the transition state between star-forming and quiescent. It has a bulge with an extent of $R \sim 2$ kpc in the major axis, a bar with half-length $\sim$ 5kpc (Wegg et al., 2015), and a stellar disk that extends out to $R \sim$ 15kpc (Robin et al., 1992; Ruphy et al., 1996; Minniti et al., 2011). We wish to place the Milky Way in the context of how it formed, especially in relation to Milky Way Analogues in the local and the higher redshift universe. One way to do this is to utilize observations of Milky Way Analogues (MWAs) at higher redshifts to trace the evolution of our galaxy over cosmic time. There are many ways to define MWAs; however, for the purpose of this paper we define them only by stellar mass.

The morphology of star-forming galaxies in the local universe suggests that star formation occurred in two phases, with bulges forming first and disks forming around them later, also known as "inside-out" formation (van den Bosch, 1998; Muñoz-Mateos et al., 2007; Wang et al., 2011; Goddard et al., 2017), with even the Milky Way's inner and outer disk forming in phases as well (Haywood et al., 2013). An alternative picture posits that the stellar disks formed first, and then bulges grew later through secular processes (Dekel et al., 2009; Martig et al., 2009), which may be the case for lower mass galaxies but not higher mass ones, which tend to quench inside-out (Cappellari, 2013). However, observations in the local universe show dwarf galaxies may have had alternating periods of outside-in and inside-out growth (Ibarra-Medel et al., 2016). There is also evidence that outside-in quenching may be linked to belonging to denser environments such as clusters and large groups (Gavazzi et al., 2013; Schaefer et al., 2017). It is still an open question whether galaxies like the Milky Way formed inside-out or outside-in, or if the color gradient present in the Milky Way and similar spirals developed in a different way.

Specifically for MWAs, some studies have approached understanding the formation of MWAs from simulations (Abadi et al., 2003b,a; Oñorbe et al., 2015; Torrey et al., 2017; Buck et al., 2020; Sotillo-Ramos et al., 2022; Hasheminia et al., 2022). Buck et al. (2020) find MW-like stellar disks form most of their mass in-situ and only 5% of the mass is from mergers. Sotillo-Ramos et al. (2022) find that MWAs can even survive major mergers with their disk intact but somewhat thicker. Hasheminia et al. (2022) found MWAs have no evolution in their half-mass radii for the last 10 Gyr, which coincides with redshift $z \sim 2$. While simulations offer one solution to uncovering a dynamic picture of the formation history of the Milky Way, there are limitations to the utility of their results. This is related to the particle resolution, the size of the region being simulated, the treatment of gas, stars, and dark matter, and other factors such as cosmological parameters or hydrodynamics, which have different treatments depending on which simulation code is used.

There are also abundance matching studies that focus on the progenitors of massive galaxies in the local universe ($M_\star > 10^{11} M_\odot$, such as Ownsworth et al. (2014); Mundy et al. (2015); Ownsworth et al. (2016), and Hill et al. (2017b). Ownsworth et al. (2014) found that major and minor mergers contribute up to 17% and 34% respectively of added stellar mass seen at $z = 0.3$ since $z \sim 3$, in comparison to the 24% added by star-formation, by comparing merger-adjusted number densities to constant number densities. However, massive galaxies are more likely to be quiescent, and are on average less star-forming compared to the Milky Way. Mundy et al. (2015) is a simulation-based study which found that the choice of number density in past epochs affects the recovered SFR and SFH of progenitors. Ownsworth et al. (2016) and Hill et al. (2017b) both find the quiescent fraction to be $\sim 90\%$ at $z < 1$, but the former used a fixed cumulative number density and the latter used an evolving cumulative number density. Therefore, at $1 < z < 2$, Ownsworth et al. (2016) find the majority of their massive galaxy progenitors to be quiescent, while for the progenitors in Hill et al. (2017b), they are still majority star-forming at the same redshift. Nevertheless, both studies agree that at earlier epochs ($z \gtrsim 2$), massive galaxies assembled mass primarily via star-formation, while at later epochs, most mass was assembled via mergers.

Three studies that use an observational approach, and which are seminal to furthering our understanding of the evolution of MWAs up to high redshift are van Dokkum et al. (2013), Patel et al. (2013), and Papovich et al. (2015). van Dokkum et al. (2013) (hereafter VD13) used a constant number density through time to select MWAs at redshifts up to $z \sim 3$, with stellar mass functions from Marchesini et al. (2009). Their results show that the bulges and disks grow together in lockstep throughout the probed redshift. Using a constant comoving number density may not be the most accurate assumption to make for high redshift observations, due to galaxy mergers changing local density (Behroozi et al., 2013a,b; Leja et al., 2013; Lin et al., 2013).

Patel et al. (2013) (hereafter P13) used a different approach for choosing their sample: the star-forming main sequence. They used the relationship between specific star-formation rate (sSFR) to stellar mass, and chose their sample of MW progenitors from the sSFR-mass plane from Karim et al. (2011). The evolution of star-forming galaxies that led to a final mass was at $10^{10.5} M_\odot$, as computed by Leitner (2012), was the basis of the stellar mass selection of their MWAs at higher redshift. On average, P13 find MWA progenitors to be more star-forming and less massive when compared to VD13 across the same redshift range. Interestingly, both studies agree in their findings that there are no strong indications for inside-out or outside-in growth in their progenitors, despite the different mass and redshift ranges. In fact, both works show that the inner and outer regions grow in lockstep with each other from $z \sim 3$ to the present epoch.

Papovich et al. (2015) (hereafter P15) utilized abundance matching in concordance with number density evaluations on the zFOURGE/CANDELS fields to define and delineate the different evolutionary phases that progenitors of MW-like and M31-like galaxies go through since $z \sim 3$. For the MW-like progenitors, the galaxies go from blue and star-forming at $z > 2$ to IR-bright and dust obscured from $1 < z < 1.8$, where the overall maximum SFR is measured, and SFR begins to steadily decrease as Sérsic indices increase at $z < 1$ to the present epoch. P15 also find that M31-like galaxies begin and end each evolutionary stage earlier than MW-like galaxies. All three of these studies listed above rely *solely* on the observed light profiles to make arguments about morphology and mass assembly. Here we aim to extend the study of mass assembly of the MW by using SED-fitting to create spatially-resolved stellar mass profiles, as well as resolved star-formation rate profiles. This should bring a clearer and more accurate picture of the underlying morphological changes that progenitors of Milky Way-like galaxies undergo in the past 10 Gyr.

In this paper, we utilize abundance matching of galaxies from redshifts $0.5 < z < 2$ to select Milky Way analogues. We build upon the stellar mass map studies in Tan et al. (2022), from which we utilize the same methods to create resolved stellar mass and SFR profiles to trace the mass assembly for MW-like progenitors over time. Our abundance matching is based on the assumption that the approximate rank order of galaxies remains consistent throughout cosmic time, even as they grow in stellar mass, but also includes merger trees to account for slowly declining number density as galaxy haloes merge together due to gravitational interactions. Abundance matching techniques have previously been employed to study both MWAs and massive galaxies (Yang et al., 2012; Moster et al., 2013; Marchesini et al., 2014; Torrey et al., 2017; Kravtsov et al., 2018).

In §2.2, we give further information on the Hubble Frontier Fields DeepSpace catalogs and which photometric filters were used, as well as the COSMOS/UltraVISTA survey from which the Schechter functions for comoving number densities is derived. Our methods for constructing resolved 1-D and 2-D stellar mass and SFR profiles are outlined in detail in §2.3. In §2.4, we present the results of our analysis on the mass assembly and change in SFR over cosmic time for our sample of MWA progenitors. Our discussions of the implications of these results in comparison to previous works that used IR light profiles, as well as comparisons to simulations of MW progenitors are in §2.5. For this work we assume a ΛCDM cosmological model of the universe with $\Omega_\Lambda = 0.7$ and $\Omega_M = 0.3$, along with a Hubble constant of $H_0 = 70$ km/s/Mpc. We assume a Chabrier IMF (Chabrier, 2003) for our determination of the stellar masses of our sample. Our magnitudes are reported in AB magnitudes.

2.2 Data Sample

2.2.1 Hubble Frontier Fields

The Hubble Frontier Fields (HFF; Lotz et al. 2017) are comprised of six lensing clusters at redshifts of $0.3 < z < 0.6$ and six flanking fields imaged in the UV, optical, and NIR with the Advanced Camera for Surveys (ACS) and Wide Field Camera 3 (WFC3) on the Hubble Space Telescope (HST). We use the DeepSpace catalog from Shipley et al. (2018) to select our sample of MWA progenitors. For this study, we primarily use the parallel flanking fields of the DeepSpace catalog, but also include the cluster fields as long as the objects' redshifts are outside the redshift range of the respective cluster's redshift by $z \pm 0.1$. This is because the Milky Way does not live within a cluster, so the number density of the fields is better suited to search for MWAs.

The redshift of our MWA sample spans from $0.3 < z < 2$, with only two galaxies at $z < 0.5$ (one at $z \sim 0.31$, another at $z \sim 0.42$). Based on the WFC3 and ACS PSF size, this implies an angular resolution of $0.25 - 0.50$ kpc per pixel and $0.8 - 1.5.$ kpc per PSF FWHM. In all modeling we use the images that are PSF-matched and convolved to the WFC3/F160W resolution from Shipley et al. (2018) to ensure consistent resolution in each filter. The F160W filter has a PSF FWHM of ~ 0.177", which translates to a pixel size of 2.95 pixels. The PSFs for each filter are derived from stacking at least 3 or more isolated and unsaturated stars. The total science area covered by HFF DeepSpace is 156.1 arcmin^2. Since we were not able to make use of Abell1063clu, the total area that is used in this work is only 150.5 arcmin^2.

For the flanking fields, each of the pointings has 7 filters (F435W, F606W, F814W, F105W, F125W, F140W, and F160W), except for the parallel field of MACS0416, which was imaged with 9 filters (the same 7 listed before, as well as F775W, and F850LP). For a more in-depth discussion on the DeepSpace catalog, we refer the reader to Sections 2 and 3 of Shipley et al. (2018).

2.2.2 Stellar Mass functions

In order to perform abundance matching to select progenitors of MWAs based on stellar mass, the stellar mass functions (SMFs) are needed. The stellar mass functions used in this paper come from the COSMOS/UltraVISTA Survey (Muzzin et al., 2013b). The SMFs were measured from a sample of over 95,000 K_s-selected galaxies up to $z = 4$. They used 30 photometric bands to cover a wavelength range of $0.15\mu\text{m} - 24\mu\text{m}$. In addition to photometry from UltraVISTA (McCracken et al., 2012), the catalog also includes additional data from GALEX, Subaru/SuprimeCAM, CFHT, and Spitzer.

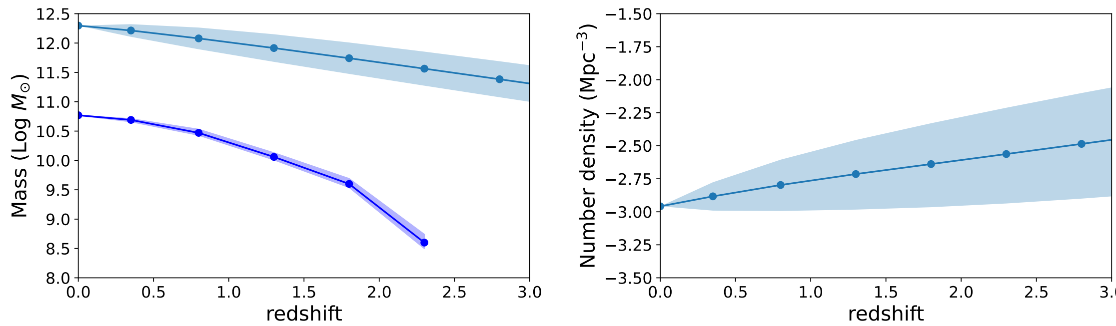

Figure 2.1: *Left panel:* The evolution of the median halo mass (light blue) and the median stellar mass (dark blue) of MWAs from $z = 3$ to $z = 0$. *Right panel:* The median integrated comoving number density for MWAs. The values at each redshift step is generated from the code by Behroozi et al. (2013b). The shaded regions represent 1σ from the median.

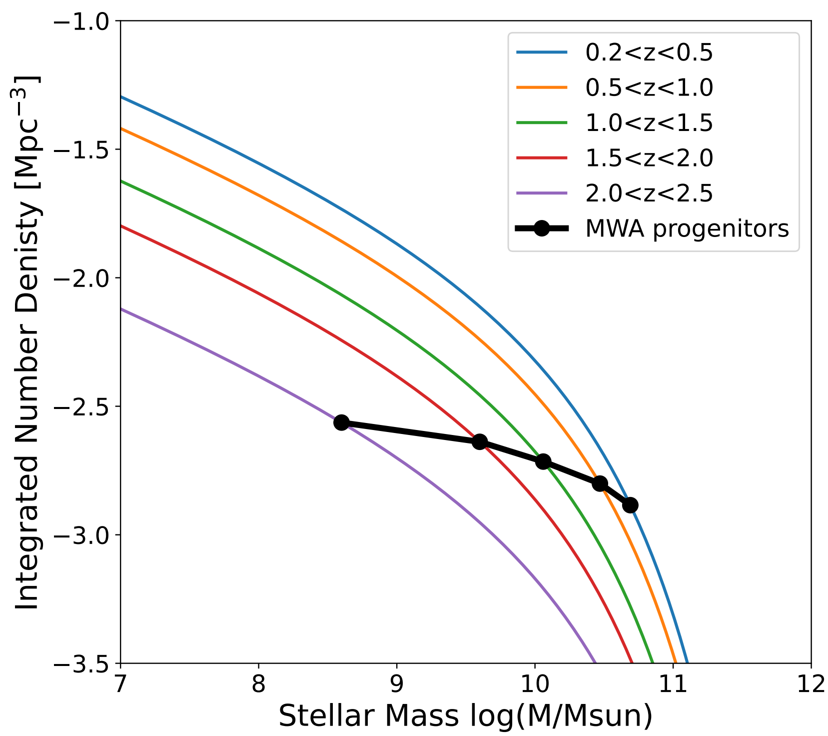

Figure 2.2: Integrated number density of galaxies from stellar mass functions (SMFs) from Muzzin et al. (2013a), and each black point is the median stellar mass of MWAs at the redshift range represented by each SMF. The number densities in black are calculated using the Behroozi et al. (2013b) code and are also shown in the right panel of Figure 2.1.

2.3 Methods

2.3.1 Abundance matching

Our goal is to connect progenitors of MWA over cosmic time to measure their stellar mass growth. To do this, we adopt the semi-empirical approach using abundance matching presented in Behroozi et al. (2013a). The Behroozi code takes into account merger rates of galaxies at higher redshifts such that the comoving number density shifts to a slightly higher number density as redshift increases. These merger trees come from simulations of dark matter halos that the galaxies inhabit. Their code matches the rank order of galaxies according to stellar mass or luminosity with dark matter halos in decreasing order of peak historical halo mass. For our stellar mass range, the comoving number density increases $\lesssim 0.1$ dex for every 0.5 increase in redshift, in comparison to assuming a constant number density throughout cosmic time.

We begin by determining the initial comoving number density for galaxies assuming the stellar mass of the Milky Way to be $10^{10.77} M_\odot$. This stellar mass value is generally within the accepted range of $10.5 \lesssim \log 10(M_\star/M_\odot) \lesssim 11$, albeit on the higher end (de Rossi et al., 2009; Bland-Hawthorn & Gerhard, 2016; Sotillo-Ramos et al., 2022). This mass agrees with values for the stellar mass and initial comoving number density given in Marchesini et al. (2009) for a MW-mass galaxy, which VD13 used in order to determine their MWA progenitors. This mass also corresponds with a comoving number density of $\log(\rho) = -2.95 \log(\mathrm{Mpc}^{-3})$, which is similar to the density used in P15 for their MW progenitor sample.

Figure 2.1 plots the range of number densities and halo masses at higher redshifts for MWAs, with the solid lines indicating the median values, and the shaded blue regions indicating the 1-σ deviation. This figure demonstrates how the code from Behroozi et al. (2013a) determines the possible previous number densities at higher redshifts, given an initial number density at $z = 0$. It is also able to determine the possible previous halo masses from the initial number density, and vice versa, using a relation between the cumulative number density to halo mass. The range of possible number densities and halo masses increases with increasing redshift because the code from Behroozi et al. (2013a) takes into account merger trees of halos. This means that a halo that exists at a given current number density at $z = 0$ could have formed either from one particular halo in the past growing in isolation, or from mergers of smaller halos.

In order to find the stellar masses of the MWA progenitors from the given previous number densities, they must be matched up to stellar mass functions from large scale observations. Figure 2.2 shows the method of obtaining the median stellar mass of the MWA progenitors using the stellar mass functions (SMFs) from the UltraVISTA survey from Muzzin et al. (2013a). For each of the SMFs that correspond to a range of redshifts, a stellar mass is matched to each of the median number densities predicted for that redshift by the code from Behroozi et al. (2013a). The minimum and maximum stellar mass for each redshift bin is taken to be the stellar mass at the median redshift ± 0.2 dex, which gives a more conservative estimate for the stellar mass range than using the corresponding stellar masses obtained from the SMFs with the number densities $\pm 1\sigma$. Performing the same exercise with mass functions from Davidzon et al. (2017) results in the progenitor masses being different by $0.01 - 0.14$ dex, making the difference in dex < 0.2 dex at all redshifts.

Our total sample of galaxies is 110 within the redshift range of $0.3 < z < 2$, after the removal of 16 galaxies from the cluster fields for having magnification values exceeding 2.5 as computed from the Bradač et al. (2009) lensing models, and a further removal of 18 galaxies from both cluster and flanking fields combined, from inspection of faults in their stellar mass maps (i.e. segmentation map falsely separated one object into two, too low signal to noise for enough spatial bins). There are 95 galaxies in the parallel fields and 15 galaxies in the cluster fields.

2.3.2 Stellar mass and SFR map construction

In Figures 2.3 and 2.4, we display the colour images and the stellar mass maps of all 110 galaxies in our sample. Figure 2.3 contains all 95 MWA progenitors from the parallel fields and Figure 2.4 contains the 15 progenitors from the cluster fields. The colour images are constructed from the filters that are the closest match to rest-frame U-band , rest-frame V-band, and the $F160W$ filter.

Figure 2.5 shows the colour image, F160W cutout, stellar mass map, and SFR map of several galaxies in our sample of various compactness. As stated before, the images are all PSF-matched and convolved to the WFC3/F160W resolution to ensure consistent resolution in each filter. The angular resolution is $0.25 - 0.50$ kpc per pixel and $0.8 - 1.5.$ kpc per PSF FWHM, for the redshift range $0.3 < z < 2$. From the HFF DeepSpace catalogs, the smallest effective radius in our sample is 3.27 pixels, and the largest effective radius is 18.1 pixels. The size of the FWHM of the PSF in pixels is 2.95, so using 2 times the effective radius as the size of the galaxy in pixels, the most compact galaxy is 2.2 times the PSF FWHM, and the most extended galaxy is 12.3 times the PSF FWHM. The effective radii are based on the detection image, which is a combination of the reddest filters from F814W to F160W as measured by `SExtractor`.

The first step to generating resolved stellar mass profiles as well as resolved SFR profiles is to spatially bin the images containing the photometry of the MWA progenitors. We apply the Voronoi tessellation algorithm from Cappellari & Copin (2003), and SED-fitting with FAST++ (Kriek et al., 2009; Schreiber et al., 2015), in order to generate the stellar mass maps of the MWA progenitors from their photometry. The reason why we chose the Voronoi tessellation method for pixel-binning is due to the geometry of the tessellated bins being able to best homogenize the SNR throughout the entire image of the galaxy, and in a way which preserves maximum spatial resolution in the geometry of the shape of the bins. For each galaxy, a lower limit for SNR of 10 is placed on each bin. But most galaxies at $z < 1.5$ have enough signal to noise that an SNR lower limit of 30 is used

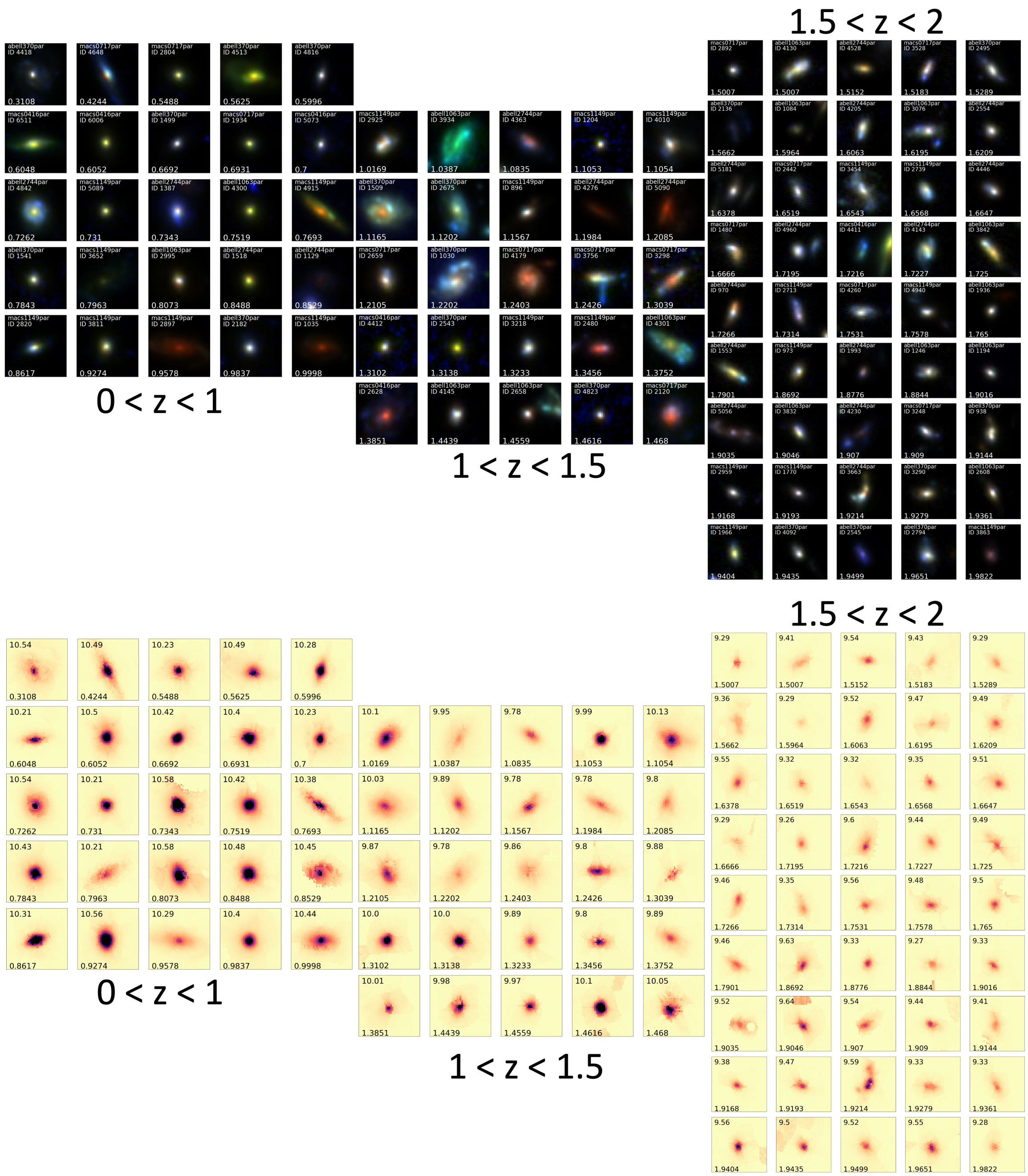

Figure 2.3: *Top:* Colour images of MW progenitors in the HFF DeepSpace parallel flanking fields at different redshifts. *Bottom:* Resolved stellar mass maps of the same MW progenitors. The min-max scale for the mass maps has the maximum set to $2 \times 10^8 M_{\odot}$. The redshift of the sources is displayed on the bottom left of each thumbnail.

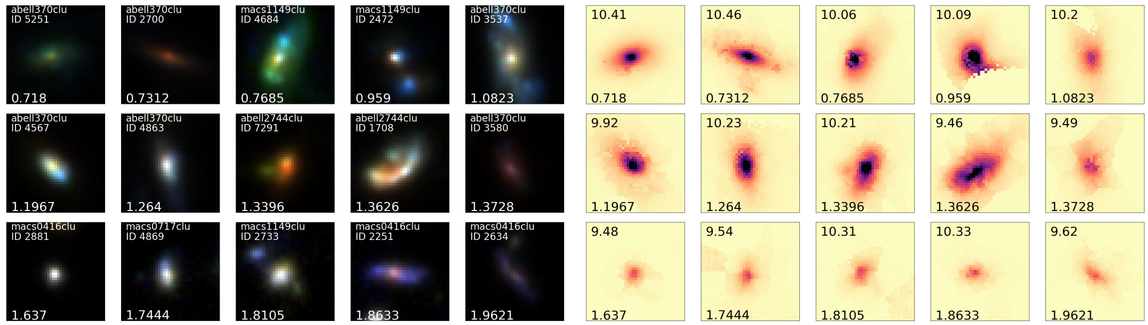

Figure 2.4: *Left:* Colour images of MW progenitors in the HFF DeepSpace cluster fields at different redshifts. Every galaxy is beyond the cluster's redshift, and also has magnification effects of < 2.5. *Right:* Resolved stellar mass maps of the same MW progenitors. The min-max scale for the mass maps has the maximum set to $2 \times 10^8 M_{\odot}$. The redshift of the sources is displayed on the bottom left of each thumbnail.

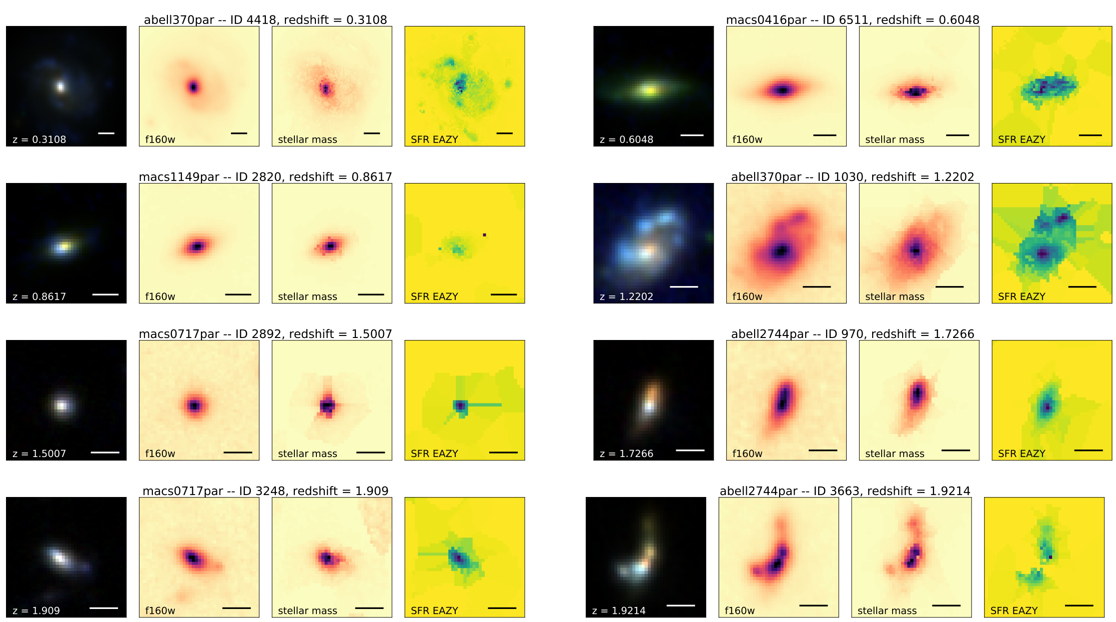

Figure 2.5: Comparison of colour image, F160W , stellar mass, and SFR profiles. The horizontal line in the bottom right represent 3×FWHM of the F160W PSF. The third object from the top, in the left column(MACS0717PAR ID 2892) is the most compact object in terms of its effective radius respective to the PSF's FWHM at that redshift.

instead.

In the SED-fitting of the photometry of the selected galaxies, we use BC03 stellar populations (Bruzual & Charlot, 2003), a Chabrier IMF Chabrier (2003), a Calzetti dust law (Calzetti et al., 2000), and a delayed tau model SFH. The SED-fitting code FAST is used due to the accuracy and robustness of the stellar mass outputs. We note that using a Calzetti dust law and a delayed tau model SFH may not be accurate to the star-formation history of the Milky Way; delayed tau models allow only for a rising SFH at the very beginning, but have a declining SFH for the vast majority of cosmic time. In the redshift range probed by this work however, a declining SFH is a reasonable assumption, since the global trend of cosmic SFR has been declining since $z \sim 2$.

Once a stellar mass is obtained for each spatial bin, we construct the stellar mass map for that object. The maps have the degraded resolution of the Voronoi tessellation, however we regain the original resolution by an additional scaling applied to each pixel. We distribute the amount of stellar mass within one bin to each of its constituent pixels according to the pixel's contribution to the F160W flux. For more information on the details of resolved stellar mass map construction, we refer the reader to Tan et al. (2022).

In addition we have also created 2-D star-formation rate maps. The SFR profiles were *not* derived from FAST SED-fitting, because while assuming a delayed tau model SFH results in reasonable stellar mass derivations up to $z \sim 3$ (see appendix of Muzzin et al. 2013a), it *does not* result in the most accurate SFRs for galaxies at higher redshifts. Therefore, we instead derive SFR from the integrated UV luminosity calculated using EAZY (Brammer et al., 2008), by placing a UV-filter (1400-1600Å) on the rest-frame fitted spectra and obtaining the total rest-frame UV luminosity. To lessen the effect of parameters on the resulting fits, we still used a delayed tau SFH, a Chabrier IMF, and a Calzetti dust law. However, the template libraries were from FSPS (Conroy & Gunn, 2010). We then apply a dust correction using the Calzetti dust law curve with the A_V derived from the HFF DeepSpace catalog (i.e. the A_V outputted by FAST while fitting for the integrated stellar mass of each object.)

Once the stellar mass maps have been constructed, we obtain 1D stellar mass density profiles for each galaxy by placing down elliptical apertures/annuli centered on the galaxy of increasing radial distance (each are 0.2 kpc in width) up to 20 kpc distance in the major axis, and then taking their stellar mass surface density. The same process is also used on the resolved SFR maps to create 1D SFR profiles, also up to 20 kpc. The major and minor axes, as well as the position angles used to determine the placement of the annuli are from the HFF DeepSpace photometric catalog, extracted from their detection filters which utilized a combination of $F814W$, $F105W$, $F125W$, $F140W$, and $F160W$ bands.

This makes it a fair comparison with the light profiles in the works of P13 and VD13 because the former also integrated the profiles out to 20 kpc and the latter out to 25 kpc. We also mask out

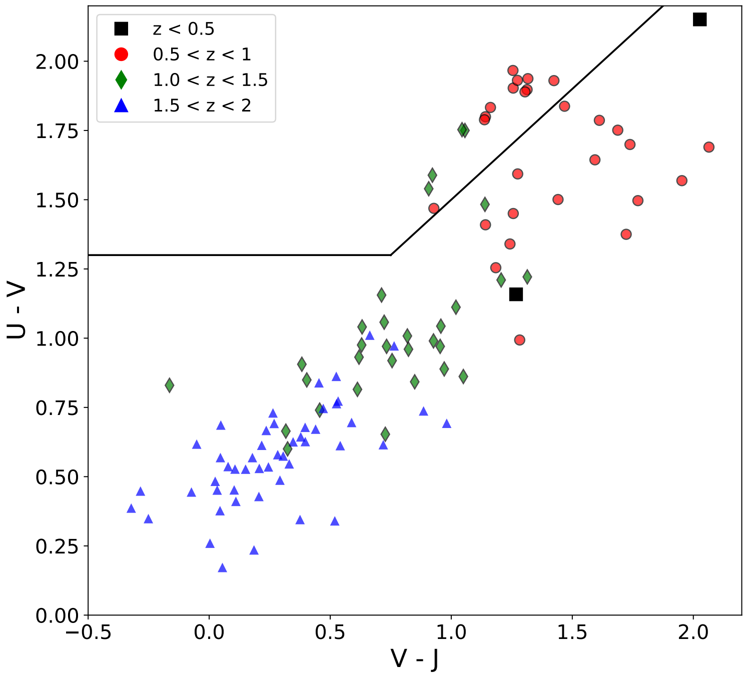

Figure 2.6: UVJ Diagram with boundaries from Shipley et al. (2018). There are 11 quiescent galaxies at redshift $0.5 < z < 1$, and 4 quiescent galaxies at redshift $1 < z < 1.5$.

nearby galaxies from the 2D profiles before creating the 1D profile so their mass or SFR does not interfere with the surface density calculations. We use a UVJ diagram (see Figure 2.6) to examine which galaxies are star-forming or quiescent in our sample. The UVJ boundaries are from Shipley et al. (2018). Out of the 110 total galaxies from all twelve cluster and parallel fields, only 15 galaxies lie within the quiescent region of the UVJ diagram. A small number of $z < 1$ galaxies are in the upper-right region of the UVJ diagram, indicating the presence of dust, although this can be an effect of viewing angle. The majority of galaxies, especially at $z > 1$ (green and blue points), are not dusty and highly star-forming.

For each redshift, we stacked and renormalized the 1-D mass profiles based on their total stellar masses from the profile, to create the averaged 1-D mass profile at that redshift range. The same was done for the star-formation rate maps in order to obtain the normalized 1-D SFR profiles at each redshift bin. The normalized mass profiles are plotted in Figure 2.7, and the normalized SFR profiles are plotted in Figure 2.8.

We expect the MWA progenitors to be highly star-forming as redshift increases, and that is reflected in the sample. The Milky Way is currently in the green valley, either because of its dust content or because it is in the process of transitioning from star-forming to quiescent.

We note that the quiescent fraction is 41% at redshift $0.5 < z < 1$, but only 13% at redshift $1 < z < 1.5$, and all MW progenitors are star-forming at $1.5 < z < 2$. The redshift bin $z < 0.5$

only contains two galaxies, and both are star-forming according to the UVJ diagram in Figure 2.6. Therefore, the galaxies being majority star-forming disk galaxies at higher redshifts matches the canonical picture of the evolutionary history of the Milky Way. (Bland-Hawthorn & Gerhard, 2016). Given that the Milky Way is currently in the green valley with a modest SFR, that $\sim 60\%$ of its progenitors (by stellar mass) at $0.5 < z < 1.0$ are star-forming and $\sim 40\%$ are quiescent is also reasonable.

For our sample, we used GALFIT (Peng et al., 2002) to fit the stellar mass maps in order to obtain the Sérsic indices and half-mass radii in the same procedure as outlined in Tan et al. (2022). We fit for Sérsic index, effective radius, axis ratio, and position angle, though the parameters of interest are only the first two. Initial guesses for the parameters were `SExtractor` values (Bertin & Arnouts, 1996) for effective radius, semiminor/semimajor axis, and position angle for each object from the HFF DeepSpace catalog, and $n = 2$ for the Sérsic index, but with constraints of $n = 0$ to $n = 8$. We will compare their redshift evolution with VD13, P13, and P15 in §2.4.6

2.4 Results

2.4.1 1-D Stellar Mass Profiles

In Figure 2.7, the stacked and normalized stellar mass surface density profiles for each redshift bin are plotted as a function of galactocentric radius R. Our main result is that these stacked and normalized $\Sigma_\star$ profiles have approximately the same overall shape up to 10 kpc. In the bottom left panel where the $\Sigma_\star$ profiles for each epoch are plotted together, it is clear that the growth in $\Sigma_\star$ between different epochs do not depend on R to a great extent. With the stellar mass density of the solar neighbourhood (from Bovy et al. 2012) overlaid on top, it is evident that by redshift 0.5, most of the stellar mass has already been built up for this sample of MWA progenitors. Even before $z = 0$, these galaxies have been able to reach the stellar mass density of the Milky Way. Although we note with only two galaxies in the redshift bin of $0 < z < 0.5$, this result could benefit from a larger sample.

At each redshift step from $z \sim 2$ to $z \sim 0$, the inner 2 kpc region appears to grow more at earlier times. The stacked $\Sigma_\star$ profile does not change at $R \lesssim 3$kpc between $z < 0.5$ (the black curve) and $0.5 < z < 1$ (the red curve). The profiles at around 8 kpc, which is the distance the solar neighbourhood is from the MW's galactic centre, increase in mass density more at earlier times ($z > 1$), and less so at later times ($z < 1$). It increased from a mass density of $\log(M_\star/M_\odot)\text{kpc}^{-2} = 6.42$ to $\log(M_\star/M_\odot)\text{kpc}^{-2} = 6.81$, which is a difference of 0.35 dex, but from $z \sim 1$ to $z \sim 0.5$, it only increased in mass density to $\log(M_\star/M_\odot)\text{kpc}^{-2} = 6.94$, a difference of 0.13 dex. To characterize the mass build-up with more accuracy, §2.4.3 charts the change in total stellar mass and stellar mass density $\Sigma_\star$ in more detail.

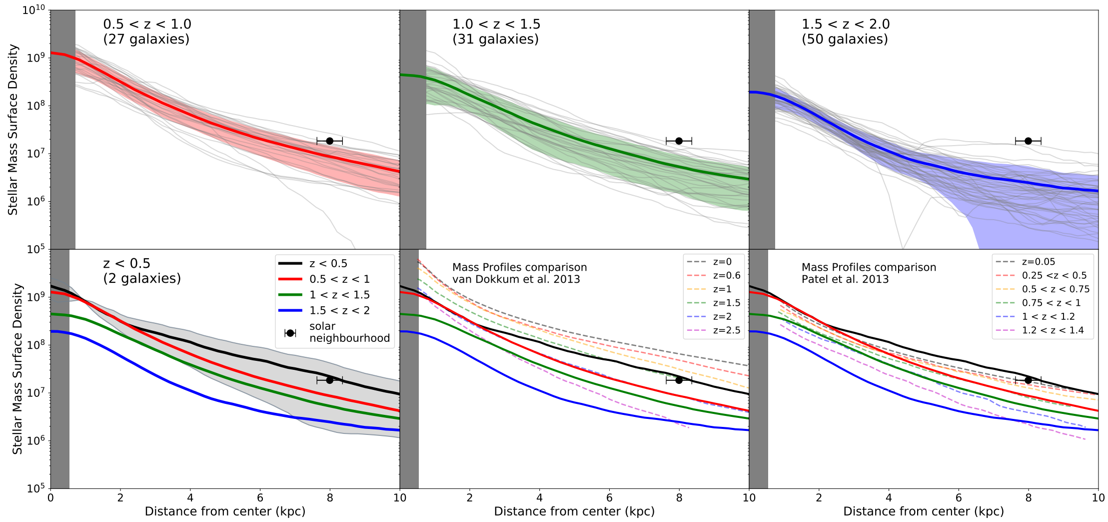

Figure 2.7: *Top Row and Bottom Left panel:* Every surface mass density profile created from stacking and normalizing each 1-D stellar mass profile at each redshift bin. Light grey lines represent the individual stellar mass profiles in each redshift bin. Shaded regions in the same colour of the profile represent the 1-σ deviation from the stacked profile. The bottom left panel also contains normalized 1-D surface mass profile for *each* redshift. The grey lines are the two galaxies which are in the redshift bin $0 < z < 0.5$, with the shaded grey region representing the 1-σ deviation. The black point is the local solar neighbourhood stellar mass density from Bovy et al. (2012). The profiles are integrated up to $r = 20$kpc. *The bottom center and right panels:* These panels compare our derived profiles at each redshift bin with previous results. Our mass profiles agree well with the profiles from P13 more than VD13, despite using abundance matching like the latter, instead of the star-formation main sequence like the former. The vertical grey regions in every panel indicate the part of the profile affected by the PSF.

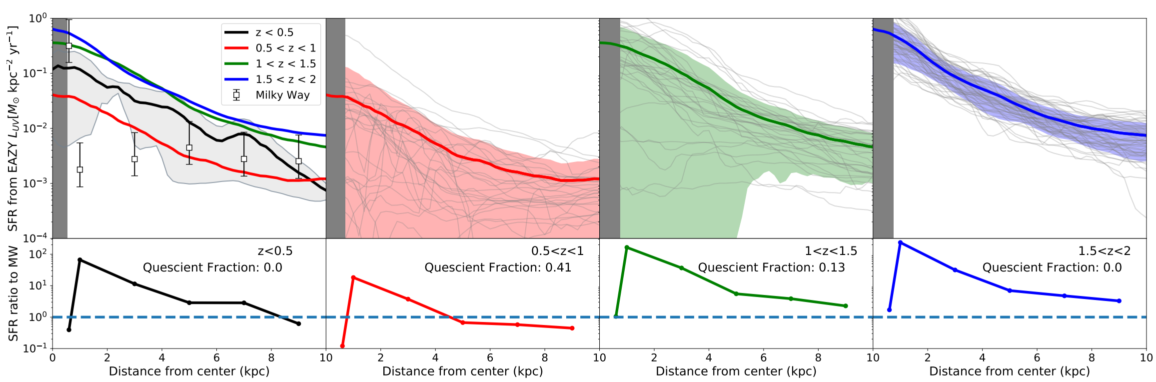

Figure 2.8: *Top Row:* Similar plots to 2.7, but for stacked and normalized SFR profiles. The same galaxies are in each redshift bin. The leftmost plot also has every stacked-normalized SFR profile from each redshift plotted on top for a comparison. In addition, the white points in the leftmost panel indicate the Milky Way's current day SFR density versus R, from Kennicutt & Evans (2012). The vertical grey regions in every panel indicates the part of the profile affected by the PSF. *Bottom Row:* Ratio between the current Milky Way Σ_{SFR} from Kennicutt & Evans (2012), and the Σ_{SFR} at the same R for each past redshift bin. The dotted line indicates where the ratio is the same. Although magnitude of change in Σ_{SFR} varies between redshifts, the overall shape remains consistent.

For comparison, we have plotted our 1-D stellar mass profiles against the mass profiles of previous works, which is displayed in the bottom center and bottom right panels of Figure 2.7 against VD13 and P13 respectively. Our stellar mass profiles are on a similar order of magnitude to P13's results, whereas VD13's stellar mass profiles are at least 1 dex greater than ours across all radii. This is slightly counter-intuitive, because both VD13 and P15 use a starting mass for the Milky Way of $5 \times 10^{10} M_{\odot}$ or $10^{10.7} M_{\odot}$, and P13's starting mass is $10^{10.5} M_{\odot}$, which is around $3 \times 10^{10} M_{\odot}$. Our starting mass of $10^{10.77} M_{\odot}$ is actually closer to the former, but we find similar MWA progenitor masses to P13. Our mass profile at $0.5 < z < 1$ follows closely P13's density profiles at $0.7 < z < 0.1$ from $R \sim 4$ kpc to $R \sim 10$ kpc. At $R \lesssim 4$ kpc, the lowest redshift mass profile shows that the stellar mass density is slightly (~ 0.1 to 0.3 dex) above P13's at a similar redshift range. Our mass profile at $1 < z < 1.5$ falls between P13's profiles at similar mass ranges, up until $R \gtrsim 8$ kpc, when our profile flattens out above P13's $1 < z < 1.2$ profile. In general, the shape of our mass profiles are less steep in the centre and level off at a higher mass density.

2.4.2 1-D star formation rate profiles

The other important factor to stellar mass growth is the star-formation rate. We make 1-D SFR profiles, representing the SFR versus galactocentric radius in kpc, and these are shown in Figure 2.8 on the top row. In the top-left panel of Figure 2.8, the star formation rate density profiles show more star formation within the $R < 2$ kpc region, but there are proportionally more stars there. Overall the distribution of the SFRs and stellar mass shows that the increase in stellar mass due to star formation in each redshift range would be approximately proportional to the stellar mass that is already present.

Figure 2.8 shows that the SFRs are overall more than 1.3 dex higher from $1 < z < 2$ as compared to $z < 1$. The sharp drop in overall SFR between these redshifts might be expected as the SFRs of all galaxies start to decline strongly at $z < 1$. Interestingly for the MWA progenitors, the drop in SFR is uniform over the entire profile, implying that the mass growth from star formation is not preferentially in the inner or outer regions of MWAs. This in conjunction with the stellar mass profiles indicate that mass assembly happens in lockstep from $z \sim 2$ onwards, and also slows down in lockstep as well.

In addition to the stacked and normalized SFR profiles for each redshift bin, in the bottom row of Figure 2.8 we also plot the ratio between the Milky Way's measured SFR density against the SFR density at the same R for each of the stack and normalized SFR density profiles. Although the magnitude of the ratio of Σ_{SFR} changes, the overall shape of this ratio of past Σ_{SFR} to current day MW Σ_{SFR} does not change qualitatively. This has implications for bulge-growth, as this implies a decrease in Σ_{SFR} over time occurred at similar rates across the entire galaxy, with no preference for inner or outer regions. Therefore it is another example of lockstep growth in both the bulge and the disk regions of MWA progenitors.

2.4.3 Mass assembly in the inner and the outer regions

To further investigate the stellar mass assembly in each redshift range, we divide the growth into inner vs. outer regions. The inner region is defined as within 2 kpc of the center of each galaxy's profile, and outer region is defined as beyond 2 kpc. The profiles are integrated out to 20 kpc, to remain consistent with the limit used in P13.

In Figure 2.9, we plot the stellar mass surface density $\Sigma_\star$ versus redshift in the top panels, and SFR density Σ_{SFR} versus redshift for the bottom panels. These are obtained by integrating over the 1-D density profiles by R up to 20 kpc. In addition, we also plot the inner ($R < 2$kpc) and outer (2kpc $< R <$ 20kpc) $\Sigma_\star$ and Σ_{SFR} against redshift, which are the red and blue lines respectively. This is not only to demonstrate overall mass assembly and change in SFR over time, but also whether the change was more pronounced towards the central regions or the outskirts of the galaxies for each epoch.

Figure 2.9 shows that the stellar masses of the inner regions ($R < 2$ kpc) are consistently around 0.5 dex lower than the outer regions at every redshift bin. Compared to the total mass and total mass density of the Milky Way from local measurements, the Galaxy is not a perfect extrapolation of the trends shown. In the top left panel of Figure 2.9, the outer regions of the Milky Way (the blue point at $z = 0$) have more stellar mass compared to and extrapolation of the trend for the MWA progenitors' outer regions ($R > 2$ kpc) at higher redshifts (the blue line) to $z = 0$. Also the stellar mass of the inner 2 kpc of the Milky Way is similar to the total stellar mass of the MWA progenitors at $z \sim 0.5$. This comparison between the Milky Way and the trend of MWAs in Figure 2.9 may imply that the inner 2 kpc of MWAs would have had more mass growth than the inner 2 kpc of the Milky Way itself.

It is useful to note that that while our MWA progenitors do not indicate a similar type of growth from $z \sim 0.5$ to $z \sim 0$ that would match the current Milky Way's properties, neither do the MWA progenitor samples of the previous works that they are compared with. If we took the full sample of all local galaxies considered *"Milky Way Analogues"*, perhaps the Milky Way's higher than expected disk growth at low redshifts is anomalous among galaxy analogues of similar mass.

2.4.4 Star-formation at different regions and different epochs

In Figure 2.9, the bottom left panel plots overall median SFR versus redshift, and the bottom right panel plots SFR density versus redshift. Those panels demonstrate the overall trend of star-formation rate decreasing with decreasing redshift. However, the drop in median SFR is more drastic from $z \sim 1.5$ to $z < 1$ than any other epoch. This holds for both the inner and outer regions of the MWA progenitor galaxies, which can be seen in the SFR profiles in the bottom row of Figure 2.9.

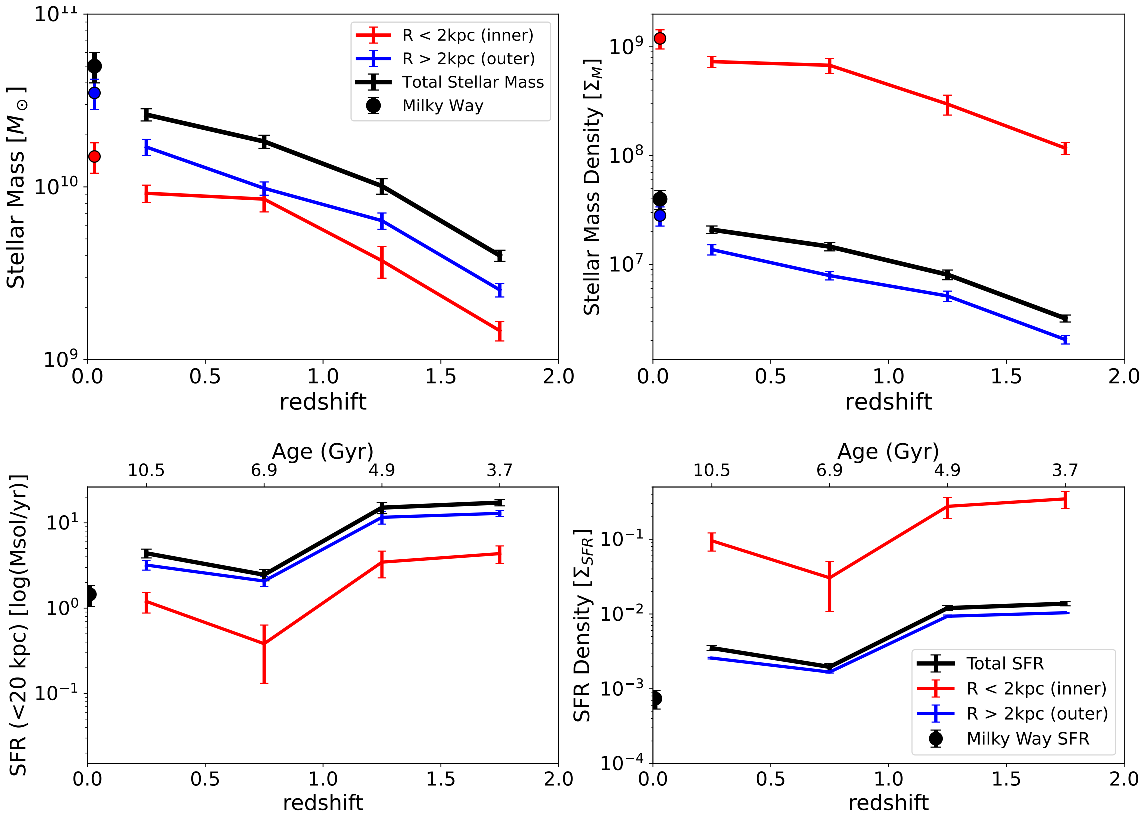

Figure 2.9: *Top row:* Evolution of the total stellar masses (left) and stellar mass densities ($\Sigma_\star$, right) of MWA progenitors out to $z \sim 2$. $\Sigma_\star$ for each region is calculated by taking the stellar mass and dividing it by the surface area of its respective regions. Black lines represent the galaxy-integrated properties out to 20 kpc, whereas red and blue lines show the inner ($R < 2$ kpc) and outer regions ($R > 2$ kpc), respectively. The Milky Way $\Sigma_\star$ were taken from the measurements of the bulge stellar mass, total stellar mass, and B/T ratio from Bland-Hawthorn & Gerhard (2016), but divided by the surface area to give a surface mass density. This is assuming the bulge is contained within a galactocentric radius of 2 kpc, and that the disk integrates out to 20 kpc, for consistency with MWA progenitor mass profiles. *Bottom row:* Similar to plots above, but showing the evolution of total SFRs (left) and SFR densities (Σ_{SFR}, right). The Milky Way ΣSFR is again derived from the total SFR in Bland-Hawthorn & Gerhard (2016) but divided by surface area. An additional axis representing the age of the universe corresponding to each redshift bin is included at the top of both SFR vs. redshift plots.

Since $z \sim 2$ is what is known as "cosmic noon" when the peak of universal star-formation occurred, the decline may be expected. However it is interesting to note that the decrease in median SFR for the MWAs (for all regions) is less drastic in the redshift bin $1.5 < z < 2$ than the redshift bin $1 < z < 1.5$. The age of the universe at $z = 1.75$ is 3.7 Gyr and the median total SFR is given as 17.3 $M_{\odot}\mathrm{yr}^{-1}$. The age of the universe at $z = 1.25$ is 4.9 Gyr with median total SFR $15.1 M_{\odot}\mathrm{yr}^{-1}$. This is a decrease in total SFR of roughly $-1.84 M_{\odot}\mathrm{yr}^{-1}\mathrm{Gyr}^{-1}$ between $1.5 < z < 2$. The age of the universe at $z = 0.75$ is 6.9 Gyr with median total SFR 2.46 $M_{\odot}\mathrm{yr}^{-1}$. This means the decrease in total SFR is roughly $-6.31 M_{\odot}\mathrm{yr}^{-1}\mathrm{Gyr}^{-1}$ between $1 < z < 1.5$, about three times as fast.

The inner region ($R < 2$ kpc) and outer regions ($R > 2$ kpc) of the MWA progenitors have similar changes in SFR when moving from one redshift bin to another. This indicates lockstep star-formation rates for MWA progenitors since $z \sim 2$. This means that when the SFR changes, it changes at the same rate over *the entire galaxy's surface area*, whether it is in the $R < 2$ kpc region or in the outer region at $R > 2$ kpc. Generally, SFR is decreasing with decreasing redshift, but there is a small increase in the median SFR when moving from the redshift bin $0.5 < z < 1$ to $0.3 < z < 0.5$, as seen in the bottom left panel of Figure 2.9. Looking instead to the bottom right panel of Figure 2.9, where the SFR density of the MWA progenitors is plotted versus redshift, there is more of an increase in the SFR density of the $R < 2$ kpc inner region than the outer region. This might be evidence of mild bulge-growth, but because it is minor, it does not break the general trend that SFR changes in lockstep across all radii.

Mosleh et al. (2017) also finds evidence that star-forming galaxies have their central and outer regions grow concurrently. Their range of stellar masses were from $10^{10.2} M_{\odot}$ to $10^{11.2} M_{\odot}$, so the Milky Way would be comparable to the star-forming galaxies in their highest mass bin.

2.4.5 Selection of MWA Progenitors and resulting difference in Mass Growth

In Figure 2.10, we plot inner, outer, and total stellar mass density vs. redshift, and compare them against similar plots but from VD13, P13, and P15. In Figure 2.11, we do the same comparison for inner, outer, and total SFR and SFR density. The mass densities for the previous studies were obtained by taking their stellar mass as a function of redshift (inner, outer, and total) and dividing it by the area consistent with their defined limits of integration in their respective works (i.e. for VD13, the outer limit is 25 kpc, and for P13 and P15 the outer limit was defined to be 20 kpc.) Although P15 did not construct mass profiles as the other two papers did, their work still included total mass assembly for MWA progenitors.

We see a clear difference in total stellar mass, as well as stellar mass density between P13 versus VD13 and P15. Additionally, P13 selected MWA progenitors using the star-forming main sequence, and VD13 selecting MWA progenitors from a constant comoving density. Despite selecting our

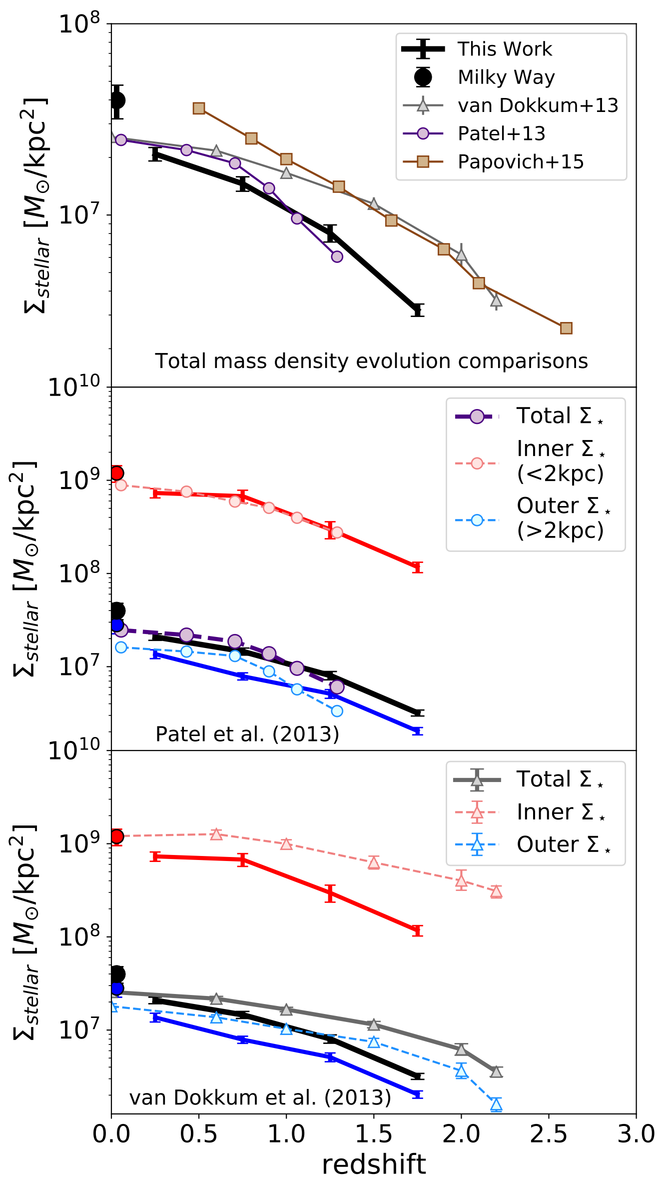

Figure 2.10: *Top Panel:* Comparison of the *total* $\Sigma_\star$ as a function of redshift between our densities and P13, VD13, and P15. *Middle panel:* The inner and outer stellar mass densities of our results and P13. *Bottom panel:* Same regional stellar mass density comparisons as the middle panel but with VD13's densities. MW mass density points are again derived from measurements listed in Bland-Hawthorn & Gerhard (2016) as in Figure 2.9.

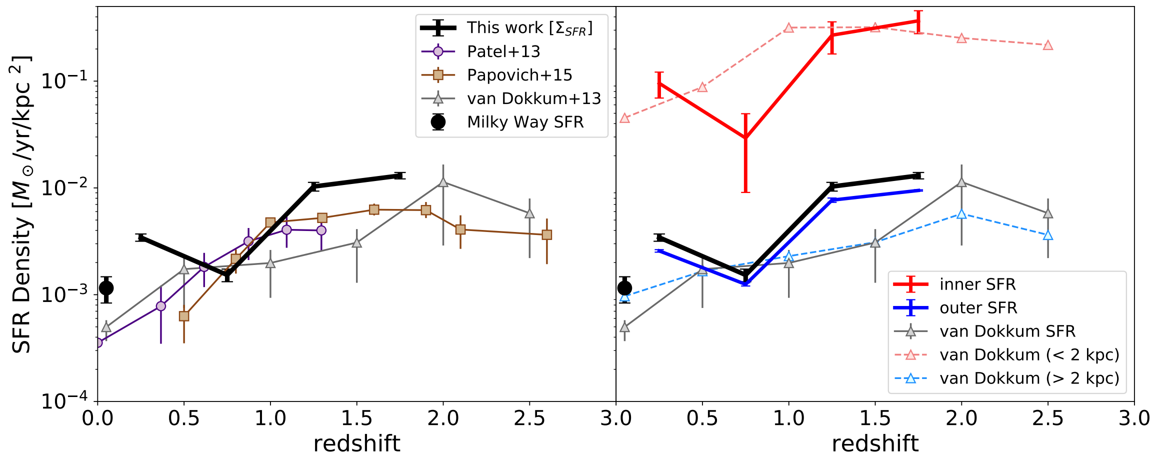

Figure 2.11: *Left panel:* Total SFR density as a function of redshift for our results against VD13, P13, and P15. At higher redshift, from $1.5 < z < 2$, our SFR densities agree well with both P15 and P13, but the SFR density drops faster for our sample. *Right panel:* Total, inner, and outer SFR density as a function of redshift from our results and VD13. Their work also used UV luminosity to derive SFRs. This shows the difference that evolving comoving number density has on the SFR of the galaxies selected as progenitors.

progenitors via an evolving comoving number density, our sample is less massive and more star-forming compared to VD13 and P15's analyses, and is a much closer match to P13. However, there are still differences such as the rate of stellar mass growth of the inner and outer regions. We note that all three previous studies used IR light profiles as a proxy for stellar mass, but we are measuring stellar mass directly from the resolved 2D mass profiles. Thus, this may account for most of the differences in mass assembly seen. All the stellar mass density plots in Figure 2.10 display signs of lockstep growth at redshifts $1 < z < 2$, but when the growth slows down at lower redshifts, it appears that the outer regions stop growing earlier than the inner regions.

In 2.11, the overall change in SFR density agrees best at $0.5 < z < 1.5$ with P15, however our sample is more star-forming at higher redshift ($1.5 < z < 2$) versus all previous studies cited. For SFR comparison between the inner and outer regions, only V13 made similar regional comparisons. V13 shows a shallower decrease in SFR in the outer regions compared to the inner regions from $z = 1.5$ to $z = 0$, while our sample shows roughly similar change in SFR in inner and outer regions between redshift epochs, which is more evidence for lockstep mass assembly.

2.4.6 Morphological parameters as a function of time

In Figure 2.12, we plot the median Sérsic index and median half-mass radius of each redshift bin. The Sérsic indices and effective radii were obtained by using GALFIT to fit a one-parameter Sérsic profile on the objects' two-dimensional stellar mass maps. The error bars indicate standard error of the mean. The Sérsic indices of the progenitor sample show a slowly increasing trend as redshift

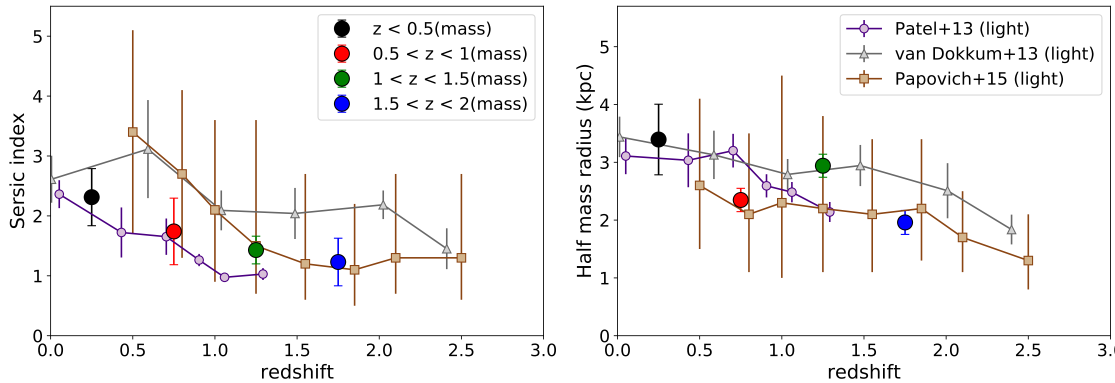

Figure 2.12: *Left panel:* Sérsic index vs redshift, as fit by GALFIT onto the stellar mass maps. Each point represents the median Sérsic index for that redshift bin. Our sample has good agreement with P13's sample in Sérsic index at similar redshifts, again showing that selecting MWA by star-formation rate and abundance matching results in similar samples. *Right panel:* Half-mass radius vs redshift. Each point represents the median half-mass radius index for that redshift bin. The average half-mass radius at each of our redshift bins are compared against the average half-light radii for P13, VD13, and P15's galaxies.

decreases at $z < 1$, but it remains constant between $1 < z < 2$. The redshift bin of $z < 0.5$ is the only epoch when the median Sérsic index is $n > 2$. Before that epoch, from $0.5 < z < 2$, the Sérsic index varies from 1.2 to 1.5, which suggests a disk-like morphology.

The left panel of Figure 2.12 shows that the evolution of the Sérsic indices between this work and P15 are very close at the epoch $1 < z < 2$, but diverges drastically at $z < 1$. P15's sample in fact, almost reaches a Sérsic index of $n = 4$, which describes a de Vaucoulers profile, in other words, an entirely bulge-dominated elliptical galaxy.

In the right panel of Figure 2.12 where the effective radii are plotted, the median half-mass radius of our sample of MWA progenitors starts at only 2.23 ± 0.19 kpc at the earliest epoch, but jumps to 3.56 ± 0.21 kpc at $1 < z < 1.5$. The median half-mass radius is also smaller overall at $0.5 < z < 1$ than at the redshift bin immediately before and after that epoch. We do note that the quiescent fraction at that epoch is higher than at other epochs, which could contribute to a smaller median half-mass radius, since quiescent galaxies are more compact than star-forming ones. In addition, the median half-mass radii at each epoch tends to match both P13 and VD13's results but only at $z < 1$. At $1.5 < z < 2$, our results agree very well with P15, but surprisingly at $1 < z < 1.5$, it does not match the effective radii of any of the previous works. However, due to the magnitude of the error bars, the overall trend of the change in half-mass radii is consistent with the changes in half-light radii of previous MWA studies.

In general, we have found that the stellar mass profiles and growth histories are reasonably consistent with previous findings which use IR light as a proxy for stellar mass. Given that galaxies can have color gradients (e.g., Figure 2.3), it is somewhat surprising how consistent these results are. This shows that IR light tracks stellar mass quite well for MWA progenitors, even though it is not fully representative of the underlying stellar mass. Perhaps one notable contrast is that our result in Figure 2.12 shows that the half-mass radius may grow drastically at early times, but plateaus in growth at more recent times, perhaps having to do with galaxies turning quiescent. This is somewhat different than the half-light radii, which have a more steady growth over cosmic time. The fact that the half-mass radius growth is slow, combined with the result that the Sérsic index increasing as redshift decreases, could imply the progenitors are growing their bulges. This is further discussed in §2.5.1.

This result could also indicate lack of evolution in the half-mass radii of MWA progenitors as much as it indicates very small growth. A simulation paper on MWA progenitors in TNG50 by Hasheminia et al. (2022) seems to find similar results (see §2.5.3 for more details).

2.5 Discussion

2.5.1 Mass Maps vs Luminosity Maps

Our analysis of MWA progenitors differs from previous work in the usage of resolved stellar mass and SFR maps instead of luminosity maps. IR luminosity is a representation of the stellar mass distribution but is not itself the mass distribution. But despite that, our results agree well with previous light profile studies. We agree particularly well with the results in P13 (as seen in Figures 2.10, 2.11, and 2.12). And our results come to the same conclusion, which is that MWA progenitors assemble their mass in inner and outer regions in lockstep since $z \sim 2$, with no preference for inside-out or outside-in growth.

Even though P13 relied on the star-forming main sequence to select MWA progenitors, the closeness of our measurements point to a link between galaxy merger rates and the star-formation history as well as mass assemby of galaxies at a certain stellar mass in a comoving volume of space. This extends even to the closeness of the Sérsic indices between our two studies. It may seem counter-intuitive that stellar mass profiles are quite similar to light profiles, since the Milky Way has a colour gradient with older stars near the center and younger stars further out in the disk. But looking back at the colour images of Figure 2.3, there are progenitors that exhibit this colour gradient at high z as well as low z.

Our Sérsic indices are $0.2 - 0.5$ greater than the Sérsic indices of P13. Previous studies that examined the difference in Sérsic indices between IR light profiles and stellar mass profiles include Suess et al. (2019) and Tan et al. (2022), which also found n_{mass} to be overall greater than n_{IR} by a similar margin. This means the MWA progenitor populations are very similar between this work and P13's work, despite using a different starting mass at $z = 0$. However, our half-mass radii are slightly larger. This is a notable departure from previous studies that typically found half-mass radii are smaller than half-light radii (again, both Suess et al. 2019 and Tan et al. 2022).

We note that differences for the two R_e points in the right panel of Figure 2.12 at redshifts $0.3 < z < 1$ are minimal between this work and P13; the differences are < 0.5 kpc for both points. But the R_e for our sample at redshift $1 < z < 1.5$ is much higher, around 1.5 kpc greater than the R_e measured by P13 at the same redshift range. Since the Frontier Fields cover a smaller region of the sky than the surveys used in VD13, P13, and P15, this could be attributed to sampling bias. In addition, P13 used a stellar mass of $10^{10.5} M_\odot$ for MWAs at $z = 0$ compared to our initial stellar mass of $10^{10.77} M_\odot$ for MWAs. Since our half-mass radii are the closest to their results, the difference in size could be due to the physical sizes of the chosen sample itself. Finally, our R_e measurement for the redshifts $1.5 < z < 2$ lies on top of the line indicating the R_e for the sample from P15, which means our R_e measurements are still on the whole consistent with previous results.

Both the MWA progenitor sample from VD13 and P15 contained more quiescent galaxies than our sample, and this can explain why their Sérsic indices are larger at later redshifts and their half-light radii are smaller. Both of those quantities are associated with quiescent galaxies. The quiescent fractions range in P15 is 74% to 41% from $0 < z < 1.1$ and 29% to 12% from $1.1 < z < 2$. This may explain why our measurement at $1.5 < z < 2$ matches the results from P15 at the same redshift range in Figure 2.12. It is because at that redshift there are mostly star-forming galaxies. P15 also used the abundance matching code from Behroozi et al. (2013a) to select their MWA progenitors, so agreement at high redshift between our results and theirs may point to light and mass profiles being more similar at higher redshift, at least for star-forming galaxies.

2.5.2 Mergers and mass assembly

The abundance matching code prescribes merger trees for any given $z = 0$ comoving number density or $z = 0$ halo mass, and then estimates the median cumulative number density at past epochs for any population of co-evolving galaxies (Behroozi et al., 2013a). Due to selecting MWA progenitors via abundance matching, it raises the question of how mergers would affect the evolution of MWAs. In the case of detecting onging major mergers, there is only one in our sample, at $z \sim 1.9$. Most galaxies in our sample appear to have star-forming clumps that do not show up in the stellar mass maps (see Figure 2.5). Despite the lack of ongoing major mergers in the sample, the assumption is still that statistically speaking, mergers still play a role in the mass assembly of MWAs on account of choosing progenitors according to an evolving co-moving number density.

If we assume the gap in total stellar mass density between our results and the results from VD13 is dominated by increase in mergers, then according to 2.10, 0.1 to 0.3 dex of the increase in total stellar mass density ($\Sigma_\star$) attributed to star-formation should instead be attributed to mergers since $z \sim 2$, as seen in the topmost panel of 2.10. For the $\Sigma_\star$ within $R < 2$kpc, this can be as high as 0.8 dex of the increase in $\Sigma_\star$, and for the region between 2 kpc $< R <$ 20 kpc, it is as high as 0.9dex, as seen in the bottom panel of 2.10.

Given that we use true stellar mass, and an evolving number density evolution, our result that the MWA progenitor Sérsic indices are growing at a slower rate than that implied by VD13 or P15 should be a more accurate picture about bulge growth. While all results suggests bulge strength is increasing in MWAs, ours suggest a slower evolution. Assuming that the difference is in part driven by incorporating the merger trees into the abundance matching, this implies that mergers may affect bulge growth. However, since the Sérsic index growth is modest, it is clear that MW-mass galaxies that are still star-forming will not have substantial morphological transformations since $z \sim 2$.

This is reflected in both the stellar mass densities, as well as the star-formation rate densities. Figure 2.9 shows very little difference in the stellar mass growth of the inner ($R < 2$ kpc) and outer ($R > 2$ kpc) regions compared to the total mass growth. There is a similar trend in the change in SFR versus redshift – when the total SFR drops, both inner and outer SFRs also drop by similar rates. Since the change in SFR is not dependent on galacto-centric radius this means the newly formed stellar mass is added to both inner and outer regions, which demonstrates lockstep growth. It may seem that this contradicts the increase in Sérsic index, but the change in Sérsic index is rather shallow (from $n = 1.23 \pm 0.39$ to $n = 2.31 \pm 0.48$), and it may be that the stellar component of these galaxies compactify from dynamic friction from the gas.

In addition, not all bulge growth is the result of mergers. Secular evolution and clump migration are other methods of bulge growth. Garrison-Kimmel et al. (2018) find that in the FIRE-2 simulations, halo spin (halo angular momentum), is the best predictor of morphology, which mergers and secular processes (such as bars or counter-rotating disks) both greatly affect. However, clump migration in simulations has been shown to contribute very little to bulge growth despite seeing large numbers of bright clumps at high redshift (Mandelker et al., 2017; Garrison-Kimmel et al., 2018), with Mandelker et al. (2017) finding that clumps only contribute $0.1 \sim 3\%$ of a galaxy's total stellar mass. Star-forming clumps occur in the majority of $z > 1$ galaxies (Elmegreen et al., 2007), but despite their brightness, observations do not show that clumps are any more massive than the surrounding galaxy in resolved spatial stellar mass profiles (Wuyts et al., 2012; Sok et al., 2022). Since the launch of JWST, galaxies with irregular features have been found to make up about 40-50% of the universe at $3 \leq z \leq 9$ (Jacobs et al., 2023; Kartaltepe et al., 2023) and it is clear that the progenitors of all but the most massive central galaxies in the current universe must have had irregular and clumpy morphologies. Due to the sheer amount of clumpy galaxies, their effect on mass assembly should still be investigated. Perhaps clumps play a more prominent role in galaxy evolution beyond $z = 2$.

There is a reasonable survival rate (35%) of disks for progenitors of MW and M31 mass galaxies in the TNG50 simulation as seen in Sotillo-Ramos et al. (2022), showing that they do not necessarily destroy the stellar disk but only add dynamical heat to all galaxy components (i.e. in thickening the stellar disk, another process which may increase the Sérsic index). This may also explain the lockstep growth in inner and outer regions. Depending on the properties of the merger itself, it may add stellar mass to all radii, especially if gas is distributed to the stellar disk and induces starburts. Sotillo-Ramos et al. (2022) also find that recent major mergers of their simulated MW/M31 analogues do not appreciably deplete the gas fraction of those galaxies, allowing for further ongoing star-formation after the merger event. There is reasonable evidence from simulations that mergers play a role in bulge growth but are not dominant over secular processes, nor do they always completely transform a galaxy's morphology.

2.5.3 Comparisons with MWA progenitors in simulations

The formation of MW and M31 progenitors have been heavily studied through simulations before, and it is useful to compare the results from observations against the results from simulations. This is especially critical to answering the question of whether or not the Milky Way is an outlier in being a massive, but still disky galaxy in the local universe. Abundance matching has been applied to the IllustrisTNG simulation in Torrey et al. (2017) to search for Milky Way and M31 progenitors in the simulation.

Hasheminia et al. (2022) found in their sample of MWA progenitors that the half-mass radius shows little evolution from $z \sim 2$ to the present epoch, while the Sérsic index evolves slowly. They do find that for their galaxies, the Sérsic index reaches upwards of $n \sim 3$ to almost $n \sim 4$, suggesting that for galaxies of Milky Way mass, they should be mostly bulge-dominated in the local universe. But we do not see this reflected in our sample from observations, where the maximum Sérsic index at the redshift bin $0 < z < 0.5$ is only $n \sim 2.3$. However, we do reproduce one of their main results which is that the half-mass radius is roughly constant for the past 10 Gyr, despite growth in stellar mass, and change in Sérsic index. This means there is something fundamental about the way that MWA progenitors assemble which is reflected in both simulation and observation.

Sotillo-Ramos et al. (2022) examined a population of MW and M31 progenitors in the TNG50 simulation, focusing specifically on the result of mergers on the diskiness of the galaxy, as well as the details of the change in morphology due to mergers. They come to two main conclusions regarding mergers: one related to bulge growth, and another related to stellar halo mass distribution. For bulge growth, they find that for their simulated MWA progenitor sample, there is no *statistically significant difference* in the bulge fraction between galaxies with one or more merger events or no merger events. Secondly, they find that for galaxies with a recent major merger in the last 5 Gyr, their bulge to halo stars ratio (with halo stars also being a proxy for disk stars) most closely match those of the MW and M31 at redshift $z = 0$, *but also* their bulge fractions are *lower* than the rest of the sample, indicating a *diskier* distribution.

Since we obtained a lower Sérsic index of 2.3 at our lowest redshift bin, this implies that accounting for mergers should still result in MWA progenitors retaining a mostly disky morphology in the current universe. This is in line with results from various simulations of MWAs, which provide reasonable explanations for mass assembly, which agrees with our results. Our observational results may indicate the Milky Way is not as much of an outlier among Milky Way Analogues as was previously thought.

2.6 Conclusion

We construct resolved stellar mass and SFR maps of MWA progenitors up to redshift $z \sim 2$ using resolved multi-wavelength photometry from the HFFs and examine the stellar mass assembly of Milky Way-mass galaxies in a spatially-resolved manner. We used abundance matching techniques that select progenitors with an evolving comoving number density, which is based on simulated merger histories of MW mass galaxies at $z = 0$. Our main conclusions are as follows:

- The stellar mass for the Milky Way Analogues increases at the same rate for both inner (< 2 kpc) and outer regions (> 2 kpc) over our redshift range, i.e. progenitors of MWAs display lockstep growth in inner and outer regions up to redshift $z \sim 2$. Our study, which focuses on resolved stellar mass profiles of galaxies agrees with previous observational results studying the Milky Way's mass assembly through light profile distributions.

- Generally speaking, morphological parameters derived from stellar mass profiles follow the trends seen in previous MWA progenitor studies. Sérsic indices derived from stellar mass profiles are smaller than Sérsic indices derived from light profiles from previous works on MWAs, with the exception of P13. However, our half-mass radii are slightly larger than the half-light radii from previous works. The difference between light-derived and mass-derived Sérsic parameters disappears around redshift $z \sim 1.5$.

- We also find evidence that accounting for merger rates at different evolutionary epochs by using abundance matching in concordance with selecting by stellar mass and comoving number density results in a higher overall star-formation rate, and diskier morphology in progenitors of Milky Way Analogues. This is shown by our stellar mass density and SFR density closely matching the results of P13, which used the star-forming main sequence to select MWA progenitors at higher redshift.

- However, according to the SFR profiles, the SFR and the SFR density does not decrease uniformly in the inner and outer regions, and in fact the inner region decreases more rapidly than the outer regions.

- We find on average slightly more mass assembly in the outer 2 kpc region the MWA progenitors, especially in the epoch $0.3 < z < 0.5$, which also matches up with slightly elevated median SFR in the outer 2 kpc region at the same epoch. But it is not a large enough amount that would make our results inconsistent with lock-step growth found in previous MWA mass assembly studies.

This work is based on data and catalog products from HFF-DeepSpace, funded by the National Science Foundation and Space Telescope Science Institute (operated by the Association of Universities for Research in Astronomy, Inc., under NASA contract NAS5-26555).

Chapter 3

Resolved mass assembly in MW progenitors since $z = 5$

A version of this chapter is published as **"Resolved mass assembly and star formation in Milky Way Progenitors since $z = 5$ from JWST/CANUCS: From clumps and mergers to well-ordered disks"** Preprint available at `https://arxiv.org/pdf/2412.07829`

Full Author List and Contributions: Vivian Yun Yan Tan (main data analysis, discussion, conclusions), Adam Muzzin (supervisor), Ghassan T. E. Sarrouh (CANUCS data reduction and catalogs, flux errors), Jacqueline Antwi-Danso (UVJ color calibration), Visal Sok (clump detection algorithm, flux errors), Naadiyah Jagga (flux errors, comments), Gregor Rihtaršič (aid with lensing magnification corrections, comments), Westley Brown (comments on merger rates in sims), Roberto Abraham (comments), Yoshihisa Asada (CANUCS data reduction and catalogs, comments), Guillaume Desprez (comments), Kartheik Iyer (CANUCS Dense Basis catalogs), Nicholas S. Martis (comments), Rosa M. Mérida (comments), Lamiya A. Mowla (comments), Gaël Noirot (comments), Kiyoaki Christopher Omori (comments), Marcin Sawicki (comments), Roberta Tripodi (comments), and Chris J. Willott (comments).

Abstract

We present a resolved study of > 900 progenitors of Milky Way Analogs (MWAs) at $0.3 < z < 5$ selected with abundance matching in the ten fields of the Canadian NIRISS Unbiased Cluster Survey (CANUCS). Utilizing 18-21 bands of deep NIRCam, NIRISS, and HST photometry, we create resolved stellar mass maps and star formation rate maps via spectral energy distribution fitting with Dense Basis. We examine their resolved stellar mass and specific star formation rate (sSFR) profiles as a function of galactocentric radius, and find clear evidence for inside-out mass assembly. The

total $M_\star$ of the inner 2 kpc regions of the progenitors remain roughly constant ($10^{9.3-9.4}M_\odot$) at $2 < z < 5$, while the total $M_\star$ of the regions beyond 2 kpc increases by 0.8 dex, from $10^{7.5}M_\odot$ to $10^{8.3}M_\odot$. Additionally, the sSFR of the outer regions increase with decreasing redshift, until $z \sim 2$. The median Sérsic index of the MWA progenitors stays nearly constant at $n \sim 1$ at $2 < z < 5$, while the half-mass radii of their stellar mass profiles double. We perform additional morphological measurements on the stellar mass maps via the Gini-M20 plane and asymmetry parameters. They show that the rate of double-peak mergers and disturbances to galaxy structure also increases as redshift increases, with $\sim 50\%$ of galaxies at $4 < z < 5$ classified as disturbed, and $\sim 20\%$ classified as ongoing mergers. Overall, the early evolution of MWAs is revealed as chaotic, with significant mergers and high SFRs. Mass growth is primarily inside-out and galaxies become more disk-like after $z = 3$.

3.1 Introduction

The present-day Milky Way is a large spiral galaxy with a total stellar mass of $\sim 5 \times 10^{10}M_\odot$ (see Bland-Hawthorn & Gerhard 2016; Helmi 2020 for reviews). It contains a thin disk with ongoing star formation, a dynamically hotter thick disk with older stars of lower metallicity (e.g. Bensby et al. 2003; Fuhrmann 2011; Licquia & Newman 2015; Kilic et al. 2017), and a central region with a bar and a pseudobulge (e.g. Shen et al. 2010; Wegg & Gerhard 2013; Wegg et al. 2015; Portail et al. 2017; Barbuy et al. 2018). Stellar streams in the Milky Way's halo reveal remnants of galaxies that merged with the Milky Way (Helmi et al., 2018; Belokurov et al., 2018; Horta & Schiavon, 2024).

Compared to its peers of similar stellar mass, the Milky Way (MW) can either be typical, or somewhat abnormal. Work from Licquia et al. (2016) shows that the MW lies on the Tully-Fisher relation for galaxies (Tully & Fisher, 1977). Fraser-McKelvie et al. (2019) finds the MW lies within two standard deviations of the star-forming main sequence (see Speagle et al. 2014; Schreiber et al. 2015; Santini et al. 2017), however its star formation rate is more consistent with a galaxy transitioning from star-forming to quiescent, green valley galaxy (Mutch et al., 2011). Its disk length scale is also more compact physically compared to other spirals of the same stellar mass (Bovy & Rix, 2013; Licquia et al., 2016). Depending on selection criteria, there exists dozens to potentially hundreds of Milky Way Analogs (MWAs) in the local universe, in terms of the galaxies' mass, morphology, and star formation rate (e.g.Fraser-McKelvie et al. 2019; Kormendy & Bender 2019; Boardman et al. 2020a; Zhou et al. 2023). By comparing the physical characteristics of the MW to its analogs (e.g. Bovy & Rix 2013; Licquia et al. 2016; Boardman et al. 2020b), we gain a better understanding of the MW as it exists in its current state. However, the galaxies of the present-day universe had complex formation histories that we have only begun to glimpse from the current era of high-redshift observations.

Recent studies of gravitationally lensed arcs via multiband photometry and spectroscopy from JWST reveal very high redshift, reionization era galaxies that are progenitors of many of the galaxies that we find in the local universe. Among these are the Sunrise arc (Vanzella et al., 2023) at $z \sim 5.9$ with a total stellar mass of $10^6 - 10^7 M_\odot$, the Firefly Sparkle (Mowla et al., 2024) at $z \sim 8.3$ with a total stellar mass of $10^{5.3} - 10^{6.3} M_\odot$, and the Cosmic Gems arc (Adamo et al., 2024; Bradley et al., 2024) at $z \sim 10.2$ with a total stellar mass of $10^{7.38} - 10^{7.75} M_\odot$ These correspond to a lookback time of ∼12.7 Gyr, ∼13.1 Gyr and ∼13.3 Gyr respectively. These galaxies are gravitationally bound star clusters with extremely high star formation rates. Although these high-z protogalaxies are a far cry from the "grand-design" spiral disks observed in the local universe, they represent the earliest stages of galaxy formation, and fall within the stellar mass range of possible progenitors of MWAs.

A recent simulation study from Rusta et al. (2024) has shown that the Firefly Sparkle's stellar mass and star formation history are consistent with that of a MW type galaxy. They provide evidence for the hierarchical assembly model of structure formation in the early universe (White & Rees, 1978), supported by studies of the chemical and kinematic properties of stars in the galactic halo of the MW (e.g. Tumlinson 2010; Salvadori et al. 2010; Belokurov et al. 2018; Belokurov & Kravtsov 2022; Xiang & Rix 2022). Hierarchical assembly also fits with the most widely accepted model of the MW's formation, the so-called "inside-out" model, which posits the bulge formed first, with the disk and halo coalescing around it (see van den Bosch 1998; Abadi et al. 2003a; Muñoz-Mateos et al. 2007; Wang et al. 2011; Licquia et al. 2015; Goddard et al. 2017).

With the advent of next generation high resolution hydrodynamical galaxy simulations such as TNG50 (Pillepich et al., 2019, 2023), FIRE (Hopkins, 2015; Oñorbe et al., 2015; Wetzel et al., 2016; Hopkins et al., 2018; Garrison-Kimmel et al., 2018), EAGLE (Schaye et al., 2015; Bignone et al., 2019), and NIHAO-UHD (Buck et al., 2020), we are now able to observe the formation of MW and M31-sized galaxies within these simulations on the sub-kpc scale, along with more complex interactions, such as the survival of the galactic disk after major and minor mergers (Sotillo-Ramos et al., 2022), or satellite galaxies that are gravitationally bound to MW and M31 analogs (Engler et al., 2023). It is now possible to verify the results from these state-of-the-art hydrodynamical simulations by comparison with spatially resolved observations from the high redshift universe (i.e. Giménez-Arteaga et al. 2023; Estrada-Carpenter et al. 2024). As we have an enormous wealth of data from JWST of many epochs from the early universe, we also have a unique opportunity to link the high-z and low-z universe via an *observational* approach. Now in the JWST era, with deep, high-resolution, multiwavelength surveys, one can trace the evolution of disk galaxies further back in time. For example, Le Conte et al. (2024) used the CEERS survey to trace the evolution of resolved galaxy structures such as bars in disks from $1 < z < 3$.

Previous studies which use observations to study MWA progenitors used rest-frame optical and NIR flux from HST as a proxy for stellar mass (van Dokkum et al. 2013; Patel et al. 2013, and

Papovich et al. 2015), and the maximum redshift reached was $z \sim 3$. Tan et al. (2024a) performed the first resolved mass assembly study but was limited to only $z \sim 2$. In all of these studies, the main disks have already formed by $z \sim 2.5$. A recent study using JWST photometry from Costantin et al. (2023) has also found a MWA at $z \sim 3$ with its disk already formed. Thus, the results from these studies favor neither inside-out nor outside-in models of formation, and the effect of galaxy interactions and mergers on mass assembly was not well explored. Galaxy mergers are known to play a role in the evolution of the MW (i.e. the last major merger of our galaxy, Gaia-Enceladus, see Belokurov et al. 2018; Helmi et al. 2018), but how common mergers are at different epochs of cosmic time, and how they may drive other processes in addition to mass assembly, such as starbursts or morphological disturbances are less well understood.

In this paper, by utilizing the data from the Canadian NIRISS Unbiased Cluster Survey (CANUCS), we extend the study of spatially resolved galaxy mass assembly to $z \sim 5$. In doing so, we are able to provide a more holistic picture of MWA formation from its earliest steps to the present day. This paper is organized as follows: Section 3.2 provides a summary of the catalogs used and the selection criteria for MWA progenitors via abundance matching. Section 3.3.3 describes the process of creating resolved stellar mass and star formation rate maps of our sample of MWA progenitors with SED-fitting using Dense Basis. Section 3.4 demonstrates the evidence for inside-out growth of MWA progenitors from $2 < z < 5$, and lockstep growth at $0 < z < 2$ from mass density and specific star formation rate densities. Section 3.5 examines the morphological evolution of MWA progenitors from chaotic, disturbed systems to rotationally supported disks. For this work we assume a ΛCDM cosmology with $\Omega_\Lambda = 0.7$, $\Omega_m = 0.3$, and $H_0 = 70$ km/s/Mpc. We assume a Chabrier (2003) IMF.

Table 3.1: The catalog version and list of all NIRCam and HST filters used for each respective CANUCS field in this work. Note that the cluster fields (CLU) also contain additional NIRISS photometry in the bands **F115WN, F150WN,** and **F200WN**, which is included in the count of total number of filters.

Field	Catalog version	NIRCam	HST	Total No. of filters
MACS0417CLU	v1p0.3	F090W, F115W, F150W, F200W, F277W, F356W, F410M, F444W	F435W, F606W, F814W, F105W, F125W, F140W, F160W	18

Cont'd on following page

Table 3.1, cont'd

Field	Catalog version	NIRCam	HST	Total No. of filters
Abell370CLU	v1p1.1	F090W, F115W, F150W, F200W, F277W, F356W, F410M, F444W	F435W, F606W, F814W, F105W, F110W, F125W, F140W, F160W	19
MACS0416CLU	v1p1.1	F090W, F115W, F150W, F200W, F277W, F356W, F410M, F444W	F435W, F606W, F814W, F105W, F110W, F125W, F140W, F160W	19
MACS1423CLU	v1p0.1	F090W, F115W, F150W, F200W, F277W, F356W, F410M, F444W	F435W, F606W, F814W, F105W, F110W, F125W, F140W, F160W	19
MACS1149CLU	v1p2.1	F090W, F115W, F150W, F200W, F277W, F356W, F410M, F444W	F435W, F606W, F814W, F105W, F110W, F125W, F140W, F160W	19
MACS0417NCF	v1p0.2	F090W, F115W, F140M, F150W, F160M, F182M, F210M, F250M, F277W, F300M,F335M, F360M, F410M, F444W	F438WU, F606WU	16
Abell370NCF	v2p0.1	F090W, F115W, F140M, F150W, F160M, F182M, F210M, F250M, F277W, F300M,F335M, F360M, F410M, F444W	F435W, F606W, F814W, F105W, F125W, F140W, F160W	21
MACS0416NCF	v1p1.1	F090W, F115W, F140M, F150W, F160M, F182M, F210M, F250M, F277W, F300M,F335M, F360M, F410M, F444W	F435W, F606W, F814W, F105W, F125W, F140W, F160W	21

Cont'd on following page

Table 3.1, cont'd

Field	Catalog version	NIRCam	HST	Total No. of filters
MACS1423NCF	v1p0.1	F090W, F115W, F140M, F150W, F160M, F182M, F210M, F250M, F277W, F300M,F335M, F360M, F410M, F444W	F438WU, F606WU, F125W, F160W	18
MACS1149NCF	v1p2.1	F090W, F115W, F140M, F150W, F160M, F182M, F210M, F250M, F277W, F300M,F335M, F360M, F410M, F444W	F435W, F606W, F814W, F105W, F110W, F125W, F140W, F160W	19

3.2 Data & Sample Selection

3.2.1 Survey Design

We use the observations from the Canadian NIRISS Unbiased Cluster Survey (CANUCS, see Willott et al. 2022, and Sarrouh et al. 2025 for its first data release) for its excellent depth at high-z and extensive photometric sampling. There are two fields for each cluster in CANUCS: CLU denotes the cluster field, and NCF denotes the "NIRCam Flanking" field. For the CLU fields, the JWST NIRCam filters used are F090W, F115W, F150W, F200W, F277W, F256W, F410M, and F444W. For the NCF fields, the same wide band filters are also used, *except for* F200W. Additionally, NCF fields are imaged by the medium band NIRCam filters F140M, F162M, F182M, F210M, F250M, F300M, F335M, F360M, and F410M. All imaging information for each field is described in Table 3.1. Details of PSF-matching and catalog creation for CANUCS are described in Willott et al. (2024) and Sarrouh et al. (2024). Source detection and aperture photometry was done using the Photutils package from astropy (Bradley et al., 2016, 2023) as described in Asada et al. (2024a). See §3.3.1 for typical aperture size used for each object in this work, and additional details on resolved photometry.

For this work, we only make use of the photometric data. Additional imaging from HST/ACS and HST/WFC3 are provided in the filters F435W, F606W, F814W, F105W, F110W, F125W, and F160W for fields that overlap with the Hubble Frontier Fields survey (Lotz et al., 2017), i.e. both CLU and NCF for Abell 370, MACS 0416, MACS 1149, as well as MACS0417CLU and

MACS1423CLU. However, for MACS0417NCF and MACS1423NCF, there is no ACS imaging, so imaging in the bluest bands is provided by WFC3/UVIS in the bands F438WU and F606WU. For exact usage of bands, and catalog version, see Table 3.1.

3.2.2 Data Reduction

Image processing and catalog construction will be discussed in detail in Sarrouh and Asada et al. (in prep.), which we briefly describe here. For more information on the data reduction process for CANUCS, we refer the reader to Noirot et al. (2023). The full CANUCS dataset includes NIRCam photometry, with spectroscopy from NIRISS and NIRSpec of five strong lensing clusters Abell 370, MACS J0416.1-2403 (hereafter MACS 0416), MACS J0417.5-1154 (hereafter MACS 0417), MACS J1149.5+2223 (hereafter MACS 1149), and MACS J1423.8+2404 (hereafter MACS 1423).

In general, the NCF fields are deeper than the cluster fields by 0.3 to 0.6 magnitudes for the same band. The shallowest median depth (3σ in 0.3" apertures) is 27.2 mag in the HST bands of F125W and F140W for MACS 0417 CLU, and the deepest median depth is the JWST NIRCam band of F277W in MACS 1149 NCF, at 30.8 mag (3σ in 0.3", see Desprez et al. 2024; Asada et al. 2024a, and Willott et al. 2024 for more information). The cluster fields are affected by gravitational lensing, albeit at different strengths for different clusters. Any object in the catalogs with a best-fit model lensing magnification of $\mu > 2.5$ are excluded from the selection. We also correct for the magnification in all stellar mass and SFR calculations, whether resolved or integrated. The process of accounting for the effects of lensing in radial profiles is outlined in §3.4.1. The Abell 370 cluster field is the field impacted the most by lensing overall, and thus our sample is the smallest in that field. The lensing models for Abell 370 are provided in Gledhill et al. (2024), for MACS0416 in Rihtaršič et al. (2025), MACS1149 in Rihtaršič et al. (in prep), and MACS 0417 and MACS 1423 in Desprez et al. (in prep).

The full CANUCS catalog is complete to AB magnitude 27 in the reddest filter F444W at all redshifts (including this work's redshift limit of $z \sim 5$). However, the signal-to-noise cutoff necessary for successful Voronoi binning is $S/N > 30$ in F444W. This signal-to-noise threshold is set to ensure that the individual spatial bins have $S/N > 5$. This means that out of all possible MWAs in the CANUCS fields, only the brightest at high-z can be retained in our sample. More information on Voronoi binning is provided in §3.3.1. Photometric redshifts in the CANUCS catalog (Asada et al., 2024a,b) were obtained with an implementation of EAZY in Python known as `eazy-py` (Brammer et al., 2008). During fitting, a systematic flux error of 5% was added in quadrature to the nominal photometric uncertainty.

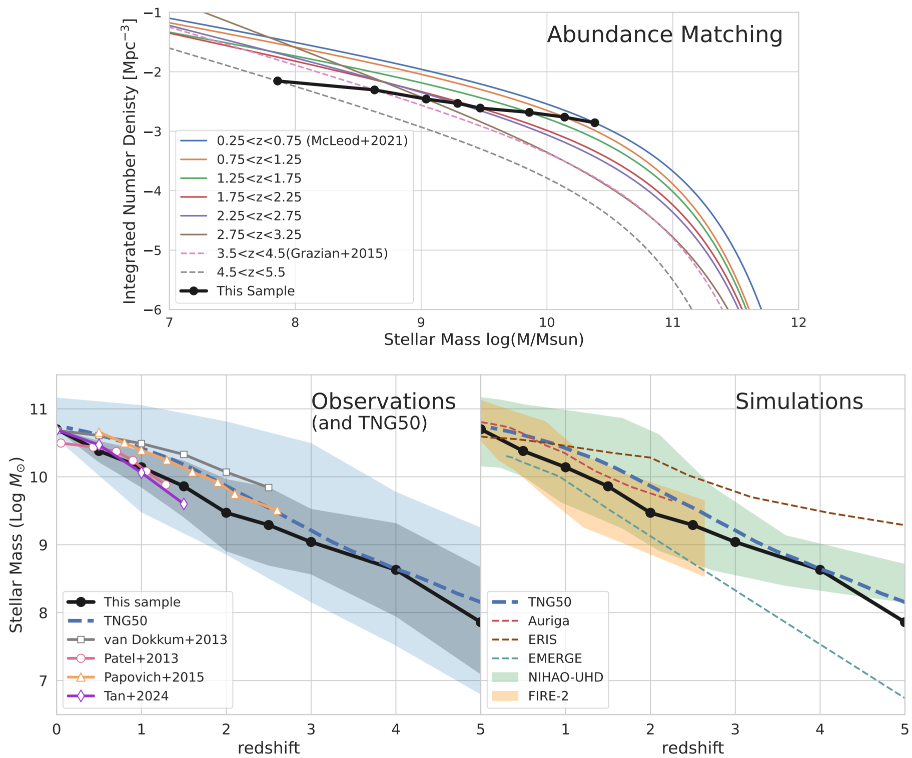

Figure 3.1: *Top Panel:* Each black point represents the intersection between the cumulative number density predicted by abundance matching (Behroozi et al., 2013a) for MWA progenitors, and the stellar mass corresponding to that number density given by the stellar mass function (SMF) at that redshift interval. The starting point is a number density of 0.0011 Mpc^{-3} at $z = 0$, corresponding to $M_\star = 10^{10.7} M_\odot$. Solid SMFs are from McLeod et al. (2021), dashed SMFs are from Grazian et al. (2015). *Bottom left:* Median stellar mass versus redshift for MWA progenitors plotted in black points. The shaded grey region is the 1σ deviation (16th to 84th percentile) of our sample, which comes from the 1σ range in number density from the abundance matching code. We compare our median stellar mass to the median stellar mass from TNG50 (Sotillo-Ramos et al., 2022; Pillepich et al., 2023) represented with the blue dashed line. The blue shaded region is the TNG50 sample's 10th to 90th percentile. Previous *observation-based* studies (van Dokkum et al., 2013; Patel et al., 2013; Papovich et al., 2015; Tan et al., 2024a) are also plotted in grey with white points. *Right panel:* Comparison of this sample's stellar mass evolution for MW progenitors versus predictions from various simulations, such as TNG50, again in blue, Auriga (Grand et al., 2017), ERIS (Guedes et al., 2011), EMERGE (Moster et al., 2018), FIRE-2 (Garrison-Kimmel et al., 2018), and NIHAO-UHD (Buck et al., 2020).

3.2.3 Sample Selection via Abundance Matching

Selecting MWA progenitors may be done via abundance matching, or using properties from simulations (such as stellar masses, halo masses, star-formation history, etc.) as a standard. We choose to use abundance matching, but we demonstrate that both methods are consistent in Figure 3.1. To estimate the range of stellar masses of progenitors of MW-mass galaxies at higher redshift, we assume an evolving co-moving number density with redshift, as determined in Behroozi et al. (2013a), with a present day number density of $\log(n/\text{Mpc}^3) = -2.95$ for MWAs. This number density corresponds to a MW stellar mass of $10^{10.7} M_\odot$ at $z = 0$. The code calculates a past median galaxy number density at z_2, given an initial number density at z_1, via peak halo mass functions. Since the merger rate per unit halo per unit Δz is roughly constant, the evolution of cumulative number density of progenitors of any given galaxy is a power law, with the change described by $0.16 \times \Delta z$ dex. Behroozi et al. (2013a) uses peak halo mass functions for which the resultant median number densities are less affected by the scatter in stellar mass and luminosity. However, this scatter does affect the 1σ errors in cumulative number density. The 1σ or 68 percentile range grows with increasing redshift. The 1σ values grow by ~ 0.16 dex per 0.5 change in redshift.

Behroozi et al. (2013a) does not assign stellar masses to the number densities, but rather determines the number density of the median *halo* mass. Thus, we obtain the stellar mass ranges of the MWA progenitors using the same number densities from the stellar mass functions (SMFs) from two studies, Grazian et al. (2015) and McLeod et al. (2021). Both studies used a combination of ground-based and HST data: Grazian et al. (2015) CANDELS-UDS, GOODS-South, and HUDF09 and HUDF12. The surveys used by McLeod et al. (2021) are a combination of UKIDSS Ultra Deep Survey, UltraVISTA, CFHTLS-D1, and all five CANDELS fields. The result of this matching of cumulative number densities for MWAs to median stellar masses is shown in the top panel of Figure 3.1. A similar analysis is done in Tan et al. (2024a) for the Hubble Frontier Fields but with SMFs from Muzzin et al. (2013a). See Mowla et al. (2024) for the extension of this abundance matching in CANUCS to $5 < z < 9$.

We take the median cumulative number densities at each Δz, to find the stellar mass associated with that number density from the corresponding SMF. In addition, the 1σ errors on the given number density for each redshift are used to determine the maximum and minimum boundaries on the stellar mass of the progenitors at each epoch. Galaxies with redshifts within ± 0.05 of the cluster's redshift are removed from our sample to prevent contamination from cluster galaxies. The full sample is plotted in the bottom panels of Figure 3.1. Also shown in Figure 3.1 are comparisons of this sample's median stellar mass and 1σ stellar mass range to past works that have studied progenitors of MWAs. The left panel focuses primarily on studies that used observational data (van Dokkum et al., 2013; Patel et al., 2013; Papovich et al., 2015; Tan et al., 2024a), while the right panel primarily focuses on studies with simulations (Guedes et al., 2011; Grand et al., 2017; Moster

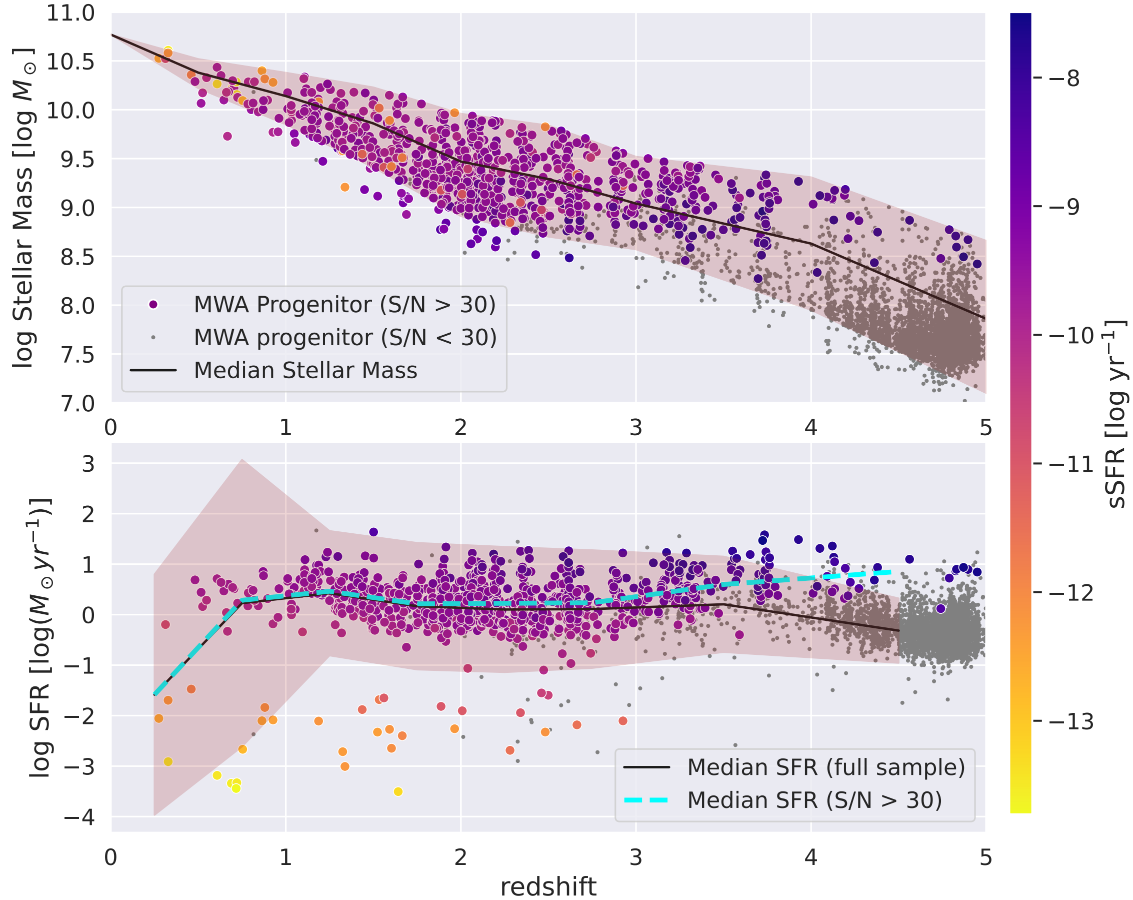

Figure 3.2: *Top panel:* Integrated stellar masses (obtained with Dense Basis) versus photometric redshift of MWA progenitors in the CANUCS fields selected by abundance matching and SMFs. The solid black line is the rolling median of the stellar mass for each redshift range, and corresponds to the solid black line in Figure 3.1, while the shaded red region represents the 1σ scatter, same as the shaded grey region in Figure 3.1. Some of the stellar masses are scattered below the 1σ region due to lensing magnification corrections. Large colored points are galaxies that have $S/N > 30$, and their color represents the specific SFR. The small grey points have too little signal-to-noise for resolved photometry, and are excluded from our final sample. *Bottom panel:* Catalog log SFR vs Redshift, same selection criteria as above. The shaded red region represents the 1σ scatter of SFR. The color of each point indicates specific SFR. Note that at higher redshifts, galaxies with $S/N > 30$ skew towards the higher mass and higher SFR end of the full distribution of possible MWAs in that redshift range. Note that quiescent galaxies are not used for the main analysis.

et al., 2018; Garrison-Kimmel et al., 2018; Buck et al., 2020; Pillepich et al., 2023). The TNG50 results from Pillepich et al. (2023) are plotted in both panels for comparison. Our stellar mass range for each redshift bin for MWA progenitors agree with the literature, for both observations and simulations.

In Figure 3.2, we apply the selection criteria as described above to the CANUCS catalogs, and plot the catalog stellar mass versus redshift in the top panel, and the catalog instantaneous SFR versus redshift in the bottom panel (unlike the photometric catalogs, the mass catalogs are obtained with Dense Basis, see §3.3.3 for more details). Note the CANUCS catalog stellar mass and instantaneous SFR (henceforth simply called 'SFR') are integrated over the whole galaxy. The color of the points show their integrated sSFR (SFR/stellar mass). The vast majority of galaxies have log(sSFR) > -11. Due to the relationship between stellar mass and redshift, lower-z galaxies tend to be more massive but have lower sSFR than higher-z galaxies with the same total SFR.

There are 5307 potential MWA progenitor galaxies at $0 < z < 5$ that fall within the 1σ boundaries as defined by applying the abundance matching code to the given SMFs. In this paper, we SED-fit galaxies in 2D, and an integrated $S/N > 30$ is required to get meaningful, spatially-resolved SED fits. Therefore, the colored dots represent the subsample of these potential MWA progenitors that have a $S/N > 30$ in their integrated F444W flux. This ensures that each spatial bin will have at least $S/N = 5$ at higher redshifts, and ensures there are at least 50 spatial bins per galaxy. We remove the small grey points from our sample, which have integrated $S/N < 30$. After additionally removing 23 more galaxies on the basis of missing photometry in all JWST bands bluer than F250M (which would make the SED fit untrustworthy for resolved modeling), our full sample of MWA progenitors for 2D SED modeling is a total of 909 galaxies.

A result of this signal-to-noise cutoff is that the higher mass galaxies at higher-z are selected over lower mass galaxies. As shown in Figure 3.2, our sample is complete to $z = 3$. Above $z = 3$, we become increasingly biased towards more massive progenitors. In addition, the median SFR, as plotted in the bottom panel of Figure 3.2, no longer peaks at $z \sim 1.5$, but continues to rise to $z \sim 5$. Ultimately, the CANUCS dataset is among the deepest JWST surveys to date, and we continue the analysis to $z = 5$. Note that at $z > 3$, there is an increasing degree of progenitor bias in the results. In order to be complete at $z = 5$ would require an order of magnitude more depth, which can only be obtained with two orders of magnitude greater exposure time. Given that the CANUCS integration times are $\sim 1 - 3$ hours, this is unlikely to be obtained within the mission (see Willott et al. 2022). Strong lensing samples, such as the Firefly and Cosmic Gems, are necessary for even higher redshifts, though they are limited in number for each lensing cluster. Thus, our sample shows a "first look" at evolution of progenitors up to $z = 5$.

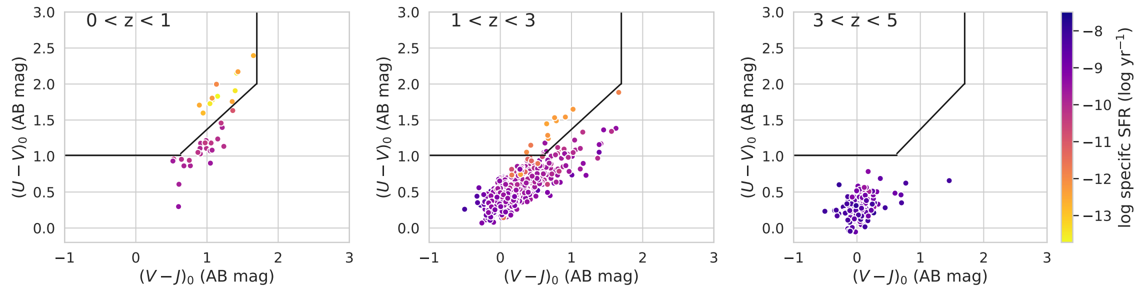

Figure 3.3: The distribution of UVJ colors for the MWA progenitors. Since the quiescent fraction of MWAs is small ($\sim 0.03\%$), The UVJ boundaries are defined with a bimodal distribution of 9615 galaxies in CANUCS at $0 < z < 5$, with a 25% quiescent fraction (See Appendix 3.9). The color calibration is adapted from Antwi-Danso et al. (2023). The color of the points represent the sSFR of the MWA progenitor sample.

3.2.4 Quiescent fraction in the MWA sample

A limitation of abundance matching is that not all selected progenitors will evolve into an MWA at $z = 0$. Since the MW is still star-forming (albeit with a much lower star formation rate that places it within the Green Valley, see Mutch et al. 2011), we only select actively star-forming galaxies within our MWA progenitor sample for an accurate picture of the mass assembly relevant to the MW itself. Even though any actively star-forming higher-z may become quiescent before reaching $z = 0$, quiescent galaxies can be discounted as MWAs.[1] Therefore, we use rest-frame UVJ colors in combination with the sSFR of this sample to find and remove quiescent galaxies.

In Figure 3.3, we plot the rest-frame colors of our progenitor sample. In order to determine the proper color-magnitude cuts, we utilize the code presented in Antwi-Danso et al. (2023). The code searches for a bimodality in color space by calculating the distance of each galaxy from the UVJ diagonal line. We refit the UVJ slope for the color calibration with the redshift range changed to $0 < z < 5$. For more information on UVJ color calibration, see Appendix 3.9. The UVJ boundaries are:

$$(V-J) < 1.7;\ (U-V) > 1.01; \tag{3.1}$$

$$(U-V) > (V-J) \times 0.91 + 0.63. \tag{3.2}$$

We lowered the $(U-V)$ boundary by 0.23 to accommodate a simple stellar population at $z \sim 6$ with an age of ~800 Myr. This corresponds to the age of a typical post-starburst galaxy at $0.5 < z < 2.5$ (Belli et al., 2019; Wild et al., 2020). At $z > 1$, the horizontal line was further lowered by 0.06 magnitudes to better match the sSFR distribution of the MWA progenitors. The divisions

[1]Rejuvenation may transform quiescent galaxies back into star-forming ones, but it is impossible to discern if rejuvenation will occur for any high-z galaxy without high S/N measurements of gas kinematics, which is beyond the scope of this work.

presented above are also shown in Figure 3.3, in each panel, as solid black lines. The color of the points represent the galaxy's sSFR.

After the signal-to-noise cut, and separating the sample into star-forming and quiescent, there are 885 star-forming galaxies, and 24 quiescent galaxies. 12 out of the 24 quiescent galaxies are at $z < 1$. Additionally, there are only star-forming galaxies at $3 < z < 5$.

3.3 Spatially resolved SED-fitting on JWST photometry

In this section, we explain the methods of creating spatially resolved maps of stellar mass and instantaneous SFR distributions for our sample of MWA progenitor galaxies. All resolved photometry is applied to the science images PSF-matched to F444W provided by CANUCS. The size of the PSF FWHM for the F444W filter is 0.15" or 2.3 pixels.

3.3.1 Voronoi binning of galaxy images

In preparation for resolved SED-fitting, we use Voronoi binning (Cappellari & Copin, 2003) on cutouts of each galaxy. The overall process is similar to the process outlined in previous works Tan et al. (2022) and Tan et al. (2024a) using Hubble photometry, however, instead of Voronoi tessellating across the whole of the cutout, the cutouts were separated into two areas: the galaxy, and the background.

The area of the image defined to be the galaxy are the pixels of the cutout contained in an elliptical aperture scaled to the Kron radius of each object via their major and minor axes a and b:

$$R_{model,a} = 2.5 R_{kron} a \quad , \quad R_{model,b} = 2.5 R_{kron} b \quad . \tag{3.3}$$

Note that this is the *modified* definition of Kron radius, as defined in Source Extractor and Photutils (see Bertin & Arnouts 1996 and Bradley et al. 2016 for details). As mentioned in §3.2, the CANUCS photometric catalogs were created with the Photutils package, so a and b multiplied by Kron radius R_{kron} would define an elliptical aperture that contains roughly 68% of the galaxy's light. Therefore, at 2.5 times the Kron radii, the aperture would capture roughly 97% of the galaxy's light within it.

For each field, from the preliminary sample chosen via stellar mass limits from abundance matching, we only select objects to perform pixel-binning if the total integrated flux in the F444W band as defined by the Kron radius of the object has $S/N = 30$ or higher.

In preparation for Voronoi binning, we set the minimum signal-to-noise threshold for the binning within the aperture to be $S/N = 10$ for galaxies at $z < 1.8$, and $S/N = 5$ for galaxies at $z \geq 1.8$. This is to ensure that higher-z galaxies have smaller spatial bins for better resolution. For the pixels outside the aperture in the cutout, the minimum signal-to-noise threshold is set at a value of $S/N = 3$. If binning fails for the background (the pixels outside the aperture), the signal-to-noise is lowered by 1 until a minimum of $S/N = 1$.

3.3.2 Accurate flux errors for photometric catalogs of Voronoi bins

In order to have resolved stellar mass maps, we must first create a new photometric catalog for the total flux and flux errors in each spatial bin of each cutout of a MWA progenitor in our sample. This ensures that resolved SED-fitting is performed in the same manner for this study as it was done on the integrated photometry of the entire CANUCS catalog.

The flux errors for each spatial bin of each galaxy were derived by approximating the size of the bin to a circularized aperture of a specific radius. The longest distance between two pixels in a single bin is taken to be the "diameter" of the aperture. This is because the Voronoi binning algorithm was set to run with both "weighted Voronoi tesselation" (WVT) and "centroidal Voronoi tesselation" (CVT) modes, and thus binned regions are close enough to circular for this distance to be a good approximation. Afterwards, the flux error of the circularized aperture is set as the background flux error for the specified bin. The flux error for the circularized apertures is calculated by taking the FWHM of the number of counts from ∼2000 empty apertures of the same size placed on empty regions across each respective CANUCS field. This means that every photometric band of every field has its own specific set of background flux errors. Similar to the photometric catalogs and mass catalogs, a systematic error of 3% was added in quadrature to each spatial bin. We chose 3% to be consistent with the mass catalogs of CANUCS, which are also fit with Dense Basis. (See Sarrouh et al. 2024 for more details related to this flux error in application to CANUCS catalog construction. See Sok et al. 2024 and Jagga et al., in prep. for a similar treatment of flux errors in Voronoi binning.) In addition, the MW foreground extinction correction factors from the catalog were also applied to the total flux of the pixel bins for each respective galaxy, to ensure that the SED fit is as accurate as possible.

3.3.3 Creating stellar mass and SFR maps

Similar to the construction of the full CANUCS mass catalogs, we use Dense Basis (Iyer & Gawiser, 2017; Iyer et al., 2019) with the FSPS libraries (Conroy & Gunn, 2010) to perform SED-fitting to the resolved photometric catalogs created for each individual galaxy in our MWA progenitor sample. Dense Basis is a non-parametric SED-fitting code that uses a Bayesian nested sampler and Gaussian process kernels to fit smooth star formation histories (SFHs) independent of functional form. This flexibility makes Dense Basis an ideal SED-fitting code for both obtaining the stellar mass density maps, and creating resolved SFR maps for specific sub-regions of a galaxy. Since higher-z galaxies contain more star-forming clumps, SFR maps can reveal a wealth of information about the mass assembly history of MWA progenitors.

The relevant information for both SED-fitting and SFH reconstruction is saved into an atlas of template SEDs, also called a pregrid, and was done for each catalog for the CANUCS fields. By default, Dense Basis uses a Chabrier IMF (Chabrier, 2003), and the Calzetti dust law (Calzetti et al., 2000). We choose a flat sSFR prior for the star-formation rate. We use an exponential dust attenuation prior with values of A_V allowed to vary between 0 and 4. We also use a flat metallicity prior with a range of $-1.5 < Z < 0.25$. For SFH reconstruction, the pregrid is given a set of timescales $\{t_x\}$ on which different SFRs are computed (i.e. $\{t_X\} = t_{10}, t_{100}, t_{300}, t_{1000}$ for the CANUCS catalogs). For consistency, we use the instantaneous SFR, which is the average SFR over the time scale at which the galaxy formed the last 1% of its mass.

In order to be consistent with the integrated stellar mass and SFR of the CANUCS catalogs, we use the same pregrid atlases for each respective CANUCS field. When Dense Basis is run on each galaxy, it is run on each spatial bin of the galaxy cutout, treating the bin as an "aperture" itself, with flux and errors distributed accordingly. We fix the redshift for each pixel bin to the photometric redshift of the galaxy. We take the best-fit median stellar mass and median SFR as the resultant stellar mass and SFR for each respective pixel bin. For better resolution in larger bins, we distribute the total stellar mass or SFR of that bin among the pixels depending on how much flux that individual pixel contributed to the total flux of the bin in the relevant band. For stellar mass maps, the filter used to determine distribution of the stellar mass within a single bin is the reddest filter, F444W, whereas for the SFR, the filter used is the closest broadband or medium band filter to rest-frame $u-$band (365 nm).

In Figure 3.4, we display 119 randomly chosen examples of the original 909 MWAs and plot their color images, stellar mass maps, and SFR maps inset into a plot of the total stellar mass versus redshift to demonstrate the evolution of the mass density and SFR density over our entire redshift range. The images are scaled to the same angular resolution to demonstrate how much progenitors have grown since $z = 5$. MWA progenitors grow significantly in total mass and size, since $z = 5$, with disk structures emerging around $z \sim 2.5$. In Figure 3.5, we present more detailed color images, stellar mass maps, and SFR maps of 16 select galaxies from this sample across a variety of redshifts. What is notable about the resolved SFR maps in Figure 3.5 is that regions of high star formation are closer to and even overlap with regions of high stellar mass density at earlier times, but the star-forming regions migrate further out at later times, decoupled from regions where stellar mass is concentrated. We further investigate these evolutionary changes in stellar mass and SFR quantitatively in §3.4 and §3.5.

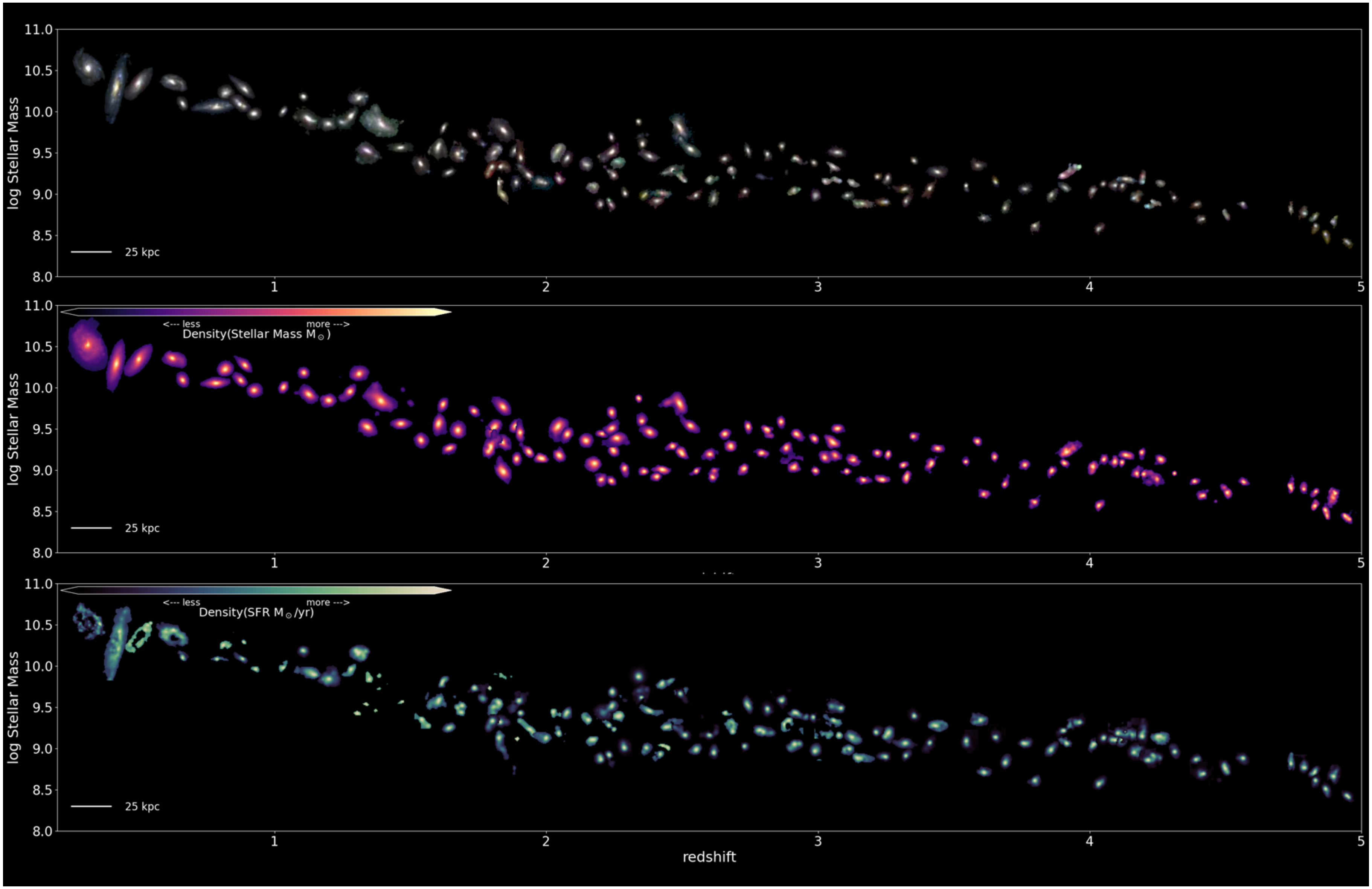

Figure 3.4: Color images (top panel), resolved stellar mass maps (middle panel), and resolved SFR maps (bottom panel) of a randomly selected subsample of 120 MWA progenitors. The plots are inset into a total stellar mass versus redshift plot to demonstrate the evolutionary trend of the progenitors. Each image has the same physical scale in kpc, displayed in the bottom-left corner. Certain galaxy images are offset by no more than $\pm0.25z$ or ±0.25 log $M_\odot$ to lessen overlap. Note that at higher redshifts, the morphologies shown are not fully representative of the progenitor population.

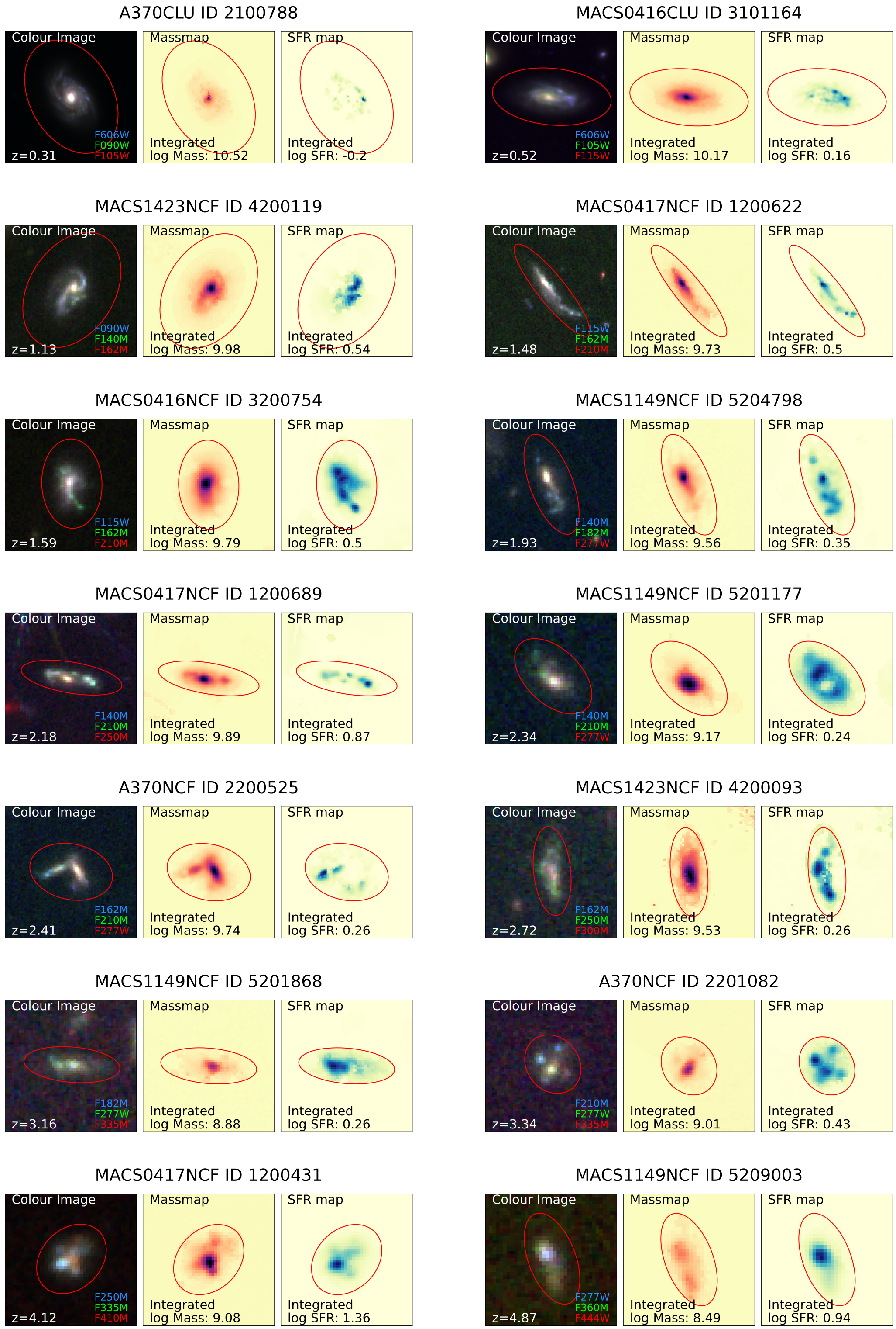

Figure 3.5: Rest frame *gri* color image, stellar mass map, and SFR map of select MWA progenitors from CANUCS. Units for integrated stellar mass are in $\log(M_\odot)$ and for integrated SFR are in $\log(M_\odot/\mathrm{yr})$. Red ellipses are defined by Equation 3.3.

3.4 Resolved mass assembly and star formation of MWA progenitors

In this section, we show measurements of the growth of MWA progenitors to better understand the mass growth history of the MW. We utilize both mass and sSFR density profiles to track the overall mass assembly since $z = 5$, which spans a time period of 12.5 Gyr. Thus, we group the MWA progenitors into redshift bins according to the redshift ranges represented by the SMFs of McLeod et al. (2021) and Grazian et al. (2015) in §3.2.3. The stellar mass boundaries of each redshift bin are represented by the grey shaded region in the bottom left panel of Figure 3.1, as well as the brown shaded region in the top panel of Figure 3.2. For each redshift bin, a stacked and normalized mass and sSFR radial density profile is created from the individual radial profile (both Σ_{star} and Σ_{sSFR}) of each galaxy. We also further separate the profiles into inner and outer regions, as defined by the positional relation to a galactocentric radius of $R = 2$ kpc. We track the inner, outer, and overall mass growth, sSFR, as well as their respective density over time to quantify the difference in mass growth over cosmic time.

3.4.1 Density profiles as a function of galactocentric radius

The 1-D mass and SFR density profiles as a function of distance from galactic center R are obtained by placing elliptical annuli centered on the galaxy cutout with a width of 0.1 kpc on the stellar mass and SFR maps. The total stellar mass or SFR within each annulus is then divided by the total area of the annulus. The shape of the annuli are defined by the galaxy's b/a ratio as found in the CANUCS catalogs.

In order to counter the effects of magnification on size measurements and radial density profiles, the conversion factor between observed angular size and the physical size in kpc were adjusted in the direction of the position angle of the galaxy (the angle of the semi-major axis to the horizontal) as well as in the direction perpendicular to the position angle. To make sure the adjustment in resolution is as close as possible to the true physical scale, we define a matrix which describes the ellipse of galaxy on the observed plane using a, b, and $\theta \equiv$ position angle. We also define a transformation matrix based on lensing shear orientation ϕ, the angle at which the lensing distortion is the strongest, $\mu_{tan} \equiv$ the magnification in the ϕ direction, and $\mu_{rad} \equiv$ the magnification in the direction perpendicular to ϕ. Applying the inverse of the transformation on the matrix that defines the ellipse and then obtaining the eigenvalues will return the de-magnified lengths of a and b, as well as the de-lensed position angle. However, since we are keeping to the observed plane and not the source plane in order to preserve resolution and the measured PSF, we scale the angular resolution by the change in length of a and b respectively from the source plane to the observed plane.

Each individual galaxy's mass density or SFR density profile is then sorted according to their

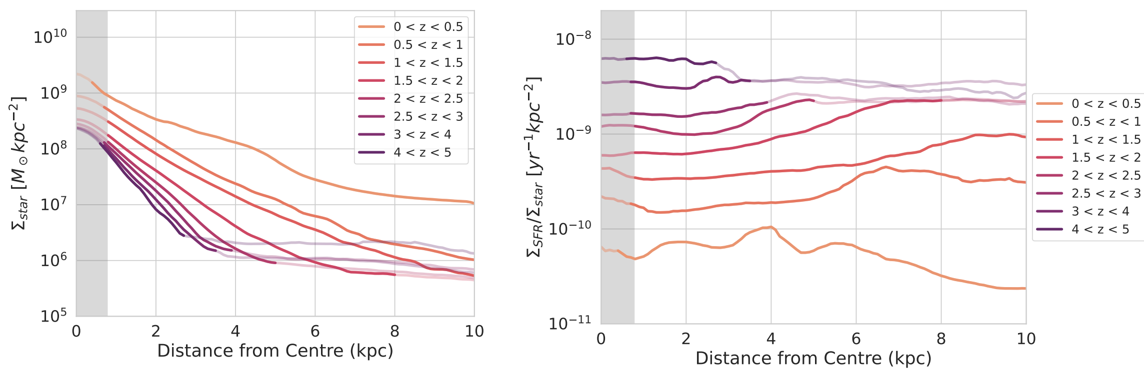

Figure 3.6: *Left Panel:* Stacked and normalized stellar mass profiles for each redshift epoch. Profiles are truncated at the boundary where the noise dominates. The grey region indicates the maximum extent of the central regions affected by the PSF. *Right Panel:* Stacked and normalized sSFR (specific star formation rate) profiles for each redshift epoch. Each sSFR profile was obtained by dividing each normalized SFR profile by the normalized mass profile of the same redshift (see Appendix 3.10). The truncation in radial profile is the same as the left panel.

redshift bin, then stacked and normalized to obtain the density profile of that redshift. These normalized density profiles are shown in Figure 3.6, with distances from the center measured along the semi-major axis. See Appendix 3.10 for the individual mass and SFR density profiles for each galaxy, divided into redshift bins.

The solid lines of the mass density profiles in the top panel of Figure 3.6 reveal that at higher redshifts ($2 < z < 5$), mass density increases between different redshift steps more at greater distance from the galactic centre. At $R < 1$ kpc, the increase in mass density is roughly $\sim 0.1 - 0.2$ dex, from $4 < z < 5$ to $2 < z < 2.5$. At a further distance of $R \sim 2.5$ kpc, the increase in mass density from one redshift epoch to the next is ~ 1 dex, an entire order of magnitude greater. This trend is reflected in the sSFR density profiles as well, as the sSFR starts off relatively flat across the entire normalized profile at $4 < z < 5$, but the highest sSFR consistently occurs at the furthest point from the centre of the galaxy, until $z \sim 0.5$ when it flattens out once more.

At higher redshifts, the mass density profiles retain a similar shape in the center, but their outskirts increase in mass. This might best be shown by the comparison of the growth in the centre ($R <$ 2kpc), to the growth at 4.5 kpc, which is approximately the effective radius of MWA at $z \sim 0$ (see §3.5.2). Over the redshift range covered by our data the central part of the MWA grows by about an order of magnitude in mass, however, the growth at $R \sim 4.5$ kpc is two orders of magnitude, implying ten times more growth at the effective radius. Likewise, in the sSFR density, while the sSFR is continuously decreasing at later times, the highest sSFR density is usually near the limits of the density profile's boundary, implying that the outskirts of the galaxies are where most of the sSFR is concentrated. This shows that towards lower redshift, galaxies are increasingly growing their disks, which is evidence for inside-out growth.

We note that this trend may be affected by PSF smearing, because the physical kpc scale of the PSF increases up to $z \sim 1.6$ (the affected regions of the density profile have greater transparency in Figure 3.6). However, since the size of the PSF is never greater than 1 kpc even at the redshift bin with the worst physical resolution, PSF smearing cannot account for all of the density profile changes within $R = 2$kpc, which is defined as the inner regions of the profiles. Additionally, the total stellar mass and total sSFR in the inner regions should be less affected by the PSF, and how those quantities change with redshift is discussed in the next section.

3.4.2 Inner regions versus outskirts

With the stacked and normalized 1-D profiles representative of each redshift epoch in Figure 3.6, we divide them into inner and outer regions with a 2 kpc cutoff point. While the 2 kpc cutoff point is most of the galaxy at higher redshift bins, especially $z > 4$, the MW in the current universe has a bulge extent of roughly 2 kpc, and thus this region represents the regions which will eventually *become* the bulge for present day MWAs.

In Figure 3.7, the outer regions, represented by the blue line on the plots, are shown in the top panels to increase in both stellar mass and in sSFR much faster than the inner regions at higher-z. In fact, the epoch between $2.5 < z < 5$ shows very little stellar mass growth in the inner 2 kpc region – only ~ 0.1 dex – while the outer region increased ~ 1 dex, an order of magnitude from the highest redshift bin to $z \sim 2.25$. The stellar masses of the outer regions at the lowest redshift bin appear to be directly in between the $M_{\star}$of the MW's thin and thick disks, while the inner regions are already more massive than the $M_{\star}$of the MW's bulge. However, one must keep in mind that the MW has an unusually small bulge for a galaxy of its size. (Shen et al., 2010). The overall SFR and the SFR of the inner regions decline as redshift decreases, but the SFR of the outer regions remains constant at earlier times at $\sim 0.2 M_{\odot}$/yr ($2 < z < 5$) and increase at later times ($z < 2$), up to $\sim 0.6 M_{\odot}$/yr at the lowest redshifts. For the median sSFR plotted in the top-right panel, we again see a consistent decline in the inner regions as redshift decreases, but from $1.5 < z < 3$ the sSFR of the outer regions are much higher, and decrease less sharply. From $z \sim 2.5$ onwards to lower redshift, the outer regions have consistently higher sSFR, until the lowest redshift bin. This demonstrates the rapid and sustained inside-out growth of this sample of progenitors.

In the bottom-left panel of Figure 3.7, the total, inner, and outer stellar mass density (Σ_{star}) is plotted as a function of redshift. From $z = 5$ to $z = 2$ the total Σ_{star} is decreasing, the outer Σ_{star} is roughly constant, while the inner Σ_{star} grows slowly. While this seems counter to the stellar mass growth in the top-left panel, recall that the galaxies themselves are also increasing in size. Therefore if the stellar mass is added to the outskirts of the galaxy, and increasing its scale-length, the decrease in mass density is expected. The stellar mass density evolution also shows evidence of MWA progenitors growing inside-out at $2 < z < 5$. It is important to note that the amount of

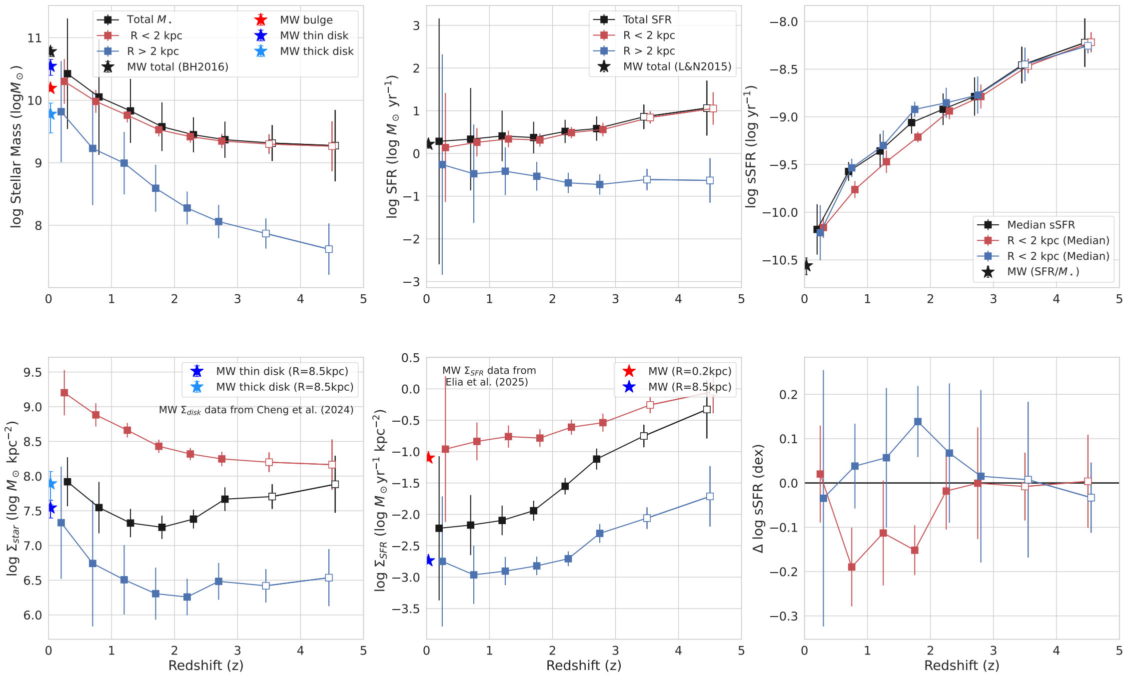

Figure 3.7: *Top Panels:* Median stellar mass growth (left), median SFR (center), and median sSFR (right) as a function of redshift. Red and blue show the change in stellar mass, SFR, or sSFR in the inner ($R < 2$ kpc) and outer ($R > 2$ kpc) regions of the galaxies. Empty points represent redshifts affected by completeness of the sample. MW values from Bland-Hawthorn & Gerhard (2016) for stellar mass and Licquia & Newman (2015) for SFR. *Bottom Panels:* Median stellar mass and SFR densities (left and center) as a function of redshift. Right panel is the difference in sSFR between inner/outer regions and the overall median sSFR. Error bars in all plots are standard error. MW mass density and SFR density values are from Cheng et al. (2024b) and Elia et al. (2025) respectively.

time between $2 < z < 5$ is roughly 2 Gyr. But in that span of time, the galaxies have grown ten times in stellar mass, and increased in size from $R_e \sim 1.0$ kpc to $R_e \sim 1.8$ kpc (see §3.5.2 for the measurement of R_e and more information on general morphological evolution). After that growth, however, the inner and outer regions increase in stellar mass density at roughly the same rate (i.e. the slope of the inner and outer mass density lines are very similar). Therefore, the mass is growing proportionally at $z < 2$, which means the growth of the inner and outer regions are in lockstep, which is consistent with previous studies.

The bottom middle panel, which displays the SFR density (Σ_{SFR}) as a function of redshift, shows that both inner and outer regions decline in SFR steadily as redshift decreases. The Σ_{SFR} at later times is consistent with the measured SFR densities of the MW's inner regions, and solar neighborhood from Elia et al. (2025). At higher redshift ($z > 2$), the $M_\star$ of the outer regions is increasing rapidly, while its Σ_{star} remains constant, so we should then expect the Σ_{SFR} to also remain constant, but that is not the case. The Σ_{SFR} of the outer regions is decreasing at $z > 2$. Additionally, there is enhanced sSFR in the outer regions from $1.5 < z < 3$, as the decline in outer sSFR is much shallower than the inner regions. This is shown more clearly in the bottom-right panel, which shows the difference in dex between the sSFR of the inner and outer regions with respect to the overall sSFR at that redshift bin. This may be an indication that the *observed* SFR may not account for all of the mass assembly of this sample.

The trends in the SFR density and the enhancement of the sSFR of the outer regions may indicate more varied star-formation activity in the outer regions at different epochs of growth, and perhaps indicate enhancement of star formation around cosmic noon. However, since this sample is only galaxies with total $S/N \geq 30$, the MWA sample is not mass complete at $z > 3$. Therefore, the stellar mass and especially the SFR trends at $z > 3$ are only representative of the most massive and highly star-forming MWAs at those epochs. Additionally, hierarchical formation and mergers are expected to play a larger role as redshift increases. Mergers and interactions can enhance SFR as well (though Moreno et al. 2021 shows in FIRE-2 that galaxy interactions can both enhance and suppress SFR differently at different radii for both main and secondary galaxies in pairs), so it is important to understand how much stellar mass is formed in-situ versus ex-situ from mergers.

3.4.3 Is SFR the main driver of mass assembly?

We seek to understand the mass growth observed over the redshift ranges that are mass-complete, whether it is dominated by in-situ SFR or if galaxy mergers may play a role. For each redshift bin, we have obtained the median total stellar mass, and the median total SFR. To test if the SFR is consistent with the total mass assembled, we first take the total resolved SFR in units of $M_\odot$/yr at each redshift bin z_{obs}, and calculate the total mass formed (M_{formed}) by the SFR by integrating over the span of time that has passed.

$$M_{formed}(z_{obs}) = \int_{t_i}^{t_f} \mathrm{SFR}_{z_{obs}}(t)dt \ , \tag{3.4}$$

where $\mathrm{SFR}_{z_{obs}}$ is the median SFR at the redshift epoch z_{obs}, t_i is the age in years of the start of z_{obs} and t_f is the age in years of the end of z_{obs}. Note that for the median SFR of each redshift range, we only consider star-forming galaxies and ignore quiescent galaxies.

This M_{formed} however does not represent the stellar mass, $M_\star$ that was added in that time period. This is because a portion of the total mass formed is returned to the interstellar medium (ISM), and must be accounted for in our calculations. Therefore, we also take into account the "mass loss" factor, which at its simplest is the percentage of formed mass that becomes stellar mass.

For every redshift epoch, we define the stellar mass that is *not* returned to the ISM as

$$M_{\star added}(z_{obs}) = \int_{t_i}^{t_f} \mathrm{SFR}_{z_{obs}}(t) f_{ret}(t)dt \ , \tag{3.5}$$

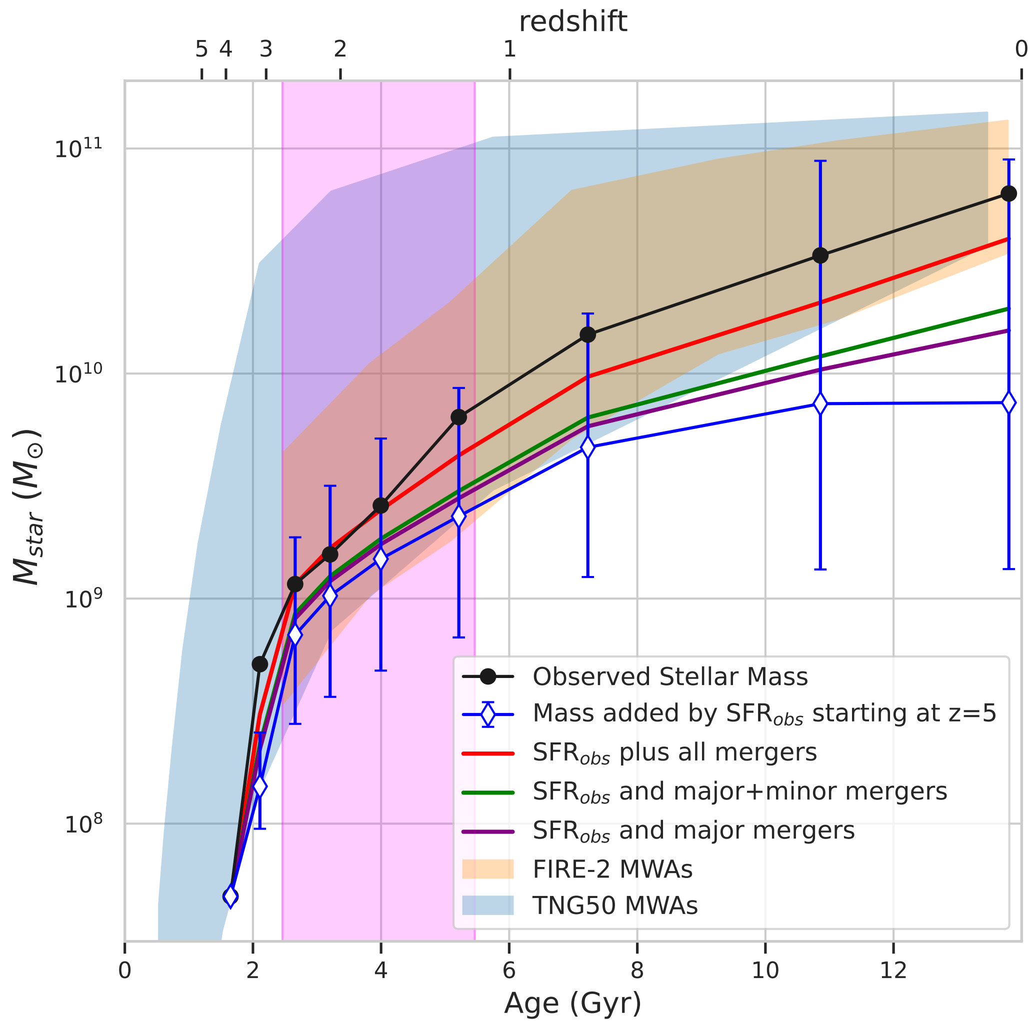

Figure 3.8: The observed stellar mass evolution over time of the full unresolved sample (solid black circles), and the stellar mass added by integrating the observed unresolved sample's SFR of the previous epoch (blue open diamonds). Error bars are upper and lower limits derived from the 1σ scatter of the SFR at each epoch. The mass added by both observed SFR and estimated accretion rate (from Rodriguez-Gomez et al. 2016, integrated over the time span of each epoch) improve the agreement when more mergers are included (red line is merger mass ratio ≥ 0.0001, green line is mass ratio ≥ 0.1, and purple line is mass ratio ≥ 0.25). Shaded purple region is the possible time frame at which the GSE merger occurred for the MW (Belokurov et al., 2018; Helmi et al., 2018)

where $f_{ret}(t)$ is the mass-loss curve from FSPS (Conroy & Gunn, 2010) that is implemented in Dense Basis to calculate SFHs from the posteriors. At redshifts of $0.5 < z < 5$, the mass loss rate is roughly $\sim 37\%$ to $\sim 43\%$, with higher mass loss at higher-z.

The SFR-derived $M_{\star added}$ is then combined with the $M_{initial}$ at the starting redshift. The starting redshift point is at $z = 3$, therefore $M_{initial} \equiv M_{obs,z=3} = 2.4\times10^9 M_\odot$, and every subsequent redshift epoch:

$$M_{\star added}(z_{obs}) = M_{obs,z=3} + \int_{t_i}^{t_f} \text{SFR}_{z_{obs}}(t) f_{ret}(t) dt \,, \tag{3.6}$$

where the integral represents all of the $M_{\star added}$ generated from integrating each median SFR at the respective redshift ranges (t_i to t_f) that they cover, with the mass loss factor f_{ret} applied. The comparison of this added stellar mass growth versus the *observed* stellar mass growth (i.e. the median total resolved stellar mass measured at each redshift bin) is presented in Figure 3.8.

Although we have resolved SFR measurements, we use the median of the integrated(unresolved) SFR and median integrated $M_\star$of each galaxy from the full sample in order to mitigate any biases from incompleteness. In Figure 3.8, the resulting mass added line, plotted in blue with white diamonds, consistently underestimates the observed stellar mass of the next redshift epoch, and at $z = 0$ would underestimate the growth by almost an order of magnitude. However, the large error bars, which are from the 1σ scatter of the SFR of the redshift bin, does marginally include the observed stellar mass. This indicates that mass formed ex-situ, or mass accreted from merging galaxies likely play a significant role in mass assembly. In order to assess the contribution of mergers to mass assembly, we would need to integrate the mass accretion rate due to mergers over time.

As the accretion rate described in Behroozi et al. (2013b) is based on halo masses, we utilize the *stellar mass accretion rate* from the Illustris simulations, ($M_0\dot{m}_{acc}(M_0, \theta, z) = d^2M_{acc}/d\theta dt$) as described in Table 1 of Rodriguez-Gomez et al. (2016) [2]. Using the mass accretion rate from Illustris is a good estimate of the "missing ex-situ mass" as Figure 3.1 shows our stellar mass from abundance matching is in very good agreement with the mass range of MWAs in TNG50. The red, green, and purple lines in Figure. 3.8 reveal that in order to properly account for the ex-situ mass fraction, mergers with a mass ratio as small as $\theta = 10^{-4}$ must be counted to get close to observed values. Only counting major mergers ($\theta \geq 0.25$) or both major and minor mergers ($\theta \geq 0.1$) is insufficient.

Comparing our results to MWA simulations from FIRE-2 (Garrison-Kimmel et al., 2018) and from TNG50 (Pillepich et al., 2023), we find that the $M_{\star added} + M_{acc}$ for the stellar mass accreted is consistent with both simulations only when nearly every merger is taken into account. Sotillo-Ramos et al. (2022) also find that MW/M31 analogs in TNG50 that have experienced ≥ 1 major mergers

[2] In Rodriguez-Gomez et al. (2016), μ was used to indicate mass ratio, but we have changed the symbol for the mass ratio to θ to avoid confusion with the μ used to describe magnification factors earlier in the paper

in the last 5 Gyr have ex-situ stars make up most (up to 90%) of their total stellar mass at $z = 0$. Furthermore, this addition does not account for how much of the observed SFR at each redshift is due to merger enhanced star formation. A closer look into merger rates is required for better understanding the mass assembly of this sample of MWA progenitors.

3.5 Morphological Measurements of MWA progenitors

Examining the morphology of the stellar mass maps can not only strengthen the arguments for inside-out growth of disks at early epochs, but also reveal whether disturbances in structure which resulted from galaxy interactions or mergers have played key roles in mass assembly apart from in-situ star formation. For the morphological measurements, we utilize Statmorph (Rodriguez-Gomez et al., 2019), a tool developed for asymmetry measurements and clump detection for galaxies. We run Statmorph on the stellar mass maps, the SFR maps, and the F444W maps.

Resolved maps are prepared for Statmorph in a similar manner as described in Tan et al. (2022) and Tan et al. (2024a) for morphological fitting.

- We take the corresponding segmentation map of each object from the catalog to define the foreground and the background pixels.
- Noise is added to the stellar mass and SFR maps according to the FWHM of the background noise present in the F444W cutout, using the segmap of the galaxy from the catalog.
- The input PSF is the F444W PSF, since all of the photometry has been PSF-matched to F444W, which means the stellar mass and SFR maps would have the same resolution as F444W.
- A high value was set for gain to allow Statmorph to generate its own weight map for the images, as the provided weight map from the catalog would not apply to derived stellar mass and SFR quantities.

3.5.1 Sérsic profiles

A Sérsic profile (Sérsic, 1963) is a function with two main parameters, n the Sérsic index, and R_e the effective radius, or the radius that contains half of the flux (or in this case, half of the stellar mass).

$$I(R) = I_0 \exp\left(-b_n \left[(R/R_e)^{1/n} - 1\right]\right) \quad (3.7)$$

When $n = 1$, the Sérsic profile is purely exponential, and indicates that the surface brightness profile of the galaxy is likely an exponential disk. When $n = 4$, the Sérsic profile likely resembles a de Vaucouleurs profile, and indicates that the galaxy may be bulge-dominated, and elliptical in

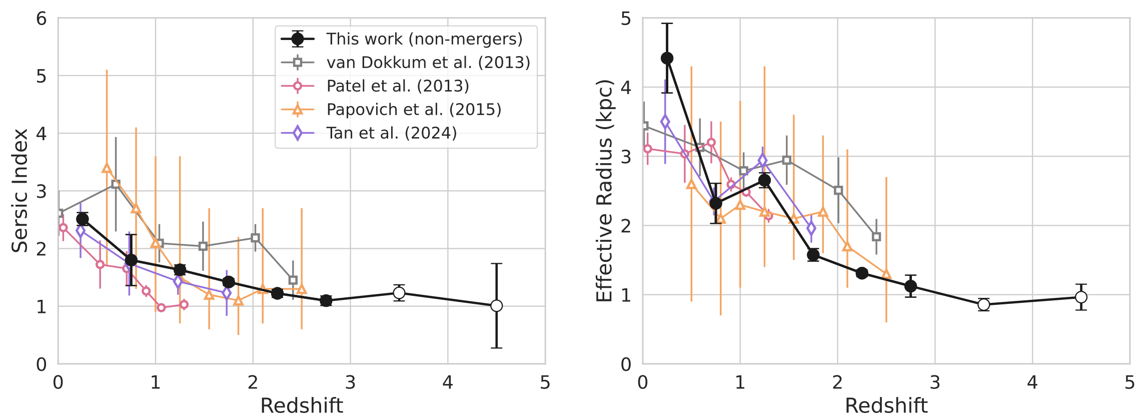

Figure 3.9: *Left:* Median Sérsic index for each redshift bin. Black circles represent this sample of MWA progenitors from CANUCS with mergers removed, open circles represent values affected by mass completeness. *Right:* Median half-mass radius R_e of each redshift bin in kpc, converted via angular diameter distance from photometric redshifts. Error bars represent the standard error in each redshift bin. Other lines are Sérsic parameter measurements from other studies: van Dokkum et al. (2013) in grey, Patel et al. (2013) in pink, Papovich et al. (2015) in orange, and Tan et al. (2024a) in purple.

morphology. Most galaxies are in-between $n = 1$ and $n = 4$, as galaxies usually consist of both a bulge and a disk component.

Statmorph utilizes astropy's `2DSersic` function and scipy's `curve-fitting` package to fit either single or double Sérsic profiles to galaxy images. Similar to Galfit (Peng et al., 2010), it takes in a galaxy image and a PSF kernel as input. When tested on fitting F444W photometry of MWA progenitors from the A370NCF field, Statmorph returned similar Sérsic profiles to Galfit when fitted to the same galaxy image, but has lower failure rates. We utilize the fitted Sérsic profile to the spatially resolved stellar mass maps to study general trends in the changes of the morphology of MWAs over cosmic time.

3.5.2 Sérsic parameters of MWA progenitors since $z = 5$

In Figure 3.9, the median Sérsic index of each redshift bin is plotted in the left panel, while the median R_e (half-mass radius) is plotted in the right panel. From $3 < z < 5$, the median Sérsic index remains constant at $n \sim 1$, and from $1.5 < z < 3$, the Sérsic index only grows to a value of $n = 1.62 \pm 0.09$. Within the same redshift ranges, the median R_e, representing the median half-mass radius of the MWA progenitors, is also increasing. In the same time frame of $2 < z < 5$, the R_e increases from 1.0 ± 0.2 kpc at $4 < z < 5$ to 1.84 ± 0.16 kpc at $1.5 < z < 2$.

While it appears at first glance as if both Sérsic index and half-mass radius are not increasing dramatically, it is only true for the Sérsic index. This is because a galaxy with a Sérsic index of $n \sim 1.6$ is still likely disk-dominated, while an increase in half-mass radius from 1.0 kpc to 1.8 kpc is representative of the galaxy's size almost doubling in the same span of time. As noted in §3.4.2, the redshift range $2 < z < 5$ is the same epoch where the MWA progenitors exhibit inside-out growth, where more stellar mass is accumulated in the outskirts of the galaxy versus in the inner regions, according to the density profiles in Figure 3.6 and in Figure 3.7. This could be another indication that disks are growing, because half-mass radius corresponds to size, while the roughly constant Sérsic index shows that the progenitors are not increasing their central concentration. Thus they are likely disk-dominated systems. Since Figure 3.8 has shown that mergers are required at all redshifts to match the observed stellar mass build-up, this indicates that any potential mergers that have occurred are most likely not morphologically transforming these galaxies from disks to bulges. However, we note that the individual measurements of Sérsic index and R_e for individual galaxies do have a large scatter, though the median values indicate that in general, our MWA progenitors tend to be disk-dominated systems.

The next stage of mass assembly takes place from $z = 2$ to $z = 0.3$, and the mass density profiles transition from inside-out growth to proportional mass build-up in both inner and outer regions. As discussed in §3.4.2, this is the epoch where the change in mass density is roughly equivalent for both inner and outer regions. Figure 3.9 shows the median Sérsic index at later times does indeed increase up to $n = 2.42 \pm 0.42$ at $0.3 < z < 0.5$. While it is impossible to directly measure the Sérsic index of the MW from an internal vantage point, the bulge-to-total mass ratio of the MW is measured to be $B/T = 0.15$ by Licquia & Newman (2015). Using conversions derived by Brennan et al. (2015) between B/T ratios and Sérsic indices, if the radius of the bulge to the radius of the disk is < 0.4, the Sérsic index of a galaxy with $B/T = 0.15$ is likely to be $n \lesssim 2$. Therefore, our Sérsic index measurement of $n \sim 2.4$ for the lowest-z progenitors is consistent, but slightly higher than the value expected for the MW. Furthermore, consensus on the MW's bulge is that its structure is a box/peanut or "X-shaped" bulge (see e.g. Barbuy et al. 2018; Helmi 2020), rather than a classical bulge that is typically described by a de Vaucouleurs profile. As mentioned before, the MW's bulge is small for a disk galaxy of its mass, so any star-forming disk galaxies within our sample at the lowest redshifts will most likely have a stronger bulge component than the MW, which results in a slightly higher Sérsic index.

Over the same redshift range, the median half-mass radius increases from $R_e = 1.7 \pm 0.2$ kpc at $1.5 < z < 2$ to $R_e = 4.4 \pm 0.3$ kpc at $0.3 < z < 0.5$. This effective radius is comparable to the measurement of the MW's effective radius from Zhou et al. (2023) at $R_e = 4 - 4.5$ kpc, assuming an exponential scale length of the disk of 2.7 kpc from Licquia & Newman (2015). This is another doubling in the average size of MWA progenitors from $z = 2$ to $z = 0.3$, but over a longer time scale, ~ 7 Gyr. The Sérsic index, while it has increased, is still below $n = 4$, the limit at which a galaxy is then considered bulge-dominated. With the assumptions made, we can infer that the MWA progenitors detected within this sample remain disk-dominated systems.

3.5.3 Gini-M20 Statistics

For our sample of galaxies, fitting a single Sérsic profile to the main galaxy in each cutout has its limitations. Sérsic profiles can only reveal the most general information about the flux distribution (or in our case the mass distribution) of the galaxy that it is fit to, and fails to capture the finer structures, such as clumps, tails, or spiral arms. Fitting the unique, finer structures of over 900 galaxies is unfeasible, but there are statistical methods to quantify the overall "clumpiness" of a galaxy image. One such method is via Gini-M20 statistics.

The Gini-M20 plane (Lotz et al., 2004) is another morphology tool which utilizes the relative flux distribution of galaxy images and the contribution of each pixel to the flux to quantify galaxy morphology. It is exceptionally useful for picking out double peaks which can either indicate pairs of merging galaxies, or star-forming clumps, depending on the filter used.

The Gini coefficient was first used for astronomical image classification by Abraham et al. (2003). It is defined for a set of n pixels each with individual flux values I_i as:

$$G = \frac{1}{\bar{I}n(n-1)} \sum_{i=1}^{n} (2i - n - 1) I_i, \tag{3.8}$$

where $\bar{I}$ is the average flux of all the pixels. The Gini coefficient is defined in a way such that the values range from 0 to 1, with $G = 0$ assigned to an image with a completely uniform flux, and $G = 1$ assigned to a field with a single bright pixel, and all other pixels containing zero flux. One limitation of the Gini coefficient is that the surface brightness of galaxies is highly redshift dependent. So the implementation of the Gini coefficient calculation in Lotz et al. (2004) and in Statmorph is to construct a Gini segmentation map, which only depends on the Petrosian radius (Petrosian, 1976), and is insensitive to redshift. The Petrosian radius R_p is defined as the radius at which the surface brightness $\mu(r)$ at R_p is equal to the mean surface brightness $\bar{\mu}$ contained within R_p, and the ratio of the two values is defined in Lotz et al. (2004) as:

$$\eta = \frac{\mu(R_p)}{\bar{\mu}(r < R_p)} \tag{3.9}$$

The default η for the Petrosian radius calculation in Statmorph is set to 0.2.

The M_{20} statistic is the second order moment of a galaxy's brightest pixels, which contains 20% of the total flux, relative to the total second order central moment μ_{tot}. For an image with n pixels located at positions (x_i, y_i) with (x_c, y_c) defined as the galactic centre, μ_{tot} is defined as:

$$\mu_{tot} = \sum_{i=1}^{n} \mu_i \equiv \sum_{i=1}^{n} I_i \left[(x_i - x_c)^2 + (y_i - y_c)^2 \right], \tag{3.10}$$

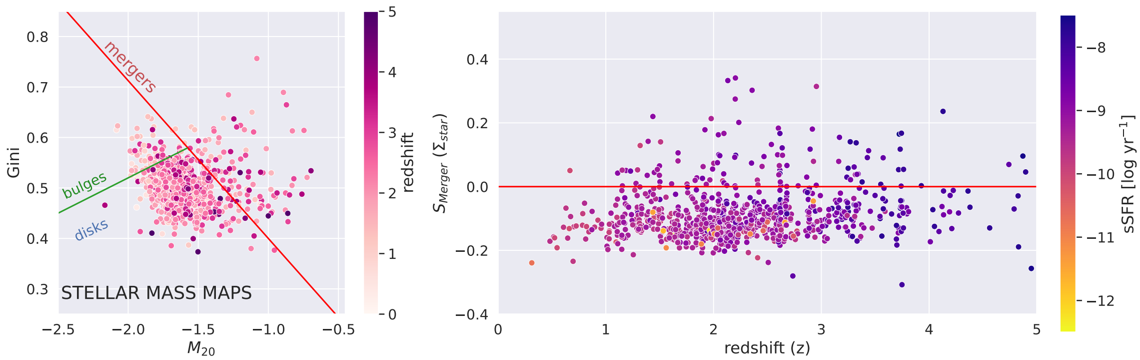

Figure 3.10: *Left Panels:* Gini-M20 plots of the stellar mass distributions of the MWA progenitors. The color of the point represents the redshift of the galaxy. The red line represents the separation between the galaxies with a positive merger statistic, versus the galaxies with a negative merger statistic (S_{merger}). The line is defined in Equation 3.12. The green line represents the division between bulged-dominated and disk-dominated galaxies. Although most high-z galaxies are in the disk region, there are some that reside in the bulge region. *Right Panels:* The Merger Statistic S_{merger} of the MWA progenitors as a function of redshift, for both the stellar mass maps . Color represents the sSFR of each galaxy.

where I_i is the flux of an individual pixel. Then, M_{20} is defined as

$$M_{20} \equiv \log_{10}\left(\frac{\sum_i \mu_i}{\mu_{tot}}\right), \text{while } \sum_i I_i < 0.2 I_{tot}, \tag{3.11}$$

where I_{tot} is the total flux of the area defined by the segmentation map of the galaxy. In general, a lower value of M_{20} indicates higher flux concentration. However, unlike the Gini coefficient, M_{20} is not measured on circular or elliptical apertures, and the center of a galaxy is left as a free parameter. M_{20} also scales with r^2 which makes it more sensitive to detecting multiple spatially resolved bright regions.

Results are presented in the Gini-M20 plane, where different regions of the plane identify roughly the morphology of the galaxy. The Gini-M20 plane for the stellar mass maps of the MWA progenitors are shown in the left half of Figure 3.10. The Gini-M20 plane also has a way to distinguish between disk and bulge-dominated galaxies. There are few galaxies in the bulge region of the diagram, and most are at lower-z. However, there are some higher-z objects lie in the bulge morphology region, indicating that not all progenitors of MWAs are disk-like. Overall, the disk/bulge distinction using Gini-M20 agrees well with the trends from Sérsic profile fitting in Figure 3.9.

One key region of the Gini-M20 plane is the top-right half, where both Gini and M_{20} are high. The galaxies in this region exhibit more than one bright peak in its flux distribution (or in our case, in its stellar mass or SFR distribution), and are thus more likely to be ongoing mergers. However, the interpretation of whether an object in that region is truly a merger is highly dependent on the filter used. Galaxies with satellites, star-forming clumps, and spiral arms can be factors that increase the merger statistic S_{merger} of a galaxy's image. Since we are using the Gini-M20 plane on a dataset that spans many redshifts, we define a new dividing line from which to measure the merger statistic. This is because the default S_{merger} from Statmorph is based on the data that Rodriguez-Gomez et al. (2019) were using for their studies, which was comparisons of the Pan-STARRS survey to simulated IllustrisTNG galaxies. We defined a new line for the Gini-M20 plane based on visual inspection that the images classified as having a positive S_{merger} indeed have more than one distinct bright peak in its distribution. The equation that defines the new dividing line is:

$$S_{merger}(G, M_{20}) = 0.322M_{20} + 1.030G - 0.090. \tag{3.12}$$

3.5.4 Mergers and disturbed galaxies at high redshift

We choose three different proxies for merger rate: S_{merger} from the Gini-M20 plane, CAS asymmetry (A_{CAS}), and RMS asymmetry (A_{RMS}). Asymmetry is sensitive to structures such as tidal disturbances, dust lanes, clumpy structures, and double cores. Asymmetry is correlated to mergers, but depending on the stage of the merger, the galaxy may not be highly asymmetric (late stage mergers for instance, do not exhibit great asymmetry). Nevertheless, asymmetry is a useful parameter for detecting disturbances in the process of galaxy evolution, which correlates with merger rate and with galaxy pair interactions.

The most well-known asymmetry parameter comes from the CAS (concentration, asymmetry, smoothness) classification system as described in Conselice (2003). Statmorph calculates the asymmetry parameter by subtracting the galaxy's image rotated 180 degrees from its original image:

$$A_{CAS} = \frac{\sum_{i,j} |I_{ij} - I_{ij}^{180}|}{\sum_{i,j} |I_{ij}|} - A_{sky}, \tag{3.13}$$

where I_{ij} and I_{ij}^{180} are pixel flux values of the original and rotated images, and A_{sky} is the average asymmetry of the sky background.

An alternative measurement of asymmetry is RMS asymmetry, which was introduced in Conselice et al. (2000). An updated version of RMS asymmetry from Sazonova et al. (2024) is currently implemented in the latest version of Statmorph:

$$A_{RMS}^2 = \frac{\sum_{i,j} (I_{ij} - I_{ij}^{180})^2 - 2\sigma_{sky}^2}{\sum_{i,j} I_{ij}^2 - \sigma_{sky}^2}, \tag{3.14}$$

where σ_{sky} is the RMS noise of the background.

Sazonova et al. (2024) argues that RMS asymmetry is a more robust asymmetry measurement as it is fully independent from noise and aperture size. However, both A_{CAS} and A_{RMS} are correlated to image resolution. Since our study compares galaxies across a wide span of redshifts, it is of the utmost importance that the *physical resolution scale* (i.e. the kpc scale per pixel) is the same.

We compare the merger statistic, CAS asymmetry, and RMS asymmetry for the galaxies' stellar mass maps in both their original resolution (which is the same resolution as the F444W photometry) versus the images that have been matched to the same *physical resolution* via the angular diameter distance obtained at each object's redshift. Therefore, the images that have been resolution-matched have one pixel represent the exact same physical extent of the galaxy with the poorest resolution (at $z \sim 1.6$, where the angular diameter distance vs. redshift reverses in our cosmology). This resolution is 0.339 kpc per pixel.

We define the merger fraction morphologically with the stellar mass maps. We use the fraction of galaxies with $S_{merger} > 0$ in stellar mass to determine the "merger candidate fraction" (Lotz et al., 2008b). The merger statistic is a reasonable predictor of "true" ongoing mergers, as shown from comparisons of the correlation of the value of S_{merger} on mock observation images of galaxy mergers at different stages produced from simulations (i.e. Lotz et al. 2008a; Snyder et al. 2015a,b; Rodriguez-Gomez et al. 2019). For our purposes, we use merger fraction synonymously with merger candidate fraction, but we note that it is not a true "merger fraction".

In the top row of Figure 3.11, we plot the median S_{merger}, A_{CAS} and A_{RMS} as a function of redshift, while in the bottom row of the same figure, we plot the merger fractions and disturbed fractions. For all parameters, both the median parameter based on the original stellar mass maps, and the median parameter based on the resolution-matched stellar mass maps, increase as redshift increases. Though the resolution-matched parameters tend to be slightly lower, with the difference increasing with increasing redshift since angular resolution decreases up to $z \sim 1.6$ and then increases with increasing redshift for $z > 1.6$). There is a similar trend with the merger fractions (derived from number of galaxies with $S_{merger} > 0$, as seen on the top-right panel of Figure 3.10) and disturbed fractions, derived from either $A_{CAS} > 0.3$ or $A_{RMS} > 0.3$ for each redshift bin. The division line was chosen to be 0.3 because the median A_{CAS} and A_{RMS} are both ~ 0.3 at the highest redshift bin.

The merger fraction on the whole follows a downward trajectory, and the peak S_{merger} is $19.3 \pm 4.0\%$ at $3 < z < 4$ for the original resolution stellar mass maps, and $20.8 \pm 9.3\%$ at $4 < z < 5$ for the resolution-matched stellar mass maps. This demonstrates that in general, the rate of active, ongoing mergers increases towards higher-z, and there were more frequent mergers in the past, as we approach the epoch of reionization. The disturbed fraction also increases with increasing redshift, whether the fraction is measured based on A_{CAS} or A_{RMS}. The maximum of the resolution-matched disturbed fraction based on A_{CAS} is $45.8 \pm 13.8\%$ and the maximum disturbed fraction based on A_{RMS} is $50.0 \pm 14.4\%$, both found at the highest redshift bin ($4 < z < 5$). Although there is a slight upward trend at the lowest redshift bin, the sample size is small, and thus it is still consistent with a decline in asymmetry and disturbed morphology.

For comparison with the implied merger rate from abundance matching with Behroozi et al.

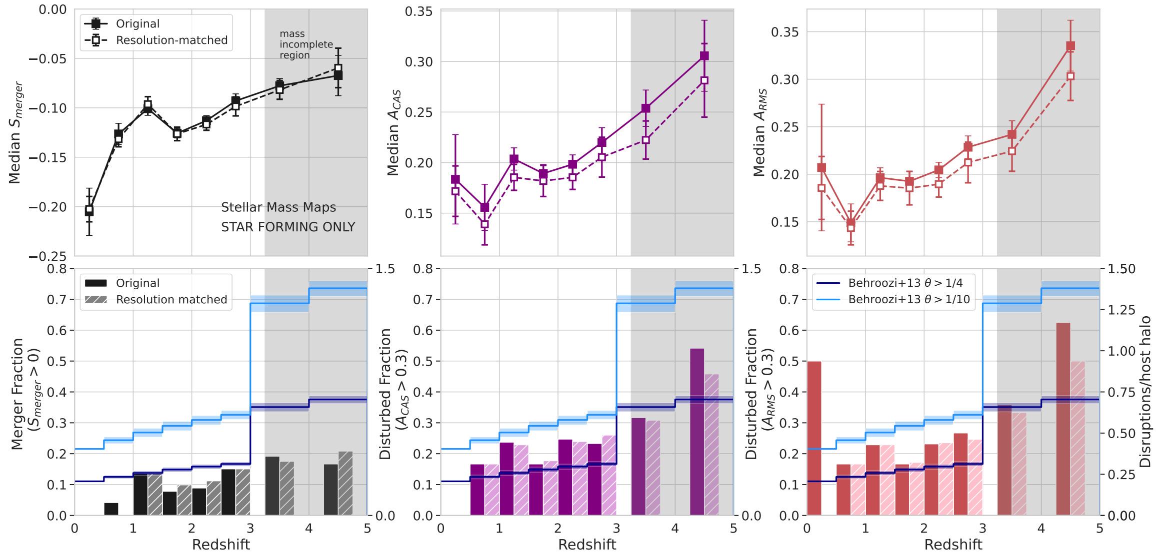

Figure 3.11: *Top:* From left to right, the median S_{merger}, A_{CAS}, and A_{RMS} for each redshift bin. In each top panel, the solid lines with filled squares represent the median of the distribution as measured from the original resolution of the stellar mass maps, and the dashed lines with unfilled squares represent the median from the *resolution matched* stellar mass maps. *Bottom:* Left panel is merger fraction as determined by number of galaxies per redshift that has $S_{merger} > 0$. Center and right panels are "disturbed" fractions, determined by galaxies with $A_{CAS} > 0.3$ or $A_{RMS} > 0.3$ respectively. In all cases, resolution matching decreases the fraction of disturbed galaxies, but increases the merger fraction at the highest redshift bins. The integrated halo disruption rate from Behroozi et al. (2013b) is plotted in dark blue for major mergers ($\theta \geq 0.25$) and major and minor mergers ($\theta \geq 0.1$) for comparison.

(2013a), we have obtained the "subhalo disruption rate per host halo per unit redshift per unit log mass ratio $\log_{10}(\theta)$ ", described in Appendix I of Behroozi et al. (2013b) which is a run of the same simulation as in Behroozi et al. (2013a). We integrate the halo disruption rate over two mass ratios: one at $\theta \geq 1/10$ representing major and minor mergers, and one at $\theta \geq 1/4$, representing major mergers only. We also integrate the function over each redshift step assuming M_0 to be the halo mass of the next time step. This becomes the number of disruptions per host halo. We find that the *trend* of the observed merger and disturbed fractions seem overall consistent with the rate of disrupted halos as from Behroozi et al. (2013b), however, the merger fraction as defined by positive S_{merger} underestimates the number of mergers at all times, but especially at the two highest redshift bins $3 < z < 4$ and $4 < z < 5$. The disturbed fraction using both $A_{CAS} > 0.3$ or $A_{RMS} > 0.3$ meanwhile, has slightly better agreement with the major and minor halo disruption rates compared to positive S_{merger}. This shows that our merger and disturbed fractions are more consistent at the redshift ranges where mass completeness is not an issue. Nevertheless, these morphological measurements can still be used to pick out ongoing mergers from observations with relative accuracy compared to simulations, if the sample was selected via abundance matching.

3.5.5 Overlap of star-forming regions with stellar mass distribution

As stated earlier in §3.5.3, S_{merger} is, in this case, a measurement of the likelihood that an image contains double or multiple peaks. Therefore, if we use S_{merger} on the SFR maps, then it could be a generalized measurement for whether a galaxy is clumpy in star formation. However, $S_{merger,SFR}$ does not reveal any information about where the clumps are located, or the intensity of the star formation (i.e. the burstiness of the star formation). Due to these limitations, we utilize an alternative method to measure clump fraction for our sample. This is based on the clump detection method outlined in Wuyts et al. (2012) and Sok et al. (2022), which is calibrated to detect clumps in both rest-frame u-band and stellar mass maps. In addition, we also measure the similarity between the stellar mass map and the SFR map for each galaxy using the Normalized Mutual Information index (NMI, Studholme et al. 1999) between the stellar mass maps and SFR maps. The more correlated two images are, the higher the NMI, and the more similar the SFR distribution is to the stellar mass distribution.

In Figure 3.12, we plot both the median NMI between stellar mass and SFR maps in the top-left, and in the bottom left, we plot the clumpiness fractions' for both stellar mass and SFR maps as well as the $S_{merger} > 0$ fraction as a function of redshift. Stellar mass maps are generally clumpier at higher redshift, although there is a slight decreasing trend from $z \sim 1$ to $z \sim 2$. For the SFR maps however, the clumpiness fraction is lower at higher redshift, though still higher than the clumpiness fraction of stellar mass. Both trends also agree well with the "clumpiness" fraction derived from the number of galaxies which have $S_{merger} > 0$ in mass maps and SFR maps respectively. In §3.4, the results show that star formation is much greater at earlier times. As such, we include the NMI measurement to see if the regions where star formation rate is occurring correspond to regions of higher stellar mass. In the median NMI, the correlation between the SFR maps and the stellar mass maps is decreasing as redshift decreases. Furthermore, we show two example galaxies, one at high-z and one at low-z, to show that indeed, the SFR maps are more similar to stellar mass maps at earlier times.

From this, we can infer that at early times, such as the galaxy that is at $z = 4.74$ in the top-right figure, regions of bursty star formation correspond more to where the stellar mass is. In that sense, it is not that bursty star formation is less clumpy, but that both SFR *and* stellar mass are *both clumpy* at higher-z. But once more stellar mass is set in place, the star-forming regions make up less and less of the galaxy, and eventually only form in the outskirts of the galaxy, which is evidenced by the bottom right images of the galaxy at $z = 0.57$, where the SFR, while technically "clumpy", does not correspond to the smooth stellar mass distribution, and is also much lower than at high-z.

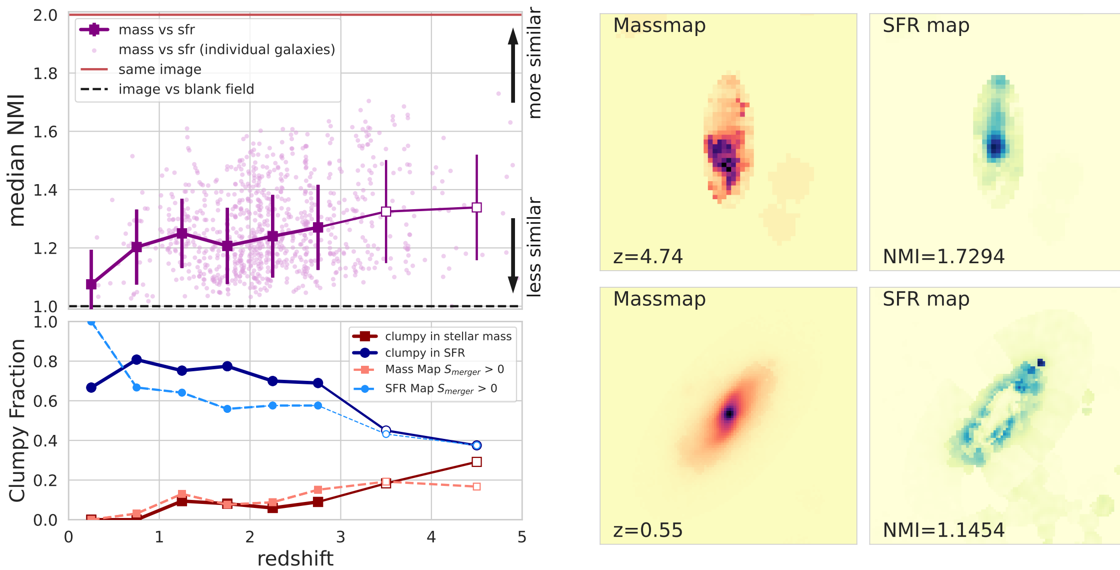

Figure 3.12: *Top-Left:* Normalized mutual information (NMI) comparing mass maps to SFR maps for each MWA progenitor (purple points). The median NMI at each redshift bin is plotted as the purple line, with the error bars as 1σ of the distribution. Red line indicates an NMI of 2, where two images are identical. Dashed black line indicates an NMI of 1, when any non-blank image is compared to a blank field. *Bottom-Left:* Clumpy fraction as a function of redshift, as determined by the clump-finding algorithm from Sok et al. (2024) for SFR maps in dark blue, and stellar mass maps in dark red. The dotted orange line and dotted blue line correspond to $S_{merger} > 0$ in mass maps and $S_{merger} > 0$ in SFR maps respectively. *Right Panel:* Example of a high-z galaxy with a high NMI (top) and a low-z galaxy with a low NMI (bottom). The amount of stellar mass covered by the clumpy star-forming regions agree less at lower redshift, resulting in decreasing NMI with decreasing redshift.

3.6 Discussion

3.6.1 Star formation, mergers, and morphology

Semi-analytic galaxy simulations (such as Benincasa et al. 2020; Grudić et al. 2023; Yu et al. 2023; Pinna et al. 2024; Semenov et al. 2024) have just begun to explore the question of how exactly the MW's disk formed and evolved, especially as we have evidence that a subset of the stars in the MW's thick disk originated from a major merger that occurred 8-11 Gyr ago known as Gaia-Enceladus (GSE merger). We will consider how the CANUCS sample of observed MWAs compares to previous simulation-based studies of MWA formation.

Although we find strong evidence for inside-out growth as well as disk assembly with our MWA sample, our mass map derived morphology parameters exhibit both opposing and agreeable trends to Yu et al. (2023). The Sérsic index of our sample increases with decreasing redshift, showing that our MWAs are becoming more *bulge-dominated* at later times, even after removing quiescent galaxies. In contrast, the circularity of stellar orbits for the FIRE-2 MWAs in Yu et al. (2023) (which

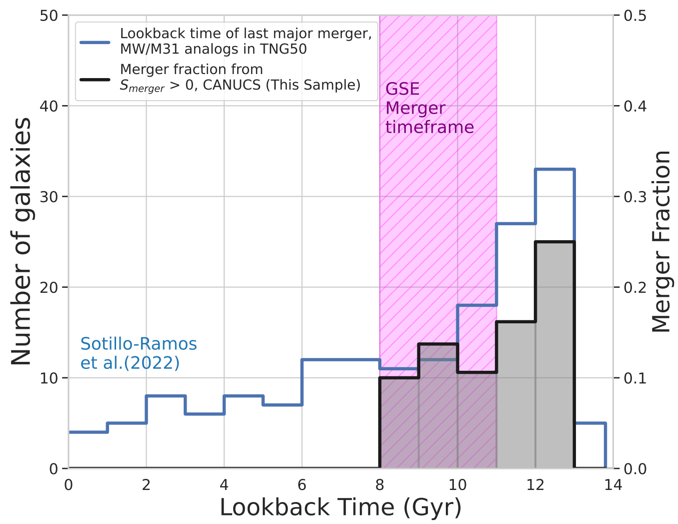

Figure 3.13: The lookback time of last major merger in TNG50 MWAs (blue line, Sotillo-Ramos et al. 2022) compared to the merger fraction at each lookback time for CANUCS MWAs (black line, grey shading).

they use as a proxy for disk-like morphology) increases with decreasing redshift, showing their mass distributions are becoming more *disk-dominated* at later times. Galaxies in general become more bulge dominated at lower redshifts (e.g. Hashemizadeh et al. 2022, therefore it is expected that the evolution of MWA progenitors would trend the same way, in spite of the MW itself having a small bulge.

Another simulation-based study with MWAs in TNG50 from Sotillo-Ramos et al. (2022) tracked both in-situ SFR and "diskiness" (measured via D/T or disk-to-total mass ratio) over time, and found that increased in-situ SFR is associated with increased diskiness of the MWAs. Their definition of disk is also dependent upon circularity ($\epsilon > 0.7$ for the disks). However, a major merger episode will disrupt diskiness, but still increase in-situ SFR (in a starburst), with the disks reforming afterwards (the orbits of the newly formed stars settling into circular orbits). It can be argued that the generally decreasing trend of the merger and disturbed fractions of the CANUCS MWAs is evidence of this settling down after the starbursts that occurred at $z > 3$. The timescale of the disk reformation according to Sotillo-Ramos et al. (2022) is anywhere from < 1 Gyr to ~ 2 Gyr. If a redshift bin covers a span of time that is $\gtrsim 1$ Gyr, then it is more likely the median Sérsic index n in our observed MWA sample will average out all of the morphology of the merging and non-merger galaxies and return a disk-like value close to $n = 1$.

On the other hand, A_{CAS}, A_{RMS}, and S_{merger} of the CANUCS MWA progenitors all show an increasing trend with *increasing* redshift. Asymmetry parameters are correlated with galaxy pair interactions and tidal features, both of which contribute to turbulence and non-circular orbits. Ultimately, Sérsic profiles are derived from surface brightness, which is not related to orbit circularity.

Meanwhile, asymmetry parameters are more closely related to orbital circularity, and thus similar trends appear between observation and simulation.

3.6.2 Merger rates over time

The time frame of the last major merger of the MW, the GSE merger, corresponds to a redshift of $1 < z < 2.5$. This is an interesting epoch because all of the parameters that track merger rates plotted in Figure 3.11 appear to show an upturn at $1 < z < 2$, despite the overall decreasing trend of merger rates and asymmetry with decreasing redshift. This upturn is the most pronounced for the merger statistic, plotted on the left panels, where the merger fraction at $1 < z < 1.5$ is $\sim 14.0 \pm 3.4\%$.

In Figure 3.13, we re-bin the merger fraction defined by $S_{merger} > 0$ of MWA progenitors, from the bottom-left panel of Figure 3.11, by lookback time instead of redshift (black solid line with grey shading). The peak of the merger fraction as broken down by lookback time is 12-13 Gyr ago, corresponding to redshifts $z > 3$, as expected. We compare the CANUCS MWA merger fraction with results from TNG50, specifically Sotillo-Ramos et al. (2022), as they focused on disk survival rates of MWAs that experienced major mergers. The number of MWAs in TNG50 for which their last major merger occurred at a certain lookback time is also plotted in Figure 3.13 as the blue dashed line.

The CANUCS MWA merger fractions also agree well with the distribution of last major merger occurrence versus lookback time from the TNG50 MWAs. Note that this is *not* a one-to-one comparison of occurrence rates of mergers. Simulations have access to the full star formation histories of each galaxy, and know when, and how many mergers occurred. Observational results are snapshots of various galaxies at only one point in their evolutionary history. Those galaxies may have had previous mergers, and/or go on to have other major (or minor) mergers as they evolve through cosmic time. But what the agreement between both samples do show is that major mergers occur with more frequency at earlier times/higher redshifts, and that high redshift major mergers *tend to* not alter the disk morphology of the progenitors of present-day disk galaxies on long time scales. This may indicate that systems like the Sunrise arc (Vanzella et al., 2023), Firefly Sparkle (Mowla et al., 2024), and Cosmic Gems (Adamo et al., 2024; Bradley et al., 2024) — glimpses into the highly chaotic formation of the central regions — can potentially go onto form disky systems at $3 < z < 5$ that remain disky and become grand design spiral galaxies at $z = 0$.

3.7 Summary

We used abundance matching on all ten fields of the CANUCS catalogs to find a sample of 909 spatially resolved MWA progenitors since $z = 5$. The stellar mass ranges of these galaxies match well with both simulations and previous observation-based studies of MWA evolution. We then performed resolved SED-fitting with Dense Basis to create stellar mass and SFR maps of our MWA progenitors in order to track the mass assembly, sSFR, and morphology evolution. Our main results are as follows:

- There is strong evidence of inside-out growth for the selected MWA progenitors before $z = 2$. From the mass density profiles (Figures 3.6 and 3.7), we find that at $2 < z < 5$, the $M_\star$ in the outer regions ($R > 2$ kpc) grows by 0.8 dex, which is eight times more than the $M_\star$ growth in the inner regions (0.1 dex within $R < 2$ kpc). The maximum sSFR of each stacked and normalized sSFR profile in Figure 3.6 from $z \sim 4$ to $z \sim 0.5$ is located at or close to the furthest point from the profile's center. The sSFR of the inner regions in Figure 3.7 decrease steadily since $z = 5$, while the sSFR of the outer regions increase between $2 < z < 5$, matching the inner regions at $z \sim 3$, and only begin to decrease after cosmic noon ($z \sim 1.75$).

- Additionally, in Figure 3.9, the median Sérsic indices of the MWA progenitors demonstrate that up to $z \sim 0.5$, these galaxies remain mostly disk-dominated systems. Meanwhile, the change in their median half-mass radius implies that the progenitors are growing rapidly from $z \sim 5$ to $z \sim 3$. The lack of strong evolution in Sérsic index combined with steady growth in R_e imply the galaxies are building their disks inside-out at earlier times.

- The merger rates of our MWA progenitors are defined using the position of the galaxy's mass map on the Gini-M20 plane ($S_{merger} > 0$, Figure 3.10). The most conservative merger fraction at $4 < z < 5$ is $16.7 \pm 8.3\%$ (Figure 3.11). Between $45.8 \pm 13.8\%$ to $62.5 \pm 16.1\%$ of MWA progenitors at $4 < z < 5$ are classified as disturbed, using either CAS or RMS asymmetry. Merger fractions and disturbed fractions have an overall decreasing trend with decreasing redshift. The mass growth of early galaxies likely involve frequent interactions and higher merger rates than low-z galaxies.

- The clumpiness of the stellar mass maps is higher at high-z, especially $4 < z < 5$, but remains at $< 20\%$ at $z < 4$ (Figure 3.12). Although the clumpiness of the SFR maps increases towards lower-z, the overall SFR decreases, so the star-forming clumps at lower-z are less bursty than their higher-z counterparts. There is also more mismatch between regions of high SFR and the underlying stellar mass distribution. This means that highly star-forming regions at higher-z are more likely to be located where there is more stellar mass, whereas the star-forming regions at low-z usually are found in regions with lower mass density. MWAs evolve from small, disturbed systems with extreme star formation activity to a large disk with pockets of star formation that surround a massive, quiescent bulge.

Since both SFR and asymmetry of the CANUCS MWA progenitors all increase as z increases, this matches simulations of MWA evolution where disk galaxies exhibit burstier star formation at earlier times that leads to less circularized/more eccentric and thus more "asymmetric" stellar orbits. Therefore, the thick disk of MWAs in general may be formed either via bursty episodes of star formation that dynamically heat a less massive disk, or via mergers disrupting the disk or inducing a starburst as the galaxy forms.

3.8 Acknowledgments

The authors wish to thank the anonymous reviewer for their comments and suggestions that greatly improved the manuscript of this paper. This research was supported by grant 18JWST-GTO1 and 23JWGO2A13 from the Canadian Space Agency (CSA), and funding from the Natural Sciences and Engineering Research Council of Canada (NSERC). The MAST DOI for CANUCS is doi:10.17909/ph4n-6n76. J. A-D. is supported by the Natural Sciences and Engineering Research Council of Canada (NSERC). Y.A. is supported by a Research Fellowship for Young Scientists from the Japan Society of the Promotion of Science (JSPS). This research used the Canadian Advanced Network For Astronomy Research (CANFAR) operated in partnership by the Canadian Astronomy Data Centre and The Digital Research Alliance of Canada with support from the National Research Council of Canada the Canadian Space Agency, CANARIE, and the Canadian Foundation for Innovation.

3.9 Appendix A: UVJ color calibration for this dataset

In §3.2.4, the UVJ diagram is used to determine the quiescent fraction of potential MWA progenitors and remove them from the analysis. In order to have unbiased UVJ boundaries, we cannot use the MWA progenitor sample itself to determine the boundaries due to the low quiescent fraction and lack of bimodality. Instead, a sample of 9516 galaxies from the cluster fields is used to fit the UVJ boundaries. The slope of the red sequence determines the slope of the calibrated line, and the local minimum of the distribution determines the y-intercept.

In Figure 3.14, we plot the full sample of galaxies that are used to calibrate the UVJ lines. The original color cuts were generated for every galaxy present in the CLU fields from $0.5 < z < 6$, which we have adjusted to $0 < z < 5$ to match the redshift range of the MWA progenitor sample in this work. The reason the cluster fields are used but not the NCF fields is because there are not enough quiescent galaxies in the NCF fields for a clear bimodal distribution in UVJ color space. The quiescent fraction of the CANUCS sample at $0 < z < 5$ in the NCF fields is only 0.07%, while in the CLU fields it is 24% in the same redshift range due to the presence of the clusters.

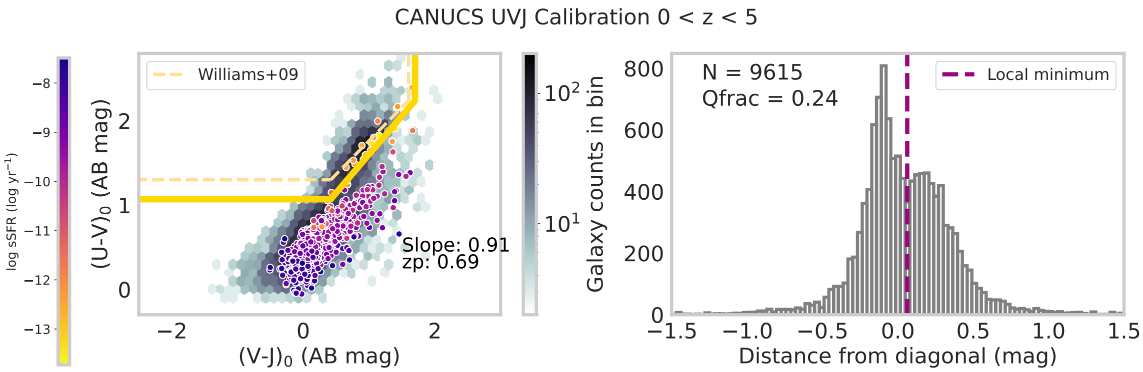

Figure 3.14: *Left Panel:* Rest-frame UVJ diagram of 9516 galaxies from the CANUCS CLU fields with redshifts $0 < z < 5$ shown as the grey bins. Darker bins indicate higher number count of galaxies. The MWA progenitors are plotted on top, with each circle representing one galaxy, and the color indicating the integrated sSFR. The UVJ boundaries used in this work are shown in yellow with dashed yellow line indicating the UVJ boundaries from Williams et al. (2009). *Right Panel:* Histogram distribution of the same 9516 galaxies and their distance from the diagonal UVJ boundary line. Purple dashed line indicates local minimum, and is analogous to the UVJ diagonal line in the left panel.

3.10 Appendix B: Creating 1-D profiles

As summarized in §3.4.1, we created 1-D stellar mass and SFR density profiles by placing down elliptical annuli with width 0.1kpc centered on the stellar mass maps and SFR maps of each respective galaxy. The stacking is performed along the semi-major axis of each galaxy for consistency. Figure 3.15 is an expanded version of Figure 3.6 from §3.4.1. Displayed are each individual galaxy's density profile divided into eight subplots by redshift bin. The stacked and normalized profile is shown in the same color as in Figure 3.6. The dashed grey lines represent profiles of quiescent galaxies while solid lines are the star-forming galaxies. The dashed colored lines represent the stacked and normalized profile for each redshift bin including both star-forming and quiescents, while the solid colored lines only include star-forming galaxies. The profiles are also not truncated by the noise floor. One difference between Figure 3.6 and Figure 3.15 is that the bottom panel of Figure 3.15 shows the SFR density instead of the sSFR density. Indeed the sSFR density profiles were created via dividing each stacked and normalized SFR density profile at each redshift by its corresponding mass density profile.

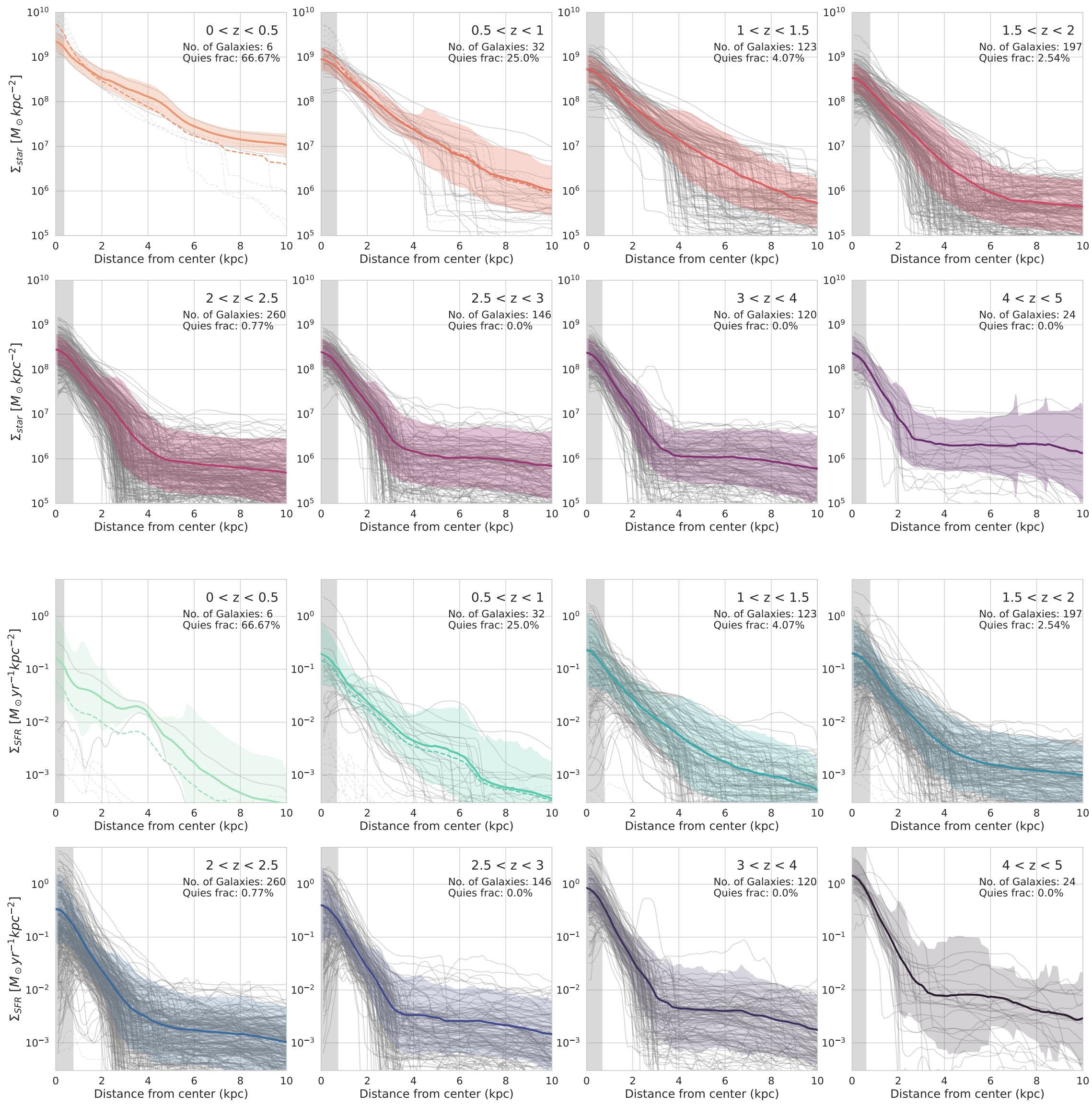

Figure 3.15: *Top Panel:* 1-D stellar mass density profiles for each MWA, plotted in grey. Colored lines are the stacked and normalized profile of all the galaxies in each redshift bin. Shaded regions represent the 1-sigma (68th percentile) region. The vertical grey shaded region near $R = 0$kpc represents the average physical size of the PSF FHWM at that redshift bin. *Bottom Panel:* Similar to the plot above but for SFR density profiles. The total number of galaxies per redshift bin, and the quiescent fraction is also displayed in the top-right corner.

Chapter 4

Resolved Ages and Stellar Metallicities in MWA Progenitors

Abstract

We present the evolution of the resolved mass-weighted age, stellar metallicity, and sSFR of 904 Milky Way Analog (MWA) progenitors up to redshift $z = 5$ from the Canadian Unbiased Cluster Survey (CANUCS). The metallicity and mass-weighted ages were obtained via spatially resolved SED-fitting with the non-parametric code Dense Basis. We split the sample into mergers versus non-mergers using the merger parameter from the Gini-M_{20} plane obtained through Gini-M_{20} analysis of the morphology of the stellar mass maps with Statmorph. Across our redshift range, non-mergers have negative or flat average age gradients from -0.03 to 0.004 dex/kpc, and positive or flat sSFR gradients from -0.051 to 0.093 dex/kpc, consistent with inside-out assembly. The average $\log(Z/Z_{\odot})$ gradients for non-mergers range from -0.019 to 0.034 dex/kpc, however, positive gradients only appear between $2 < z < 3$. At every redshift epoch, mergers typically have flatter age gradients, more negative sSFR gradients, and similar metallicity gradients compared to non-mergers. We divide the property maps of ongoing mergers into separate regions based on their component galaxies, and find little to no difference between the components' average ages or metallicities, but the less massive of the merging system is on average $0.1 - 0.4$ dex higher in sSFR. Our results point to major mergers contributing some momentary disruption to the general trend of inside-out mass assembly, but does not upend the overall picture of MWA disks growing inside-out over cosmic time.

4.1 Introduction

The most widely accepted theoretical model of the formation of disk galaxies like the Milky Way is the inside-out growth of the disk (e.g. van den Bosch 1998; Abadi et al. 2003b; Muñoz-Mateos et al. 2007; Wang et al. 2011; Bird et al. 2013; Licquia et al. 2015). For the Milky Way, this is reflected in an older central bulge and thick disk and a younger, extended thin disk(Kilic et al., 2017; Frankel et al., 2019). From chemical abundance ratios, such as [Fe/H] measured from Cepheid variables (e.g. Lemasle et al. 2007, 2008; Luck et al. 2011; Luck & Lambert 2011; Cheng et al. 2012; Genovali et al. 2014; Lemasle et al. 2018), the Milky Way's radial metallicity gradient is measured as having a shallow declining slope with values ranging from from -0.06 to -0.04 dex/kpc. Other studies using abundances such as [O/H], or [N/H] in HII regions also give similar results (Maciel et al., 2015; Cunha et al., 2016; Stanghellini & Haywood, 2018; Peña & Flores-Durán, 2019). This agrees with high resolution observations of galaxies in the local universe that show that age and metallicity gradients in disk galaxies both generally decline with galactocentric radius for galaxies with stellar masses $9 < \log(M_{\odot}) < 12$ (e.g. Sánchez et al. 2014; González Delgado et al. 2015; Belfiore et al. 2017; Goddard et al. 2017; Zheng et al. 2017; Sánchez-Menguiano et al. 2018; Boardman et al. 2020a).

Negative metallicity gradients have usually been interpreted as evidence of "inside-out" growth, due to the correlation of star-formation efficiency with stellar mass (e.g. Prantzos & Boissier 2000; Marcon-Uchida et al. 2010). However, measurements of elemental abundances of stellar populations in the Milky Way's thick disk show an inverse relation with velocity and with radii (e.g. Spagna et al. 2010; Lee et al. 2011; Curir et al. 2012). Lian et al. (2023) found with APOGEE data that the Milky Way has a "bow shaped" [Fe/H] gradient, rising from the center, but declining after $R \gtrsim 6$ kpc. Early studies found negative gradients in the α-element abundances of the Milky Way (e.g. Matteucci & Francois 1989; Chiappini et al. 1997), but this has been challenged by newer results that indicate there are two separate populations of stars in the MW's thick disk: one with a high-α and one with a low-α. These two separate populations provide strong evidence for a past merger event known as Gaia-Enceladus with a remnant now embedded in the thick disk (e.g. Fuhrmann 2011; Hayes et al. 2018; Helmi et al. 2018).

Inverse/positive metallicity gradients are rare in the local universe, but occur with more frequency at higher redshift. Studies using gas-phase metallicity such as Cresci et al. (2010); Jones et al. (2013); Curti et al. (2020); Simons et al. (2021), and Li et al. (2022) find star-forming galaxies at $1 \lesssim z \lesssim 3$ may have positive metallicity gradients. However, for the most massive galaxies, their metallicity gradients remain negative even at higher redshifts (Wuyts et al., 2016). While metallicity gradients are more diverse at higher redshift, recent studies on resolved ages at high redshift such as Akhshik et al. (2023) for massive galaxies $10.6 < \log(M_{\star}/M_{\odot}) < 12$ and Abdurro'uf et al. (2023) for a wide range of stellar masses $8.5 < \log(M_{\star}/M_{\odot}) < 12$ show that radial age gradients remain negative up to $z \sim 6$. However, Jin et al. (2024) finds evidence of positive color gradients (blue centers, red outskirts) in $z > 4$ galaxies, and color gradients are highly correlated to age. Jain et al. (2024) compared ages of the central and outskirts of galaxies from $0.5 < z < 2$ and found that galaxies above the star-forming main sequence tend to have younger centers while galaxies below the main sequence have older centers.

Rupke et al. (2010); Stott et al. (2014) and Curti et al. (2020) find a correlation between galaxies having higher specific star-formation rate (sSFR) and metal-poor centers, and suggest that the cause is the funnelling of pristine or metal-poor gas towards the center during episodes of intense star-formation. Ma et al. (2017) argues feedback is more efficient for low mass systems, which leads to the flattening of metallicity gradients. Tissera et al. (2022) found in the EAGLE simulations that only negative [O/H] gradients have a mass evolution dependence, while flat or inverted [O/H] gradients are the result of galaxy interactions such as mergers. Grossi et al. (2020) argues that two dwarf galaxies in the Virgo cluster have positive [O/H] gradients due to a a recent merger triggering inflow of metal-poor gas from the intergalactic medium. Schönrich & McMillan (2017) showed that increased SFR can flatten or invert the stellar metallicity gradient, but may steepen negative gas-phase metallicity gradients.

This has implications for the MW, as the thick disk's metallicity gradient is unusual for the local universe, and its formation was the result of a past merger event. Ciucă et al. (2024) shows the Gaia-Enceladus merger may have triggered a starburst, and then induced gas to condense into the MW's thin disk afterwards. However, Kawata et al. (2018) found in an N-body simulation of the thick disk that the most likely formation scenario is still inside-out. Radial mixing transforms the initial mildly positive [Fe/H] radial gradient to a mildly negative one. Sotillo-Ramos et al. (2022) find in the TNG50 simulation that many disks remain intact after a major merger, and destroyed disks can also reform. Yu et al. (2023) find in FIRE-2 that a bursty phase of star-formation led to the thick disk, and a steady phase of star-formation led to the thin disk. These simulations all provide support that mergers do not always disrupt inside-out formation of disk galaxies.

In our previous paper Tan et al. (2024b), we showed that the stellar mass and SFR density for MWAs in CANUCS (Canadian Unbiased Cluster Survey) are generally in line with inside-out formation up to $z = 5$, although the $z > 3$ universe is burstier and has more merger events. In this paper, we obtain mass-weighted age and stellar metallicity radial gradients for MWA progenitors, and uncover their implications for the mass assembly history of the Milky Way. Furthermore, we separate our samples into non-mergers, ongoing mergers, and late stage mergers to understand the role that merging galaxies play in the age and metallicity distribution of star-forming disk galaxies. We assume a flat ΛCDM cosmology with $\Omega_M = 0.3$, $\Omega_\Lambda = 0.7$, $H_0 = 70$ km s^{-1} Mpc^{-1}, and a Chabrier (2003) IMF.

4.2 Data

4.2.1 The CANUCS Catalog

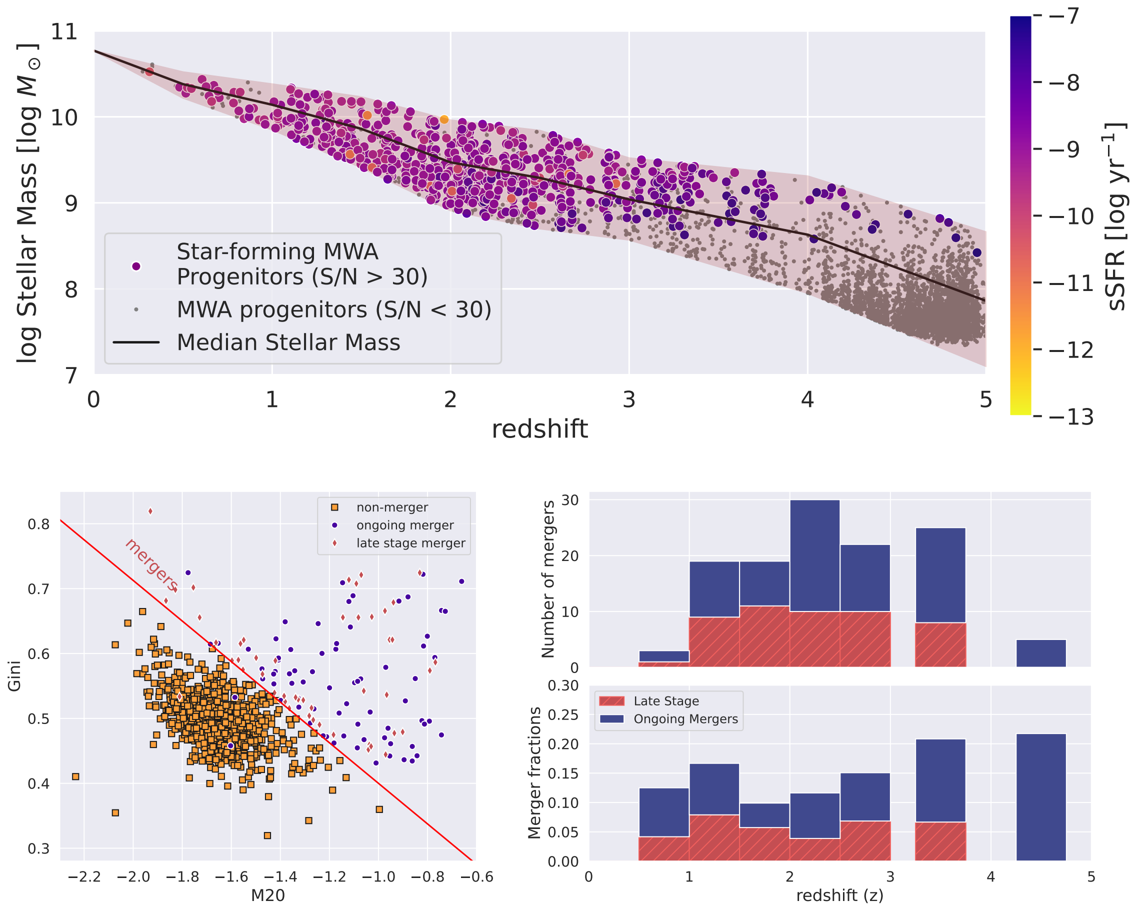

Figure 4.1: Top panel: Integrated stellar mass of all star-forming MWA progenitors in our sample from the CANUCS catalogs, as a function of redshift. their color indicates specific star formation rate (sSFR). Bottom left: Gini-M_{20} distribution of our sample. Yellow squares are non-mergers, red diamonds are late stage mergers, blue circles are ongoing mergers. The three non-yellow points below the dividing line were objects at low redshift $z < 1.5$ reclassified as mergers upon visual inspection. Bottom right: Number of mergers, as well as merger fractions per redshift bin.

As with the previous paper Tan et al. (2024b) in this series, we use the observations from the Canadian NIRISS Unbiased Cluster Survey (CANUCS, see Willott et al. 2022) for its broad wavelength coverage in the infrared and depth of field. The full CANUCS dataset includes NIRCam photometry, with spectroscopy from NIRISS and NIRSpec of five strong lensing clusters Abell 370, MACS J0416.1-2403 (hereafter MACS 0416), MACS J0417.5-1154 (hereafter MACS 0417), MACS J1149.5+2223 (hereafter MACS 1149), and MACS J1423.8+2404 (hereafter MACS 1423). Lensing models for Abell 370 are provided in Gledhill et al. (2024), for MACS0416 in Rihtaršič et al. (2025), MACS1149 in Rhitarsic et al. (in prep), and MACS 0417 and MACS 1423 in Desprez et al (in prep).

The work in this paper uses the most up-to-date photometric catalogs from CANUCS (v2p0.3), and includes up to 29 different filters in some flanking fields. Details of image processing are described in Sarrouh et al. (2025). Details of PSF-matching and catalog creation for CANUCS are described in Willott et al. (2024) and Sarrouh et al. (2024). Source detection and aperture photometry was done using the Photutils package from astropy (Bradley et al., 2016, 2023) as described in Asada et al. (2024a,b). For more information on the data reduction process for CANUCS, see Noirot et al. (2023); Desprez et al. (2024); Asada et al. (2024a), and Willott et al. 2024.

The signal-to-noise cutoff necessary for successful Voronoi binning is $S/N > 30$ in F444W. This threshold is set to ensure that the individual spatial bins have $S/N > 5$. This means that out of all possible MWAs in the CANUCS fields, only the brightest at high-z can be retained in our sample. More information on Voronoi binning is provided in Tan et al. (2024b). Photometric redshifts in the CANUCS catalog (Asada et al., 2024a) were obtained with an implementation of EAZY in Python known as `eazy-py` (Brammer et al., 2008). During fitting, a systematic flux error of 5% was added in quadrature to the nominal photometric uncertainty.

4.2.2 MWA Progenitor Selection

For this work, we use the same sample of MWA progenitors as selected in Tan et al. (2024b). However, as we have updated photometry, we make use of the additional photometric bands in the flanking fields (NCF) for more robust SED-fitting results.

A summary of the selection criteria for our progenitors is as follows:

1. The abundance matching algorithm from Behroozi et al. (2013a) was applied to a galaxy of stellar mass and cumulative number density as the current Milky Way.

2. We extrapolate the cumulative number density of possible progenitors up to $z = 5$.

3. We take stellar mass functions from Grazian et al. (2015) and McLeod et al. (2021), using the number densities and their $1 - \sigma$ errors to determine the range of stellar masses of MWA progenitors at that redshift range.

4. We search for galaxies in the CANUCS catalog with an integrated stellar mass within the bounds obtained from abundance matching to stellar mass functions at that redshift.

5. Galaxies in the cluster fields with a magnification $\mu > 2.5$ were removed.

6. Galaxies which have overall signal-to-noise $S/N > 30$ were also removed, as they cannot be successfully Voronoi-binned for which every bin has $S/N > 10$.

The integrated stellar mass versus catalog photometric redshift is plotted in the top panel of Figure 4.1. The galaxies with enough overall signal-to-noise are large colored circles with the color representing their specific star-formation rate (sSFR). The grey circles are objects in the catalog which are within the stellar mass range of that redshift epoch, but do not have enough signal-to-noise. Therefore, our sample is not entirely mass complete at $z > 3$. The sample is more biased towards more massive and more star-forming progenitors as redshift increases.

4.2.3 Selecting the merger sample

Selecting galaxy mergers is a deceptively tricky task, as clumpy galaxies may masquerade as merging systems. Given that a large number of star-forming clumps are low in stellar mass, despite their brightness (e.g. Wuyts et al. 2012; Sok et al. 2022), we therefore use Gini-M_{20} statistics (Lotz et al., 2004, 2008b) on the resolved stellar mass maps to identify merging galaxies.

Categorizing mergers via the Gini-M_{20} plane was described in detail in §5 of Tan et al. (2024b), which we summarize in this section. We use the code Statmorph (Rodriguez-Gomez et al., 2019) on the stellar mass maps of our galaxies to obtain their Gini coefficients and M_{20} statistics. Since we are working with stellar mass distributions, any time a flux was given in the original equations from Lotz et al. (2004), we instead replace that quantity with a stellar mass density σ.

The Gini coefficient is given as:

$$G = \frac{1}{\bar{\sigma} n(n-1)} \sum_{i=1}^{n} (2i - n - 1)\sigma_i, \tag{4.1}$$

where $\bar{\sigma}$ is the average stellar mass of all the pixels in an image with n pixels, σ_i is the stellar mass at each individual pixel. A high Gini coefficient indicates higher concentration of stellar mass within a few pixels, with a Gini coefficient of 1 indicating all of the stellar mass is contained in a single pixel.

Meanwhile, the M_{20} statistic finds the "brightest pixels" — the pixels that contain 20% of all of the image's flux, and where those pixels are distributed relative to the center of the image. Again, for our purposes, flux is replaced with stellar mass and the M_{20} statistic is tasked with finding the spatial distribution of the "most massive" pixels. It does so by calculating the second order of the brightest(most massive) moments μ_i compared to the second order of all of the moments μ_{tot}, which identifies galaxy bulges, clumps, and spiral arms. M_{20} is defined as:

$$M_{20} \equiv \log_{10}\left(\frac{\sum_i \mu_i}{\mu_{tot}}\right), \text{while} \sum_i \sigma_i < 0.2\sigma_{tot}, \tag{4.2}$$

Potential mergers are identified as galaxies positioned in the top right half of the plane, with a division line dividing mergers and non-mergers cutting through the diagram from top left to bottom right. Galaxies on the right side of the division line are assigned a positive S_{merger} parameter while galaxies on the left have a negative S_{merger} parameter. We take the merger sample as all galaxies with a positive S_{merger} in their stellar mass distribution. According to Sazonova et al. (2024), morphology parameters at various redshifts are affected by angular resolution, and in Tan et al. (2024b), the merger sample was taken to be the S_{merger} parameter of the stellar mass maps resolution matched to the redshift with the poorest angular resolution ($z \sim 1.6$). However, to take into account as many merging galaxies as possible, the merging population was drawn from galaxies that have either a positive S_{merger} of its original resolution *or* a positive S_{merger} from the reprojected resolution.

The merger sample is then separated by visual inspection into two main categories: ongoing mergers, and potential late stage mergers. Ongoing mergers have two or more distinguishable peaks in the stellar mass distribution, while potential late stage mergers only have a single peak but are asymmetric or otherwise irregular in structure. Furthermore, false positives, where two galaxies are spatially close in the image, but have photometric redshifts greater than $\Delta z = 0.25$ apart were removed from the sample, or reclassified as late-stage mergers if there are enough irregular or asymmetric features. In the bottom left panel of Figure 4.1, the Gini-M_{20} plane is plotted for all star-forming MWA progenitors, with the ongoing and late stage mergers plotted in blue and red points respectively. The two blue and red points that are below the merger division line are mergers which had a negative S_{merger} statistic, but upon inspection of their color images and stellar mass maps, are indeed examples of an ongoing or a late stage merger. The bottom right panel of Figure 4.1 have the number of mergers per redshift bin, as well as the merger fraction per redshift range. Example color images, as well as example property maps of non-merger versus merger galaxies are shown Figure **4.2.**

4.3 Methods

4.3.1 SED-fitting

Our goal is to create spatially resolved property maps from SED-fitting, not only for the stellar mass and star-formation rate, but also for metallicity and age. The latter properties, in conjunction mass and SFR, produces a more complete picture of the evolution and growth of MWAs. We use the same spatial bins for our galaxies as Tan et al. (2024b), which were generated by Voronoi binning Cappellari (2013), because we are studying the same sample of galaxies. We use Dense Basis (Iyer & Gawiser, 2017; Iyer et al., 2019) to perform non-parametric SED-fitting, with the stellar population synthesis code FSPS (Conroy & Gunn, 2010) loaded into the backend. The default initial mass function (IMF) for Dense Basis is from Chabrier (2003), and the default dust law is Calzetti et al. (2000).

In addition to using the most updated version of the CANUCS photometry and the photometric catalogs that include the Technicolor filters, we have also updated the prior limits for Dense Basis

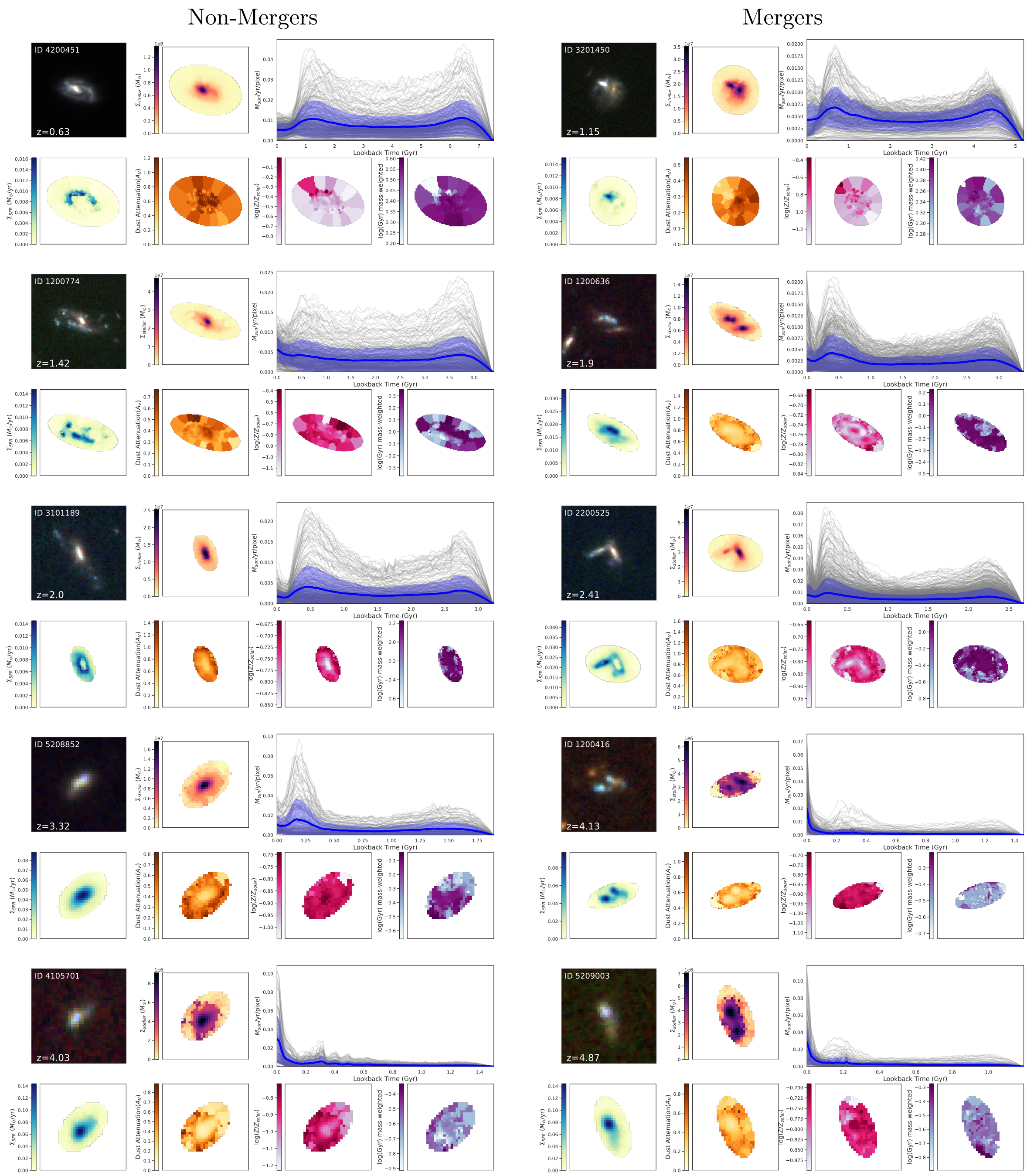

Figure 4.2: Color image, property maps, and SFHs for select galaxies in our sample. Each grey line represents the SFH of one bin (divided by bin size) and the blue line is the average SFH of the every bin's SFH, with the shaded region as the 1σ distribution (18% to 84%). Properties are: Stellar mass density $\Sigma_{\star}$, SFR density (Σ_{SFR}), dust attenuation (A_V), stellar metallicity ($\log(Z/Z_{\odot})$), and mass-weighted age.

SED-fitting to obtain more accurate metallicities and ages. This does not affect the derived stellar mass and SFR. We use a flat sSFR prior with $-13 \leq \log(\mathrm{yr}^{-1}) \leq -6$, a flat dust A_V prior with a range of 0 to 4, and the range for metallicity in the prior is $-2.5 < \log(Z/Z_{\odot}) < 0.3$. Note the choice of priors for metallicity and dust attenuation has changed slightly from the ones used in Tan et al. (2024b). The priors as described in Tan et al. (2024b) were the same priors as for the CANUCS Dense Basis mass catalogs (see Table 4 in §6 of Sarrouh et al. 2025). This is reasonable for measuring resolved stellar mass and SFR (although there is also a slight degeneracy between SFR and both metallicity and dust A_V, see Iyer et al. 2019 for a detailed discussion of SFH uncertainties). However, properties such as metallicity, dust, and age, which are more degenerate with each other (Conroy, 2013; Santini et al., 2015; Nagaraj et al., 2022) and thus more prior dependent, may not be as accurate with the catalog priors. For example, the catalog priors had narrower boundaries ($-1.5 < \log(Z/Z_{\odot}) < 0.25$.) and the dust prior is exponential. This is in order to accommodate for the large number of high redshift galaxies ($z >> 5$, around $z \sim 10$) which have low signal-to-noise. However, a wider metallicity range with a flat dust prior is more accurate for $z < 5$ galaxies with high enough signal-to-noise for spatial binning.

Since stellar metallicities from broadband photometry remain poorly constrainted, results may be more dominated by uncertainties for galaxies with less photometric data. This means the NCF sample, with its larger swath of medium band photometry from Technicolor may be more robust in its results than the CLU sample. Greater wavelength coverage necessarily results in better SED-fitting.

4.3.2 SFHs and Mass-weighted ages

In practice, a mass-weighted age of a galaxy is similar to the average age of all of the stars within that galaxy. Since it is weighed by stellar mass, there is less outshining bias from newly formed stars. Therefore, the mass-weighted age can be a more accurate measurement of the overall amount of star-formation that has occurred up to time of observation of the galaxy.

We obtain the mass-weighted age of each spatial bin with the function `calc_mw_age()` from piXedfit (Abdurro'uf et al., 2021). Given an SFH returned by Dense Basis for a particular galaxy (or spatial bin within a galaxy), we get the total mass formed since the birth of the galaxy by integrating the entire SFH over time:

$$M_{formed}(t) = \int_{t_0}^{t_{age}} \mathrm{SFR}(t)\mathrm{d}t \quad , \tag{4.3}$$

where t_{age} is the age of the galaxy at time of observation, and t_0 is when the galaxy first began forming stars. Since Dense Basis returns SFHs in SFR versus lookback time, we must convert it to "common time" by flipping the time array. Note that M_{formed} is distinct from stellar mass $M_{\star}$, because a portion of the formed mass will be returned to the interstellar medium via stellar evolution. Then we obtain the mass-weighted age t_{MWage} by multiplying the age t_i at each time step by its corresponding M_{formed} at t_i, taking the sum, and then dividing by the total mass formed over all

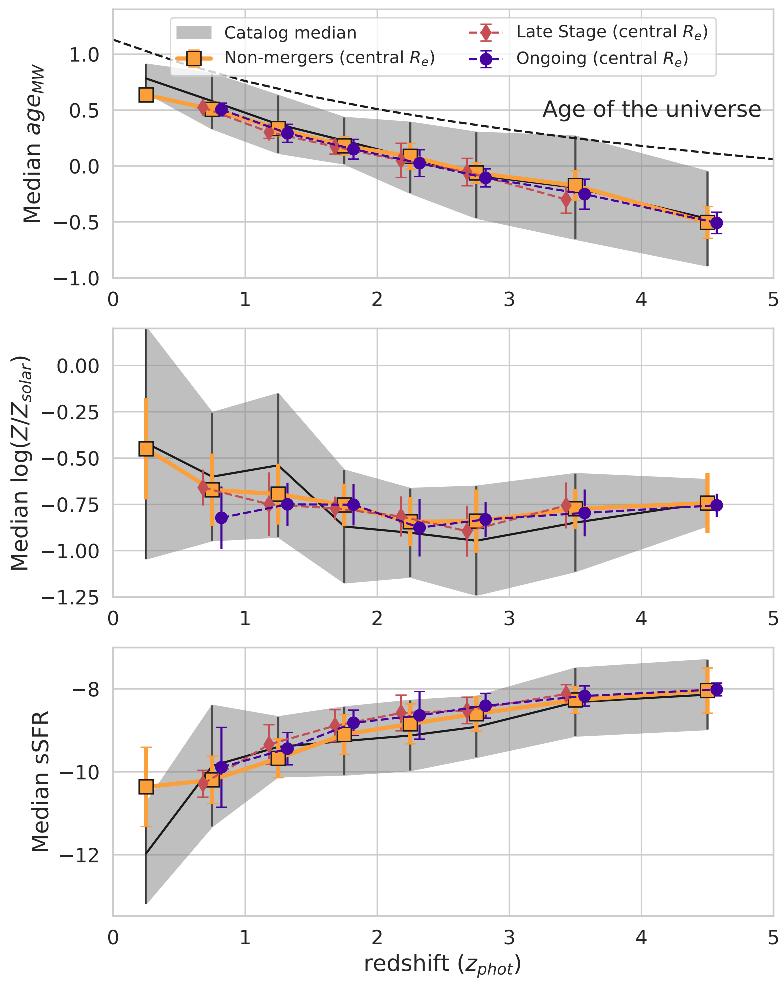

Figure 4.3: Median mass-weighted age (top panel, stellar metallicity (middle panel), and sSFR (bottom panel) of the inner $1R_{eff}$ (half-light radius) of the resolved MWA progenitor sample for every redshift bin. Error bars are the 1σ scatters of the properties' distributions. The black solid lines and the grey shaded regions represent the median and the 1σ scatter respectively, of the *integrated* (unresolved) properties of all possible MWA progenitors from the catalog. The catalog's age is t_{50} (age when 50% of stellar mass has formed in the galaxy) instead of derived from Equation 4.4.

time:

$$t_{MWage} = \frac{\sum_{t_0}^{t_{age}} t_i M_{formed}(t_i)}{\sum M_{formed}(t)} \quad . \tag{4.4}$$

The mass-weighted age is more closely associated with the median age of the stars rather than the age of the brightest stellar populations observed for that region of the galaxy.

4.4 Radial Profiles across the redshift range

In this section, we present the results of creating radial property gradients for each of the 904 MWA progenitors, divided into distinct redshift epochs. This was done both with elliptical annuli of 0.1 kpc

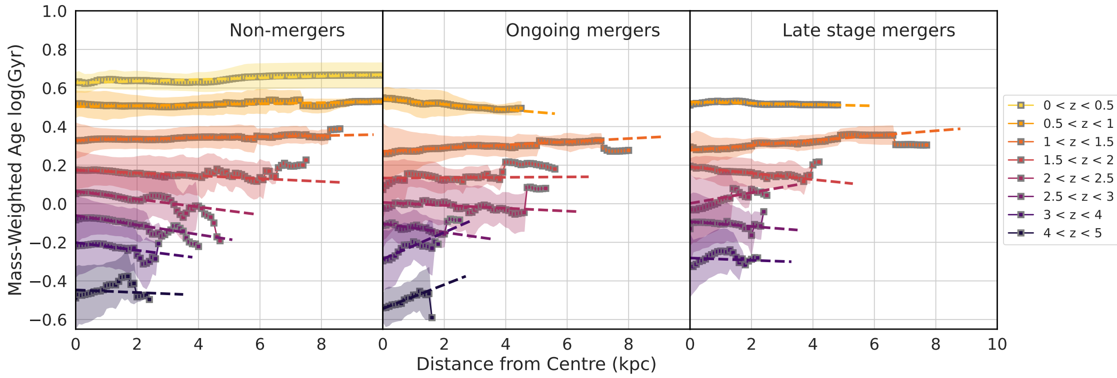

Figure 4.4: The average mass-weighted age gradients for each redshift epoch created by stacking and normalizing each mass-weighted age profile. The distance from the galactic center is shown in kpc. The shaded regions represent the 1σ scatter, or the 16th-84th percentile range of the properties. Left panel is the non-merger sample, middle are ongoing mergers, and right panel are late stage mergers. Dashed lines indicate line of best fit to the averaged gradient, which was fit via a weighted linear regression method, with the weights coming from the 1σ errors of the average profiles (i.e. the shaded regions).

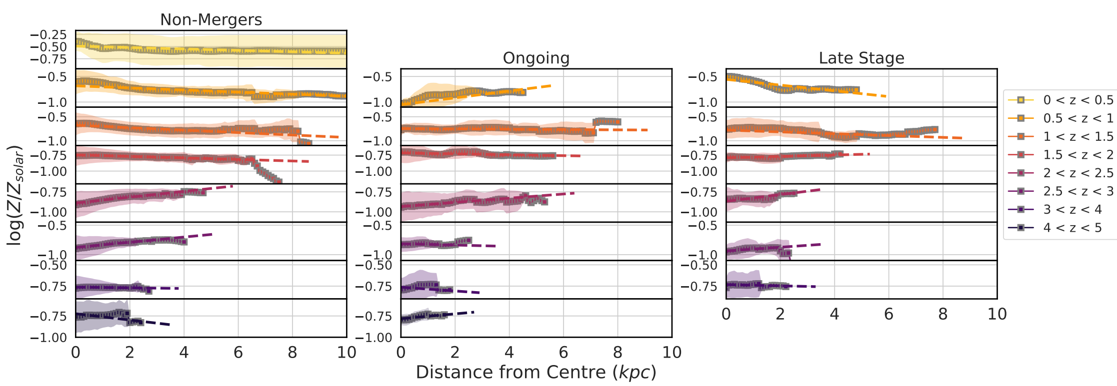

Figure 4.5: Similar plots as Figure 4.4, but for stellar metallicity $\log(Z/Z_{\odot})$, equivalent to [Z/H]. Each radial gradient is on its own axis for visual clarity.

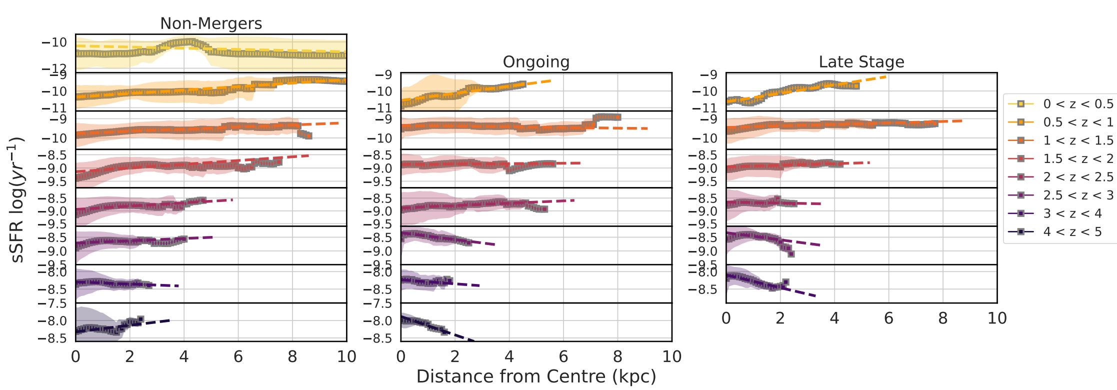

Figure 4.6: Similar plots as Figures 4.4 and 4.5, but for sSFR. Each radial gradient is on its own axis for visual clarity.

width, as well as 0.1 effective radii (R_{eff}, circularized half-light radii from the CANUCS photometry catalogs [1]) in width, centered on the central pixel of each respective galaxy (or the more massive galaxy for ongoing mergers). Unlike the stellar mass and SFR maps, the metallicity and age maps are not densities. For the individual age and metallicity gradients, we take the weighted average of the respective property of the pixels of that annulus, with the weight for each pixel determined by its $\Sigma_\star$. Radial gradients for sSFR are created by taking $\Sigma_{SFR}/\Sigma_\star$ at each annulus. The radial gradients scaled to kpc are to put into context the changes to the spatial distribution of those properties *phyiscally*, as measured between different redshift epochs for MWA progenitors. For this reason, most of our results are presented as radial profiles measured in kpc. However, the majority of radial gradients measured at low-z are presented as a function of effective radius. For the purposes of comparison with local universe resolved studies, the same profiles as a function of R_{eff} and their resultant slopes are shown in Appendix 4.8.1.

In Figure 4.3, we take the median properties: mass-weighted age, stellar metallicity, and sSFR, in of the inner 1 R_{eff} of each galaxy for each subsample (non-merger, ongoing merger, and late stage merger) as a function of redshift. They are also plotted against the median values for the full, unresolved MWA sample, with integrated properties from the CANUCS catalog (Sarrooh&Asada et al., 2025). Our resolved sample has median properties which agree well at all redshifts with the integrated catalog properties. For median ages, since the catalog does not include a mass-weighted age defined in the same way as in 4.4, we instead plot it against the t_{50} age distribution. The change in mass-weighted age implies the galaxies are "ageing" slower than the universe (indicated by the dashed line on the topmost panel), which is in line with the sample being selected for star-forming galaxies.

The median metallicity shows almost no evolution with redshift, the values in the middle panel of Figure 4.3 are all below $-0.6\log(Z/Z_\odot)$ for all three subsamples, except for the non-merger sample at the lowest redshift. The median metallicity of the ongoing mergers also appear to diverge slightly from the non-merger and late stage merger at $z < 1$, being roughly 0.2 dex lower in metallicity. However, the error bars still indicate general agreement between all three populations.

The bottom panel of Figure 4.3 shows the sSFR evolution with redshift. Although Tan et al. (2024b) shows SFR increases up to $z \sim 2$ (cosmic noon) before decreasing once more until $z = 0$, the sSFR on the other hand, is consistently decreasing with respect to time.

4.4.1 Average radial gradients for each redshift epoch

To better understand the relationships between star-formation, ages, and metallicity within galaxies, we must examine the behaviour of the radial gradients of their properties. In Tan et al. (2024b), we have shown using radial gradients of $\Sigma_\star$ and sSFR that the MWA progenitors are building mass

[1] measured in Photutils from the F150W 20mas resolution image

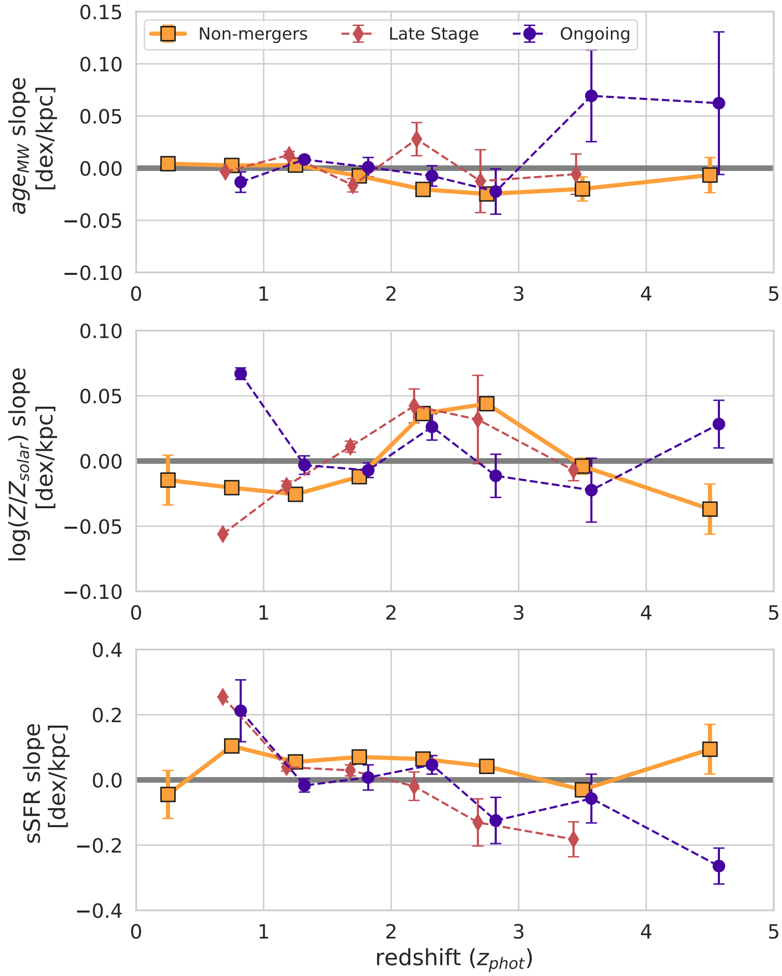

Figure 4.7: Slopes of the mass-weighted age (top panel), metallicity (middle panel) and sSFR density (bottom panel) gradients for each redshift bin. Yellow squares are non-mergers, red diamonds are late stage mergers, blue circles are ongoing mergers. Error bars represent the fitting error in the slope, weighed by the scatter in the distribution.

inside-out.

We obtain an averaged radial gradient by stacking every profile in each redshift bin, and then normalizing the stacked profile by dividing by the number of galaxies. This is done for the non-merger, ongoing merger, and late stage merger subsamples. These averaged profiles are plotted in Figures 4.4, 4.5, and 4.6 for mass-weighted age, metallicity, and sSFR respectively, as the colored square points. The shaded regions represent the 1σ scatter for the profiles at each redshift. Since the property maps are cut off at 2.5 times the kron radius of the galaxy from the catalog, each individual gradient may be "cut off" at a different kpc. Therefore at larger radii, the average gradient is the average of less galaxies, similarly for the error bars.

To obtain the slope of the radial gradients, we perform a linear fit to each average profile with SciPy's `curve_fit()` function. We use the standard error at each ΔR as uncertainty in the optimization of the parameters, and set `absolutes_sigma = True`. Standard error ensures a more accurate linear fit, because as previously stated, different galaxies have different radial cutoffs, in effect biasing the stacking for the average profiles at larger radii as there are fewer galaxies to stack. Standard error fixes the bias because it scales the standard deviation by the square root of the number of objects ($\sigma/\sqrt{N_{galaxies}}$). When there is no standard error available (i.e. on the edges of the gradient where there is only data from one galaxy in the average profile), the uncertainty was set to 1, since the optimized function is $\chi^2 = \sum(r/\sigma)^2$. The line of best fit to each average profile is represented by the dashed lines in Figures 4.4, 4.5, and 4.6 .

4.4.2 Mass-weighted age gradients

In each each column of Figure 4.4, the averaged non-merger $\log(\langle \text{age} \rangle_{MW})$ gradients are are well-separated for each redshift epoch. In the left panel, non-merger age gradients are shown, which are the majority of the galaxies in our MWA progenitor sample (756 out of 904). Gradients are flat for redshift bins $z < 2$, are negative at $2 < z < 3$, but become flat again at $3 < z < 5$. A negative age gradient indicates that galaxies have younger stars on their outskirts versus their inner regions, which is in line with inside-out mass assembly. A flat age gradient at high-z is expected, because galaxies are still young, so most of their stars will have formed at the same time (at cosmic dawn) and subsequent rounds of star formation are more or less occurring at similar rates and time scales. A flat age gradient at lower-z however, when galaxies have grown to a certain size and have established stellar populations, would require more complex mechanisms, such as radial mixing of stars, or non-preferred location for pristine gas accretion.

If we assume our progenitor selection via abundance matching is accurate, that the galaxies at a higher redshift bin will evolve into the galaxies at a lower redshift bin, then the steepening and then flattening of the age gradient (for non-mergers) may indicate that galaxies are assembling inside-out, but after a certain point, switch to lockstep assembly. However the turnaround in the $\log(\langle \text{age} \rangle_{MW})$ slope versus redshift plot in Figure 4.7 place this turnaround for non-mergers at $z \sim 2.5$ instead of at $z \sim 2$, as we previously argued in Tan et al. (2024b). Although non-mergers are not merging at the moment we observe them, they may have experienced mergers in their past, or at the very least interactions with other galaxies. This could have induced more radial mixing of stars of different ages, or a starburst in the central regions to "even out" their ages. Due to the low merger fractions overall in our sample, mergers would not be the primary mechanism for flattening age gradients, especially since merger fractions are decreasing with decreasing redshift (as seen in the bottom right panel of Figure 4.1).

For ongoing mergers, the age gradients are also generally flat at all redshifts, with possible signs of positive gradients at $3 < z < 5$. However, the large error bars and small amplitude of the average slope at those redshifts still show consistency with overall flat age slopes. Additionally, at higher redshift, small differences in age between merger components (measured in log(Gyr)) are amplified. Since the middle and right panels of Figure 4.4 shows the age gradients for the merger populations are well-separated, the merger population in our sample mainly consists of galaxies that contain stellar populations of similar ages. The flatness of the $\log(\langle \text{age} \rangle_{MW})$ gradients in the case of ongoing mergers at $z < 3.5$ is also evidence of this. The trends for the mass-weighted age gradients' slopes versus redshift are plotted in the top panel of Figure 4.7, as a function of redshift, for more clarity.

4.4.3 Metallicity gradients

In Figure 4.5, for each subsample, we plot the averaged stellar metallicity ($\log(Z/Z_\odot)$, equivalent to [Z/H]) gradient of each redshift bin by stacking and normalizing all the individual metallicity profiles of the galaxies within that redshift epoch. At lower redshift ($z < 2$), our non-merger results agree with local universe measurements of an overall negative gradient in star-forming galaxies, with a shallow slope. However at $2 < z < 3$, the metallicity gradient is mildly positive for both redshift bins. At $3 < z < 5$, the average metallicity gradient is flat. For star-forming galaxies, there exists measurements of a positive *gas phase* metallicity gradients at $2 < z < 3$ (e.g. as seen in Li et al. 2022). Unlike studies from the local universe (González Delgado et al., 2015; Goddard et al., 2017; Zheng et al., 2017), we do not find a correlation between negative $\log(\langle \text{age} \rangle_{MW})$ gradients and negative metallicity gradients, even for non-mergers. However, we emphasize that our age and metallicity slopes at all redshifts are close to flat.

While positive metallicity gradients are rare in the local universe, they can appear in low mass systems. If positive gradients are associated with higher sSFR for the galaxy (Stott et al., 2014; Ma et al., 2017; Curti et al., 2020), it stands to reason that a low mass galaxy would be more likely to have a flat or positive metallicity gradient. As Figure 4.3 shows, the global sSFR of our sample of galaxies is decreasing as redshift decreases, and galaxies are less massive at earlier times. The increased number of low mass galaxies, particularly objects with $M_\star < 9 \log(M_\odot)$, combined with higher sSFR, means there are higher instances of positive metallicity gradients at $2 < z < 3$.

For the merger samples in Figure 4.5, both the ongoing mergers and the late stage merger gradients appear to follow the trend in redshift as the non-merger sample. If we assume from the flat $\log(\langle \text{age} \rangle_{MW})$ slopes in Figure 4.4 are a result of mergers occurring between galaxies with similar star-formation histories, this may explain why their gradients are similar despite galaxy interactions. The underlying stellar populations are not different enough for any distinguishable effect on the average metallicity gradient to differ from the non-merger sample. The only redshift range where the slopes of the merger samples are a drastic departure from the non-merger sample is at $0.5 < z < 1$. However, there are only two ongoing mergers and one late stage merger at that redshift. Metallicity gradients and overall stellar metallicity appears to evolve slowly with redshift, and not evolve much between $3 < z < 5$.

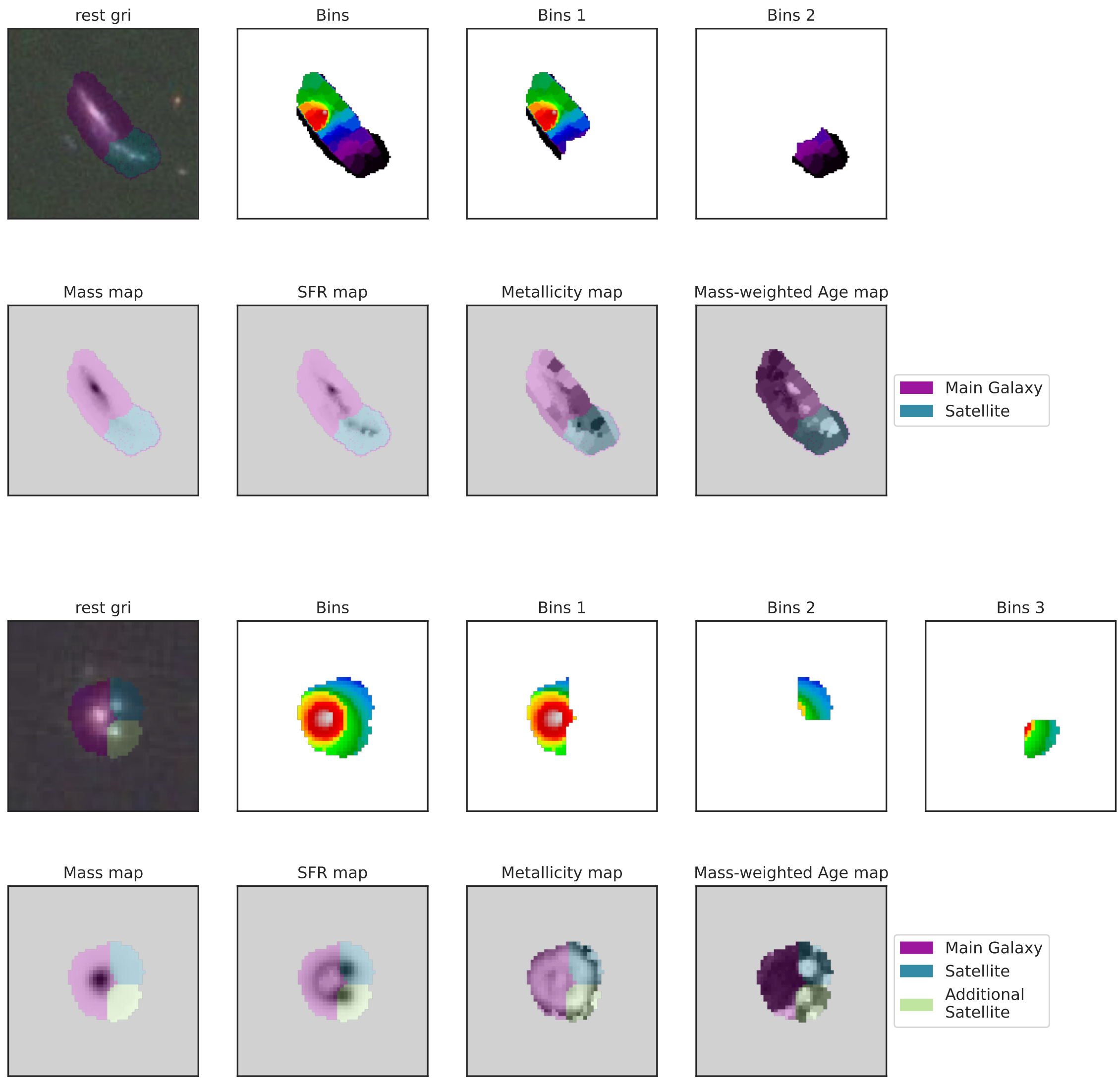

Figure 4.8: Two examples of ongoing mergers being divided into separate regions, using the watershed algorithm on a combination of the $\Sigma_\star$ and Σ_{SFR} maps. The first cutout is divided into two regions, and the second cutout is divided into three regions. From top left to top right: we display the color image with the regions overlaid on top, the Voronoi bins of all the regions, followed by the Voronoi bins of each separate region separately. From bottom left to bottom right: the watershed segmentation map overlaid on top of the $\Sigma_\star$, Σ_{SFR}, $\log(Z/Z_\odot)$, and $\log(\langle \mathrm{age} \rangle_{MW})$ maps. The most massive object is defined by the purple region, the second most massive is highlight in teal, and the least massive is highlighted in light green (when there are three objects present).

4.4.4 Specific star-formation rate gradients

The link between higher rates of star-formation and lower mass-weighted age is clear through the definition of mass-weighted age as outlined in Equation 4.4 in §4.3. However, it does not appear that age gradients and sSFR gradients have inverse trends, or are even correlated. As Figure 4.7

demonstrates, the non-merger sSFR slopes start off flat at $4 < z < 5$, and then the slopes are on an overall increasing trend with decreasing redshift, while the $\log(\langle \mathrm{age} \rangle_{MW})$ slopes start off flat at earlier times, become negative, and then flatten out once more closer to the present day. This may appear incongruous with the sSFR slope versus redshift for non-mergers, because the average sSFR gradient slope is positive even at $z \sim 0.5$. However, recall that sSFR is the rate of SFR proportional to the stellar mass. Central regions have more stellar mass, so the amount of newly formed stars contribute less to their average age. Once outer regions build up more stellar mass at later times, the age of the younger stars also affect the average age to a lesser degree. In addition, the bottom panel of Figure 4.3 shows sSFR is decreasing globally towards lower redshift, and $z < 2$ is after the epoch of cosmic noon. This also generally means that the rate of newly formed stars is decreasing overall, which results in flatter age gradients. Effectively, the outer regions begin to "catch up" to the inner regions in terms of the age of the stars.

The sSFR slopes for both ongoing and late stage mergers start off negative, and increase to positive at later times, while their $\log(\langle \mathrm{age} \rangle_{MW})$ slopes are either mildly positive/negative or flat without any discernable relation to either redshift nor with sSFR slopes. Both merger samples (ongoing and late stage) having a similar sSFR slope trend with redshift that is distinct from the non-merger sample may indicate that galaxy interactions tend to enhance star-formation more in regions that already have higher SFR. This may be why the merger samples' sSFR slopes are more steeply negative at $2.5 < z < 5$, flat at $1 < z < 2.5$, and more steeply positive at $z < 1$.

4.5 Properties of component galaxies in ongoing mergers

Since papers like Grossi et al. (2020) and Tissera et al. (2022) find a correlation between mergers and inverted metallicity gradients seen in the local universe, we must examine the properties of the merging sample in more detail. As §4.4 shows, the general distribution of the slopes of property gradients from mergers are not statistically different from non-mergers. We know that the ongoing merger sample does consist of visually separated objects in both the $\Sigma_\star$ maps and the color images. We can therefore take divide the ongoing merger sample's property maps into regions that are associated with each object, and determine if there are distinct differences in their average properties.

4.5.1 Separating galaxies in merger pairs

The process for separating the ongoing merger maps into different regions based on their component galaxies is as follows:

1. We combine the normalized stellar mass map and SFR map into one detection image.

2. We create an initial segmentation map (only segmenting foreground and background pixels)

from the detection image with the function `detect_sources` from Photutils. This segmentation map was then expanded by 5 pixels.

3. The shortest distance for each pixel within the segmentation map to the background is obtained as the scaled distance array.

4. The watershed algorithm, which finds local maxima/peaks in images, was applied to the scaled distance array multiplied by the combined normalized stellar mass and SFR maps. We limit the number of peaks identified in the watershed algorithm to 5, so the initial watershed segmentation maps had up to five regions.

The initial segmentation maps were then inspected for accuracy, and any regions that did not correspond to a peak in the detection image was combined with another region such that no map contained more than three distinct areas for ongoing mergers. These areas were then masked to the property maps of the object's data cube to obtain the averaged properties of each pair of mergers. Any objects separated into three sections would have their third section count as an additional satellite. Two examples are shown in Figure 4.8

4.5.2 Properties of galaxies in merger pairs

To identify differences in age and metallicity, we first find which region of the segmentation map contains the most stellar mass. The other region(s) are then counted as "satellites" of the first galaxy. In Figure 4.9, we plot the mass fraction of the main galaxy and its satellite(s). The purple, teal, and green points display individual mass fractions for the three distinct regions outlined in Figure 4.8, while the purple, teal, and green trend lines are the median mass fractions. The central galaxy of the merging system can be between $\sim 40\%$ to $\gtrsim 80\%$of the total mass of the system. The median mass fraction is between 60 and 80 percent, implying roughly a 3:1 or 5:1 ratio for major mergers. There does not appear to be an obvious size evolution with redshift in the mass ratios between the central galaxy and the companion(s), and at all redshifts, there is a large scatter in the distribution of the mass fractions.

One possible explanation for the closeness in mass fraction between the two main components of these merger systems is that the ongoing mergers were selected by visual inspection. Perhaps some of the mergers identified by the Gini-M_{20} plane that were sorted visually into "late stage" mergers are ongoing mergers that have a satellite galaxy that is not massive enough to be seen by eye on the stellar mass maps.

On the right side of Figure 4.9, we take the difference between the average properties for the entire system and the average properties of each galaxy in the merging system. Note that for ages and metallicity, it is a mass-weighted average, whereas for sSFR, the average was not weighed by stellar mass, as sSFR is already dependent on $\Sigma_\star$. Any object in our merger sample which was

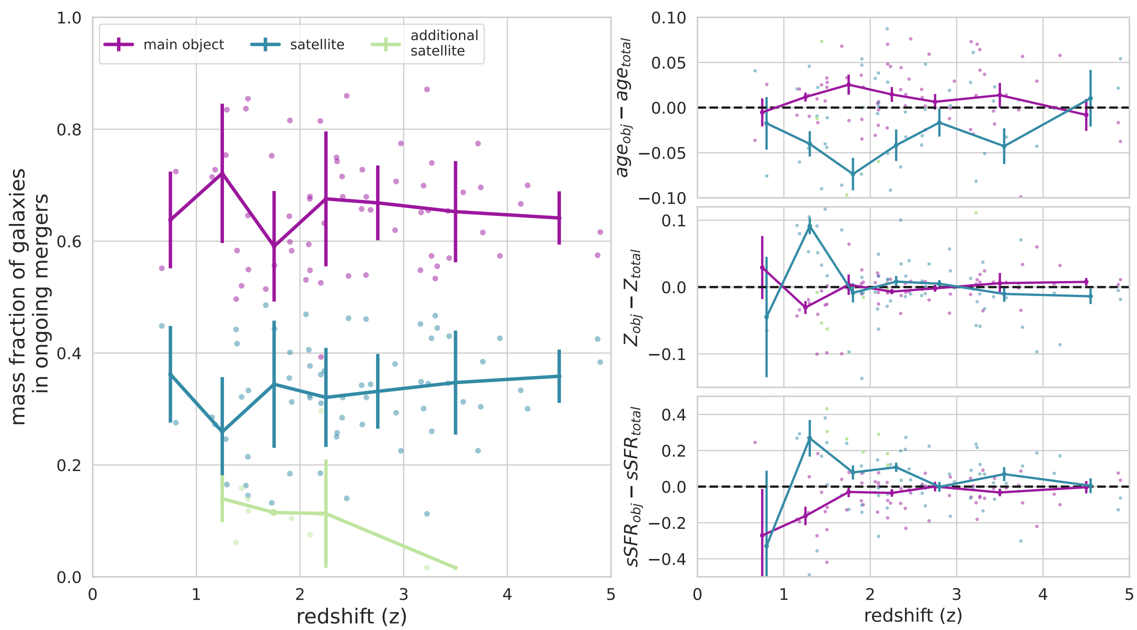

Figure 4.9: *Left Panel:* Mass fractions of merger components. Error bar is the $1-\sigma$ scatter. *Right panels:* Difference in average age, average metallicity and average sSFR of the components of the merger versus the average properties of the entire merger system. Errors are standard error of the mean for more visual clarity of the property differences as a function of redshift. The individual property differences for the main and satellite galaxies are also plotte to demonstrate the true scatter in the relationship.

divided into three regions have their two less massive regions count as separate data points for the satellites. The average difference at each redshift bin is plotted as the purple and teal trend lines. In the top right plot of differences in age, overall, the more massive galaxy tends to have older stars, which holds true for all redshifts, except for the highest redshift bin. However, there is a large scatter in age, and individual merger pairs may have the less massive galaxy contain older stars. The middle plot in the right column shows that on average, there is almost no difference in metallicity between the more massive and the less massive galaxy in an ongoing merger, until $z < 1.5$. Although we note that the individual metallicity differences do have a scatter of ~ 0.07dex. Additionally, whether the more metal-rich pair is the more massive or the less massive of the pair does not seem to have a redshift dependence. The bottom right plot of differences in sSFR shows that sSFR is the only property where merger components can be distinctly different, although the differences are still moderate. The average difference in age and sSFR start off with an inverse relationship which holds until $z < 1.5$, where the sSFR of the less massive appear to increase drastically without a similar decrease in the age. However, this does correspond with the redshift bin where metallicity differences are non-negligible. Generally speaking, there is still a slight trend that the more massive component of a merger is slightly older and the difference in age increases with time, while the less massive component of a merger has more active star-formation, and the difference also increases with time.

4.5.3 Difference between merger components and non-mergers

We have established in Figure 4.9 this sample of mergers are between galaxies with similar masses. This means that these mergers are the ones most likely to disrupt the "status quo" established by the non-mergers: which is inside-out growth. However, the difference in age, metallicity and sSFR between the component galaxies of the mergers are small. The age differences of the merger components compared to entire system are below 0.1 dex, which explains the flatness of the ongoing merger slopes in Figure 4.7. The lack of difference in metallicity between merger components can also explain why the metallicity gradients for the merger samples evolve similarly with redshift as the non-merger sample in Figure 4.7. The most prominent mergers are occurring between galaxies with extremely similar chemical abundances in their stars. Once the merging pairs have notable differences in metallicity, which occurs at $z < 1.5$, the average metallicity gradient slopes of the mergers also diverge from the non-mergers. Overall, the component galaxies of the ongoing mergers do not appear to differ greatly in age at all redshifts, and only differ *at most* ~ 0.1 dex in metallicity and ~ 0.4 dex sSFR at $z < 1.5$.

This raises the question of how do the global properties of the merger galaxies (both ongoing and late stage mergers) differ from the *non-merger properties* at the same redshift. In Figure 4.10, we demonstrate this by taking the difference between the mass-weighted average $\log(\langle \text{age} \rangle_{MW})$ and $\log(Z/Z_\odot)$ of the ongoing merger components with the non-merger median properties. These are displayed as the purple and teal trend lines. Additionally, we also take the difference between the non-merger and merger sample medians in Figure 4.3. These are plotted as the red diamonds for the late stage mergers and large blue circles for the ongoing mergers.

Recall that the median values in Figure 4.3 are only the central $1R_{eff}$ of those galaxies at each redshift, and are more representative of the more massive central galaxy of the merger system. Interestingly, while the merger components do not have a statistically significant age difference, both components have on average, lower ages than the average non-merger age at the same redshift. Merger components still have similar $\log(Z/Z_\odot)$ to non-mergers until $z < 1.5$, and higher sSFR than non-mergers at all times, save for the highest-z bin ($4 < z < 5$) and the lowest-z bin ($z < 0.5$). Both the central and the satellite galaxy in the merger exhibit the same trends versus non-mergers, which indicates that when the properties are different between the two populations, they affect both merger components, and tend to affect the less massive component to a greater extent. Note that the ongoing merger trend line (in blue) is not always between the merger components because it only accounts for the central R_{eff} of the radial profiles, whereas the averages of the merger components are across the entire region defined by the watershed algorithm, which would include areas further from the galaxies. The late stage mergers are generally closer in median age to the non-mergers, but have similar sSFRs to ongoing mergers, implying that merging galaxies on the whole have more active star-formation. Since these are the central $1R_{eff}$, this also implies that star-formation enhancement from close interaction of galaxies is not just at the outskirts, but across all radii.

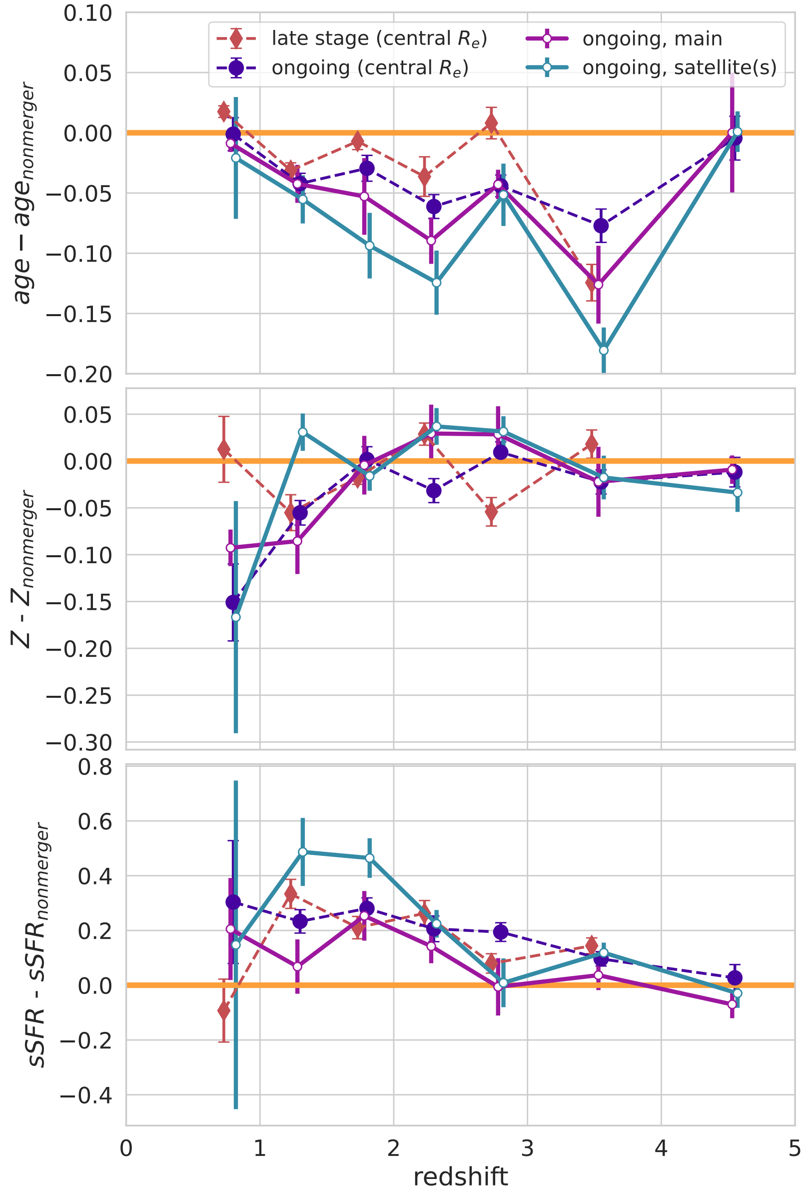

Figure 4.10: Difference between the median $\log(\langle \text{age} \rangle_{MW})$, $\log(Z/Z_{\odot})$, and sSFR of the late stage mergers, ongoing mergers, and the average values of the ongoing merger components. Median values for the radial profile measurements come from Figure 4.3, which means that they are the median of the inner $1R_{eff}$ of the galaxies at each redshift bin. The ongoing merger samples' average values are from the Watershed segmentation maps.

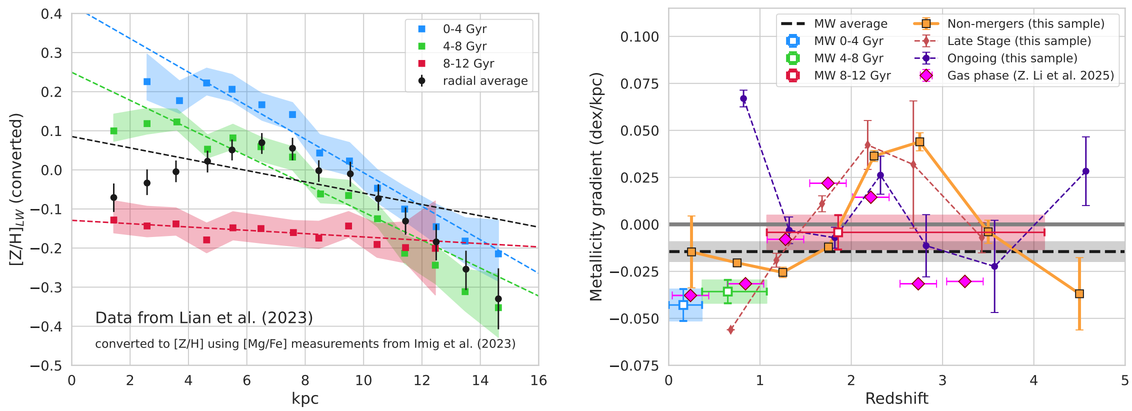

Figure 4.11: *Left Panel:* Light-weighted [Z/H] radial gradients of the Milky Way from Lian et al. (2023), converted from their [Fe/H] gradients using Equation 4.5 and Equation 4.6. Blue points are stars with ages 0-4 Gyr, green points have ages 4-8 Gyr, and brown points have ages 8-12 Gyr. Black circles are the average at that kpc. Dashed lines are the slope fitted to the gradients of the respective colors. *Right Panel:* The average metallicity gradients from this work are compared to the average slopes of gas-phase metallicity gradients from Li et al. (2025b), as well as the converted [Z/H] slopes from the Milky Way (white squares, same slopes as the middle panel in Figure 4.7). The ages for each population of MW stars are converted to redshift according to our cosmology, and shaded regions in the horizontal represent the age range. Error bars in the vertical represent the weighted error in the slope.

4.6 Discussion

4.6.1 Metallicity and age gradients in the context of other studies

In order to demonstrate that our results are consistent with the Milky Way itself, we make a comparison with abundance gradients obtained from studies of our own galaxy. Lian et al. (2023) obtained light-weighted radial [Fe/H] gradients of the Milky Way from the APOGEE survey (Blanton et al., 2017; Ahumada et al., 2020; Jönsson et al., 2020), split into three different age groups. They compared the gradients with both local analogues in MaNGA as well as simulations in TNG50. We converted their radial [Fe/H] gradients of the Milky Way from Lian et al. (2023) to [Z/H] using the equation

$$\log(Z/Z_{\odot}) = [\text{Z/H}] = [\text{Fe/H}] + 0.94 \times [\text{Mg/Fe}] \quad , \tag{4.5}$$

which was previously used in Thomas et al. (2003); Kriek et al. (2019), and Carnall et al. (2024) to convert elemental abundances from iron ratios to global stellar metallicity. The [Mg/Fe] abundances can be approximated from a relation described by Equation 1 of Imig et al. (2023), which is a survey of the distributions of [Fe/H] and α-element abundances in the Milky Way, also from the final data release of APOGEE (Majewski et al., 2017; Abdurro'uf et al., 2022). Their equation is as follows:

$$[\text{Mg/Fe}] = \begin{cases} 0.15 + 0.13 \times [\text{Mg/Fe}] & \text{if } [\text{Fe/H}] \leq 0 \\ 0.15 & \text{if } [\text{Fe/H}] > 0 \end{cases} \tag{4.6}$$

The resulting [Z/H] radial gradients are shown in the left panel of Figure 4.11. The slopes fit to the metallicity gradients of the different stellar populations, as well as the Milky Way average are plotted on the right panel of Figure 4.11. This shows the average metallicity gradients of our MWA progenitors are in fairly good agreement with the metallicity gradient present in the Milky Way itself. The average [Z/H] slope for the present day Milky Way especially agree well with our sample of non-mergers at $z < 1.5$. The metallicity gradient of the oldest population of stars in the Milky Way (which would primarily be thick disk stars) also show good agreement with the average metallicity slopes at $z \sim 2$ and $z \sim 3.5$ for our sample, for both mergers and non-mergers.

Recently, Li et al. (2025b) measured spatially resolved gas-phase metallicities up to redshift $z = 9$ from the surveys FRESCO, NGDEEP, and ASPIRE, and found that gas phase metallicity gradients evolve with the star formation rate density (SFRD) of the universe. From $z \sim 9$, metallicity gradients start off very steeply negative (around -0.5 dex/kpc), flatten around cosmic noon ($2 < z < 3$) and then decline slowly to $z = 0$. The first phase of star formation at cosmic dawn may have rapid inside-out growth with efficient cold gas accretion but limited radial mixing, resulting in the steeply negative gradients in gas phase. The flattening of metallicity gradients at cosmic noon is attributed a combination of gas accretion and strong stellar feedback, which affects low mass galaxies more. Finally, after the decline of the SFRD, galaxies switch to more gradual star formation and secular evolution. This steepens metallicity gradients once more, but not to the extremes seen at $5 < z < 9$. Interestingly, Figure 4.11 shows that the evolution of our stellar metallicity gradients match the evolution of the gas metallicity gradients in Li et al. (2025b) for $0 < z < 4$ remarkably well.

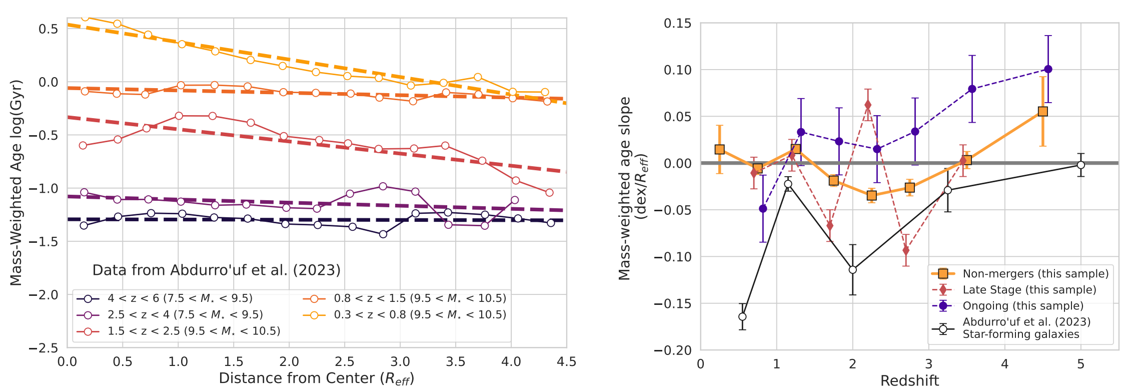

Figure 4.12: *Left:* Averaged mass-weighted age gradients as a function of R_{eff} from Abdurro'uf et al. (2023) that match the stellar mass range of our MWA progenitors at the same redshift range, with dashed lines for the fitted slope to the age gradient. *Right:* The evolution of the Abdurro'uf et al. (2023) age gradient slopes over time in black, compared to the evolution of our age gradient slopes, fitted to R_{eff} instead of kpc (see §4.8.1 for details).

In Figure 4.12, we fit slopes to the mass-weighted age gradients presented in Abdurro'uf et al. (2023) for the star-forming galaxies at the stellar mass range that matched the redshift range for the MWA progenitors of our sample. This is a reasonable comparison because our resolved $\log(\langle \text{age} \rangle_{MW})$ maps are produced using the same method as outlined in Abdurro'uf et al. (2021). Despite using different pixel binning methods (Abdurro'uf et al. 2023 used their piXedfit binning algorithm while we used Voronoi tessellation), our mass-weighted age gradient slopes do have fairly good agreement, especially for our non-merger sample at higher redshift. Although there may be spatial sampling bias as higher redshift galaxies are more affected by lower resolution and lower signal-to-noise. The evolution of the age gradients with respect to redshift also follows a similar trend until $z \sim 1$, which still indicates agreement between our results, despite the resolution effects. The difference between the average age gradient for our sample at $z < 1$ and the star-forming sample from Abdurro'uf et al. (2023) may be due to the difference in mass range (our sample spans a stellar mass range of $10 < \log(M_{\odot}) < 10.7$ at $z < 1$) or it could be from small number statistics, since there are only 23 galaxies with redshift $z < 1$ and only 2 galaxies with redshift $z < 0.5$.

4.6.2 Feedback, sSFR, and metallicity gradients

In this study, the average age and metallicity gradients for this sample of MWA progenitors are generally flat or negative. However, there are certain cases where the average gradients are positive, although the amplitude of the slopes are small. This is consistent with studies of local universe metallicity and age gradients obtained from star-forming galaxies. In the local universe, both very low mass and very high mass galaxies can have flat metallicity gradients, or even positive gradients. In González Delgado et al. (2015), they find that disk galaxies in CALIFA with stellar mass $9.1 < \log(M_{\odot}) < 9.6$ had an overall mildly positive mass-weighted metallicity ($\log(Z/Z_{\odot})$) gradient with a mildly negative log age gradient. In fact, all of the inner metallicity gradient values (gradient within $1R_{eff}$) for their mass bins $\log(M_{\odot}) < 10$ are either positive or flat, while all of their average age gradients are negative. In Zheng et al. (2017), using MaNGA data, they find that negative metallicity gradients may sometimes correspond to a flat age or even mildly positive age gradient for low mass systems. In Goddard et al. (2017), also with MaNGA, their lowest mass bin $\log(M_{\star}) \sim 9.58 \pm 0.26 M_{\odot}$ has a mass-weighted age slope of -0.053 ± 0.012 dex$/R_{eff}$ and a close to flat [Z/H] slope of -0.001 ± 0.038 dex$/R_{eff}$. In all cases, studies from the local universe have large scatters in their gradient slopes, similar to the scatter we find in higher redshift gradients in this sample.

Additionally, positive metallicity gradients are consistent with studies of gas-phase metallicity of star-forming galaxies at cosmic noon (i.e. Cresci et al. 2010; Jones et al. 2013; Curti et al. 2020; Simons et al. 2021, and Li et al. 2022), when the global sSFR is much higher, and galaxies were less massive. One argument for why increasing sSFR is correlated to more instances of positive metallicity gradients is that sSFR is linked to stronger feedback. Sun et al. (2024) find this link in the FIRE-2 simulations, where there is a correlation between positive radial metallicity gradients and the overall sSFR of the galaxy. They also find that galaxies with lower stellar mass, in particular galaxies with $M_\star < 8.5 \log M_\odot$ have higher instances of positive metallicity gradients. Interestingly, they also found a relationship between morphology and metallicity gradients, with irregular and thick disks displaying flatter or positive gradients, and thin disks displaying more negative gradients. This may also be linked to the fact that lower mass galaxies have smaller potentials. Hopkins et al. (2023) demonstrates with the FIRE simulations that galaxies with lower potentials are much more responsive to feedback, and the ISM can be completely reset. However, they do not find a morphological correlation between bursty/feedback-heavy star-formation and non-disky systems. Both thick, thin, and non-disks can equally exhibit bursty or smooth star-formation. They also do not find any differences between disk and non-disk radial gas phase $Z/Z_\odot$ profiles. Nevertheless, our results of average stellar metallicity gradients that are *mildly positive* in the era of cosmic noon agrees with gas-phase observational results as well as simulations.

4.6.3 Galaxy interactions and overall mass assembly history for MWAs

In general, the ongoing and late stage mergers in our sample do not have statistically significant differences in their radial gradients, nor their overall average properties from the non-merger sample. This indicates that mergers do not significantly alter the age or metallicity of MWAs, but they still contribute to the mass assembly through the addition of stellar mass, enhanced star formation, and merger-induced feedback.

From observations, Lofthouse et al. (2017) probed the fraction of disturbed, star-forming spheroids in CANDELS at $z \sim 2$ as a probe for morphological transformation, and found that major mergers (mass ratios > 5:1) were *not* a driver of transforming disks into spheroids. From simulations, Li et al. (2025a) finds in the FIRE-2 Simulations that starbursts from galaxy interactions or mergers come from torque due to the inflow of gas into the central galaxy. However, mergers are not the only mechanism that triggers starbursts, and they did not find the SFR increase from galaxy interactions to be any greater than from other starburst events. They also do not see a significant imprint of mergers' effects on MW-mass galaxies' SFHs. Qi et al. (2025) compared both resolved star-forming main sequence (rSFMS) and resolved mass-metallicity relations (rMZR) within galaxies from simulations in TNG50 against resolved surveys such as CALIFA, MaNGA, ALMaQUEST, and PHANGS, and the EAGLE simulations, and find that while resolved SFR has a dependence on the host galaxy's mass, the rMZR (from gas phase metallicities) are *localized* properties and are independent of host galaxy mass. Our results of generally flat and mildly evolving age gradients do differ from Jung et al. (2025), who find more evolution in age gradients of simulated MW progenitors in AGORA at $1 < z < 5$. They showed that stellar migration explained the positive age gradients in their simulated galaxies. Signatures of stellar migration are strongest for galaxies that experienced mergers, and little to no stellar migration occurs for galaxies that show the strongest signs of inside-out assembly. Since merger galaxies in our sample do have larger average age gradients than non-mergers, it is possible that stellar migration can flatten out stronger age gradients caused by mergers.

In general, our are in agreement with these studies that demonstrate that major mergers may alter the radial gradients as they occur, but ultimately the average trends show they do not disrupt the general process of inside-out mass assembly of disk galaxies. There is also the possibility that if a merger induced starburst quenches the galaxy, its quiescent "descendants" will be excluded from the next redshift bin of our progenitor sample. This can also explain the shift to negative metallicity gradients at lower redshifts. There may be a "survivorship bias" in the case of lower redshift progenitors needing to still be actively star-forming to remain a MWA progenitor.

4.7 Summary

In this study we used spatially resolved SED-fitting on NIRCam, NIRISS, and HST photometry to produce specific star-formation rate, mass-weighted age, and stellar metallicity maps for MWA progenitors up to $z = 5$. Using a combination of statistical morphology classification tools (the Gini-M_{20} plane) and visual inspection, we separated the sample of 904 galaxies into ongoing mergers, late stage mergers, and non-mergers. We analyzed the radial gradient of the property maps of the galaxies as a function of redshift. Our main conclusions are:

- The age gradient slopes of non-mergers are consistently flat across the redshift range. The most negative age gradient slope is at $z \sim 3$, and age gradients at $z \sim 5$ and $z < 0.5$ are both relatively flat. This corresponds with a mostly positive sSFR gradient for the non-merger sample, save for the lowest and highest redshift bins. Since the sSFR gradients are still positive, there are two main interpretations: MWAs may still be growing inside-out at $z < 2$, but there is good radial mixing of stars, or MWAs switch from inside-out growth to lockstep growth at all radii, and due to the sSFR decreasing globally at $z < 2$, the higher sSFR at the outer regions relative to the inner regions do not translate to a noticeable age difference in the age gradients.

- Metallicity gradients of non-mergers are typically flat or negative, but the average metallicity gradient is mildly positive at $2 < z < 3.5$. However, the average age gradients at those redshifts are still negative, and the most negative at all times, and the sSFR gradients are positive, which means the positive metallicity gradients do not contradict inside-out growth.

- For merging galaxies, age gradients are typically flat for ongoing and late stage mergers, but some redshift bins have average age gradients which are positive, and correspondingly negative sSFR gradients. This potentially points to enhanced star-formation in the central regions during the merging process.

- For ongoing mergers, the average age difference (in log Gyr) between the more massive and the less massive object is < 0.1 dex at every redshift bin, but there is a large scatter. There is almost no difference in the average metallicity between the more massive and less massive object in the ongoing mergers until $z \sim 1.5$, although again, there is a scatter of ~ 0.07 dex in the individual metallicity differences. This shows that typically, MWA mergers are usually between galaxies with similar star-formation histories, especially at $z > 1.5$.
- Although the merger components have relatively similar properties (except perhaps in sSFR), they are quite different in sSFR and age than the non-merger sample. Ongoing mergers are overall younger, have more star-formation enhancement, and slightly more metal-poor than non-mergers. Late stage mergers have properties in between ongoing mergers and non-mergers. Differences in metallicity and sSFR become more pronounced at lower redshift, but differences in age lessen.

Mergers may comprise $10 - 20\%$ of the MWA progenitor sample at any given redshift, which means that barring instances where mergers quench the galaxy, almost all MWAs in the local universe have experienced at least one merger. Our results show that mergers, especially before $z \sim 2$ do not appear to disrupt the inside-out picture of mass assembly for disk galaxies.

This research was supported by grant 18JWST-GTO1 and 23JWGO2A13 from the Canadian Space Agency (CSA), and funding from the Natural Sciences and Engineering Research Council of Canada (NSERC). The MAST DOI for CANUCS is doi:10.17909/ph4n-6n76. This research used the Canadian Advanced Network For Astronomy Research (CANFAR) operated in partnership by the Canadian Astronomy Data Centre and The Digital Research Alliance of Canada with support from the National Research Council of Canada the Canadian Space Agency, CANARIE, and the Canadian Foundation for Innovation.

4.8 Appendix

4.8.1 Radial profiles as a function of effective radius

For this study, we have done the bulk of the analysis with gradients scaled to dex/kpc. This is because our aim is to compare progenitor samples at different redshifts to show growth and evolution in the resolved properties, which is better served with physical units. However, many studies of resolved properties such as age and metallicity gradients present their results scaled to dex/R_{eff}, and the effective radius varies for each galaxy. In order to also draw proper comparisons to the literature, we plot the average (stacked and normalized) property gradients at each redshift bin as a function of

R_{eff}, shown in Figure 4.13. Each gradient is divided into elliptical annuli of width $0.1R_{eff}$ and the gradients ar plotted out to 3 R_{eff}. The effective radius for each galaxy is the circularized half-light radius from the CANUCS catalogs measured in Photutils on the F150W 20mas resolution image.

In Figure 4.14, we plot the slope evolution over redshift with the slopes in dex/R_{eff}, in a similar fashion to Figure 4.7. Overall, the average slopes for each redshift bin follow similar trends whether they were measured in kpc or in R_{eff}. However, the amplitude of the slope is larger in R_{eff}, and increases with decreasing redshift, which is the result of galaxies physically increasing in size. Interestingly, the property whose slopes exhibited the most change from scaling in dex/kpc to dex/R_{eff} are the sSFR slopes. The non-merger slopes for sSFR and age as a function of redshift seem to be more inversely related when scaled to R_{eff} than scaled to kpc. This potentially strengthens the interpretation that MWAs switch to lockstep growth at $z \sim 2$ rather than continue growing inside-out.

4.8.2 Dust Gradients and Age-Dust-Metallicity Degeneracy

Age, metallicity, and dust are three factors which can redden the spectrum of a galaxy. This is known as the age-dust-metallicty degeneracy. For degeneracy between age and metallicity, with modern multiband SED-fitting, it is possible for separation of age and metallicity without full spectral fitting (e.g. Lee et al. 2007; Eminian et al. 2008). This is because the bluer filters can probe the main-sequence turn off point to obtain age, while red and NIR filters are sensitive to the giant branch stars, which probe stellar metallicity (Bell & de Jong, 2000; MacArthur et al., 2004). However, the degeneracy between dust and metallicity remains, as well as age and dust for star-forming galaxies (The UVJ diagram can effectively separate quiescent and highly dusty star-forming galaxies, see Wuyts et al. 2007 and Williams et al. 2009). Modern SED-fitting codes use an energy balance model between UV and IR emission. The portion of IR emission coming from dust is balanced against the energy lost to attenuation from the UV (e.g. Burgarella et al. 2005; da Cunha et al. 2015; Salim et al. 2018; Jones & Stanway 2023). Although this energy balance is better constrained with far-IR data that is most sensitive to dust temperature and mass (Iyer et al., 2025), and we are limited to NIRCam and NIRISS data, it is still possible to show that the age-dust-metallicity degeneracy does not affect our results. If this degeneracy has a noticeable effect on the properties of galaxies, we would expect the radial profile of dust to be the *inverse* of either the age or the metallicity gradient. We test this by comparing the dust gradients against the gradients of the other degenerate properties below.

In the top panel of Figure 4.15, we plot each individual radial dust gradient scaled by kpc for our sample of MWA progenitors, separated into eight subplots by their redshift bin. The thin grey lines are non-mergers while the thin blue lines are mergers. The stacked and normalized average dust gradient plotted as the thicker colored line. As a comparison, the middle and bottom panels of Figure

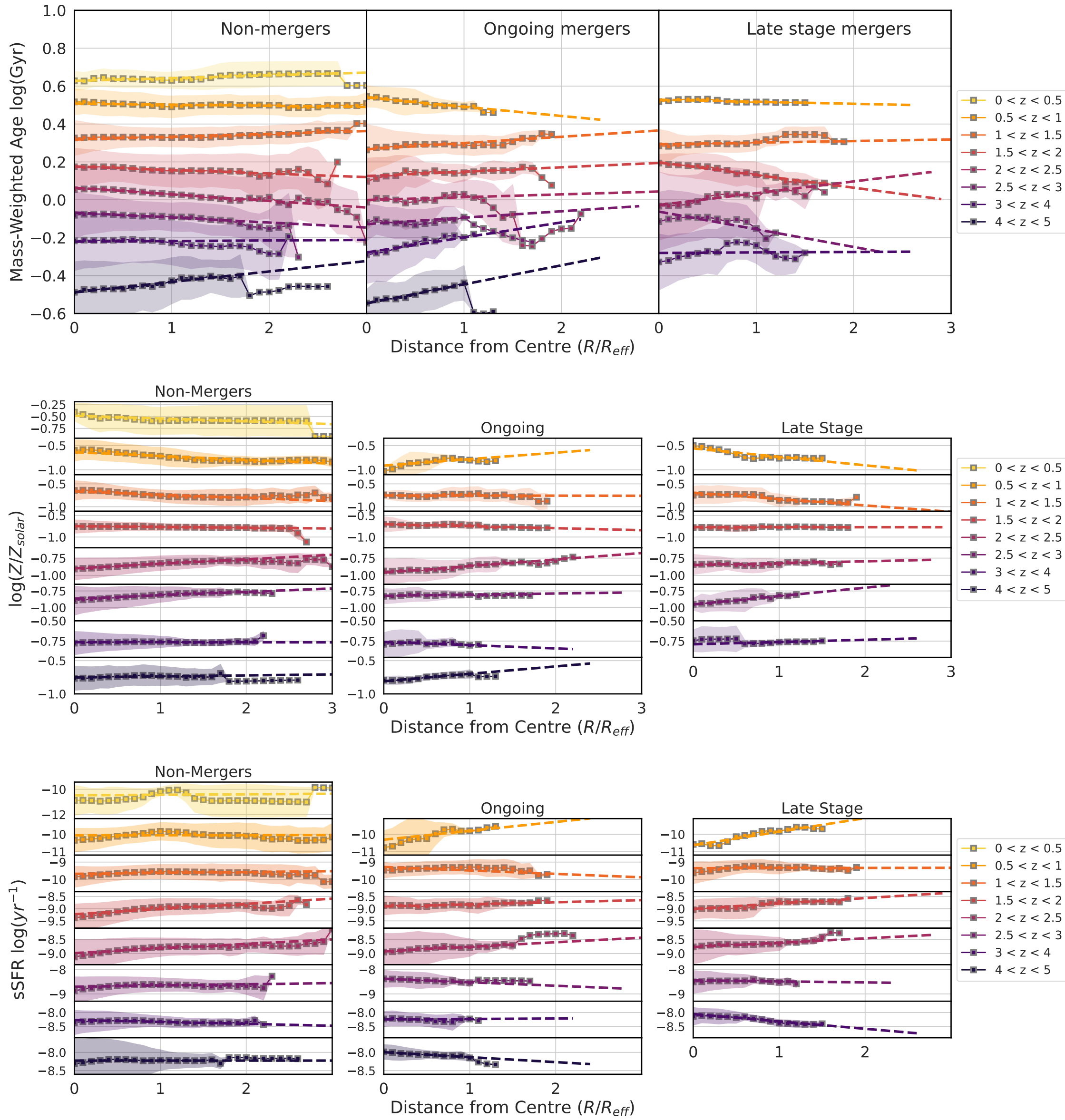

Figure 4.13: Stacked and normalized property gradients at each redshift bin, similar to Figures 4.4, 4.5 and 4.6, but as a function of the galaxy's effective radius (R_{eff}) instead of kpc.

4.15 is a similar plot for each individual *metallicity* and *mass-weighted age* gradient respectively, as well as their stacked and normalized average gradient at each redshift bin. Note that these average gradients is slightly different from the ones presented in Figures 4.4 and 4.5 because it is an average of both merger and non-merger samples, but it is very similar to the non-merger profiles because 756 out of the 904 objects in our sample are non-mergers). A typical $L_\star$ galaxy, which is a star-forming spiral at $z = 0$ and what the Milky Way is classified as, would have $A_V \sim 1$. The evolution of the A_V gradient with redshift for our sample is in line with what is expected for $L_\star$ galaxies. Outliers with $A_V \geq 1.25$, which is roughly 1σ above the average A_V consists of only 33 out of the total 904

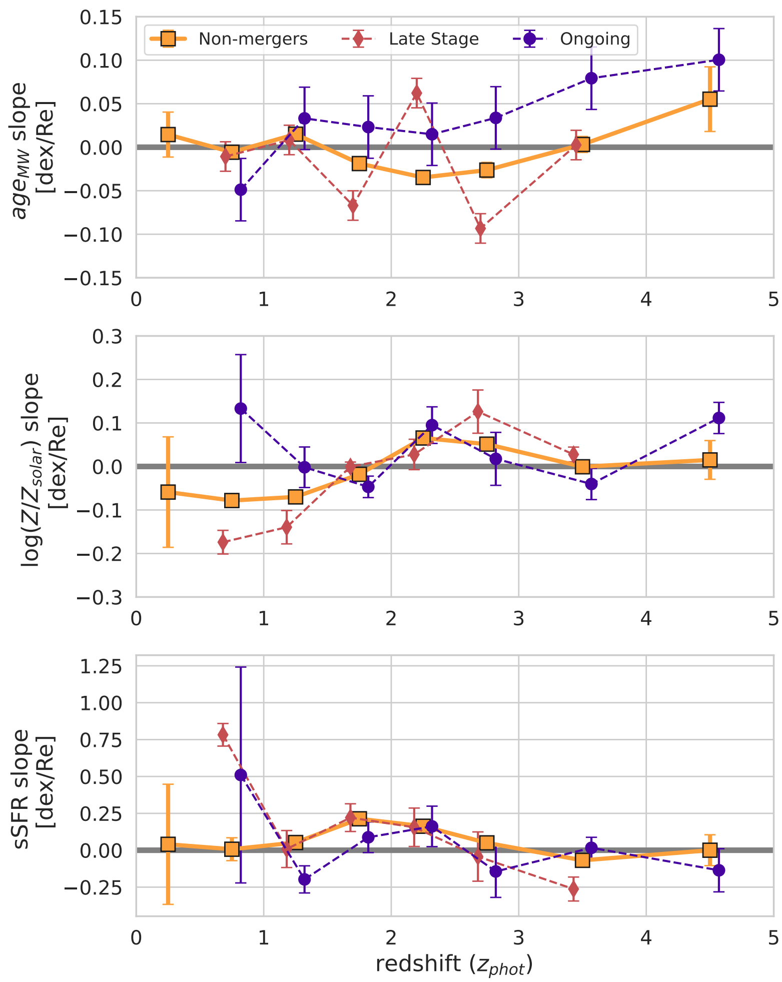

Figure 4.14: Slopes of property gradients as a function of redshift in units of dex/R_{eff}. Overall, the slopes have similar evolution with redshift, but the magnitude of the slope is larger when measured in R_{eff} than in kpc.

galaxies in our MWA progenitor sample.

The average dust gradient at each redshift shows that as a whole, dust gradients have slopes with amplitudes that are larger than the age and metallicity slopes. The gradients in each redshift bin also have slopes which *follow* the trend of the non-merger sample's metallicity slopes, instead of an inverse relationship, which one would expect if the dust and metallicity were degenerate. The dust slopes also do not have an inverse relationship with the age gradients. Merging galaxies tend to have lower A_V at all radii compared to non-merging galaxies (Only 2 of the 33 "dusty" outliers are mergers). Notably, this is not seen in the metallicity gradients, as mergers do not have particularly high or low metallicity compared to the non-merger sample (which was also shown in §4.4.3 and Figure 4.10 in §4.5.3. Mergers also tend to have younger ages than non-mergers, which would also not make sense if dust and age were degenerate, since if they were degenerate, we would expect mergers to either be younger and dustier, or older and less dusty. Since dust attenuation in A_V is generally not an issue for merging galaxies, this also means that the enhanced sSFR for ongoing mergers is also not affected by dust attenuation.

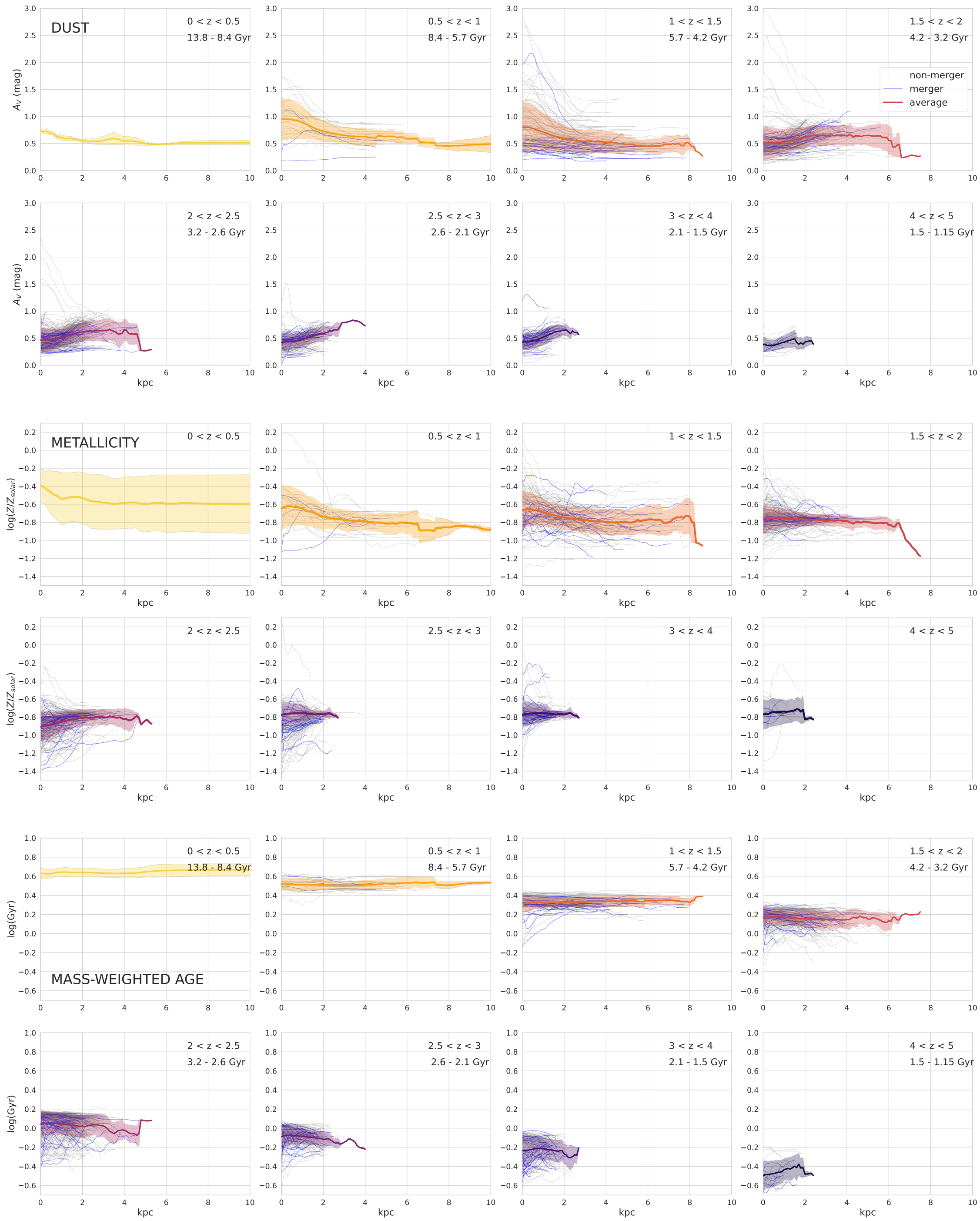

Figure 4.15: *Top panel:* The radial dust attentuation (A_V transmission) gradient of each galaxy in our sample, separated into eight redshift bins, as a function of kpc. Solid colored lines in each subplot represent the stacked and normalized average of that redshift bin. Shaded regions is the 1σ scatter, or the 18th-84th percentile. Thin grey lines are the individual dust gradients for non-mergers, thin blue lines are mergers. The values of A_V, accounting for the 18th-84th percentile scatter range from 0.25 to 1.25. *Middle and bottom panels:* Similar to the top panel but for metallicity in $\log(Z/Z_{\odot})$ and mass-weighted age in log(Gyr).

Chapter 5

Conclusions

In this thesis, we uncovered the spatially resolved properties of two samples of abundance matching selected Milky Way Analog progenitors. In Chapter 2, we used data from the Hubble Frontier Fields Deep Space catalogs to map out the mass assembly of MWA progenitors up to $z = 2$. We find evidence that on average, MWAs grow in lock step from cosmic noon to present day. In Chapter 3, we expanded the search for progenitors up to $z \sim 5$ with combined JWST and HST photometry from the Canadian NIRISS Unbiased Cluster Survey. Before cosmic noon, at the redshift range ($2 < z < 5$) MWA progenitors are assembling mass inside-out, shown in both the growth in $\Sigma_\star$ concentrated at larger radii at that redshift, as well as the sSFR profile's peak at the outskirts. The average Sérsic index does not change drastically, but the half-mass radii double in size. There are also higher merger fractions at high redshift, rising to $\sim 20\%$ at $4 < z < 5$. Star-forming clumps appear at low redshift, but contribute less to overall mass assembly. In Chapter 4, we determined the mass-weighted age and metallicity gradients of the MWA progenitors, and measured how their slopes evolved over redshift. We find that all MWA progenitors have mild age and metallicity gradients at all redshifts, however non-mergers are more likely to have mildly negative gradients (except for metallicity at cosmic noon) consistent with inside-out growth, while ongoing and late stage mergers tend to have flatter gradients at early times/higher redshift, and steeper gradients (both positive and negative) at later times/lower redshift. The specific star formation rate is more enhanced for mergers than non-mergers overall, indicating that the act of merging leads to a starburst.

5.1 Overview of the formation history of Milky Way-like galaxies

From the results of this thesis, a galaxy like the Milky Way could have began forming its disk as early as 12 Gyr in the past. Compared to disk galaxies of the present day, this disk would not have a strong potential as its stellar mass density may be $\Sigma_\star \sim 10^{8.5} M_\odot/\text{kpc}^2$ in the central regions, and even lower in the outskirts ($\Sigma_\star \sim 10^{6.5} M_\odot/\text{kpc}^2$). This means that the stellar feedback would be incredibly bursty (according to simulations such as Hopkins et al. 2023). At $4 < z < 5$, the region with the most star formation is the central 2 kpc (see Figures 3.6 and 3.7). As the disk grows inside out, the radial distance at which the maximum sSFR occurs also moves outwards (Figure 3.6 right panel and Figure 4.4for age gradients). This however, does not increase the outer $\Sigma_\star$ but rather decreases it (Fig. 3.7 left panel). As a result, the lack of a strong gravitational potential in the vertical plane leads to extreme outflows of metal-rich gas after episodes of intense star formation (Figure 4.5). Therefore at $2 < z < 4$, the initially mildly negative metallicity gradient flattens, or even turn positive, as star formation on the outskirts are more likely to incorporate the metal-rich outflows into its stellar population.

Some time between 12 to 8 Gyr, this galaxy will experience at least one major merger event that enhances its SFR from tidal interactions and gas mixing (see Figures 4.6 and 4.10). However, both galaxies will most likely have similar ages and metallicities such that ultimately, the merger does not affect the *overall* metallicity of this galaxy, apart from a starburst that led to many newly formed stars that can be traced back to a singular star formation event (i.e. the spike in ages of stars in the thick disk and halo at ~ 10 Gyr due to the GSE merger).

Right after cosmic noon, this hypothetical galaxy starts to grow both the central regions and the outer regions at the same rate (Figures 2.9, 2.11, and 3.7). The cause of this may be that the gas fraction in the galaxy has dropped such that star formation switches from bursty to smooth. Essentially, the mass density has increased enough that the potential in the vertical direction for the disk is strong enough to regulate feedback. The increase in the potential may also be the mechanism that switches inside-out growth to lockstep growth. The mass density in both regions increase more or less at the same rate. The deeper potential is able to regulate outflows, so metal-rich gas remains in the ISM and is recycled back into new stars.

After cosmic noon ($z < 2$), SFRs globally begin to decline, so although there is still more specific star formation on the outskirts, the amount of newly formed stellar mass added is much less compared to the stars that already exist. However, since active star formation will necessarily involve more inflows of metal poor gas, the metallicity gradient becomes mildly negative once more. The Sérsic index changes at $z < 2$, and increases from $n \sim 1.2 - 1.5$ to $n \sim 2.5$ (Figures 2.12 and 3.9), meaning the central regions become more concentrated, and the bulge grows. Since sSFR is lower in the central regions than the outskirts, some of the bulge growth would be from secular processes, which may radially mix the stars. This results in the age gradient flattening (Fig. 4.4). Eventually, in the local universe, this disk galaxy would be mildly star-forming or in the green valley, with most of its star formation occurring in the thin disk. It will likely have a mildly negative radial metallicity gradient, and a mildly negative age gradient.

5.2 Future Work

This thesis offers the big picture look at the evolution and mass assembly of galaxies similar to the Milky Way. In order to delve into the specifics, there are higher resolution measurements which can be made to complete the picture at different redshift ranges. Spectroscopic follow-up of subsamples with good signal-to-noise, or targeting lensed MWA progenitors will give us the data required for more a more detailed analysis of the star formation history of MWAs. This big picture analysis can also be extended to higher redshifts, such as the epoch of reionization at $z \gtrsim 6$ with data of greater depth, such as from JADES.

5.2.1 Spectroscopic followup for gas-phase metallicity

A natural question that arises from Chapter 4 is how does the gas phase metallicity evolve with redshift for MWAs. Gas phase metallicity is intrinsically tied to feedback mechanisms of galaxies, and considering that high redshift galaxies are more gas rich, the gas phase becomes a complementary measurement to the stellar metallicities we already have. In order to obtain gas phase metallicity, we would need spectroscopic data such as emission line ratios such as [NII]/Hα. Fortunately, CANUCS has NIRISS slitless spectroscopy for two of the cluster fields. Astrada-Carpenter et al. (in prep) has done such a study with $z \sim 1 - 2$ clumpy galaxies at cosmic noon. They compared gas phase metallicity of the clumps against the host galaxy and found that gas phase metallicities are lower for star forming clumps. A similar study can be performed for MWAs that have NIRISS data in those fields. SED-fitting to spectra can also better determine the stellar metallicity derived from the continuum.

Spectroscopy can also provide kinematic data of the gas, which could confirm whether outflows from star-formation are indeed stronger early in the universe. Gas kinematics can also determine if inflows of metal poor/pristine gas to the centers of galaxies is responsible for the steeper positive stellar metallicities seen in our merger samples. Comparisons between mergers and non-mergers could reveal how merging changes or enhances gas inflows/outflows, and which regions of the galaxies they affect the most. Unfortunately, NIRISS is not powerful enough for kinematic studies, so this would require NIRSpec IFU spectroscopy. Depending on the redshift of the MWA progenitor, lensed galaxies may be needed to provide enough S/N for kinematic data.

5.2.2 Abundance ratios

A useful avenue to further expand this research would be to determine the α-element abundances of MWA progenitors at various redshifts. One of the key pieces of information we have about the galaxy that merged with the Milky Way in the GSE merger is that the remnants of the merged galaxy have different abundances of α-elements, pointing to a different star formation history than stars originally born in the Milky Way. These abundance ratios may not be obvious when considering an overall metallicity measurement, because the latter is the ratio of all metals against hydrogen (i.e. [Z/H]). Measuring an alpha abundance, such as [Mg/Fe], similar to what is done within the Milky Way, would uncover such distinctions in the metallicity. Similar work has been done for massive quiescent galaxies in Cheng et al. (2024a). Measuring [Mg/Fe] does require SED-fitting codes specifically made for determining abundance ratios from spectral features, such as ALF ("absorption line fitting", Conroy & van Dokkum 2012; Conroy et al. 2018). Again, we emphasize that progenitors of MWAs, even at $1 < z < 3$ would not have enough S/N for abundance ratio determination. However, a lensing sample with magnifications of $\mu = 20 - 40$ could make this measurement possible.

5.2.3 Expand to higher redshift with JADES, compare to other progenitors with MINERVA

In terms of non-lensing extensions, there exist a large number of galaxies at $3.5 < z < 5$ which are identified as MWA progenitors by abundance matching, but do not have enough S/N to be part of our resolved sample. The JADES survey contains fields that are deeper than CANUCS, such as the JADES Origin Field (Eisenstein et al., 2023) with up to 46 hours integration time in nine filters. At the photometric redshift $5 < z < 8$, some pointings in F444W reach AB magnitude 30. This could provide $S/N = 5$ per bin for spatially resolved property maps at that redshift. With more lower mass and lower SFR galaxies added to the higher-z end of the progenitor sample, we can examine if our initial assumptions about star formation being burstier at high redshift also holds for lower mass systems. Additionally, utilizing the JADES Origin Field could extend the redshift limit of integrated $S/N = 30$ or $S/N \sim 5$ per bin possibly to $z \sim 7$, which would be during the epoch of reionization. The JADES fields also have medium band imaging, which is better at constraining the stellar mass and SFRs of galaxies with extreme emission lines (Sarrouh et al., 2024), which are far more common at higher redshifts (Withers et al., 2023). This could bridge the gap between our redshift limit of $z = 5$ to objects such as the Firefly Sparkle, a possible MWA progenitor at $z \sim 8$, from Mowla et al. (2024).

Another possible avenue to explore is the comparison of the progenitors of more massive, ellipticals with the progenitors of Milky Way mass galaxies. Not only is the Milky Way in the green valley considering its current SFR, the mass of the Milky Way also places it in between the average mass of galaxies in the red sequence ($M_\star > 10^{11} M_\odot$ ellipticals), and the blue cloud ($M_\star < 10^{10} M_\star$ star-forming galaxies such as the LMC) . This would be similar to the work done in Hill et al. (2017a) but using JWST photometry and an SED-fitting code with non-parametric SFHs, which as shown in this work, are better equipped to determine SFR and ages. The upcoming MINERVA survey is ~ 1 magnitude shallower than CANUCS, but covers more area, allowing for comparable numbers of progenitors of quiescent galaxies to the number of MWA progenitors in this thesis.

5.2.4 Barred galaxies at high redshift

The Milky Way is a barred spiral, and the bar is an important structure in the inner regions of our galaxy. As mentioned in §1.2, at time of writing, how the Milky Way's bulge formed and its relationship to the formation of the bar is still an area of active research. Recent observations from JWST have discovered barred disk galaxies at redshifts up to $z \sim 4$ (e.g. Guo et al. 2023; Le Conte et al. 2024; Géron et al. 2025). One caveat is that galaxies with detected bars at high redshift are generally more massive ($M_\star \sim 10^{10} M_\odot$) than progenitors of the Milky Way. Determining when a MWA progenitor could have started forming a bar, and why certain MWA progenitors do or do not form bars may be very revealing. One method for obtaining a measurement of the bar fraction of MWA progenitors would be to perform a citizen science study (e.g. via Galaxy Zoo, which was done in Géron et al. 2025) with an abundance-matching selected sample of MWA progenitors, or to see which galaxies which are already classified as barred or unbarred are within the mass range of a MWA progenitor. Machine learning approaches can be used on extremely large data sets for determining bar fractions, with proper validation checks in place performed by researchers.

Another reason to study bars at high redshift is that simulations show that bars develop through secular processes within the disk. One of the key ideas is that bars drive radial mixing of stars in the disk. Sánchez-Blázquez et al. (2014) measured the metallicity and age gradients of barred versus unbarred galaxies in the local universe to determine if barred galaxies had flatter property gradients, which may be a result of radial mixing of stars. They did not find any difference between barred and unbarred galaxies. However, this measurement has not been made for the high redshift universe. At cosmic noon, galaxies in general have flatter gradients than at lower redshift, although bar fraction studies show decreased instances of bars as redshift increases (Géron et al., 2025). A study of the gradients of barred and unbarred galaxies at higher redshifts may resolve the issue of radial mixing as well as other lingering questions, such as if young bars may have stronger gradients than older bars.

5.3 Final thoughts

With the work done in this thesis, I have offered a big picture analysis of the ways that a typical Milky Way Analogue may have grown and evolved over the last 12.5 billion years of cosmic evolution. This resolved analysis allows direct comparisons with resolved studies in the local universe and even within the Milky Way itself. We have learned that the inside-out model of stellar mass growth used in many simulations is accurate for MWA progenitors at the redshift range $2 < z < 5$, which is from the end of reionization to the peak of cosmic star formation at cosmic noon. We have also learned that inside out growth slows or becomes more lock step growth at the redshift range $0 < z < 2$, which is when star formation rates decline globally, and possibly when disk galaxies switch from extreme feedback and bursty star formation to smooth and regulated star formation. We have also learned that mergers should play an important role in mass assembly as they become more common at high redshift, and the act of merging, especially between more gas rich high redshift progenitors, can enhance star formation above the general SFR without merging. The next steps to take are to complete the picture at specific epochs with other types of data, especially spectroscopic data, that could clarify remaining questions such as gas metallicity, kinematics, and perhaps even abundance ratios. Expanding the current method of analysis to higher redshift could also reveal when the transition is between hierarchical assembly of protogalaxies to the beginning of inside-out disk formation. With higher resolution and signal-to-noise from deeper surveys like JADES, this can also allow us to probe the lower mass end of the MWA progenitors in the redshift ranges we currently cover. The future of research into MWA mass assembly could hopefully answer crucial questions such as the formation of the bulge and bar, and a more detailed look into kinematics of merging progenitors as well as high redshift feedback mechanisms.

Appendix A

Priors and Parameter boundaries for SED-fitting

In this appendix, we include three tables with parameter and prior boundaries for the three chapters that make up this work. The first table is for Chapter 2, which uses FAST, a parametric SED-fitting code. The second and third tables are for Chapters 3 and 4 respectively, which use Dense Basis, a code with non-parametric SFHs that fits SEDs from a pregrid atlas generated from priors.

Table A.1: Parameters for SED-fitting with FAST (for stellar mass) and EAZY (L_{UV} for SFR) in Chapter 2.

Parameter	FAST		EAZY (if different from FAST)	
	range	Prior type	range	Prior type
AB Zeropoint	25		–	–
SFH		delayed exponential	–	–
		$\mathrm{SFR}(t) = t\exp(\tau/t)$	–	–
$log(\tau/\mathrm{yr})$	(6.5, 11)		–	–
log(age/yr)	(6.0, 11)		–	–
Z	0.02 (solar)	fixed	–	–
z	(0.01, 12)	flat	(0.01, 6)	flat
A_V	(0, 6)	flat	–	–
SPS Library		Bruzual & Charlot (2003)		Conroy & Gunn (2010)
Dust Law		Calzetti et al. (2000)	–	–
IMF		Chabrier (2003)	–	–

Table A.2: Parameters and prior ranges for SED-fitting with Dense Basis in Chapter 3. Note these are the same priors as the CANUCS DR1 catalogs as that chapter uses the same atlases as the catalog.

Parameter	Range	Prior
log M_*	(7, 12)	flat
log sSFR	(-14,-7)	flat
α_{SFH}	3 (at t_{25}, t_{50}, and t_{75})	Dirichlet
log $Z/Z_\odot$	(-1.5, 0.25)	flat
z	(0.005,12)	flat
A_V	(0, 4)	exp
SPS Library		Conroy & Gunn (2010)
Dust Law		Calzetti et al. (2000)
IMF		Chabrier (2003)

Table A.3: Parameters and prior ranges for SED-fitting with Dense Basis in Chapter 4. Since we are no longer using the atlases from the CANUCS DR1 catalog, we create new atlas pregrids using the priors below.

Parameter	Range	Prior
log M_*	(6, 12)	flat
log sSFR	(-13,-6)	flat
α_{SFH}	3 (at t_{25}, t_{50}, and t_{75})	Dirichlet
log $Z/Z_\odot$	(-2.5, 0.3)	flat
z	(0.001,5)	flat
A_V	(0, 4)	flat
SPS Library		Conroy & Gunn (2010)
Dust Law		Calzetti et al. (2000)
IMF		Chabrier (2003)

Bibliography

Abadi, M. G., Navarro, J. F., Steinmetz, M., & Eke, V. R. 2003a, Astrophys. J., 597, 21, doi: 10.1086/378316

—. 2003b, Astrophys. J., 591, 499, doi: 10.1086/375512

Abdurro'uf, Lin, Y.-T., Wu, P.-F., & Akiyama, M. 2021, Astrophys. J. Suppl. Ser., 254, 15, doi: 10.3847/1538-4365/abebe2

Abdurro'uf, Accetta, K., Aerts, C., et al. 2022, Astrophys. J. Suppl. Ser., 259, 35, doi: 10.3847/1538-4365/ac4414

Abdurro'uf, Coe, D., Jung, I., et al. 2023, Astrophys. J., 945, 117, doi: 10.3847/1538-4357/acba06

Abraham, R. G., van den Bergh, S., & Nair, P. 2003, Astrophys. J., 588, 218, doi: 10.1086/373919

Adamo, A., Bradley, L. D., Vanzella, E., et al. 2024, arXiv e-prints, arXiv:2401.03224, doi: 10.48550/arXiv.2401.03224

Ahumada, R., Allende Prieto, C., Almeida, A., et al. 2020, Astrophys. J. Suppl. Ser., 249, 3, doi: 10.3847/1538-4365/ab929e

Aihara, H., Allende Prieto, C., An, D., et al. 2011, Astrophys. J. Suppl. Ser., 193, 29, doi: 10.1088/0067-0049/193/2/29

Akhshik, M., Whitaker, K. E., Leja, J., et al. 2023, Astrophys. J., 943, 179, doi: 10.3847/1538-4357/aca677

Allen, J. T., Croom, S. M., Konstantopoulos, I. S., et al. 2015, Mon. Not. R. Astron. Soc., 446, 1567, doi: 10.1093/mnras/stu2057

Antwi-Danso, J., Papovich, C., Leja, J., et al. 2023, Astrophys. J., 943, 166, doi: 10.3847/1538-4357/aca294

Asada, Y., Sawicki, M., Abraham, R., et al. 2024a, Mon. Not. R. Astron. Soc., 527, 11372, doi: 10.1093/mnras/stad3902

Asada, Y., Desprez, G., Willott, C. J., et al. 2024b, arXiv e-prints, arXiv:2410.21543, doi: 10.48550/arXiv.2410.21543

Athanassoula, E., Rodionov, S. A., & Prantzos, N. 2017, Mon. Not. R. Astron. Soc., 467, L46, doi: 10.1093/mnrasl/slw255

Bahcall, J. N., & Soneira, R. M. 1984, Astrophys. J. Suppl. Ser., 55, 67, doi: 10.1086/190948

Barbuy, B., Chiappini, C., & Gerhard, O. 2018, Annu. Rev. Astron. Astrophys., 56, 223, doi: 10.1146/annurev-astro-081817-051826

Behroozi, P. S., Marchesini, D., Wechsler, R. H., et al. 2013a, Astrophys. J. Lett., 777, L10, doi: 10.1088/2041-8205/777/1/L10

Behroozi, P. S., Wechsler, R. H., & Conroy, C. 2013b, Astrophys. J., 770, 57, doi: 10.1088/0004-637X/770/1/57

Belfiore, F., Maiolino, R., Tremonti, C., et al. 2017, Mon. Not. R. Astron. Soc., 469, 151, doi: 10.1093/mnras/stx789

Bell, E. F., & de Jong, R. S. 2000, Mon. Not. R. Astron. Soc., 312, 497, doi: 10.1046/j.1365-8711.2000.03138.x

Bell, E. F., McIntosh, D. H., Katz, N., & Weinberg, M. D. 2003, Astrophys. J. Suppl. Ser., 149, 289, doi: 10.1086/378847

Belli, S., Newman, A. B., & Ellis, R. S. 2019, Astrophys. J., 874, 17, doi: 10.3847/1538-4357/ab07af

Belokurov, V. 2013, New Astron. Rev., 57, 100, doi: 10.1016/j.newar.2013.07.001

Belokurov, V., Erkal, D., Evans, N. W., Koposov, S. E., & Deason, A. J. 2018, Mon. Not. R. Astron. Soc., 478, 611, doi: 10.1093/mnras/sty982

Belokurov, V., & Kravtsov, A. 2022, Mon. Not. R. Astron. Soc., 514, 689, doi: 10.1093/mnras/stac1267

Benincasa, S. M., Loebman, S. R., Wetzel, A., et al. 2020, Mon. Not. R. Astron. Soc., 497, 3993, doi: 10.1093/mnras/staa2116

Bensby, T., Feltzing, S., & Lundström, I. 2003, Astron. Astrophys., 410, 527, doi: 10.1051/0004-6361:20031213

Bertin, E., & Arnouts, S. 1996, Astron. Astrophys. Suppl. Ser., 117, 393, doi: 10.1051/aas:1996164

Bezanson, R., van Dokkum, P. G., Franx, M., et al. 2011, Astrophys. J. Lett., 737, L31, doi: 10.1088/2041-8205/737/2/L31

Bignone, L. A., Helmi, A., & Tissera, P. B. 2019, Astrophys. J. Lett., 883, L5, doi: 10.3847/2041-8213/ab3e0e

Bird, J. C., Kazantzidis, S., Weinberg, D. H., et al. 2013, Astrophys. J., 773, 43, doi: 10.1088/0004-637X/773/1/43

Bland-Hawthorn, J. 1999, Nature, 400, 220, doi: 10.1038/22230

Bland-Hawthorn, J., & Gerhard, O. 2016, Annu. Rev. Astron. Astrophys., 54, 529, doi: 10.1146/annurev-astro-081915-023441

Blanton, M. R., Bershady, M. A., Abolfathi, B., et al. 2017, Astron. J., 154, 28, doi: 10.3847/1538-3881/aa7567

Blumenthal, G. R., Faber, S. M., Primack, J. R., & Rees, M. J. 1984, Nature, 311, 517, doi: 10.1038/311517a0

Boardman, N., Zasowski, G., Seth, A., et al. 2020a, Mon. Not. R. Astron. Soc., 491, 3672, doi: 10.1093/mnras/stz3126

Boardman, N., Zasowski, G., Newman, J. A., et al. 2020b, Mon. Not. R. Astron. Soc., 498, 4943, doi: 10.1093/mnras/staa2731

Bovy, J., & Rix, H.-W. 2013, Astrophys. J., 779, 115, doi: 10.1088/0004-637X/779/2/115

Bovy, J., Rix, H.-W., & Hogg, D. W. 2012, Astrophys. J., 751, 131, doi: 10.1088/0004-637X/751/2/131

Bradač, M., Treu, T., Applegate, D., et al. 2009, Astrophys. J., 706, 1201, doi: 10.1088/0004-637X/706/2/1201

Bradley, L., Sipocz, B., Robitaille, T., et al. 2016, Photutils: Photometry tools, Astrophysics Source Code Library, record ascl:1609.011

Bradley, L., Sipőcz, B., Robitaille, T., et al. 2023, astropy/photutils: 1.10.0, 1.10.0, Zenodo, doi: 10.5281/zenodo.1035865

Bradley, L. D., Adamo, A., Vanzella, E., et al. 2024, arXiv e-prints, arXiv:2404.10770, doi: 10.48550/arXiv.2404.10770

Brammer, G. B., van Dokkum, P. G., & Coppi, P. 2008, Astrophys. J., 686, 1503, doi: 10.1086/591786

Brammer, G. B., Whitaker, K. E., van Dokkum, P. G., et al. 2011, Astrophys. J., 739, 24, doi: 10.1088/0004-637X/739/1/24

Brennan, R., Pandya, V., Somerville, R. S., et al. 2015, Mon. Not. R. Astron. Soc., 451, 2933, doi: 10.1093/mnras/stv1007

Bressan, A., Marigo, P., Girardi, L., et al. 2012, Mon. Not. R. Astron. Soc., 427, 127, doi: 10.1111/j.1365-2966.2012.21948.x

Brook, C. B., Kawata, D., Gibson, B. K., & Freeman, K. C. 2004, Astrophys. J., 612, 894, doi: 10.1086/422709

Bruzual, G. 1983, Astrophys. J., 273, 105, doi: 10.1086/161352

Bruzual, G., & Charlot, S. 2003, Mon. Not. R. Astron. Soc., 344, 1000, doi: 10.1046/j.1365-8711.2003.06897.x

Buck, T., Obreja, A., Macciò, A. V., et al. 2020, Mon. Not. R. Astron. Soc., 491, 3461, doi: 10.1093/mnras/stz3241

Bundy, K., Bershady, M. A., Law, D. R., et al. 2015, Astrophys. J., 798, 7, doi: 10.1088/0004-637X/798/1/7

Burgarella, D., Buat, V., & Iglesias-Páramo, J. 2005, Mon. Not. R. Astron. Soc., 360, 1413, doi: 10.1111/j.1365-2966.2005.09131.x

Calzetti, D., Armus, L., Bohlin, R. C., et al. 2000, Astrophys. J., 533, 682, doi: 10.1086/308692

Cappellari, M. 2013, Astrophys. J. Lett., 778, L2, doi: 10.1088/2041-8205/778/1/L2

Cappellari, M., & Copin, Y. 2003, Mon. Not. R. Astron. Soc., 342, 345, doi: 10.1046/j.1365-8711.2003.06541.x

Carnall, A. C., Cullen, F., McLure, R. J., et al. 2024, Mon. Not. R. Astron. Soc., 534, 325, doi: 10.1093/mnras/stae2092

Carollo, D., Chiba, M., Ishigaki, M., et al. 2019, Astrophys. J., 887, 22, doi: 10.3847/1538-4357/ab517c

Chabrier, G. 2003, Publ. Astron. Soc. Pac., 115, 763, doi: 10.1086/376392

Cheng, C. M., Kriek, M., Beverage, A. G., et al. 2024a, Mon. Not. R. Astron. Soc., 532, 3604, doi: 10.1093/mnras/stae1739

Cheng, J. Y., Rockosi, C. M., Morrison, H. L., et al. 2012, Astrophys. J., 746, 149, doi: 10.1088/0004-637X/746/2/149

Cheng, X., Anguiano, B., Majewski, S. R., & Arras, P. 2024b, Mon. Not. R. Astron. Soc., 527, 959, doi: 10.1093/mnras/stad3013

Chiappini, C., Matteucci, F., & Gratton, R. 1997, Astrophys. J., 477, 765, doi: 10.1086/303726

Choi, J., Dotter, A., Conroy, C., et al. 2016, Astrophys. J., 823, 102, doi: 10.3847/0004-637X/823/2/102

Ciucă, I., Kawata, D., Ting, Y.-S., et al. 2024, Mon. Not. R. Astron. Soc., 528, L122, doi: 10.1093/mnrasl/slad033

Cole, S., Norberg, P., Baugh, C. M., et al. 2001, Mon. Not. R. Astron. Soc., 326, 255, doi: 10.1046/j.1365-8711.2001.04591.x

Combes, F., Debbasch, F., Friedli, D., & Pfenniger, D. 1990, Astron. Astrophys., 233, 82

Conroy, C. 2013, Annu. Rev. Astron. Astrophys., 51, 393, doi: 10.1146/annurev-astro-082812-141017

Conroy, C., & Gunn, J. E. 2010, Astrophys. J., 712, 833, doi: 10.1088/0004-637X/712/2/833

Conroy, C., & van Dokkum, P. 2012, Astrophys. J., 747, 69, doi: 10.1088/0004-637X/747/1/69

Conroy, C., Villaume, A., van Dokkum, P. G., & Lind, K. 2018, Astrophys. J., 854, 139, doi: 10.3847/1538-4357/aaab49

Conselice, C. J. 2003, Astrophys. J. Suppl. Ser., 147, 1, doi: 10.1086/375001

Conselice, C. J., Bershady, M. A., & Jangren, A. 2000, Astrophys. J., 529, 886, doi: 10.1086/308300

Costantin, L., Pérez-González, P. G., Guo, Y., et al. 2023, Nature, 623, 499, doi: 10.1038/s41586-023-06636-x

Cowie, L. L., Songaila, A., Hu, E. M., & Cohen, J. G. 1996, Astron. J., 112, 839, doi: 10.1086/118058

Cresci, G., Mannucci, F., Maiolino, R., et al. 2010, Nature, 467, 811, doi: 10.1038/nature09451

Cunha, K., Frinchaboy, P. M., Souto, D., et al. 2016, Astronomische Nachrichten, 337, 922, doi: 10.1002/asna.201612398

Curir, A., Lattanzi, M. G., Spagna, A., et al. 2012, Astron. Astrophys., 545, A133, doi: 10.1051/0004-6361/201118558

Curti, M., Maiolino, R., Cirasuolo, M., et al. 2020, Mon. Not. R. Astron. Soc., 492, 821, doi: 10.1093/mnras/stz3379 da Cunha, E., Walter, F., Smail, I. R., et al. 2015, Astrophys. J., 806, 110, doi: 10.1088/0004-637X/806/1/110

Davidzon, I., Ilbert, O., Laigle, C., et al. 2017, Astron. Astrophys., 605, A70, doi: 10.1051/0004-6361/201730419

Davis, M., Efstathiou, G., Frenk, C. S., & White, S. D. M. 1985, Astrophys. J., 292, 371, doi: 10.1086/163168

de Rossi, M. E., Tissera, P. B., De Lucia, G., & Kauffmann, G. 2009, Mon. Not. R. Astron. Soc., 395, 210, doi: 10.1111/j.1365-2966.2009.14560.x

Dekel, A., Birnboim, Y., Engel, G., et al. 2009, Nature, 457, 451, doi: 10.1038/nature07648

DESI Collaboration, Aghamousa, A., Aguilar, J., et al. 2016, arXiv e-prints, arXiv:1611.00036, doi: 10.48550/arXiv.1611.00036

Desprez, G., Martis, N. S., Asada, Y., et al. 2024, Mon. Not. R. Astron. Soc., 530, 2935, doi: 10.1093/mnras/stae1084

Duan, Q., Li, Q., Conselice, C. J., et al. 2024, arXiv e-prints, arXiv:2411.04944, doi: 10.48550/arXiv.2411.04944

Duncan, K., Conselice, C. J., Mundy, C., et al. 2019, Astrophys. J., 876, 110, doi: 10.3847/1538-4357/ab148a

Efremov, Y. N. 2011, Astronomy Reports, 55, 108, doi: 10.1134/S1063772911020016

Eggen, O. J., Lynden-Bell, D., & Sandage, A. R. 1962, Astrophys. J., 136, 748, doi: 10.1086/147433

Eisenstein, D. J., Johnson, B. D., Robertson, B., et al. 2023, arXiv e-prints, arXiv:2310.12340, doi: 10.48550/arXiv.2310.12340

Eldridge, J. J., Stanway, E. R., Xiao, L., et al. 2017, Proc. Astron. Soc. Aust., 34, e058, doi: 10.1017/pasa.2017.51

Elia, D., Evans, N. J., Soler, J. D., et al. 2025, Astrophys. J., 980, 216, doi: 10.3847/1538-4357/adaeb2

Elmegreen, D. M., Elmegreen, B. G., Ravindranath, S., & Coe, D. A. 2007, Astrophys. J., 658, 763, doi: 10.1086/511667

Emerson, J. P., Sutherland, W. J., McPherson, A. M., et al. 2004, The Messenger, 117, 27

Eminian, C., Kauffmann, G., Charlot, S., et al. 2008, Mon. Not. R. Astron. Soc., 384, 930, doi: 10.1111/j.1365-2966.2007.12742.x

Engler, C., Pillepich, A., Joshi, G. D., et al. 2023, Mon. Not. R. Astron. Soc., 522, 5946, doi: 10.1093/mnras/stad1357

Estrada-Carpenter, V., Sawicki, M., Brammer, G., et al. 2024, Mon. Not. R. Astron. Soc., 532, 577, doi: 10.1093/mnras/stae1368

Faber, S. M. 1973, Astrophys. J., 179, 731, doi: 10.1086/151912

Falcón-Barroso, J., Sánchez-Blázquez, P., Vazdekis, A., et al. 2011, Astron. Astrophys., 532, A95, doi: 10.1051/0004-6361/201116842

Förster Schreiber, N. M., Genzel, R., Bouché, N., et al. 2009, Astrophys. J., 706, 1364, doi: 10.1088/0004-637X/706/2/1364

Fragos, T., Andrews, J. J., Bavera, S. S., et al. 2023, Astrophys. J. Suppl. Ser., 264, 45, doi: 10.3847/1538-4365/ac90c1

Frankel, N., Sanders, J., Rix, H.-W., Ting, Y.-S., & Ness, M. 2019, Astrophys. J., 884, 99, doi: 10.3847/1538-4357/ab4254

Fraser-McKelvie, A., Merrifield, M., & Aragón-Salamanca, A. 2019, Mon. Not. R. Astron. Soc., 489, 5030, doi: 10.1093/mnras/stz2493

Frebel, A., & Norris, J. E. 2015, Annu. Rev. Astron. Astrophys., 53, 631, doi: 10.1146/annurev-astro-082214-122423

Freeman, K., & Bland-Hawthorn, J. 2002, Annu. Rev. Astron. Astrophys., 40, 487, doi: 10.1146/annurev.astro.40.060401.093840

Freeman, K., Ness, M., Wylie-de-Boer, E., et al. 2013, Mon. Not. R. Astron. Soc., 428, 3660, doi: 10.1093/mnras/sts305

Fuhrmann, K. 2011, Mon. Not. R. Astron. Soc., 414, 2893, doi: 10.1111/j.1365-2966.2011.18476.x

Gadotti, D. A. 2009, Mon. Not. R. Astron. Soc., 393, 1531, doi: 10.1111/j.1365-2966.2008.14257.x

Gaia Collaboration, Brown, A. G. A., Vallenari, A., et al. 2018, Astron. Astrophys., 616, A1, doi: 10.1051/0004-6361/201833051

Gallart, C., Bernard, E. J., Brook, C. B., et al. 2019, Nature Astronomy, 3, 932, doi: 10.1038/s41550-019-0829-5

Garrison-Kimmel, S., Hopkins, P. F., Wetzel, A., et al. 2018, Mon. Not. R. Astron. Soc., 481, 4133, doi: 10.1093/mnras/sty2513

Gavazzi, G., Fumagalli, M., Fossati, M., et al. 2013, Astron. Astrophys., 553, A89, doi: 10.1051/0004-6361/201218789

Gavazzi, G., Pierini, D., & Boselli, A. 1996, Astron. Astrophys., 312, 397

Genovali, K., Lemasle, B., Bono, G., et al. 2014, Astron. Astrophys., 566, A37, doi: 10.1051/0004-6361/201323198

Géron, T., Smethurst, R. J., Dickinson, H., et al. 2025, arXiv e-prints, arXiv:2505.01421, doi: 10.48550/arXiv.2505.01421

Gilmore, G., & Reid, N. 1983, Mon. Not. R. Astron. Soc., 202, 1025, doi: 10.1093/mnras/202.4.1025

Giménez-Arteaga, C., Oesch, P. A., Brammer, G. B., et al. 2023, Astrophys. J., 948, 126, doi: 10.3847/1538-4357/acc5ea

Gledhill, R., Strait, V., Desprez, G., et al. 2024, arXiv e-prints, arXiv:2403.07062, doi: 10.48550/arXiv.2403.07062

Goddard, D., Thomas, D., Maraston, C., et al. 2017, Mon. Not. R. Astron. Soc., 466, 4731, doi: 10.1093/mnras/stw3371

González Delgado, R. M., García-Benito, R., Pérez, E., et al. 2015, Astron. Astrophys., 581, A103, doi: 10.1051/0004-6361/201525938

Grand, R. J. J., Gómez, F. A., Marinacci, F., et al. 2017, Mon. Not. R. Astron. Soc., 467, 179, doi: 10.1093/mnras/stx071

Grazian, A., Fontana, A., Santini, P., et al. 2015, Astron. Astrophys., 575, A96, doi: 10.1051/0004-6361/201424750

Grogin, N. A., Kocevski, D. D., Faber, S. M., et al. 2011, Astrophys. J. Suppl. Ser., 197, 35, doi: 10.1088/0067-0049/197/2/35

Grossi, M., García-Benito, R., Cortesi, A., et al. 2020, Mon. Not. R. Astron. Soc., 498, 1939, doi: 10.1093/mnras/staa2382

Grudić, M. Y., Hafen, Z., Rodriguez, C. L., et al. 2023, Mon. Not. R. Astron. Soc., 519, 1366, doi: 10.1093/mnras/stac3573

Guedes, J., Callegari, S., Madau, P., & Mayer, L. 2011, Astrophys. J., 742, 76, doi: 10.1088/0004-637X/742/2/76

Guo, Y., Jogee, S., Finkelstein, S. L., et al. 2023, Astrophys. J. Lett., 945, L10, doi: 10.3847/2041-8213/acacfb

Harikane, Y., Inoue, A. K., Ellis, R. S., et al. 2025, Astrophys. J., 980, 138, doi: 10.3847/1538-4357/ad9b2c

Hasheminia, M., Mosleh, M., Tacchella, S., et al. 2022, Astrophys. J. Lett., 932, L23, doi: 10.3847/2041-8213/ac76c8

Hashemizadeh, A., Driver, S. P., Davies, L. J. M., et al. 2022, Mon. Not. R. Astron. Soc., 515, 1175, doi: 10.1093/mnras/stac1195

Hayes, C. R., Majewski, S. R., Shetrone, M., et al. 2018, Astrophys. J., 852, 49, doi: 10.3847/1538-4357/aa9cec

Haywood, M., Di Matteo, P., Lehnert, M. D., Katz, D., & Gómez, A. 2013, Astron. Astrophys., 560, A109, doi: 10.1051/0004-6361/201321397

Helmi, A. 2020, Annu. Rev. Astron. Astrophys., 58, 205, doi: 10.1146/annurev-astro-032620-021917

Helmi, A., Babusiaux, C., Koppelman, H. H., et al. 2018, Nature, 563, 85, doi: 10.1038/s41586-018-0625-x

Hennebelle, P., & Grudić, M. Y. 2024, Annu. Rev. Astron. Astrophys., 62, 63, doi: 10.1146/annurev-astro-052622-031748

Hill, A. R., Muzzin, A., Franx, M., & Marchesini, D. 2017a, Astrophys. J. Lett., 849, L26, doi: 10.3847/2041-8213/aa951a

Hill, A. R., Muzzin, A., Franx, M., et al. 2017b, Astrophys. J., 837, 147, doi: 10.3847/1538-4357/aa61fe

Hopkins, P. F. 2015, Mon. Not. R. Astron. Soc., 450, 53, doi: 10.1093/mnras/stv195

Hopkins, P. F., Wetzel, A., Kereš, D., et al. 2018, Mon. Not. R. Astron. Soc., 480, 800, doi: 10.1093/mnras/sty1690

Hopkins, P. F., Gurvich, A. B., Shen, X., et al. 2023, Mon. Not. R. Astron. Soc., 525, 2241, doi: 10.1093/mnras/stad1902

Horta, D., & Schiavon, R. P. 2024, arXiv e-prints, arXiv:2404.16939, doi: 10.48550/arXiv.2404.16939

Hubble, E. 1929, Proceedings of the National Academy of Science, 15, 168, doi: 10.1073/pnas.15.3.168

Hubble, E. P. 1925, Astrophys. J., 62, 409, doi: 10.1086/142943

Ibarra-Medel, H. J., Sánchez, S. F., Avila-Reese, V., et al. 2016, Mon. Not. R. Astron. Soc., 463, 2799, doi: 10.1093/mnras/stw2126

Imig, J., Price, C., Holtzman, J. A., et al. 2023, Astrophys. J., 954, 124, doi: 10.3847/1538-4357/ace9b8

Iyer, K., & Gawiser, E. 2017, Astrophys. J., 838, 127, doi: 10.3847/1538-4357/aa63f0

Iyer, K. G., Gawiser, E., Faber, S. M., et al. 2019, Astrophys. J., 879, 116, doi: 10.3847/1538-4357/ab2052

Iyer, K. G., Pacifici, C., Calistro-Rivera, G., & Lovell, C. C. 2025, arXiv e-prints, arXiv:2502.17680, doi: 10.48550/arXiv.2502.17680

Jacobs, C., Glazebrook, K., Calabrò, A., et al. 2023, Astrophys. J. Lett., 948, L13, doi: 10.3847/2041-8213/accd6d

Jain, S., Tacchella, S., & Mosleh, M. 2024, The Open Journal of Astrophysics, 7, 113, doi: 10.33232/001c.126775

Jin, B., Ho, L. C., & Sun, W. 2024, arXiv e-prints, arXiv:2412.03455, doi: 10.48550/arXiv.2412.03455

Jones, G. T., & Stanway, E. R. 2023, Mon. Not. R. Astron. Soc., 525, 5720, doi: 10.1093/mnras/stad2683

Jones, T., Ellis, R. S., Richard, J., & Jullo, E. 2013, Astrophys. J., 765, 48, doi: 10.1088/0004-637X/765/1/48

Jönsson, H., Holtzman, J. A., Allende Prieto, C., et al. 2020, Astron. J., 160, 120, doi: 10.3847/1538-3881/aba592

Jung, M., Kim, J.-h., Nguyen, T. H., et al. 2025, arXiv e-prints, arXiv:2505.05720, doi: 10.48550/arXiv.2505.05720

Karim, A., Schinnerer, E., Martínez-Sansigre, A., et al. 2011, Astrophys. J., 730, 61, doi: 10.1088/0004-637X/730/2/61

Kartaltepe, J. S., Rose, C., Vanderhoof, B. N., et al. 2023, Astrophys. J. Lett., 946, L15, doi: 10.3847/2041-8213/acad01

Kauffmann, G., White, S. D. M., & Guiderdoni, B. 1993, Mon. Not. R. Astron. Soc., 264, 201, doi: 10.1093/mnras/264.1.201

Kawata, D., Allende Prieto, C., Brook, C. B., et al. 2018, Mon. Not. R. Astron. Soc., 473, 867, doi: 10.1093/mnras/stx2464

Kennicutt, R. C., & Evans, N. J. 2012, Annu. Rev. Astron. Astrophys., 50, 531, doi: 10.1146/annurev-astro-081811-125610

Kilic, M., Munn, J. A., Harris, H. C., et al. 2017, Astrophys. J., 837, 162, doi: 10.3847/1538-4357/aa62a5

Koekemoer, A. M., Faber, S. M., Ferguson, H. C., et al. 2011, Astrophys. J. Suppl. Ser., 197, 36, doi: 10.1088/0067-0049/197/2/36

Kormendy, J., & Bender, R. 2019, Astrophys. J., 872, 106, doi: 10.3847/1538-4357/aafdff

Kravtsov, A. V., Vikhlinin, A. A., & Meshcheryakov, A. V. 2018, Astronomy Letters, 44, 8, doi: 10.1134/S1063773717120015

Kriek, M., van Dokkum, P. G., Labbé, I., et al. 2009, Astrophys. J., 700, 221, doi: 10.1088/0004-637X/700/1/221

Kriek, M., Price, S. H., Conroy, C., et al. 2019, Astrophys. J. Lett., 880, L31, doi: 10.3847/2041-8213/ab2e75

Kroupa, P. 2001, Mon. Not. R. Astron. Soc., 322, 231, doi: 10.1046/j.1365-8711.2001.04022.x

Kroupa, P., Weidner, C., Pflamm-Altenburg, J., et al. 2013, in Planets, Stars and Stellar Systems. Volume 5: Galactic Structure and Stellar Populations, ed. T. D. Oswalt & G. Gilmore, Vol. 5, 115, doi: 10.1007/978-94-007-5612-0_4

Krumholz, M. R., & Dekel, A. 2010, Mon. Not. R. Astron. Soc., 406, 112, doi: 10.1111/j.1365-2966.2010.16675.x

Le Conte, Z. A., Gadotti, D. A., Ferreira, L., et al. 2024, Mon. Not. R. Astron. Soc., 530, 1984, doi: 10.1093/mnras/stae921

Lee, H.-c., Worthey, G., Trager, S. C., & Faber, S. M. 2007, Astrophys. J., 664, 215, doi: 10.1086/518855

Lee, Y. S., Beers, T. C., An, D., et al. 2011, Astrophys. J., 738, 187, doi: 10.1088/0004-637X/738/2/187

Leitner, S. N. 2012, Astrophys. J., 745, 149, doi: 10.1088/0004-637X/745/2/149

Leja, J., van Dokkum, P., & Franx, M. 2013, Astrophys. J., 766, 33, doi: 10.1088/0004-637X/766/1/33

Lemasle, B., François, P., Bono, G., et al. 2007, Astron. Astrophys., 467, 283, doi: 10.1051/0004-6361:20066375

Lemasle, B., François, P., Piersimoni, A., et al. 2008, Astron. Astrophys., 490, 613, doi: 10.1051/0004-6361:200810192

Lemasle, B., Hajdu, G., Kovtyukh, V., et al. 2018, Astron. Astrophys., 618, A160, doi: 10.1051/0004-6361/201834050

Li, F., Rahman, M., Murray, N., et al. 2025a, Astrophys. J., 979, 7, doi: 10.3847/1538-4357/ad94ef

Li, Z., Wang, X., Cai, Z., et al. 2022, Astrophys. J. Lett., 929, L8, doi: 10.3847/2041-8213/ac626f

Li, Z., Cai, Z., Wang, X., et al. 2025b, arXiv e-prints, arXiv:2506.12129, doi: 10.48550/arXiv.2506.12129

Lian, J., Bergemann, M., Pillepich, A., Zasowski, G., & Lane, R. R. 2023, Nature Astronomy, 7, 951, doi: 10.1038/s41550-023-01977-z

Licquia, T. C., & Newman, J. A. 2015, Astrophys. J., 806, 96, doi: 10.1088/0004-637X/806/1/96

Licquia, T. C., Newman, J. A., & Bershady, M. A. 2016, Astrophys. J., 833, 220, doi: 10.3847/1538-4357/833/2/220

Licquia, T. C., Newman, J. A., & Brinchmann, J. 2015, Astrophys. J., 809, 96, doi: 10.1088/0004-637X/809/1/96

Lilly, S. J., Le Fevre, O., Hammer, F., & Crampton, D. 1996, Astrophys. J. Lett., 460, L1, doi: 10.1086/309975

Lin, Y.-T., Brodwin, M., Gonzalez, A. H., et al. 2013, Astrophys. J., 771, 61, doi: 10.1088/0004-637X/771/1/61

Lofthouse, E. K., Kaviraj, S., Conselice, C. J., Mortlock, A., & Hartley, W. 2017, Mon. Not. R. Astron. Soc., 465, 2895, doi: 10.1093/mnras/stw2895

Lotz, J. M., Jonsson, P., Cox, T. J., & Primack, J. R. 2008a, Mon. Not. R. Astron. Soc., 391, 1137, doi: 10.1111/j.1365-2966.2008.14004.x

Lotz, J. M., Primack, J., & Madau, P. 2004, Astron. J., 128, 163, doi: 10.1086/421849

Lotz, J. M., Davis, M., Faber, S. M., et al. 2008b, Astrophys. J., 672, 177, doi: 10.1086/523659

Lotz, J. M., Koekemoer, A., Coe, D., et al. 2017, Astrophys. J., 837, 97, doi: 10.3847/1538-4357/837/1/97

Luck, R. E., Andrievsky, S. M., Kovtyukh, V. V., Gieren, W., & Graczyk, D. 2011, Astron. J., 142, 51, doi: 10.1088/0004-6256/142/2/51

Luck, R. E., & Lambert, D. L. 2011, Astron. J., 142, 136, doi: 10.1088/0004-6256/142/4/136

Ma, X., Hopkins, P. F., Feldmann, R., et al. 2017, Mon. Not. R. Astron. Soc., 466, 4780, doi: 10.1093/mnras/stx034

MacArthur, L. A., Courteau, S., Bell, E., & Holtzman, J. A. 2004, Astrophys. J. Suppl. Ser., 152, 175, doi: 10.1086/383525

Maciel, W. J., Costa, R. D. D., & Cavichia, O. 2015, Rev. Mexicana Astron. Astrofis., 51, 165, doi: 10.48550/arXiv.1505.07640

Madau, P., & Dickinson, M. 2014, Annu. Rev. Astron. Astrophys., 52, 415, doi: 10.1146/annurev-astro-081811-125615

Madau, P., Ferguson, H. C., Dickinson, M. E., et al. 1996, Mon. Not. R. Astron. Soc., 283, 1388, doi: 10.1093/mnras/283.4.1388

Majewski, S. R., Schiavon, R. P., Frinchaboy, P. M., et al. 2017, Astron. J., 154, 94, doi: 10.3847/1538-3881/aa784d

Mandelker, N., Dekel, A., Ceverino, D., et al. 2017, Mon. Not. R. Astron. Soc., 464, 635, doi: 10.1093/mnras/stw2358

Marchesini, D., van Dokkum, P. G., Förster Schreiber, N. M., et al. 2009, Astrophys. J., 701, 1765, doi: 10.1088/0004-637X/701/2/1765

Marchesini, D., Muzzin, A., Stefanon, M., et al. 2014, Astrophys. J., 794, 65, doi: 10.1088/0004-637X/794/1/65

Marcon-Uchida, M. M., Matteucci, F., & Costa, R. D. D. 2010, Astron. Astrophys., 520, A35, doi: 10.1051/0004-6361/200913933

Martig, M., Bournaud, F., Teyssier, R., & Dekel, A. 2009, Astrophys. J., 707, 250, doi: 10.1088/0004-637X/707/1/250

Matteucci, F., & Francois, P. 1989, Mon. Not. R. Astron. Soc., 239, 885, doi: 10.1093/mnras/239.3.885

Mayer, L., Tamburello, V., Lupi, A., et al. 2016, Astrophys. J. Lett., 830, L13, doi: 10.3847/2041-8205/830/1/L13

McCracken, H. J., Milvang-Jensen, B., Dunlop, J., et al. 2012, Astron. Astrophys., 544, A156, doi: 10.1051/0004-6361/201219507

McLeod, D. J., McLure, R. J., Dunlop, J. S., et al. 2021, Mon. Not. R. Astron. Soc., 503, 4413, doi: 10.1093/mnras/stab731

McWilliam, A., & Zoccali, M. 2010, Astrophys. J., 724, 1491, doi: 10.1088/0004-637X/724/2/1491

Minniti, D., Saito, R. K., Alonso-García, J., Lucas, P. W., & Hempel, M. 2011, Astrophys. J. Lett., 733, L43, doi: 10.1088/2041-8205/733/2/L43

Moreno, J., Torrey, P., Ellison, S. L., et al. 2021, Mon. Not. R. Astron. Soc., 503, 3113, doi: 10.1093/mnras/staa2952

Morishita, T., Ichikawa, T., Noguchi, M., et al. 2015, Astrophys. J., 805, 34, doi: 10.1088/0004-637X/805/1/34

Mosleh, M., Tacchella, S., Renzini, A., et al. 2017, Astrophys. J., 837, 2, doi: 10.3847/1538-4357/aa5f14

Moster, B. P., Naab, T., & White, S. D. M. 2013, Mon. Not. R. Astron. Soc., 428, 3121, doi: 10.1093/mnras/sts261

—. 2018, Mon. Not. R. Astron. Soc., 477, 1822, doi: 10.1093/mnras/sty655

Mowla, L., Iyer, K., Asada, Y., et al. 2024, arXiv e-prints, arXiv:2402.08696, doi: 10.48550/arXiv.2402.08696

Muñoz-Mateos, J. C., Gil de Paz, A., Boissier, S., et al. 2007, Astrophys. J., 658, 1006, doi: 10.1086/511812

Mundy, C. J., Conselice, C. J., & Ownsworth, J. R. 2015, Mon. Not. R. Astron. Soc., 450, 3696, doi: 10.1093/mnras/stv860

Mutch, S. J., Croton, D. J., & Poole, G. B. 2011, Astrophys. J., 736, 84, doi: 10.1088/0004-637X/736/2/84

Muzzin, A., Marchesini, D., Stefanon, M., et al. 2013a, Astrophys. J., 777, 18, doi: 10.1088/0004-637X/777/1/18

—. 2013b, Astrophys. J. Suppl. Ser., 206, 8, doi: 10.1088/0067-0049/206/1/8

Nagaraj, G., Forbes, J. C., Leja, J., Foreman-Mackey, D., & Hayward, C. C. 2022, Astrophys. J., 932, 54, doi: 10.3847/1538-4357/ac6c80

Nataf, D. M., Udalski, A., Gould, A., Fouqué, P., & Stanek, K. Z. 2010, Astrophys. J. Lett., 721, L28, doi: 10.1088/2041-8205/721/1/L28

Noirot, G., Desprez, G., Asada, Y., et al. 2023, Mon. Not. R. Astron. Soc., 525, 1867, doi: 10.1093/mnras/stad1019

Norman, C. A., Sellwood, J. A., & Hasan, H. 1996, Astrophys. J., 462, 114, doi: 10.1086/177133

Oñorbe, J., Boylan-Kolchin, M., Bullock, J. S., et al. 2015, Mon. Not. R. Astron. Soc., 454, 2092, doi: 10.1093/mnras/stv2072

Ownsworth, J. R., Conselice, C. J., Mortlock, A., et al. 2014, Mon. Not. R. Astron. Soc., 445, 2198, doi: 10.1093/mnras/stu1802

Ownsworth, J. R., Conselice, C. J., Mundy, C. J., et al. 2016, Mon. Not. R. Astron. Soc., 461, 1112, doi: 10.1093/mnras/stw1207

Pacifici, C., Iyer, K. G., Mobasher, B., et al. 2023, Astrophys. J., 944, 141, doi: 10.3847/1538-4357/acacff

Papovich, C., Labbé, I., Quadri, R., et al. 2015, Astrophys. J., 803, 26, doi: 10.1088/0004-637X/803/1/26

Patel, S. G., Fumagalli, M., Franx, M., et al. 2013, Astrophys. J., 778, 115, doi: 10.1088/0004-637X/778/2/115

Peña, M., & Flores-Durán, S. N. 2019, Rev. Mexicana Astron. Astrofis., 55, 255, doi: 10.22201/ia.01851101p.2019.55.02.13

Peebles, P. J. E. 1982, Astrophys. J. Lett., 263, L1, doi: 10.1086/183911

Peng, C. Y., Ho, L. C., Impey, C. D., & Rix, H.-W. 2002, Astron. J., 124, 266, doi: 10.1086/340952

—. 2010, Astron. J., 139, 2097, doi: 10.1088/0004-6256/139/6/2097

Petrosian, V. 1976, Astrophys. J. Lett., 210, L53, doi: 10.1086/18230110.1086/182253

Pillepich, A., Nelson, D., Springel, V., et al. 2019, Mon. Not. R. Astron. Soc., 490, 3196, doi: 10.1093/mnras/stz2338

Pillepich, A., Sotillo-Ramos, D., Ramesh, R., et al. 2023, arXiv e-prints, arXiv:2303.16217, doi: 10.48550/arXiv.2303.16217

Pinna, F., Grand, R. J. J., Martig, M., & Fragkoudi, F. 2024, Astron. Astrophys., 691, A61, doi: 10.1051/0004-6361/202450843

Portail, M., Gerhard, O., Wegg, C., & Ness, M. 2017, Mon. Not. R. Astron. Soc., 465, 1621, doi: 10.1093/mnras/stw2819

Prantzos, N., & Boissier, S. 2000, Mon. Not. R. Astron. Soc., 313, 338, doi: 10.1046/j.1365-8711.2000.03228.x

Qi, J., Garcia, A. M., Torrey, P., et al. 2025, arXiv e-prints, arXiv:2501.18687, doi: 10.48550/arXiv.2501.18687

Quinn, P. J., Hernquist, L., & Fullagar, D. P. 1993, Astrophys. J., 403, 74, doi: 10.1086/172184

Raha, N., Sellwood, J. A., James, R. A., & Kahn, F. D. 1991, Nature, 352, 411, doi: 10.1038/352411a0

Rihtaršič, G., Bradač, M., Desprez, G., et al. 2025, Astron. Astrophys., 696, A15, doi: 10.1051/0004-6361/202451117

Rix, H.-W., & Bovy, J. 2013, A&A Rev., 21, 61, doi: 10.1007/s00159-013-0061-8

Robin, A. C., Creze, M., & Mohan, V. 1992, Astrophys. J. Lett., 400, L25, doi: 10.1086/186640

Rodriguez-Gomez, V., Pillepich, A., Sales, L. V., et al. 2016, Mon. Not. R. Astron. Soc., 458, 2371, doi: 10.1093/mnras/stw456

Rodriguez-Gomez, V., Snyder, G. F., Lotz, J. M., et al. 2019, Mon. Not. R. Astron. Soc., 483, 4140, doi: 10.1093/mnras/sty3345

Roman, N. G. 1950, Astrophys. J., 112, 554, doi: 10.1086/145367

Ruphy, S., Robin, A. C., Epchtein, N., et al. 1996, Astron. Astrophys., 313, L21

Rupke, D. S. N., Kewley, L. J., & Barnes, J. E. 2010, Astrophys. J. Lett., 710, L156, doi: 10.1088/2041-8205/710/2/L156

Rusta, E., Salvadori, S., Gelli, V., Koutsouridou, I., & Marconi, A. 2024, arXiv e-prints, arXiv:2407.06255, doi: 10.48550/arXiv.2407.06255

Salim, S., Boquien, M., & Lee, J. C. 2018, Astrophys. J., 859, 11, doi: 10.3847/1538-4357/aabf3c

Salpeter, E. E. 1955, Astrophys. J., 121, 161, doi: 10.1086/145971

Salvadori, S., Ferrara, A., Schneider, R., Scannapieco, E., & Kawata, D. 2010, Mon. Not. R. Astron. Soc., 401, L5, doi: 10.1111/j.1745-3933.2009.00772.x

Sánchez, S. F., Rosales-Ortega, F. F., Iglesias-Páramo, J., et al. 2014, Astron. Astrophys., 563, A49, doi: 10.1051/0004-6361/201322343

Sánchez-Blázquez, P., Rosales-Ortega, F. F., Méndez-Abreu, J., et al. 2014, Astron. Astrophys., 570, A6, doi: 10.1051/0004-6361/201423635

Sánchez-Menguiano, L., Sánchez, S. F., Pérez, I., et al. 2018, Astron. Astrophys., 609, A119, doi: 10.1051/0004-6361/201731486

Santini, P., Ferguson, H. C., Fontana, A., et al. 2015, Astrophys. J., 801, 97, doi: 10.1088/0004-637X/801/2/97

Santini, P., Fontana, A., Castellano, M., et al. 2017, Astrophys. J., 847, 76, doi: 10.3847/1538-4357/aa8874

Sarrouh, G. T., Muzzin, A., Iyer, K. G., et al. 2024, arXiv e-prints, arXiv:2401.08781, doi: 10.48550/arXiv.2401.08781

Sarrouh, G. T. E., Asada, Y., Martis, N. S., et al. 2025, arXiv e-prints, arXiv:2506.21685, doi: 10.48550/arXiv.2506.21685

Sazonova, E., Morgan, C., Balogh, M., et al. 2024, arXiv e-prints, arXiv:2404.05792, doi: 10.48550/arXiv.2404.05792

Schaefer, A. L., Croom, S. M., Allen, J. T., et al. 2017, Mon. Not. R. Astron. Soc., 464, 121, doi: 10.1093/mnras/stw2289

Schaye, J., Crain, R. A., Bower, R. G., et al. 2015, Mon. Not. R. Astron. Soc., 446, 521, doi: 10.1093/mnras/stu2058

Schönrich, R., & Binney, J. 2009, Mon. Not. R. Astron. Soc., 399, 1145, doi: 10.1111/j.1365-2966.2009.15365.x

Schönrich, R., & McMillan, P. J. 2017, Mon. Not. R. Astron. Soc., 467, 1154, doi: 10.1093/mnras/stx093

Schreiber, C., Pannella, M., Elbaz, D., et al. 2015, Astron. Astrophys., 575, A74, doi: 10.1051/0004-6361/201425017

Scoville, N., Aussel, H., Brusa, M., et al. 2007, Astrophys. J. Suppl. Ser., 172, 1, doi: 10.1086/516585

Searle, L., Sargent, W. L. W., & Bagnuolo, W. G. 1973, Astrophys. J., 179, 427, doi: 10.1086/151882

Searle, L., & Zinn, R. 1978, Astrophys. J., 225, 357, doi: 10.1086/156499

Semenov, V. A., Conroy, C., Smith, A., Puchwein, E., & Hernquist, L. 2024, arXiv e-prints, arXiv:2409.18173, doi: 10.48550/arXiv.2409.18173

Sérsic, J. L. 1963, Boletin de la Asociacion Argentina de Astronomia La Plata Argentina, 6, 41

Shen, J., Rich, R. M., Kormendy, J., et al. 2010, Astrophys. J. Lett., 720, L72, doi: 10.1088/2041-8205/720/1/L72

Shipley, H. V., Lange-Vagle, D., Marchesini, D., et al. 2018, Astrophys. J. Suppl. Ser., 235, 14, doi: 10.3847/1538-4365/aaacce

Simons, R. C., Papovich, C., Momcheva, I., et al. 2021, Astrophys. J., 923, 203, doi: 10.3847/1538-4357/ac28f4

Snyder, G. F., Lotz, J., Moody, C., et al. 2015a, Mon. Not. R. Astron. Soc., 451, 4290, doi: 10.1093/mnras/stv1231

Snyder, G. F., Torrey, P., Lotz, J. M., et al. 2015b, Mon. Not. R. Astron. Soc., 454, 1886, doi: 10.1093/mnras/stv2078

Sok, V., Muzzin, A., Jablonka, P., et al. 2022, Astrophys. J., 924, 7, doi: 10.3847/1538-4357/ac2f40

—. 2024, arXiv e-prints, arXiv:2410.21370, doi: 10.48550/arXiv.2410.21370

—. 2025, Astrophys. J., 979, 14, doi: 10.3847/1538-4357/ad96bb

Sotillo-Ramos, D., Pillepich, A., Donnari, M., et al. 2022, Mon. Not. R. Astron. Soc., 516, 5404, doi: 10.1093/mnras/stac2586

Spagna, A., Lattanzi, M. G., Re Fiorentin, P., & Smart, R. L. 2010, Astron. Astrophys., 510, L4, doi: 10.1051/0004-6361/200913538

Speagle, J. S., Steinhardt, C. L., Capak, P. L., & Silverman, J. D. 2014, Astrophys. J. Suppl. Ser., 214, 15, doi: 10.1088/0067-0049/214/2/15

Spinrad, H., & Taylor, B. J. 1971, Astrophys. J. Suppl. Ser., 22, 445, doi: 10.1086/190232

Spite, F., & Spite, M. 1979, The Messenger, 16, 7

Springel, V., & Hernquist, L. 2005, Astrophys. J. Lett., 622, L9, doi: 10.1086/429486

Stanghellini, L., & Haywood, M. 2018, Astrophys. J., 862, 45, doi: 10.3847/1538-4357/aacaf8

Steinmetz, M., & Muller, E. 1995, Mon. Not. R. Astron. Soc., 276, 549, doi: 10.1093/mnras/276.2.549

Stott, J. P., Sobral, D., Swinbank, A. M., et al. 2014, Mon. Not. R. Astron. Soc., 443, 2695, doi: 10.1093/mnras/stu1343

Studholme, C., Hill, D., & Hawkes, D. 1999, Pattern Recognition, 32, 71, doi: https://doi.org/10.1016/S0031-3203(98)00091-0

Suess, K. A., Kriek, M., Price, S. H., & Barro, G. 2019, Astrophys. J., 877, 103, doi: 10.3847/1538-4357/ab1bda

Sun, X., Wang, X., Ma, X., et al. 2024, arXiv e-prints, arXiv:2409.09290, doi: 10.48550/arXiv.2409.09290

Tan, V. Y. Y., Muzzin, A., Marchesini, D., et al. 2024a, arXiv e-prints, arXiv:2402.12433, doi: 10.48550/arXiv.2402.12433

Tan, V. Y. Y., Muzzin, A., Marsan, Z. C., et al. 2022, Astrophys. J., 933, 30, doi: 10.3847/1538-4357/ac7051

Tan, V. Y. Y., Muzzin, A., Sarrouh, G. T. E., et al. 2024b, arXiv e-prints, arXiv:2412.07829, doi: 10.48550/arXiv.2412.07829

Thomas, D., Maraston, C., & Bender, R. 2003, Mon. Not. R. Astron. Soc., 339, 897, doi: 10.1046/j.1365-8711.2003.06248.x

Tinsley, B. M. 1968, Astrophys. J., 151, 547, doi: 10.1086/149455

—. 1980, Fundam. Cosmic Phys., 5, 287, doi: 10.48550/arXiv.2203.02041

Tinsley, B. M., & Gunn, J. E. 1976, Astrophys. J., 203, 52, doi: 10.1086/154046

Tissera, P. B., Rosas-Guevara, Y., Sillero, E., et al. 2022, Mon. Not. R. Astron. Soc., 511, 1667, doi: 10.1093/mnras/stab3644

Tononi, J., Torres, S., García-Berro, E., et al. 2019, Astron. Astrophys., 628, A52, doi: 10.1051/0004-6361/201834267

Torrey, P., Wellons, S., Ma, C.-P., Hopkins, P. F., & Vogelsberger, M. 2017, Mon. Not. R. Astron. Soc., 467, 4872, doi: 10.1093/mnras/stx370

Tully, R. B., & Fisher, J. R. 1977, Astron. Astrophys., 54, 661

Tumlinson, J. 2010, Astrophys. J., 708, 1398, doi: 10.1088/0004-637X/708/2/1398

van den Bosch, F. C. 1998, Astrophys. J., 507, 601, doi: 10.1086/306354 van Dokkum, P. G., Whitaker, K. E., Brammer, G., et al. 2010, Astrophys. J., 709, 1018, doi: 10.1088/0004-637X/709/2/1018

van Dokkum, P. G., Leja, J., Nelson, E. J., et al. 2013, Astrophys. J. Lett., 771, L35, doi: 10.1088/2041-8205/771/2/L35

Vanzella, E., Claeyssens, A., Welch, B., et al. 2023, Astrophys. J., 945, 53, doi: 10.3847/1538-4357/acb59a

Vazdekis, A., Sánchez-Blázquez, P., Falcón-Barroso, J., et al. 2010, Mon. Not. R. Astron. Soc., 404, 1639, doi: 10.1111/j.1365-2966.2010.16407.x

Wake, D. A., Bundy, K., Diamond-Stanic, A. M., et al. 2017, Astron. J., 154, 86, doi: 10.3847/1538-3881/aa7ecc

Walcher, C. J., Wisotzki, L., Bekeraité, S., et al. 2014, Astron. Astrophys., 569, A1, doi: 10.1051/0004-6361/201424198

Wang, J., Kauffmann, G., Overzier, R., et al. 2011, Mon. Not. R. Astron. Soc., 412, 1081, doi: 10.1111/j.1365-2966.2010.17962.x

Wegg, C., & Gerhard, O. 2013, Mon. Not. R. Astron. Soc., 435, 1874, doi: 10.1093/mnras/stt1376

Wegg, C., Gerhard, O., & Portail, M. 2015, Mon. Not. R. Astron. Soc., 450, 4050, doi: 10.1093/mnras/stv745

Wetzel, A. R., Hopkins, P. F., Kim, J.-h., et al. 2016, Astrophys. J. Lett., 827, L23, doi: 10.3847/2041-8205/827/2/L23

White, S. D. M., & Rees, M. J. 1978, Mon. Not. R. Astron. Soc., 183, 341, doi: 10.1093/mnras/183.3.341

Wild, V., Taj Aldeen, L., Carnall, A., et al. 2020, Mon. Not. R. Astron. Soc., 494, 529, doi: 10.1093/mnras/staa674

Williams, R. J., Quadri, R. F., Franx, M., van Dokkum, P., & Labbé, I. 2009, Astrophys. J., 691, 1879, doi: 10.1088/0004-637X/691/2/1879

Willott, C. J., Doyon, R., Albert, L., et al. 2022, Publ. Astron. Soc. Pac., 134, 025002, doi: 10.1088/1538-3873/ac5158

Willott, C. J., Desprez, G., Asada, Y., et al. 2024, Astrophys. J., 966, 74, doi: 10.3847/1538-4357/ad35bc

Withers, S., Muzzin, A., Ravindranath, S., et al. 2023, Astrophys. J. Lett., 958, L14, doi: 10.3847/2041-8213/ad01c0

Wuyts, E., Wisnioski, E., Fossati, M., et al. 2016, Astrophys. J., 827, 74, doi: 10.3847/0004-637X/827/1/74

Wuyts, S., Labbé, I., Franx, M., et al. 2007, Astrophys. J., 655, 51, doi: 10.1086/509708

Wuyts, S., Förster Schreiber, N. M., Genzel, R., et al. 2012, Astrophys. J., 753, 114, doi: 10.1088/0004-637X/753/2/114

Xiang, M., & Rix, H.-W. 2022, Nature, 603, 599, doi: 10.1038/s41586-022-04496-5

Yang, X., Mo, H. J., van den Bosch, F. C., Zhang, Y., & Han, J. 2012, Astrophys. J., 752, 41, doi: 10.1088/0004-637X/752/1/41

York, D. G., Adelman, J., Anderson, Jr., J. E., et al. 2000, Astron. J., 120, 1579, doi: 10.1086/301513

Yu, S., Bullock, J. S., Gurvich, A. B., et al. 2023, Mon. Not. R. Astron. Soc., 523, 6220, doi: 10.1093/mnras/stad1806

Zheng, Z., Wang, H., Ge, J., et al. 2017, Mon. Not. R. Astron. Soc., 465, 4572, doi: 10.1093/mnras/stw3030

Zhou, S., Aragón-Salamanca, A., Merrifield, M., et al. 2023, Mon. Not. R. Astron. Soc., 521, 5810, doi: 10.1093/mnras/stad853